Design of Soft Rigid Devices for Assistive Robotics and Industrial Applications

Muhammad Zubair Iqbal

Supervisor: Prof. Domenico Prattichizzo
Co-Supervisors: Prof. Monica Malvezzi, Prof. Gionata Salvietti
External Co-Supervisor: Prof. Irfan Hussain

Ph.D. Thesis

UNIVERSITÀ DEGLI STUDI DI SIENA
Dipartimento di Ingegneria dell'Informazione e Scienze Matematiche

DOTTORATO DI RICERCA IN INGEGNERIA E SCIENZE DELL'INFORMAZIONE

– CICLO XXXIII –

UNIVERSITÀ
DI SIENA
1240

Design of Soft Rigid Devices for Assistive Robotics and Industrial Applications

Muhammad Zubair Iqbal,
Ph.D. Thesis, University of Siena,
May 2021.

A digital version of the thesis is available at
https://drive.google.com/drive/folders/1CKDrAp4xy2cIFd15dmoNr96B8bmbJXdJ?usp=sharing
or can be obtained by e-mail on request from the author:
mxuberiqbal@gmail.com.

Muhammad
Zubair Iqbal
30.08.2021
23:25:19
GMT+01:00

To My Family and Friends

Muhammad
Zubair Iqbal
30.08.2021
23:25:19
GMT+01:00

Acknowledgements

I would like to Thank Almighty Allah for giving me the courage and strength to complete this thesis. Verily without Allah help no one is able to complete what he/she has started.

I would like to thank my advisor Prof. Domenico Prattichizzo for continuous guiding and support over these years. You have been a tremendous mentor and have set a wonderful example of excellence as instructor and role model. Prof, I really thank you so much for encouraging my research and for allowing me to grow as a research scientist. Your advice and ideas related to my research have always been fruitful.

I would like to thank Prof. Monica Malvezzi for helping me out in my research and thesis, whenever I needed a direction you have provided me with an excellent direction.

I would also like to thank Prof. Gionata Salvietti for supporting me in thesis and refining my ideas about the research. You have been a guide starting from my very first day of research till today.

I would like to thank my thesis committe members for all their guidance through the process, discussion, ideas and feedback have been absolutely invaluable.

A very special thank to my family for the love, support and constant encouragement throughout my Ph.D. In particular, I am very grateful to my parents and my sisters. No doubt I would have not been able to complete it.

I wish to thank my fellow lab mates for helping me during these years of hard work. It has always been a great experience to share the lab space with such brilliant minds, they are always willing to support my endeavors and extend a helping hand in my research.

At the end, I would like to thank all my friends, especially here in Siena. They have always been supportive through the tough time, providing me with time to relax the mind and start off with a fresh mind. The good company of friends is really important and I can say I have enjoyed the company of good friends.

Muhammad
Zubair Iqbal
30.08.2021
23:25:19
GMT+01:00

Abstract

Soft robots are getting more and more popular in rehabilitation and industrial scenarios. They often come into play where the rigid robots fail to perform certain functions. The advantage of using soft robots lies in the fact that they can easily conform to the obstacles and depict delicacy in gripping, manipulating, and controlling deformable and fragile objects without causing them any harm. In rehabilitation scenarios, devices developed on the concept of soft robots are pretty helpful in changing the lives of those who suffer body impairments due to stroke or any other accident. These devices provide support in carrying out daily life activities without the need and support of another person. Also, these devices are beneficial in the training phase where the patient is going through the rehabilitation phase and has to do multiple exercises of the upper limb, wrist, or hand. Similarly, the grippers developed on the basic principle of soft robots are very common in the industries or at least getting common. Their advantages are a lot as compared to the rigid robotics manipulators. Soft grippers tend to adapt to the shape of the object without causing any damage to it, providing a stable grasp. It can also help reduce the complexity in the design and development, for example, underactuated. Underactuated grippers use the minimum number of actuators to provide the same function that requires more actuators with a rigid gripper. Also, the soft structure allows to design specific trajectories to complete a certain grasping and manipulation task. This thesis presents devices for rehabilitation and assistive application to help people with upper limb impairment, especially wrist and hand functions. These devices have been designed to provide the people, with limited capabilities of hand and wrist functions, to live their lives with ease without being dependent on any other family member. Similarly, I present different soft grippers and a soft environment that provides different advantages and can do various grasp and manipulation tasks. I have presented results for each device, rehabilitation and assistive devices are used by a patient suffering from stroke and having limited movement of wrist and hand function. At the same time, the grippers are supported with a set of experiments that provide deep insight into the advantages of each gripper in industrial applications.

Muhammad
Zubair Iqbal
30.08.2021
23:25:19
GMT+01:00

Table of contents

Chapter 1

Introduction

"*And that man shall have nothing but what he strives for. And that his striving shall soon be seen.*"

Al-Quran 53:39-40

Robotics has considerably improved industrial processes and is expected to become an important part of our daily life [1] soon. Human labor has always been associated with the acquisition of specific skills, methods, and tools, making the world and its environment easier and more effective. Increasing competition from industrial robots for tasks normally carried out by human hands has led to the need for more effective handling equipment. Grasping and manipulation of different objects are fundamental functions of both humans and robots. Grasping, in simple words, can be defined as the ability to pick up and hold an object against external disturbances, while manipulation is the ability to exert forces on the object and thus cause its rotation and displacement concerning the reference frame of the manipulator. Human do so with their hands; the Human hand can be regarded as a complex end effector allowing the human to carry out different task related to grasping and manipulation of different objects in everyday life, while robot grippers are the end effector used by robots to interact with the environment or that comes in direct contact with the workpiece. Furthermore, these end effectors of the robots can gather sensory information about the physical properties of the objects.

1.1 Rigid Gripper

In the recent era, industrial production is loaded with many conventional manipulators or end effectors such as rigid operators and dexterous hands. Traditional robotic gripper consists of a set of mostly rigid joints and links [2]. Actuators can be installed within the links or joints or in the base of the gripper utilizing cables or tendon-like structures. A wide range of sensors can be installed in the robotic grippers; the most common are Hall-effect sensors, encoders, torque sensors, tendon tension sensors. They can be used to estimate the position and velocity of the gripper components. Similarly, to gather information about the objects, many sensors

like pressure sensors, optical sensors, resistive and conductive sensors, electromagnetic sensors, etc., can be used. The design of a robotic gripper can be a simple one finger with a fixed plate to support the grasp, or it can be two fingers making a parallel gripper, or it can be more fingers making a dexterous hand. The choice of a dexterous hand is often motivated by the quest for flexibility and dexterity of human hands [3]. The structure of these rigid manipulators composed of metals or plastic materials. The design contains complex mechanical transmission structures, sophisticated sensors, and closed-loop control systems, relying on precise control to grasp objects. However, when it comes to grasping and manipulating flexible or delicate objects like fruits, glass etc., there is a higher demand in grasping motion by rigid manipulators. Unlike industrial robots requiring high precision and rigidity, compliance is one of the major concerns in robotic studies because hard contacts make robots unadaptable to the most natural environment, especially dynamic human environment, and pose high risks to humans and objects. Similarly, to make a rigid gripper more adaptive to the shape of the object to be grasped includes adding a lot of mechanisms and actuators, which makes it cumbersome and not very easy to use. Also, it makes the gripper less robust in terms of use, and the overall weight can increase a lot, bearing a lot of load on the robot arm itself. To overcome the issue of weight and adaptability, soft robots came to attention due to their superiority compared with traditional robots in their adaptability to complex environments. In the last few decades, a lot of work has been carried on soft grippers for various functions. Especially when it comes to grasping brittle and delicate objects, soft grippers are considered the best choice as compared to rigid grippers. Recently, more compliant and mechanical simpler, anthropomorphic grippers have been described that resort to flexible and partly soft components [4, 5]. These grippers are often cited as an example of morphological computation where control complexity is reduced by material softness and mechanical compliance [6].

1.2 Soft Gripper

Advanced materials and soft components are increasingly studied for the design of lighter, simpler, and possibly more universal grippers. The importance of compliance in grasping has long been recognized. Unless very carefully controlled, making contact between a hard gripper and a hard object leads to shocks that could damage the object or push it out of the desired path. A simple but only partial solution, widely employed in robotic end effectors, is to add compliant materials to the gripping elements (for instance, in the simple form of rubber pads). Contact between bodies introduces constraints to the movement of those bodies. For this reason, underactuation (i.e., having a higher number of degrees of freedom than the number of actuators) is essential for grippers since it can allow them to conform to the objects' shape without active position control. Human fingers are an example of such underactuation, each one consisting of one tendon and three links (two degrees of freedom). Soft grippers integrate underactuation and compliance by replacing rigid joints with a structure made of hyper-elastic materials that deform continuously in response to external or internal actuators and to the interaction with the objects. Complaint materials thus play a key role in soft grippers: material characteristics such as maximum elastic deformation, stiffness, and viscoelasticity influence the stroke of the gripper, the force it can generate, and its response time. The selection and

engineering of materials are therefore crucial in the design of soft grippers with enhanced capabilities. The most widely used material for soft grippers is elastomers; thanks to the large stains, they can reversibly sustain (>100 %). Silicone rubbers have been the most popular choice for grippers thanks to their ease of fabrication, low toxicity, robustness, and low mechanical damping coefficients. The work presented in this Thesis dealt with different soft devices used for Assistive and Industrial Applications. It also incorporates a mathematical model for the design of soft components of the soft gripper as well as the design of stiff parts to make them act like a soft compliant part. The Thesis is oriented on the Design and Development of devices that comprise the soft and rigid structure, and the application lies in rehabilitation and industrial scenarios. The next section will shed some light on the organization and contribution of this Thesis.

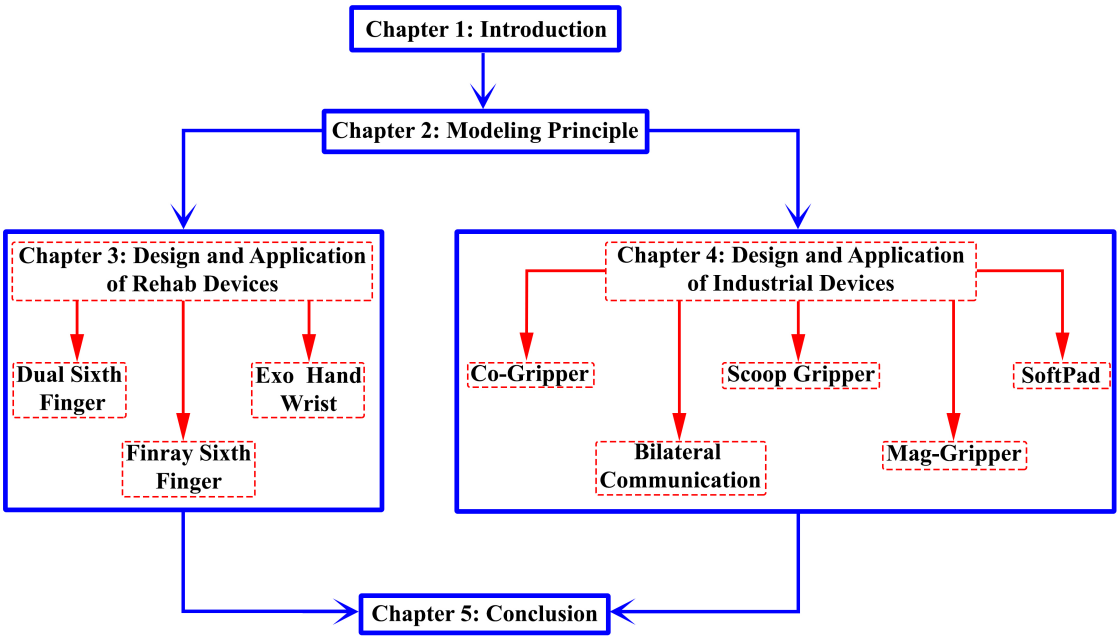

Fig. 1.1 Structure of Thesis

1.3 Organization and Main Contribution of Thesis

The Thesis is organized as in Fig. 1.1. The Thesis starts with the first chapter of the Introduction, and the Second chapter explains Mathematical Models for the design of soft components of the devices. The third chapter explains the design and application of devices related to Rehabilitation, which include dual sixth finger design for stroke patients, a completely new structure to design a complaint sixth finger using stiff material and an Exo hand and wrist device design for the rehabilitation of hand and wrist functions. The fourth chapter explains different devices for industrial applications, which include cooperative gripper, bilateral haptic

collaboration for human-robot cooperation, Soft ScoopGripper with embodied constraints, Mag gripper design to precisely handle clothes. In the end, the chapter explains the soft sensorized surface to be used with rigid grippers. The Thesis concludes with Chapter 5.

1.3.1 Design of multiple wearable robotic extra fingers for human hand augmentation

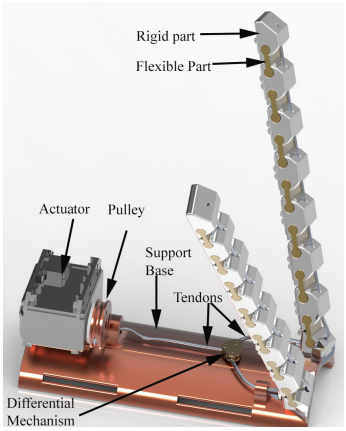

This section describes the main criteria that were followed to design a double robotic extra finger for compensating and augmenting human hand abilities. This work includes re-designing all the mechanical components in a parametric way to further exploit the modularity of the device and adapt it to different users and applications. It describes a solution with two extra fingers actuated with a single motor, and It analyses the requirements and main design aspects of the differential mechanism that is necessary to guarantee the proper closure movement of each finger. The device that will be described in the main section consists of two main parts: the support base and the mobile part, composed of two modular robotic fingers actuated by means of two tendons and a single motor to control. The end edge of each tendon is fixed on the distal module, while the opposite side is fastened to an element sliding inside the differential box. Fingers are composed of rigid phalanges connected by compliant interphalangeal joints that can be approximated as simple 1-DoF revolute joints. When the motor actuates the differential by pulling the sliding element, both tendons flex the fingers, which assume a configuration that allow them to grasp objects, while when the torque of the motor is released, the passive elastic elements in the joints restore the fingers to their initial extended configuration.

1.3.2 Discrete Cosserat Approach for Closed-Chain Soft Robots: Application to the Fin-Ray Finger

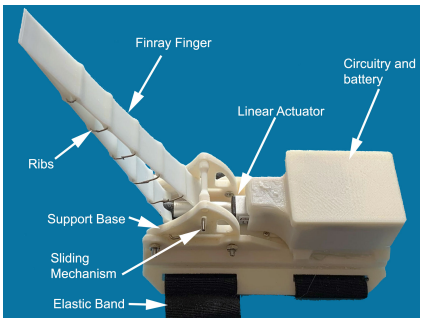

This section describes a general mathematical formulation for the analysis of closed-chain soft robots and, in particular, of Fin- Ray structures. The model is based on the Discrete Cosserat approach, which has been extended to consider closed-chain hybrid geometries composed of soft and rigid elements. The model has been employed to investigate an optimal design for a soft robotic Fin-Ray finger, and finally, a prototype has been fabricated. The FRE structure's ability to conform to an external force while maintaining rigidness out of its grasping plane inspired us to exploit its use as supernumerary robotic fingers to meet their ergonomics and functional requirements.

1.3.3 Design, Development, and Control of a Hand/Wrist Exoskeleton for Rehabilitation and Training

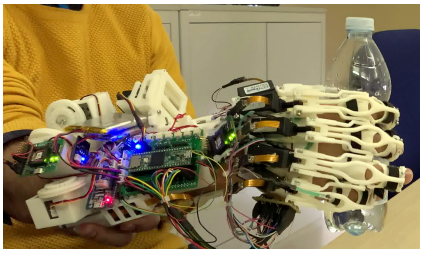

In particular, robot-augmented therapy is a clinically verified path forward to improve rehabilitation outcomes for several neuromuscular conditions, such as cerebrovascular and spinal cord injuries. Technology advancements in the medical and assistive field allow people with disabilities and diseases to have a life that, in many cases, is almost completely autonomous. This section describes an exoskeleton for hand and wrist motion assessment and training. Unlike most of the available devices, the one described here has been designed from the user's point of view to be easily and independently wearable, easy to control and manage, modular and versatile. The patient can use the device in collaboration with the therapist or autonomously and is composed of two independent and modular elements: the wrist actuation and the hand actuation systems. To the best of our knowledge, the proposed device represents the first attempt to realize a wearable hand/wrist exoskeleton able to record and playback motions and, at the same time, store data for further analyses.

1.3.4 The Co-Gripper: a Wireless Cooperative Gripper for Safe Human Robot Interaction

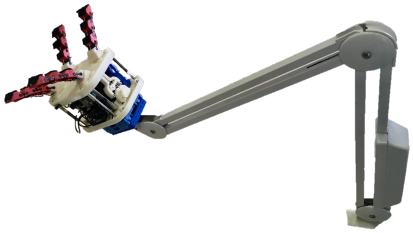

Exploiting compliance and environment constraints with underactuated compliant hands is also a lively research branch for robotic end-effectors. In all these works, however, the attention was mostly devoted to analyzing hand/gripper manipulation capabilities and adaptability rather than specifically evaluating the interaction with humans. Although robot end-effectors are most of the time the part of the robot more proximal to the human partner in collaborative scenarios, only a few works have been dedicated to the design and the control of collaborative grippers. This section describes some design guidelines and proposes a prototype of a soft–gripper explicitly devoted to easy and safe interaction with human operators in cooperative tasks. The key ingredient of the soft-grippers is the intrinsic softness of the devices, i.e., their embodied ability to comply and adapt to features of the objects and the environment.

1.3.5 Bilateral Haptic Collaboration for Human-Robot Cooperative Tasks

Human-Robot collaboration is an important field. However, to achieve effective collaboration, the robots should not only be safe and respond to a human command but should also be able to communicate with the human collaborator, as this is an essential feature for human dyads.

The work carried out to achieve effective collaboration includes mainly receiving acknowledgment from the robot in vibrotactile feedback. The haptic interfaces are used to inform the human that the robotic system detected a particular behavior of its collaborator. The concept of bilateral haptic collaboration described in this section goes beyond the simple communication of intention or posture detection. The interface we propose can be used both to control the robotic gripper motion and to haptically display information related to the tasks that are measured by the robot.

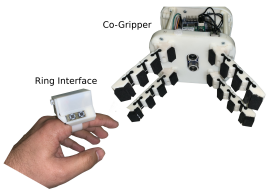

1.3.6 Soft Hands with Embodied Constraints: The Soft ScoopGripper

As designed up to now, one of the main issues of soft hands is that the enabling environmental constraints are not always reachable or detectable by the grasp planning system, making it difficult to exploit the primitives of grasping developed for soft hands. The Soft ScoopGripper comprises two soft modular fingers actuated by a single tendon through a differential system, similar to the fingers designed for the soft gripper. Flexible joints connect rigid links to build a deformable structure able to adapt to the shape of the grasped object. The scoop, representing the constraint, is connected through a flexible hinge to the hand palm. This allows to easily adapt the scoop orientation to the surface where it slides. The soft hinge also allows actuating the scoop to move toward the fingers, increasing grasp stability.

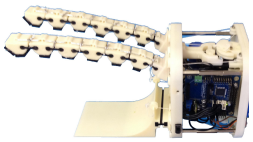

1.3.7 A Soft-Rigid Gripper Augmented with an Electromagnet to Precisely Handle Clothes

This section describes a novel approach to the execution of autonomous clothing manipulation by exploiting the presence of an attractive magnetic force established between the gripper and the garment. As a suitable tool, it describes Mag-gripper, an augmented jaw gripper embedding an electromagnet. As it will become clear in the following, this design choice allows to achieve a repeatable extended point-like grasp: Since the location where clothing is grasped causes its configuration after the grasp has occurred, having a repeatable grasping capability results in having repeatable clothing configuration. To the best of my knowledge, no grippers exploiting the magnetic force so far have been exploited for clothing manipulation. Moreover, the difference with commercially available grippers exploiting the presence of a magnet is desired to exploit the magnetic force only to establish the contact between the gripper and the garment, whereas the presence of a permanent magnet would need an opposite magnetic field to allow the object detachment any time the grasp has to be released. After the extended point-like grasp has occurred, the magnetic force is no more

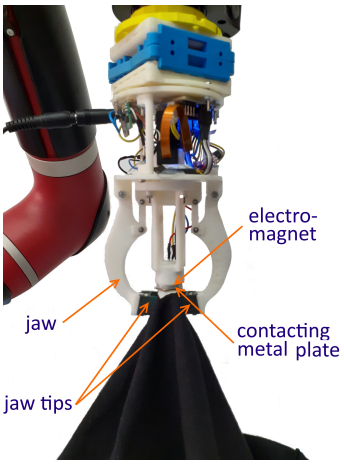

needed: the electromagnet is deactivated to avoid overheating, and secure grasp maintenance is achieved by exploiting the gripper jaws. In this approach, the garment has to embed a metallic part. During data acquisition for Machine Learning-based approaches, researchers can easily insert these parts in the desired locations to meet grasp precision requirements. However, the implementation of autonomous garment manipulation applications for the general public will be possible only by establishing a synergy between companies and researchers. Such synergy will be encapsulated in novel clothing production lines specifically thought to allow autonomous manipulation. These novel garments will have the needed metal parts embedded as ornamental or brand elements, such as buttons and small plates.

1.3.8 Grasping with the SoftPad, a soft sensorized surface for exploiting environmental constraints with rigid grippers

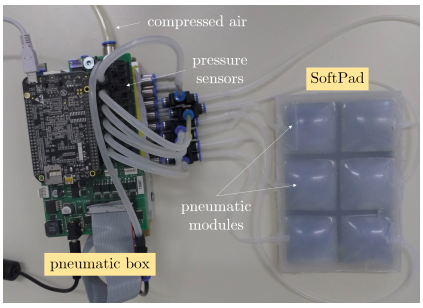

A common trend in robotic manipulation is to build compliant hands that can exploit environmental constraints to perform robust grasps. Different from classical rigid robotic hands, soft hands can safely interact with constraints present in the environment. Thus, grasp planning with soft hands does not rely on exact models and precise positioning of contact points but aims to use direct physical interaction with the environment to constrain and grab the object. Since, in large-scale industrial applications, end-effectors are primarily rigid. This is not possible with rigid grippers. How can we exploit environmental constraints using rigid industrial grippers? This section describes a novel solution to take advantage of the strengths of both soft and rigid robotics approaches. We propose to use rigid robotic grippers while adding compliance to the surface laying beneath the objects to be grasped. In other terms, we shift the focus from the gripper to the environment.

Chapter 2

Modeling Principle

"*Science and technology can solve all the world's problems, and historically it has been shown to make the world* better and better."

Zoltan Istvan

2.1 Modeling Principle Soft Rigid Links

This section focuses on Mathematical model devised for the design of Soft Rigid Links.

2.1.1 Mechanical model of a soft–rigid finger

In this section we extend the mathematical formulation presented in [7]. In such work we applied the general mathematical model introduced in [8] to a modular structure composed of rigid links connected through compliant joints. We choose this type of formulation since it allows to model three dimensional deformations, while other simplified models that we used in our previous works, e.g., the one introduced in [9], considered only bending deformation in the principal flexion/extension plane of the finger. In particular, in the model we use in this work the compliant joint is represented as a continuous beam with a distributed three-dimensional deformation, rather than as an ideal revolute joint with a single stiffness value. For the sake of clarity, we reported in the Appendix in Section A a summary of the kinematic formulation previously introduced in [7]. The modular structure of a finger, the reference frames for the components, and the main transformations are reported in Fig. 2.1.

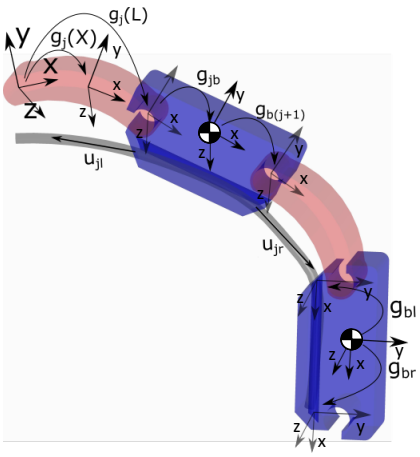

Fig. 2.1 Modular structure of a finger, composed of soft (red) and rigid (blue) parts. Reference frames for each component, and main transformations.

In the following we derive the generalized dynamic equation for a soft-rigid structure by means of the d'Alembert's principle.

2.1.1.1 Rigid Body dynamics

The equations of motion for the dynamics of a rigid phalanx of the i^{th} module are obtained from the Poincaré variational calculus of [10]. Including the loads due to the adjacent soft bodies, this calculus yields to

$$\begin{aligned} &\mathscr{M}_{ib}\dot{\boldsymbol{\eta}}_{ib} + \mathrm{ad}^*_{\boldsymbol{\eta}_{ib}}\mathscr{M}_{ib}\boldsymbol{\eta}_{ib} = \\ &\mathrm{Ad}^{*-1}_{\boldsymbol{g}_{ib}}\mathscr{F}_{J_{iR}} - \mathrm{Ad}^*_{\boldsymbol{g}_{b(i+1)}}\mathscr{F}_{J_{(i+1)L}} + \mathscr{F}_{e_{ib}} \end{aligned} \tag{2.1}$$

where $\mathscr{M}_{ib} \in \mathbb{R}^{6\times 6}$ is the screw inertia matrix, $\{\boldsymbol{\eta}_{ib}$ is the twist of the rigid phalanx, $\mathscr{F}_{e_{ib}} \in \mathbb{R}^6$ is the external load and $\mathscr{F}_{J_{iR}}$, $\mathscr{F}_{J_{(i+1)L}} \in \mathbb{R}^6$ are the forces transmitted across the clamping with the soft articulation of the same module i and of the next module $i+1$ respectively (the subscript R and L stand for the right and left boundary of a soft body), $\mathrm{Ad}^*_{\boldsymbol{g}}$ is the adjoint representation ($\in \mathbb{R}^{6\times 6}$) of the Lie group $SE(3)$ (see Appendix A.1). All the quantities are evaluated locally.

By indicating with $\boldsymbol{q}$ the equivalent joint vector and with $\boldsymbol{J}_{ib}$ the locally evaluated geometric Jacobian of the body, let us define a virtual displacement $\boldsymbol{\zeta}_{ib} \in \mathbb{R}^6$ which satisfies $\boldsymbol{\zeta}_{ib} = \boldsymbol{J}_{ib}\delta\boldsymbol{q}$. In order to eliminate the constraint force, we have to project the equation of motion onto the linear space generated by $\boldsymbol{\zeta}^T_{ib} = \delta\boldsymbol{q}^T\boldsymbol{J}^T_{ib}$. Applying this projection to (2.1), we obtain

$$\begin{aligned} &\forall \delta\boldsymbol{q} \in \mathbb{R}^{2N}: \\ &\delta\boldsymbol{q}^T\left\{\boldsymbol{J}^T_{ib}\left[\mathscr{M}_{ib}\left(\boldsymbol{J}_{ib}\ddot{\boldsymbol{q}} + \dot{\boldsymbol{J}}_{ib}\dot{\boldsymbol{q}}\right) + \mathrm{ad}^*_{\boldsymbol{J}_{ib}\dot{\boldsymbol{q}}}\left(\mathscr{M}_{ib}\boldsymbol{J}_{ib}\dot{\boldsymbol{q}}\right)\right]\right. \\ &\left.-\boldsymbol{J}^T_{ib}\left(\mathrm{Ad}^{*-1}_{\boldsymbol{g}_{ib}}\mathscr{F}_{J_{iR}} - \mathrm{Ad}^*_{\boldsymbol{g}_{b(i+1)}}\mathscr{F}_{J_{(i+1)L}}\right) - \boldsymbol{J}^T_{ib}\mathscr{F}_{e_{ib}}\right\} = \boldsymbol{0}, \end{aligned} \tag{2.2}$$

which leads to the generalized dynamic equation

$$\begin{aligned}&\left(\boldsymbol{J}_{ib}^{T}\mathscr{M}_{ib}\boldsymbol{J}_{ib}\right)\ddot{\boldsymbol{q}}+\boldsymbol{J}_{ib}^{T}\left(\mathrm{ad}^{*}_{\boldsymbol{J}_{ib}\dot{\boldsymbol{q}}}\mathscr{M}_{ib}\boldsymbol{J}_{ib}+\mathscr{M}_{ib}\dot{\boldsymbol{J}}_{ib}\right)\dot{\boldsymbol{q}}=\\&\boldsymbol{J}_{ib}^{T}\left(\mathrm{Ad}^{*-1}_{\boldsymbol{g}_{ib}}\mathscr{F}_{J_{iR}}-\mathrm{Ad}^{*}_{\boldsymbol{g}_{b(i+1)}}\mathscr{F}_{J_{(i+1)L}}\right)+\boldsymbol{J}_{ib}^{T}\mathscr{F}_{e_{ib}}=\boldsymbol{0}.\end{aligned}\tag{2.3}$$

In our case, the external loads acting on the rigid body are given by the cable actuation $\mathscr{F}_{a_{ib}}$, the gravity force $\mathscr{F}_{g_{ib}}$ and the concentrated contact forces $\mathscr{F}_{p_{ib}}$ due to the manipulation interactions, *i.e.*:

$$\mathscr{F}_{e_{ib}}=\mathscr{F}_{a_{ib}}+\mathscr{F}_{g_{ib}}+\mathscr{F}_{p_{ib}}.\tag{2.4}$$

Regarding the cable actuation, let's define $\boldsymbol{g}_{bl}$ and $\boldsymbol{g}_{br}$ the fixed rigid transformation between the body frame of the rigid body and the cable frame while it enters and leaves the rigid body respectively (Fig. 2.1). Then, the direction of action of the cable entering $\boldsymbol{u}_{il}/\|\boldsymbol{u}_{il}\|$ and leaving $\boldsymbol{u}_{ir}/\|\boldsymbol{u}_{ir}\|$ the rigid phalanx of the i^{th} module can be expressed in the cable frame as:

$$\begin{pmatrix}\mathbf{R}_{il} & \mathbf{u}_{il}\\ \mathbf{0}^{T} & 1\end{pmatrix}=\boldsymbol{g}_{bl}^{-1}\boldsymbol{g}_{ib}^{-1}\boldsymbol{g}_{i}(L)^{-1}\boldsymbol{g}_{bi}^{-1}\boldsymbol{g}_{br}\,,\tag{2.5}$$

$$\begin{pmatrix}\mathbf{R}_{ir} & \mathbf{u}_{ir}\\ \mathbf{0}^{T} & 1\end{pmatrix}=\boldsymbol{g}_{br}^{-1}\boldsymbol{g}_{b(i+1)}\boldsymbol{g}_{(i+1)}(L)\boldsymbol{g}_{(i+1)b}\boldsymbol{g}_{bl}\,,\tag{2.6}$$

which yields to

$$\begin{aligned}&\mathscr{F}_{a_{ib}}=\mathscr{F}_{al_{ib}}+\mathscr{F}_{ar_{ib}}\\&=T_{i}\mathrm{Ad}^{*}_{\boldsymbol{g}_{bl}}\begin{bmatrix}0\,0\,0\,\dfrac{\boldsymbol{u}_{il}^{T}}{\|\boldsymbol{u}_{il}\|}\end{bmatrix}^{T}+T_{i+1}\mathrm{Ad}^{*}_{\boldsymbol{g}_{br}}\begin{bmatrix}0\,0\,0\,\dfrac{\boldsymbol{u}_{ir}^{T}}{\|\boldsymbol{u}_{ir}\|}\end{bmatrix}^{T},\end{aligned}\tag{2.7}$$

where T_i is the tension of the cable of module i. It should be noticed that the cable tension decreases along its path to the tip due to the frictional interaction exerted at the corners produced while entering and leaving the rigid phalanx (considering straight path while inside). Using the capstan equation, the frictional effect can be modeled as:

$$T_{i}=T_{i-1}e^{-\mu\phi_{i}}\,,\tag{2.8}$$

where μ is the coefficient of friction and ϕ_i is the angle swept by the turns within the i^{th} module. Since there are two cable turns for each module, *i.e.* one at the base and one at the tip of the soft joint, we have:

$$\phi_{i}=\cos^{-1}\left(\frac{u_{(i-1)rx}}{\|\boldsymbol{u}_{(i-1)r}\|}\right)+\cos^{-1}\left(-\frac{u_{ilx}}{\|\boldsymbol{u}_{il}\|}\right)\,.\tag{2.9}$$

It's worth to notice that, in case of 2D configuration (no torsion), the sweep angle simplify to:

$$\phi_{i}=L\theta_{i}\,,\tag{2.10}$$

because, in this case, $L\theta_i$ fully represents the relative orientation of two consecutive phalanxes.

The contact force $\mathscr{F}_{p_{ib}}$ is considered to be a given input, while the gravity force is found by

$$\mathscr{F}_{g_{ib}} = \mathscr{M}_{ib}\mathrm{Ad}^{-1}_{\boldsymbol{g}_{si_b}}\mathscr{G}\,, \tag{2.11}$$

where $\mathscr{G} = [0\,0\,0\,0\,\,-9.81\,0]^T$ is the gravity twist with respect to the spatial frame.

2.1.1.2 Soft Body dynamics

The equations of motion for the dynamics of a soft body i are obtained from the extension to continuum media of the Poincaré variational calculus [11]. Evaluated with respect to the body frame, this calculus yields to the strong form of a Cosserat beam, *i.e.*, the partial differential equations and their boundary conditions

$$\begin{aligned} &\mathscr{M}_i\dot{\boldsymbol{\eta}}_i + \mathrm{ad}^*_{\boldsymbol{\eta}_i}\mathscr{M}_i\boldsymbol{\eta}_i = \mathscr{F}'_{i_i} + \mathrm{ad}^*_{\boldsymbol{\xi}_i}\mathscr{F}_{i_i} + \bar{\mathscr{F}}_{e_i}\,,\\ &\mathscr{F}_{i_i}(0) = -\mathscr{F}_{J_{iL}}\,,\ \mathscr{F}_{i_i}(L) = -\mathscr{F}_{J_{iR}}\,, \end{aligned} \tag{2.12}$$

where $\mathscr{M}_i = \mathrm{diag}(J_x, J_y, J_z, A, A, A)\rho_i \in \mathbb{R}^{6\times 6}$ is the screw inertia matrix of the cross section (with mass density ρ_i), $\boldsymbol{\eta}_i$ is its twist, $\bar{\mathscr{F}}_{e_i}(X) \in \mathbb{R}^6$ is the distributed external load and $\mathscr{F}_{i_i}(X) \in \mathbb{R}^6$ is the internal force due to the elasticity of the soft body. All the quantities are evaluated locally.

Let us define a virtual displacement field $\boldsymbol{\zeta}_i(\cdot)$ which satisfies $\boldsymbol{\zeta}_i(X) = \boldsymbol{J}_i(X)\delta\boldsymbol{q} \in \mathbb{R}^6$. Following steps similar to what we have done for the rigid body case, we obtain the following generalized dynamics for a soft body [8]

$$\begin{aligned} &\left(\int_0^L \boldsymbol{J}_i^T\,\mathscr{M}_i\boldsymbol{J}_i\,dX\right)\ddot{\boldsymbol{q}} + \int_0^L \boldsymbol{J}_i^T\left(\mathrm{ad}^*_{\boldsymbol{J}_i\dot{\boldsymbol{q}}}\mathscr{M}_i\boldsymbol{J}_i + \mathscr{M}_i\dot{\boldsymbol{J}}_i\right)dX\\ &\dot{\boldsymbol{q}} = \int_0^L \boldsymbol{J}_i^T\left(\mathscr{F}'_{i_i} + \mathrm{ad}^*_{\boldsymbol{\xi}_i}\mathscr{F}_{i_i}\right)dX + \int_0^L \boldsymbol{J}_i^T\bar{\mathscr{F}}_{e_i}\,dX. \end{aligned} \tag{2.13}$$

Regarding the internal elastic force, a linear viscoelastic constitutive model, based on the Kelvin–Voigt assumptions, is chosen [12].

$$\mathscr{F}_{i_i} = \boldsymbol{\Sigma}_i\left(\boldsymbol{\xi}_i - \boldsymbol{\xi}^*\right) + \boldsymbol{\Upsilon}_i\dot{\boldsymbol{\xi}}_i\,, \tag{2.14}$$

where

$$\boldsymbol{\Sigma}_i = \mathrm{diag}(G_iJ_x, E_iJ_y, E_iJ_z, E_iA, G_iA, G_iA) \in \mathbb{R}^{6\times 6} \text{ and}$$

$$\boldsymbol{\Upsilon}_i = \mathrm{diag}(J_x, 3J_y, 3J_z, 3A, A, A)\nu \in \mathbb{R}^{6\times 6}$$

are the screw stiffness and viscosity matrix of the i^{th} module (E_i being the young modulus, G_i the shear modulus, ν the shear viscosity, A the cross sectional area and $J_{(x,y,z)}$ the moments of area), $\boldsymbol{\xi}_i$ is the strain twist, and $\boldsymbol{\xi}^*$ is the reference configuration strain twist. Considering a constrained strain state defined by the matrix $\boldsymbol{B}$ (as detailed in [7] and summarized in

Appendix A.2, eq. (A.3)) the expression of the internal elastic force becomes

$$\mathscr{F}_{i_i} = \boldsymbol{\Sigma}_i \boldsymbol{B}\left(\boldsymbol{q}_i - \boldsymbol{q}^*\right) + \boldsymbol{\Upsilon}_i \boldsymbol{B}\dot{\boldsymbol{q}}_i \,. \tag{2.15}$$

Regarding the distributed external load, only the gravity force need to be considered (*i.e.* $\bar{\mathscr{F}}_{e_i} = \bar{\mathscr{F}}_{g_i}$), which can be expressed as

$$\bar{\mathscr{F}}_{g_i}(X) = \mathscr{M}_i \mathrm{Ad}^{-1}_{\boldsymbol{g}_{si}} \mathscr{G} \,. \tag{2.16}$$

2.1.1.3 Soft-Rigid Finger

The virtual work of the whole finger is the sum of the virtual works of each subsystem. Thus, the equation of motion for a soft-rigid multi-body system is evaluated as the sum of equations like (2.3) and (2.13) over all the bodies of the system. This operation yields to the generalized dynamics equation in the classical form

$$\begin{aligned} \boldsymbol{M}(\boldsymbol{q})\ddot{\boldsymbol{q}} + \left(\boldsymbol{C}(\boldsymbol{q},\dot{\boldsymbol{q}}) + \boldsymbol{D}\right)\dot{\boldsymbol{q}} + \boldsymbol{K}\left(\boldsymbol{q} - \boldsymbol{q}^*\right) = \\ \boldsymbol{\tau}(\boldsymbol{q}) + \boldsymbol{F}(\boldsymbol{q}) + \boldsymbol{N}(\boldsymbol{q})\mathscr{G} \,, \end{aligned} \tag{2.17}$$

where $\boldsymbol{M} \in \mathbb{R}^{2N\times 2N}$ is the generalized mass matrix, $\boldsymbol{C} \in \mathbb{R}^{2N\times 2N}$ is the generalized Coriolis matrix, $\boldsymbol{D} \in \mathbb{R}^{2N\times 2N}$ is the generalized damping matrix, $\boldsymbol{K} \in \mathbb{R}^{2N\times 2N}$ is the generalized stiffness matrix, $\boldsymbol{F} \in \mathbb{R}^{2N}$ is the vector of generalized external forces, $\boldsymbol{N} \in \mathbb{R}^{2N\times 6}$ is the gravitational matrix and $\boldsymbol{\tau} = \left[\boldsymbol{\tau}_1^T \cdots \boldsymbol{\tau}_N^T\right]^T \in \mathbb{R}^{2N}$ is the vector of applied actuation forces.

It can be shown from eq. (2.3)-(2.13) that the internal elasticity and actuation forces exchanged by the soft and rigid bodies in the tree cancel each others, yielding to

$$\boldsymbol{M} = \sum_{i=1}^{N} \int_0^L \boldsymbol{J}_i^T \mathscr{M}_i \boldsymbol{J}_i dX + \boldsymbol{J}_{ib}^T \mathscr{M}_{ib} \boldsymbol{J}_{ib} \,, \tag{2.18}$$

$$\begin{aligned} \boldsymbol{C} = \sum_{i=1}^{N} \int_0^L \boldsymbol{J}_i^T \left(\mathrm{ad}^*_{\boldsymbol{J}_i\dot{\boldsymbol{q}}} \mathscr{M}_i \boldsymbol{J}_i + \mathscr{M}_i \dot{\boldsymbol{J}}_i\right) dX + \\ \boldsymbol{J}_{ib}^T \left(\mathrm{ad}^*_{\boldsymbol{J}_{ib}\dot{\boldsymbol{q}}} \mathscr{M}_{ib} \boldsymbol{J}_{ib} + \mathscr{M}_{ib} \dot{\boldsymbol{J}}_{ib}\right) \,, \end{aligned} \tag{2.19}$$

$$\boldsymbol{D} = \mathrm{diag}\left(\boldsymbol{B}^T \boldsymbol{\Upsilon}_1 \boldsymbol{B}, \boldsymbol{B}^T \boldsymbol{\Upsilon}_2 \boldsymbol{B}, \cdots, \boldsymbol{B}^T \boldsymbol{\Upsilon}_n \boldsymbol{B}\right) L \,, \tag{2.20}$$

$$\boldsymbol{K} = \mathrm{diag}\left(\boldsymbol{B}^T \boldsymbol{\Sigma}_1 \boldsymbol{B}, \boldsymbol{B}^T \boldsymbol{\Sigma}_2 \boldsymbol{B}, \cdots, \boldsymbol{B}^T \boldsymbol{\Sigma}_n \boldsymbol{B}\right) L \,, \tag{2.21}$$

$$\boldsymbol{\tau}_i = {}^{ib}\boldsymbol{S}_i^T \mathscr{F}_{al_{ib}} \,, \tag{2.22}$$

$$\boldsymbol{F} = \sum_{i=1}^{N} \boldsymbol{J}_{ib}^T \mathscr{F}_{p_{ib}} \,, \tag{2.23}$$

$$\boldsymbol{N} = \sum_{i=1}^{N} \int_0^L \boldsymbol{J}_i^T \mathscr{M}_i \mathrm{Ad}^{-1}_{\boldsymbol{g}_{si}} dX + \boldsymbol{J}_{ib}^T \mathscr{M}_{ib} \mathrm{Ad}^{-1}_{\boldsymbol{g}_{si_b}} \,. \tag{2.24}$$

Remark: The mathematical development above has been presented for the case of small strains and constant cross-section soft joints, both for simplicity and since the majority of the

existing soft grippers satisfy those assumptions. However, it should be notice that the proposed model is not restricted to this case. In fact, the integrals in (2.18), (2.19) and (2.24) can easily accommodate variable cross-section, if necessary. Furthermore, it can be shown that, in the general case, the 2×1 blocks of the resultant internal force vector take the form $\boldsymbol{B}^T \int_0^L \mathscr{F}_{i_i} dX$ [13], which can accomodate any constitutive relation and reduces to the damping and stiffness matrix (2.20), (2.21) for the linear Kelvin-Voigt case.

2.1.1.4 Quasi–static analysis

Let us consider eq. (2.17) in stationary conditions, i.e. $\ddot{\mathbf{q}} = \dot{\mathbf{q}} = \mathbf{0}$, let us neglect the term that takes into account gravity effects and consider a condition in which the finger does not have manipulation interaction, i.e. $\mathscr{F}_{g_{ib}} = \mathscr{F}_{p_{ib}} = \mathbf{0}$ in eq. (2.4). Then, it is possible to reformulate eq. (2.17) as

$$\mathbf{f}_{qs}(\mathbf{q}, T) = \mathbf{0}. \tag{2.25}$$

The problem can be solved, finding finger configuration $\mathbf{q}$ for a given cable tension T:

$$\mathbf{q} = \mathbf{f}_{inv,qs}(T). \tag{2.26}$$

It is important to notice that relationships $\mathbf{f}_{qs}$ and $\mathbf{f}_{inv,qs}$ depend also on $\mathbf{p}_{mat}$, $\mathbf{p}_{geom}$, that are vectors containing the properties of materials and the geometrical parameters of soft joints.

Let us indicate with $\mathbf{q}_{des}$ the desired configuration that we want to obtain when the tendon is pulled with a force T and there are no other external forces applied to the finger, our synthesis problem consists in finding suitable sets of soft joint properties $\mathbf{p}_{mat}$, $\mathbf{p}_{geom}$ that minimize the error

$$\mathbf{e}_q = \|\mathbf{q}_{des} - \mathbf{q}\|. \tag{2.27}$$

In [14] a simplified version of the mechanical model was used to design passive joints of an underactuated modular soft gripper for fingertip trajectory tracking. The simplification consisted in modelling the passive soft element as a lumped 1DoF joint with a fixed constant stiffness. Due to the simplicity of the model the problem could be solved in a closed form. The generalization presented in this paper allows to take into account a more general three dimensional deformation of the joint.

2.1.1.5 Analysis of single fingers

The dynamic model developed above can be used, in its steady-state form, to calculate manipulability, force and stiffness ellipsoid of the modular gripper's fingers at any configuration.

Manipulability Ellipsoid: The manipulability ellipsoid is the projection into the tangent task space of a $2N$ dimensional sphere in the tangent joint space given by $\dot{\boldsymbol{q}}^T \dot{\boldsymbol{q}} = 1$. Making use of results from differential kinematics analysis (see Appendix A.2, eq, (A.12) for more details),

we obtain the following three dimensional linear and angular ellipsoids:

$$\mathsf{v}_{tip}^T \left(\boldsymbol{J}_{v_{tip}} \boldsymbol{J}_{v_{tip}}^T \right)^{-1} \mathsf{v}_{tip} = 1 \,, \tag{2.28}$$

$$\mathsf{w}_{tip}^T \left(\boldsymbol{J}_{w_{tip}} \boldsymbol{J}_{w_{tip}}^T \right)^{-1} \mathsf{w}_{tip} = 1 \,, \tag{2.29}$$

where $\boldsymbol{J}_{Nb} = \boldsymbol{J}_{tip} = \left[\boldsymbol{J}_{w_{tip}}^T \; \boldsymbol{J}_{v_{tip}}^T \right]^T$ and we have considered full rank Jacobians.

Force Ellipsoid: Similarly, the force ellipsoid is the projection into the dual tangent task space of a $2N$ dimensional sphere in the dual tangent joint space given by $\boldsymbol{\tau}^T \boldsymbol{\tau} = 1$. Let's define the wrench that the tip phalanx exerts on the environment as $\mathscr{F}_{tip} = \left[\mathsf{T}_{tip}^T \; \mathsf{P}_{tip}^T \right]^T = -\mathscr{F}_{p_{Nb}}$, where T_{tip} and P_{tip} are the tip torque and force respectively. Then, from the steady-state form of the dynamics equation (2.17) the tip wrench due to the joint torques $\boldsymbol{\tau}$ satisfies $\boldsymbol{\tau} = \boldsymbol{J}_{tip}^T \mathscr{F}_{tip}$, which yields to the three dimensional linear and angular force ellipsoids

$$\mathsf{P}_{tip}^T \left(\boldsymbol{J}_{v_{tip}} \boldsymbol{J}_{v_{tip}}^T \right) \mathsf{P}_{tip} = 1 \,, \tag{2.30}$$

$$\mathsf{T}_{tip}^T \left(\boldsymbol{J}_{w_{tip}} \boldsymbol{J}_{w_{tip}}^T \right) \mathsf{T}_{tip} = 1 \,. \tag{2.31}$$

Stiffness Ellipsoid The stiffness ellipsoid is the projection into the dual tangent task space of a six dimensional sphere in the tangent task space determined by the passive elasticity of the soft-rigid structure. The original sphere is given by $\boldsymbol{\zeta}_{tip}^T \boldsymbol{\zeta}_{tip} = 1$, where $\boldsymbol{\zeta}_{tip} = \left[\mathsf{s}_{tip}^T \; \mathsf{r}_{tip}^T \right]^T = \boldsymbol{\eta}_{tip} \delta t$ are the infinitesimal rotation and displacement of the tip phalanx. Similarly to the force ellipsoid, using the steady-state form of the dynamics equation (2.17) and the joint elasticity equation (2.21), we obtain $\boldsymbol{\zeta}_{tip} = \boldsymbol{J}_{tip} \boldsymbol{K}^{-1} \boldsymbol{J}_{tip}^T \mathscr{F}_{tip}$, which yields to the following three dimensional linear and angular stiffness ellipsoids

$$\mathsf{P}_{tip}^T \left(\boldsymbol{J}_{v_{tip}} \boldsymbol{K}^{-1} \boldsymbol{J}_{v_{tip}}^T \right)^2 \mathsf{P}_{tip} = 1 \,, \tag{2.32}$$

$$\mathsf{T}_{tip}^T \left(\boldsymbol{J}_{w_{tip}} \boldsymbol{K}^{-1} \boldsymbol{J}_{w_{tip}}^T \right)^2 \mathsf{T}_{tip} = 1 \,. \tag{2.33}$$

Compliance Ellipsoid Inversely to the stiffness ellipsoid, the compliance ellipsoid is the projection into the tangent task space of a six dimensional sphere in the dual tangent task space given by $\mathscr{F}_{tip}^T \mathscr{F}_{tip} = 1$. Following the same steps as before, we obtain the following three dimensional linear and angular compliance ellipsoids:

$$\mathsf{r}_{tip}^T \left(\boldsymbol{J}_{v_{tip}} \boldsymbol{K}^{-1} \boldsymbol{J}_{v_{tip}}^T \right)^{-2} \mathsf{r}_{tip} = 1 \,, \tag{2.34}$$

$$\mathsf{s}_{tip}^T \left(\boldsymbol{J}_{w_{tip}} \boldsymbol{K}^{-1} \boldsymbol{J}_{w_{tip}}^T \right)^{-2} \mathsf{s}_{tip} = 1 \,. \tag{2.35}$$

where again we have considered full rank Jacobian matrices.

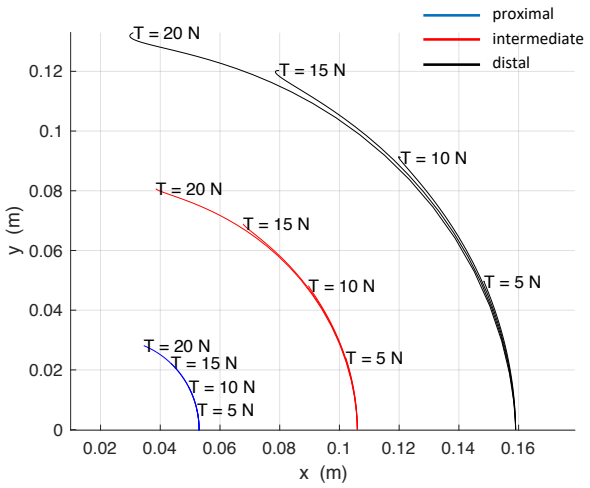

a)

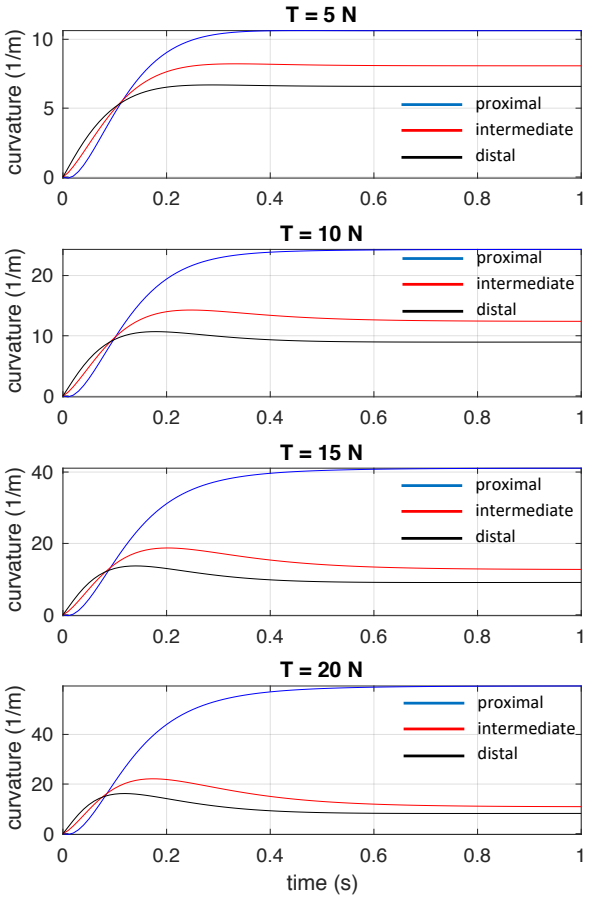

b)

Fig. 2.2 Simulation of a single finger composed of three identical links, subject to a constant tendon tension applied in $t = 0$. a) Trajectories of the origins of the frames on rigid links. Blue, red and black curves corresponds to proximal, intermediate and distal links, respectively. b) Soft link curvature during as a function of time for different tendon tension values. Blue, red and black curves corresponds to proximal, intermediate and distal joints, respectively.

Example: single finger simulation In this section, we apply the formulation described in the previous section to simulate the dynamics of a modular underactuated soft–rigid finger

in which we set the same values for all joint stiffness. The finger is composed of three modules, in which the rigid part is a parallelepiped with dimensions (width $\times$ length $\times$ height) $20 \times 30 \times 12$ mm, while the compliant part can be approximated with a parallelepiped with dimensions $20 \times 21 \times 4$ mm. Three identical soft modules are considered in this first simulation, the density of the rigid link is $\rho_r = 1070\ \mathrm{kg/m^3}$, the density of the soft joint is $\rho_s = 1200\ \mathrm{kg/m^3}$, its Young's modulus is $E_s = 15.2$ MPa, its Poisson's coefficient is $\nu_s = 0.5$. Two DoF are considered for each module: principal bending, i.e. rotation in the xy plane indicated in Fig. 2.1 and torsion, i.e. rotation w.r.t. e x axis indicated in Fig. 2.1. Friction between the cable and the link is simulated, assuming a static friction coefficient $\mu_s = 1$. In the simulations, we applied a constant tension T at time $t = 0$ s to the tendon and we observed the dynamics of the finger for 2 s. Different T values from 5 to 20 N were considered in the simulation. Main simulation results are reported in Fig. 2.2, in particular in Fig. 2.2 a) we reported the trajectories of the points on the rigid links in which we fixed the local frame origins. Trajectories are reported in the xy plane for the sake of clarity. Fig. 2.2 b) reports for different values of T tension the variation of curvatures in soft joints as a function of time. It is interesting to notice that, even if all the three soft joints have the same geometrical and material properties, and therefore have the same equivalent stiffness values, after the application of tendon tension their curvatures reach different steady state values, due to the presence of friction.

2.1.2 Model testing and validation

To further investigate the potentialities and limits of the model that we proposed in the previous section, we compared finger movement numerically simulated with the one measured using the experimental setup shown in Fig. 2.4 and Fig. 2.6. The base of the gripper was fixed on the table. We used a Vicon system (Vicon Capture Systems, UK) consisting of 8 cameras to track finger movement. Fifteen passive optical markers were used to track finger motion.

In this paper, in particular, we focused on single finger simulation and modelling, since we are interested in understanding the advantages and limits of the distributed parameter model and to compare it with other modelling techniques, in particular with standard lumped parameter model in which flexible joints are represented as revolute hinges. Different configurations were considered in the tests: we applied the synthesis procedure introduced in [9, 14] and generalised in the previous section to design deformable joints with different stiffness values so to obtain desired closure motions. In particular we regulated Young's moduli and density of soft joints, maintaining the same geometric shape and dimensions, so to obtain on the gripper, when actuated, a power grasp and a pinch grasp, respectively.

As detailed in [7], using an underactuated tendon-driven structure with three modules for each finger, a closure movement allowing a power grasp can be obtained by regulating soft joint parameters so that the corresponding normalised stiffness values, conventionally defined as $\tilde{k}_i = k_i/k_1$, with $i = 1 \cdots 6$), are

$$\tilde{k}_1 = \tilde{k}_4 = 1;\ \ \tilde{k}_2 = \tilde{k}_5 = 0.48;\ \ \tilde{k}_3 = \tilde{k}_6 = 0.48; \tag{2.36}$$

while to get a pinch grasp, the following normalised stiffness values can be employed:

$$\tilde{k}_1 = \tilde{k}_4 = 1; \;\; \tilde{k}_2 = \tilde{k}_5 = 3.33; \;\; \tilde{k}_3 = \tilde{k}_6 = 3.33. \tag{2.37}$$

Such normalised stiffness values can be obtained by realising soft joints with the same geometrical dimensions, and by selecting 3D printing parameters that allow to obtain the following Young's moduli, for the power grasp:

$$E_{1,4} = 6.22 \;\; E_{2,5} = 3.02 \;\; E_{3,6} = 3.02 \;\; (\text{MPa}), \tag{2.38}$$

and for the pinch grasp:

$$E_{1,4} = 1.75 \;\; E_{2,5} = 6.22 \;\; E_{3,6} = 6.22 \;\; (\text{MPa}). \tag{2.39}$$

2.1.2.1 Closure movement

In the first set of tests we analyse closure motion of three versions of the underactuated finger, obtained by varying the grasp type (i.e. power grasp and pinch grasp) and by varying the length of the passive elastic element in the joints, L_s ($L_s = 21$ and $L_s = 28$ mm). The configurations that we consider are three: *i*) power grasp, $L_s = 21$ mm; *ii*) power grasp, $L_s = 28$ mm, *iii*) pinch grasp, $L_s = 21$ mm. Five acquisitions are considered for each configuration. Although the model is three dimensional, finger closure motion is substantially planar in these tests, so we represent it on the plane xy. No significant displacements have been observed in z direction.

We compare the trajectories of three points on the proximal, intermediate and distal phalanges respectively, measured by the tracking system and estimated by the model presented in this work. We also evaluate point trajectories by means of a lumped parameter model modelling the interphalangeal joints as simple revolute hinges with a fixed rotation axis. Results are reported in Fig. 2.3. An initial calibration phase has been necessary to align tracking system markers with the points evaluated in the simulations. Results show that both the lumped parameter and the distributed model are able to describe the closure motion of an underactuated compliant finger with a reasonable precision: the distance between measured and simulated trajectories are quite limited (~ 5 mm in the worst cases). It is also interesting to notice that for the gripper with $L_s = 21$ mm (plots in the first row of Fig. 2.3) the difference between lumped parameter and distributed model is quite limited (~ 2 mm in the final closed configuration), such a difference becomes more evident, as expected, for fingers with $L_s = 28$ mm (second and third rows of Fig. 2.3), in which the lumped parameter approximation becomes less realistic.

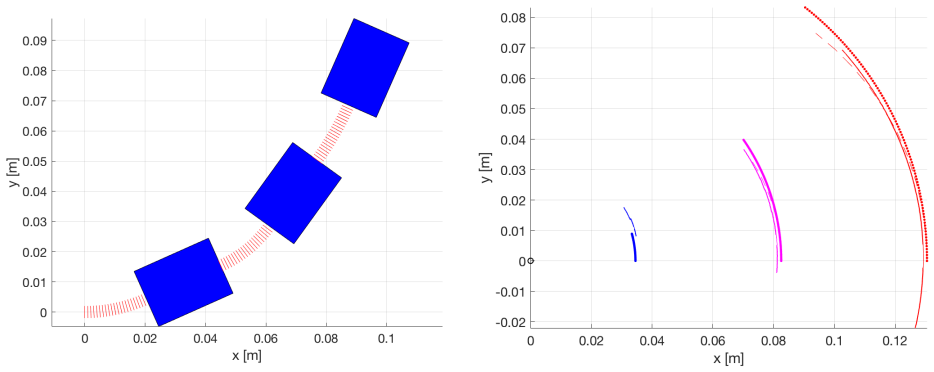

a)

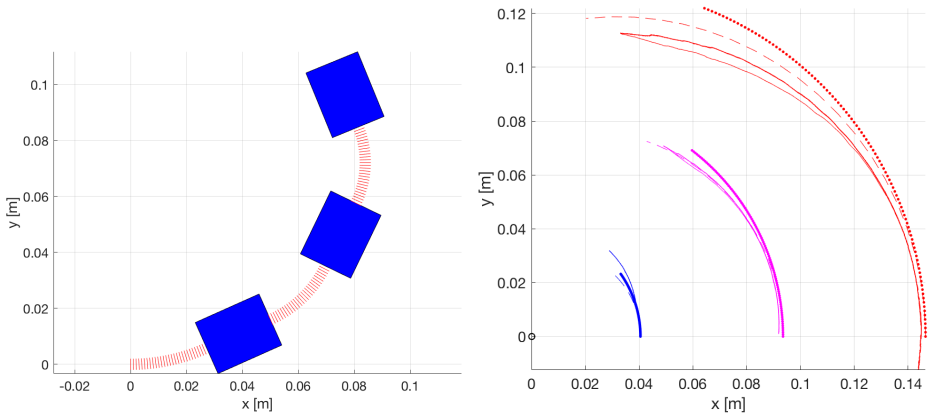

b)

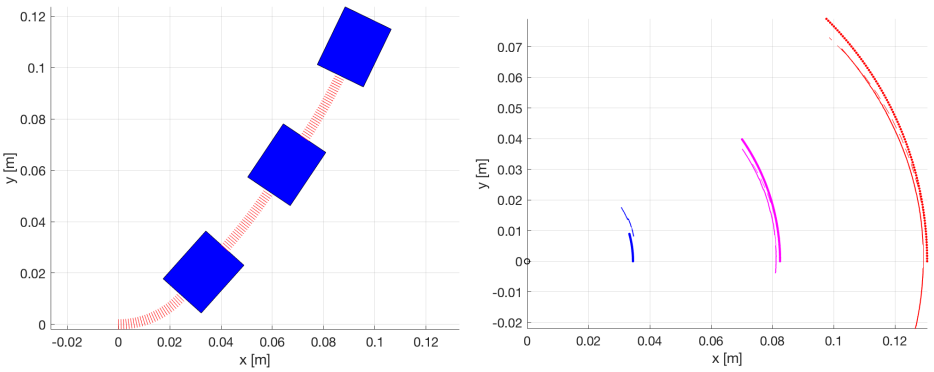

c)

Fig. 2.3 Analysis of three closure motions. Left column: simulated finger final configurations; right column: trajectories of points on the intermediate (magenta), and distal (red) phalanges; continuous curves represent data from tracking system, dashed lines represent trajectories calculated with the mathematical model described in this paper, thick dotted curves represent trajectories calculated with a simple lumped parameter model. a) Power grasp, $L_s = 21$ mm; b) Power grasp, $L_s = 28$ mm; c) Pinch grasp, $L_s = 28$ mm.

2.1.2.2 Load in the direction of gravity

The second set of tests is aimed at verifying the accuracy of fingertip equivalent stiffness estimation. We 3D printed a customized cylindrical object to be attached at the fingertip. Small spheres with different sizes and weights can be inserted into an opening on top of the object. The 3D object and spheres act as a load in the direction of parallel to gravity (z axis). We track the finger with the applied load during a closure motion, that is enough slow to limit the dynamics effect. Fig. 2.4 a) shows the experimental setup with the finger, the tracking system markers and the external loading at the tip. Fig. 2.4 b) shows the trajectories of three points on finger phalanges during closure motion, projected on the xy plane. Also in these figures we reported both the trajectories measured in the experiments (continuous lines) and the ones predicted by the mathematical model (dashed lines). For this test we use only the finger designed for a power grasp, with $L_p = 21$ mm. We could not use the version with the longer joint because, due to its higher compliance, we could have buckling deformations. Three tests are considered for the following evaluation. By measuring the displacement on the z direction, Δz_{tip} of the fingertip, and since the applied loading is known ($F_z \sim 1$ N), we can estimate approximately the equivalent z direction finger stiffness as

$$k_{z,m} \cong \frac{F_z}{\Delta z_{tip}}.$$

Elaborating test measures, we can evaluate $k_{z,m}$ for different finger configurations and we can compare the obtained results with the equivalent fingertip stiffness in the same direction, that is evaluated by means of eq. (2.32). Results are shown in Fig. 2.5, in which we reported stiffness values as a function of a non-dimensional parameter describing finger closure, varying from 0 (open) to 1 (close). Measured stiffness values are reported with continuous lines, the value estimated with the mathematical model is reported with a dashed line. It is interesting to notice that the model is able to estimate the equivalent stiffness at the fingertip with a reasonably good approximation when the finger is closed (closure value greater that 40%), while it greatly overestimate the stiffness when the finger is straight (closure value lower than 30%). This difference can be motivated with the choice of the constrained strain state, that in the simulation that we performed considered only inextensible bending in principal loading plane and torsion (see the definition of B_i matrix detailed in the Appendix section, eq. (A.3), (A.4)). With this type of constraints, when the finger is straight no deformations in z direction are possible and this is the reason why stiffness in z direction assumes very high values close to this configuration. A better approximation could be obtained modelling the joint with more degrees of freedom.

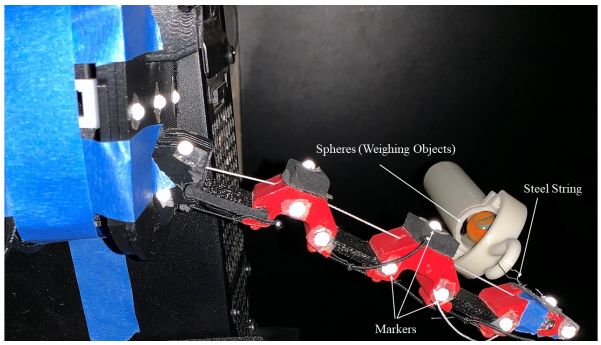

a)

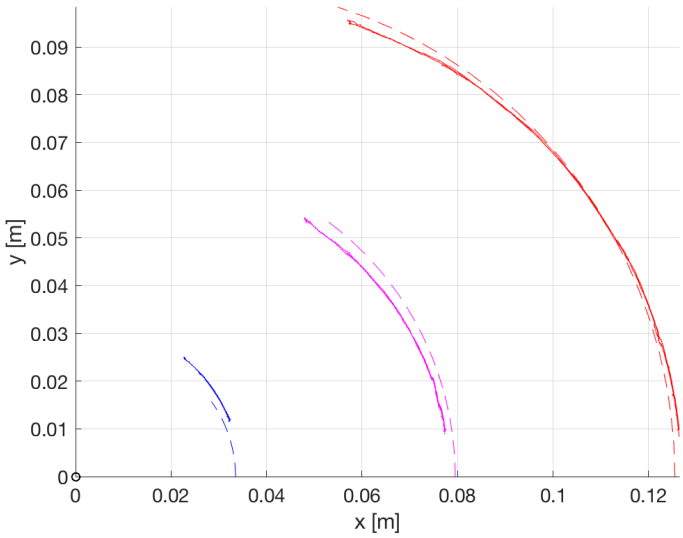

b)

Fig. 2.4 Experimental setup to record the joints trajectories using Vicon under the load in the direction of gravity, trajectories of points on the gripper measured with the tracking system (continuous lines) and simulated with the mathematical model (dashed lines), blue: reference point on the proximal phalanx, magenta: reference point on the intermediate phalanx, red: reference point on the distal phalanx.

2.1.2.3 Mixed bending/torsional load

In this test, the 3D printed support for the external load has been modified as shown in Fig. 2.6, so that it can apply also a torsional torque to the fingertip. The length of moment arm is set to 18 mm. The experiment has been repeated with two different external loads i.e. 1 and 2 N, the corresponding torsional torques are then $\tau_{ext} = 0.018$ Nm and $\tau_{ext} = 0.036$ Nm. Five tests have been considered for the evaluation. Also in this case, we measure trajectories of three points on finger phalanges while the finger, subject to the external load, is closing. The closure movement has been set enough slow so that dynamical effect could be neglected. The external load in this case produced both a deformation in z direction and a torsion deformation,

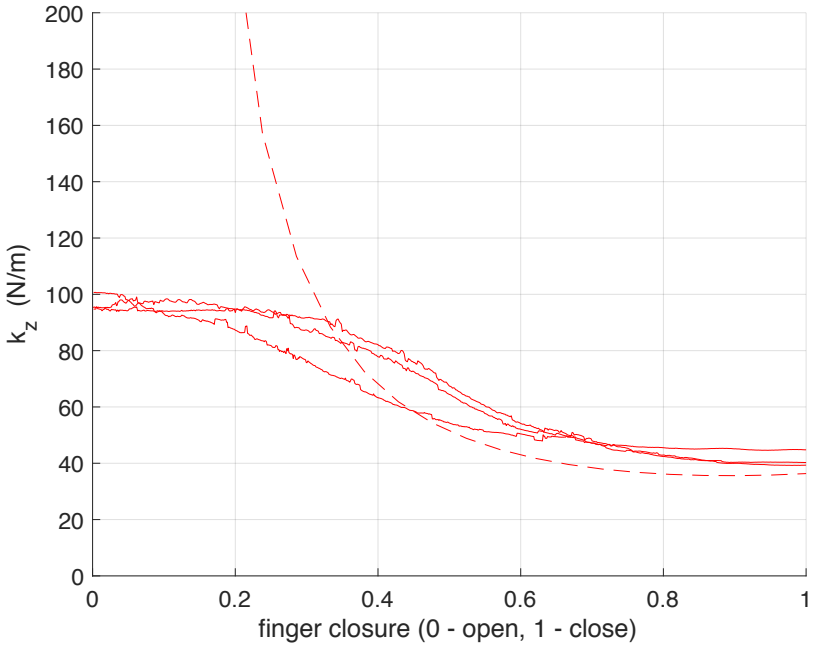

Fig. 2.5 Equivalent fingertip stiffness in z direction: measured stiffness k_{zm} (continuous curves) and stiffness evaluated with the mathematical model (dashed curve) as a function of finger closure.

so we needed to consider not only the trajectories of the reference points, but also the relative orientation of reference frames on finger phalanges during the motion. We evaluated the overall torsional deformation as

$$\Delta\phi = \sum_{i=1}^{3} \Delta\phi_i,$$

where $\Delta\phi_i$ was the relative rotation with respect x_{i-1} direction between frames i and $i-1$. We therefore estimated torsional stiffness as

$$k_{tors,m} \cong \frac{\tau_{ext}}{\Delta\phi}.$$

We can also estimate the linear stiffness in z direction, k_z, with the same procedure described in the previous section. Fig. 2.7 shows the results that we obtained by moving the finger from an open to a close configuration. Fig. 2.7 a) reports k_{tors} values estimated from the measurements (continuous curves), compared with the value calculated by means of eq. (2.33) (dashed curve). In this case we can observe a general agreement between the stiffness estimated from measured data and the one predicted by the theoretical model: the curves show similar values and behaviours, the difference are due to factors that could be not properly be considered in the theoretical analysis (e.g. material anisotropic behaviour, friction, etc.). Fig. 2.7 b) reports the evaluation of k_z linear stiffness, we can observe that the obtained results are similar to the ones reported in Fig. 2.5, even if they have been obtained with different loading conditions.

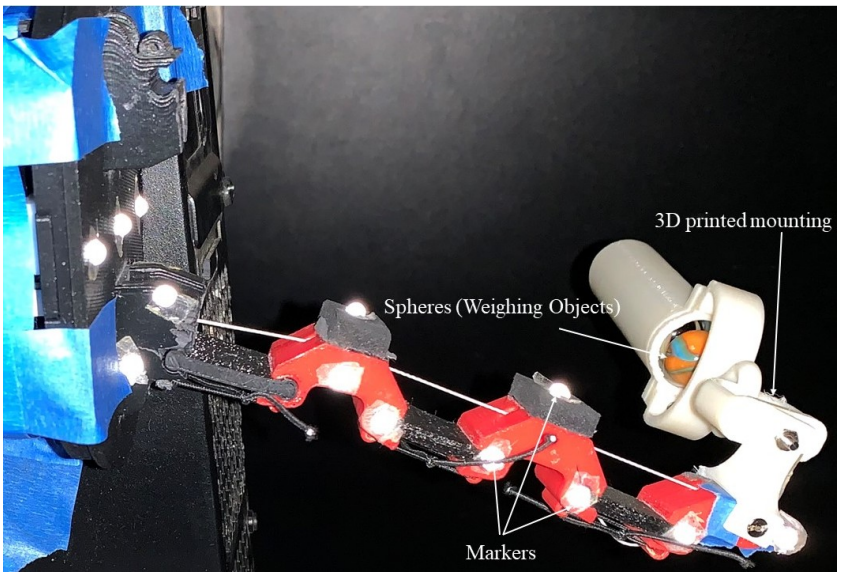

Fig. 2.6 Experimental setup to record the joints trajectories using Vicon under torsional load.

2.1.2.4 Dynamics

We realized a set of tests for validating the dynamical model described in the previous sections. A direct comparison between simulations and experiments during a closure motion, in which the motor of the finger is actuated, was not possible due to the unmodelled parameters in the simulation since some relevant parameters (e.g. tendon force) could not be measured with the available setup with a suitable precision. Since the proposed mathematical model focuses on the mechanical part of the finger, to compare its accuracy and capability of properly describe finger dynamic behavior, we experimentally measured the free response of a modular finger, subject to an initial displacement of the fingertip. The first configuration adopted in Sec. 2.1.2.1 (i.e. power grasp, $L_s = 21$mm) was employed in this set of tests, also in this case the proximal joint of finger was connected to a fixed frame. The free response of the finger was compared with the results of simulations in which we reproduced the same initial conditions. The procedure to realize this comparison was the following.
(i) With the same experimental setup previously introduced, with the actuators released, we manually moved the initial configuration of the fingertip in a non-equilibrium configuration and then released it.
(ii) We therefore tracked the trajectory of a point on the distal phalanx until the equilibrium configuration was reached, with a sampling frequency of 100Hz. Five different trials, with the same finger but slightly different initial configurations, were measured.
(iii) We then post-processed the data to set the initial time at the instant in which the finger is released and we shifted the measures to set as reference the final equilibrium configuration. This post processing, consisting in a simple translation of the reference frame and of the starting time, did not influence the significant information from the tests but simplified the comparison with the simulation.
(iv) In the simulation environment, with an inverse kinematic analysis we evaluated the same

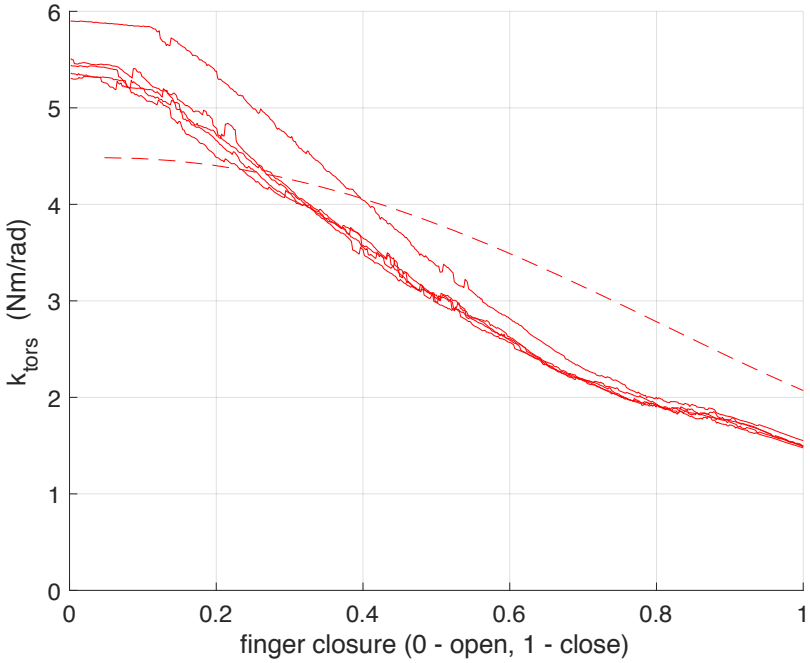

a)

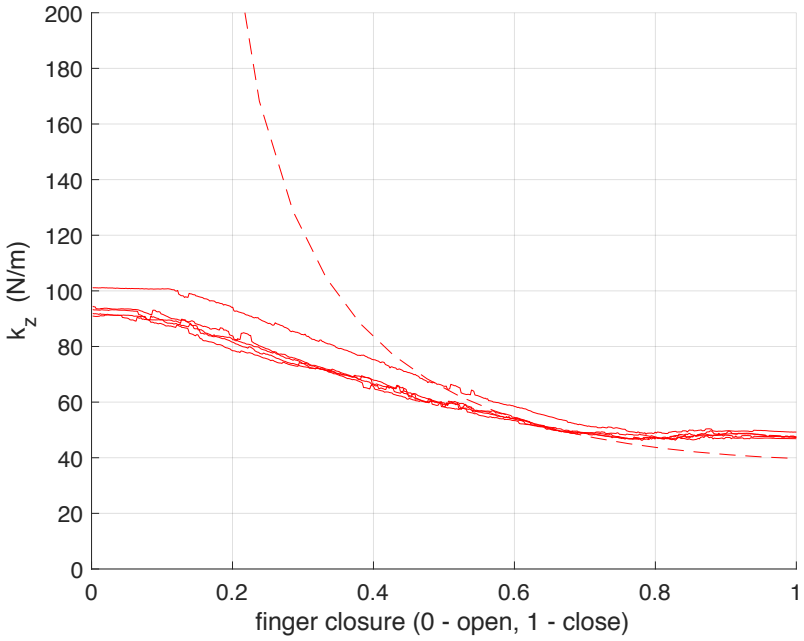

b)

Fig. 2.7 Mixed bending/torsional loading condition. a) Equivalent fingertip torsional stiffness. b) Equivalent fingertip linear stiffness in z direction, measured from the data (continuous curves) and evaluated with the mathematical model (dashed curve), as a function of finger closure.

initial configuration of the tests.
(v) We then evaluated by simulation the free response of the finger starting from the same initial reference configurations of the tests.
Since mechanical properties of TPU vary in a wide range, also depending on the manufacturing process, the results of one of the trials were used to tune the value of the damping. In particular, the shear viscosity was set $\nu = 0.112$MPas. For the elasticity properties, we used the same values defined in the previous tests. Two examples of fingertip trajectories, measured with the experimental setup and simulated, are shown in Fig. 2.8. It can be noticed that the difference, in the time domain, between the experimental measure (blue curves) and the simulated one (red curves) is rather limited.

Test id	Max overshoot	Settling time	Oscillation freq.
Test 1, meas.	37%	0.44 s	5.2 Hz
Test 1, sim.	40%	0.42 s	4.0 Hz
Test 2, meas.	47%	0.46 s	4.5 Hz
Test 2, sim.	37%	0.42 s	4.0 Hz
Test 3, meas.	42%	0.51 s	3.9 Hz
Test 3, sim.	40%	0.42 s	4.0 Hz
Test 4, meas.	39%	0.45 s	4.8 Hz
Test 4, meas.	40%	0.40 s	3.9 Hz

Table 2.1 Comparison between experimental measures and simulation results in dynamics tests. Free response of the finger from a non-equilibrium configuration was considered. Maximum overshoot, settling time, and oscillation frequency were considered.

Since the dynamical responses that have been observed present a damped oscillating behavior, instead of directly comparing the trajectories, we could compare some specific features of their measured and simulated values, in particular we considered the maximum overshoot (evaluated as the ratio between the first oscillation peak and the initial value, and reported as a percentage value), the settling time (evaluated as. the time that the system needs to reduce the oscillation amplitude to 5% of the initial value) and the oscillation frequency. Results are summarized, for the four tests not used for model calibration, in Table 2.1. As it can be seen there are some differences between measured and simulated parameters. The maximum difference in overshoot was 10% in Test 2, the maximum error in settling time was 0.09 s in Test 3, the maximum difference in oscillation frequency was observed in Test 1 and was 0.7 Hz. These differences can be motivated by the approximations that were made in the modeling phase, and in particular in considering a homogeneous linear elastic material in passive joints. Furthermore, material properties were not known with a suitable precision, and the inertia matrices of rigid links were evaluated with some approximations. By observing the x components of measured oscillations, we can notice higher frequency small oscillations $\sim$ 8Hz that are over-damped in the simulations. The experimental setup also could introduce some errors, for example the non-perfectly stiff link between the finger and the support and the motion capture setup precision. Although all these limitations, the obtained results are in line with other results available in the literature either for soft and rigid robots e.g. [15], [16], [17].

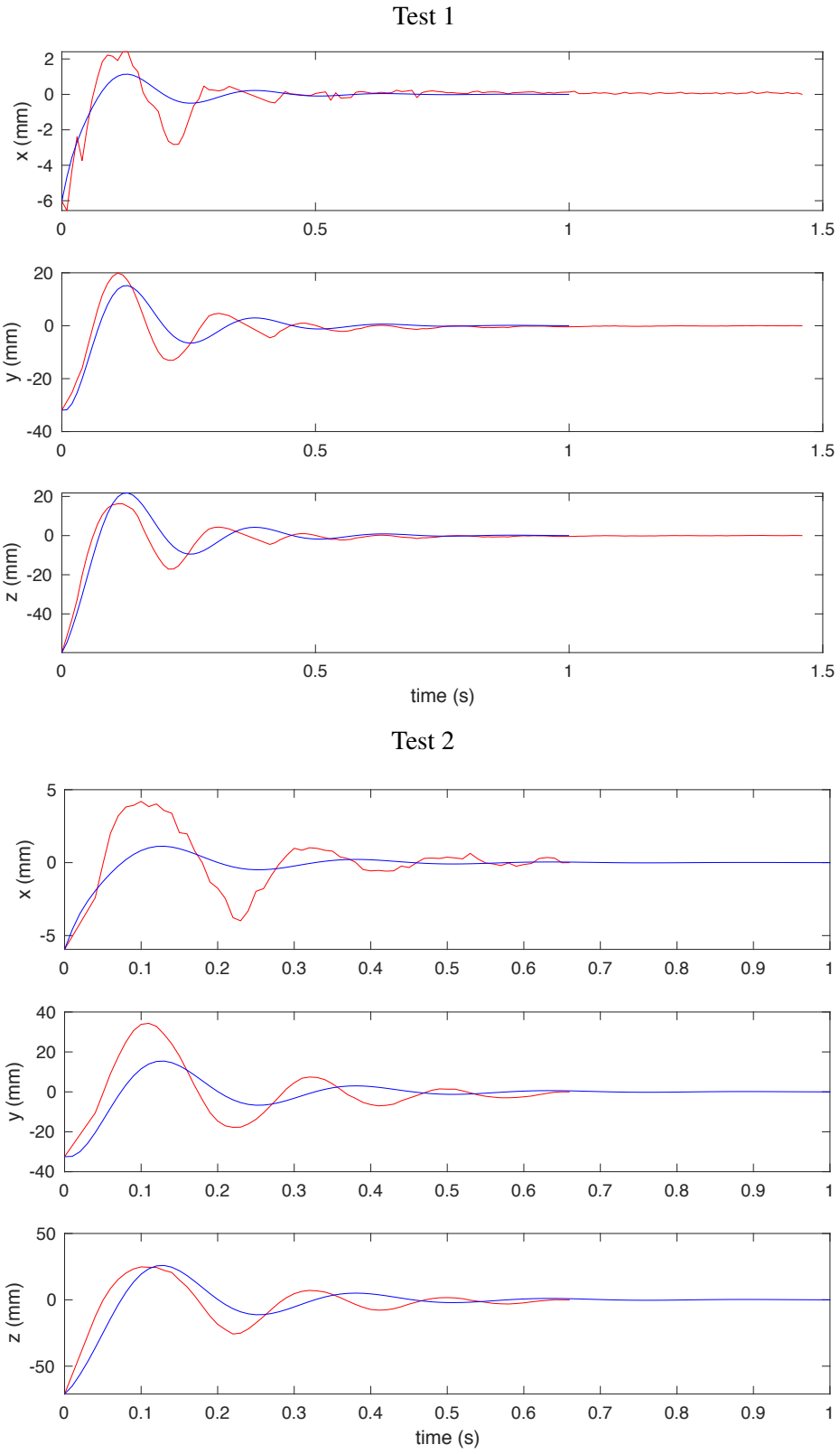

Fig. 2.8 Cartesian coordinates of a point on the distal phalanx of a finger in free response tests with three identical phalanges, comparison between measured values (red curves) and simulations (blue curves), results relative to two different tests.

2.1.3 Discussion

In general, a distributed model of soft joints has several advantages with respect to a lumped model. Not only a distributed model can give higher accuracy for a wider range of operational conditions and configurations, but also requires minimal parameter identification procedure while the result has a clear physical meaning as much as it is usually done for traditional rigid manipulators. This is not possible for a lumped parameter model of soft gripper, which does not provide a systematic procedure to build the equation of motion from the physical properties of the system components. Furthermore, a soft joint has intrinsically multiple degrees of freedom (multi-DOFs) and although one could use a lumped multi-DOFs model which is not usually done and should be approached with care in order not to introduce geometrical inaccuracies. For instance, the kinematic model used in this paper encompass torsion and bending around the lateral z-axis only, in order to model the very high bending stiffness of our soft joint around the vertical y-axis. The span of these two screws ($\mathfrak{m}_i \subset \mathfrak{se}(3)$) does not generate a Lie sub-algebra of $\mathfrak{se}(3)$, thus, it would be geometrically wrong to model them as a chain of two revolute joints, as demonstrated in [18]. Our approach, on the contrary, is geometrically exact and systematically solves those issues without any additional work. In this paper, we showed its potentialities to analyse the role and optimize some design parameters of the soft robotic hands to obtain their desired properties. The proposed extended model, allows to get more information about robotic finger behaviour, for instance, its time-response to external inputs. We can easily integrate the model with the main grasp properties presented in [19]. In particular, such model can be used to calculate important properties of the system, i.e. the kinematics, manipulability, force, stiffness and compliance ellipsoids of the modular finger and how we can exploit such results in the analysis of robotic manipulation systems.

At this stage, we focused on presenting the mathematical model as an analysis tool to define some important design parameters of soft grippers once their kinematics structure is fixed. In future, we are aiming to exploit the model for soft gripper synthesis by formulating the design problem as an optimization procedure, for example as proposed in [20, 21]. Moreover, although, overall model consists of geometric and material properties. But, at the moment, we are using the model as a tool to study the behavior of gripper by exploiting the material properties only while given its geometry. It would be interesting to make use of model to design and optimize the soft link geometries also, e.g. in terms of bending, torsional and lateral directions stiffness. Furthermore, new materials introduced by additive manufacturing techniques open a set of possibilities for designers. Beside infill density percentage, additional parameters such as chemical composition, surface treatments, printing pattern, etc. can be used to get the desired mechanical properties [22]. Currently, we are investigating further the properties of the materials and manufacturing technologies and exploiting them in extended experiments with the whole soft gripper focusing on the manipulation. Moreover, we are also planning to continue the validation process by comparing the distributed parameter model that we proposed in this work with other models available in the literature, e.g. [23, 24]. Furthermore, we are designing versions of soft grippers with multiple fingers to target complex manipulations problems.

2.2 Finray Mechanism Sixth Finger Model

> "*Technology is important because it creates the future. We're able to be a part of the "next" and create things that don't* exist."
>
> MC Hammer

The Fin-Ray principle, inspired by the physiology of fish rays, represents the foundation of a large number of robotic devices. However, despite their popularity, there is not any effective theoretical model technique for the analysis of this family of fingers. This lack is the main motivation of the presented work, which provides the mathematical modeling, analysis and prototyping of a closed-chain Fin-Ray finger. In this scenario, the contribution of this work is twofold. At one end, we provide a general discrete Cosserat approach for Closed-Chain Soft Robots and we show how to apply it to Fin-Ray Effect (FRE) fingers. On the other end, the approach is employed to perform an optimization procedure, aiming at exploring the possible designs of Fin-Ray fingers. Finally, the optimal design, which is able to conform to contacting surfaces, while maintaining rigidness out of its grasping plane, is fabricated. These features inspired us to exploit the new design as a supernumerary robotic finger, to meet the ergonomics and functional requirements for chronic stroke patients to help in bi-manual tasks.

2.2.1 Introduction

While traditional robots are composed of rigid joints and links, soft robotics exploits the capability of some materials to exhibit high deformations to design compliant and under-actuated devices. In particular, soft robotics appears as a promising research shift in the design of robotic manipulators and fingers, which can massively profit from the employment of deformable materials and structures to gain higher compliance and therefore adaptability [25–27]. A finger's compliance is defined as its ability to adapt to a certain shape or object. Higher compliance results in higher robustness when working in unstructured environments and higher ability to manipulate fragile objects with different shapes.

Many approaches in soft robotics are inspired by nature, aiming to achieve reliable and lightweight design which can perform high performance tasks with lower energy consumption. One of the most famous bio-inspired design for soft robotic fingers is based on the so called Fin Ray principle, invented in 1997 by Leif Kniese [28]. During a fishing trip, he observed that, when pushing the side of fish fins, these do not bend in the direction of the applied force, but only in the opposite one. After this discovery, Leif Kniese and Rudolf Bannasch analyzed the anatomy of this biological phenomenon in the laboratory of *EvoLogics GmbH* (Berlin, Germany) and finally developed the adaptive geometry named Fin-Ray [29]. This structure is composed of two vertical fins bound at one end, with horizontal ribs joining them throughout

their length. This particular design, when realized with flexible materials, allows the finger to adapt its shape to the one of the grasped object, allowing a simple yet reliable manipulation. In particular, the Fin- Ray structure has proven to be capable of larger payloads with no reduction in compliance [30], paving the way to a new family of soft manipultators and robotic fingers, as shown in Fig. 2.9 [31].

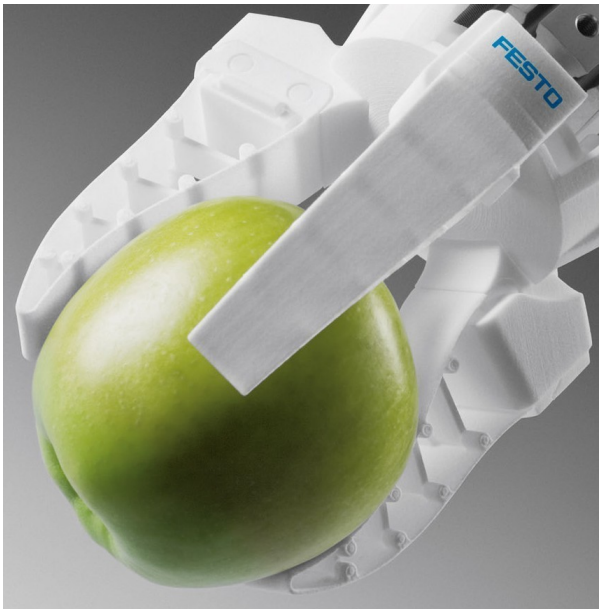

Fig. 2.9 Festo's soft gripper based on Fin-Ray® effect [31].

Despite their popularity in grasping and manipulation applications, the state of the art is lacking of an effective modeling technique to predict the behavior of FRE fingers, mostly because of their closed-chain structure which necessarily increases the number of constraints. However, every design and fabrication process can highly benefit from a reliable mathematical model, which allows the optimization of the design, avoiding unnecessary manufacturing iterations. This is demonstrated by some recent works focused mostly on the modeling of continuum closed-chain manipulators, composed of flexible elements. In [32], the deformation of the elements composing the robot are modeled using continuous Cosserat rod theory, while in [33] the prediction of unstable solution has been tackled, in order to prevent the buckling of the slender legs composing the robot. Finally, some of the previous results on the modeling and analysis on continuum robots have been summarized and implemented in [34].

In this work, we propose a general mathematical formulation for the analysis of closed-chain soft robots and, in particular, of Fin- Ray structures. The model is based on Discrete Cosserat approach [8], which has been extended to consider closed-chain hybrid geometries composed of both soft and rigid elements. The model has been employed to investigate an optimal design for a soft robotic Fin-Ray finger and finally a prototype has been fabricated. The FRE structure's ability to conform to an external force, while maintaining rigidness out of its grasping plane, inspired us to exploit its use as supernumerary robotic fingers to meet their ergonomics and functional requirements [35].

The work is organized as follows. In Section 2.3 we propose a generalized theoretical model for soft-rigid closed-chain structures, which is applied in Section 2.4 to Fin-Ray effect based fingers. The model is used to test the design of a FRE soft robotic finger previously present in [36] and the results have been validated both through Finite Element Modeling (FEM) simulations and experimentally in Section 2.5. After drawing some conclusions on the performances of the previous design, an optimization procedure is carried out in Section 2.6 and finally a new prototype is fabricated and tested in 2.7. We then present, in Section 3.2, the complete design and fabrication of the proposed supernumerary robotic finger inspired by the Fin-Ray effect. The device grasping ability was tested in different activity daily living (ADL) tasks consisting of different objects with various sizes and shapes. Finally in Sec. 3.2.5 conclusions are outlined.

2.3 Dynamic Model of Closed-Chain Soft-Rigid Systems

In this section we extend the mathematical model presented in [8] to closed-chain robots composed of soft as well as rigid bodies. We start by recalling the open-chain dynamic model for soft-rigid multibody system [13], which will then be augmented with the inclusion of the closed-loop joint wrenches [37]. In the following, all the quantities are expressed in the local (body) coordinate frame if not specified otherwise, while $\cdot$ and $'$ superscripts represent partial differentiation with respect to time and space, respectively.

2.3.1 Open-Chain Dynamics

2.3.1.1 Kinematics

The configuration of a soft body i (respectively a rigid body) with respect to its predecessor in the chain is defined as a curve $\boldsymbol{g}_i(\cdot) : X \in [0, L_i] \mapsto \boldsymbol{g}_i(X) \in SE(3)$ (respectively by a point $\boldsymbol{g}_i \in SE(3)$) with

$$\boldsymbol{g}_i(X) = \begin{pmatrix} \mathbf{R}_i & \mathbf{u}_i \\ \mathbf{0}^T & 1 \end{pmatrix}.$$

The continuous models of the position, velocity and acceleration of a soft body can be derived from the Cosserat rod theory, which gives [11]:

$$\begin{aligned} \boldsymbol{g}_i' &= \boldsymbol{g}_i \widehat{\boldsymbol{\xi}}_i \,, \\ \boldsymbol{\eta}_i' &= \dot{\boldsymbol{\xi}}_i - \mathrm{ad}_{\boldsymbol{\xi}_i} \boldsymbol{\eta}_i \,, \\ \dot{\boldsymbol{\eta}}_i' &= \ddot{\boldsymbol{\xi}}_i - \mathrm{ad}_{\dot{\boldsymbol{\xi}}_i} \boldsymbol{\eta}_i - \mathrm{ad}_{\boldsymbol{\xi}_i} \dot{\boldsymbol{\eta}}_i \,, \end{aligned} \tag{2.40}$$

where

$$\widehat{\boldsymbol{\xi}}_i(X) = \begin{pmatrix} \tilde{\mathsf{k}}_i & \mathsf{p}_i \\ \mathbf{0}^T & 0 \end{pmatrix} \in \mathfrak{se}(3) \,, \; \boldsymbol{\xi}_i(X) = \left(\mathsf{k}_i^T \,, \mathsf{p}_i^T\right)^T \in \mathbb{R}^6 \,,$$

defines the strain state (with $\tilde{\mathsf{k}}_i(X) \in \mathfrak{so}(3)$,$\mathsf{k}_i(X) \in \mathbb{R}^3$ and $\mathsf{p}_i(X) \in \mathbb{R}^3$ respectively the angular and linear strain);

$$\widehat{\boldsymbol{\eta}}_i(X) = \begin{pmatrix} \tilde{\mathsf{w}}_i & \mathsf{v}_i \\ \mathbf{0}^T & 0 \end{pmatrix} \in \mathfrak{se}(3) \, , \, \boldsymbol{\eta}_i(X) = \left(\mathsf{w}_i^T, \mathsf{v}_i^T\right)^T \in \mathbb{R}^6 \, .$$

is the cross-section velocity twist (with $\tilde{\mathsf{w}}_i(X) \in \mathfrak{so}(3)$,$\mathsf{w}_i(X) \in \mathbb{R}^3$ and $\mathsf{v}_i(X) \in \mathbb{R}^3$ respectively the angular and linear velocity); and $\mathrm{ad}_{(.)} \in \mathbb{R}^{6\times 6}$ is the adjoint operator of the Lie algebra (see Appendix A). To model constrained rod, such as the Kirchhoff-Love case with angular strain only, the strain field is specified as:

$$\boldsymbol{\xi}_i(X) = \boldsymbol{B}_i \boldsymbol{q}_i + \bar{\boldsymbol{\xi}}_i \, ,$$

where $\boldsymbol{B}_i \in \mathbb{R}^{6\times n_i}$ forms a basis for the allowed motion subspace, $\boldsymbol{q}_i(X) \in \mathbb{R}^{n_i}$ contains the values of the allowed strains and, $\bar{\boldsymbol{\xi}}_i \in \mathbb{R}^6$ is a fixed twist modeling constant yet non-zero strains (*e.g.*, for inextensible rod with $x-$axis tangent to the centerline $\bar{\boldsymbol{\xi}}_i = [0\,0\,0\,1\,0\,0]^T$)

Now, assuming piece-wise constant strains [38], equations (2.40) can be analytically integrated using the matrix exponential method, leading to:

$$\begin{aligned} \boldsymbol{g}_i(X) =& e^{X\widehat{\boldsymbol{\xi}}_i} \, , \\ \boldsymbol{\eta}_i(X) =& \mathrm{Ad}^{-1}_{\boldsymbol{g}_{hi}\boldsymbol{g}_i} \boldsymbol{\eta}_h + \mathrm{Ad}^{-1}_{\boldsymbol{g}_i} \mathrm{T}_{\boldsymbol{g}_i} \boldsymbol{B}_i \dot{\boldsymbol{q}}_i \, , \\ \dot{\boldsymbol{\eta}}_i(X) =& \mathrm{Ad}^{-1}_{\boldsymbol{g}_{hi}\boldsymbol{g}_i} \dot{\boldsymbol{\eta}}_h + \mathrm{Ad}^{-1}_{\boldsymbol{g}_i} \int_0^X \mathrm{Ad}_{\boldsymbol{g}_i(s)} \mathrm{ad}_{\boldsymbol{\eta}_i(s)} ds \boldsymbol{B}_i \dot{\boldsymbol{q}}_i + \\ & \mathrm{Ad}^{-1}_{\boldsymbol{g}_i} \mathrm{T}_{\boldsymbol{g}_i} \boldsymbol{B}_i \ddot{\boldsymbol{q}}_i \, , \end{aligned} \tag{2.41}$$

where $\mathrm{Ad}_{\boldsymbol{g}_i}(X) = e^{X\mathrm{ad}_{\boldsymbol{\xi}_i}} \in \mathbb{R}^{6\times 6}$ is the Adjoint operator of the Lie group, $\boldsymbol{g}_{hi} \in SE(3)$ is the rigid transformation between two consecutive bodies $h < i$ in the chain reference configuration and $\mathrm{T}_{\boldsymbol{g}_i}(X) = \int_0^X e^{s\mathrm{ad}_{\boldsymbol{\xi}_i}} ds$ is the tangent operator of the exponential map. An analytic expression of the exponentials above, derived from [39], is given in the Appendix A. Remarkably, the kinematics (2.41) is a generalization to soft and hybrid systems of the geometric theory of rigid robots due to Brockett [40] and popularized by Murray and Sastry [41]. In fact, in the case of lumped joint, we just let $\boldsymbol{q}_i$ be the usual joint coordinates and $X = L_i = 1$.

Successive applications of the kinematics (2.41) for all the bodies of the hybrid system, yields to the definition of the geometric Jacobian $\boldsymbol{J}_i(X) \in \mathbb{R}^{6\times n}$ and its derivative $\dot{\boldsymbol{J}}_i(X) \in \mathbb{R}^{6\times n}$ (n being the total number of DOFs) for each soft/rigid body, which relates the generalized coordinate vector $\boldsymbol{q} = \left[\boldsymbol{q}_0^T \; \boldsymbol{q}_1^T \cdots \boldsymbol{q}_{N-1}^T\right]^T \in \mathbb{R}^n$ (N being the total number of bodies) and the i^{th}

velocity twist as shown below.

$$\begin{aligned}
\boldsymbol{\eta}_i(X) &= \sum_{h=0}^{i} \mathrm{Ad}^{-1}_{\boldsymbol{g}_h \cdots \boldsymbol{g}_i} \mathrm{T}_{\boldsymbol{g}_h} \boldsymbol{B}_h \dot{\boldsymbol{q}}_h = \sum_{h=0}^{i} {}^{i}\boldsymbol{S}_h \dot{\boldsymbol{q}}_h = \boldsymbol{J}_i \dot{\boldsymbol{q}} \,, \\
\dot{\boldsymbol{\eta}}_i(X) &= \sum_{h=0}^{i} {}^{i}\boldsymbol{S}_h \ddot{\boldsymbol{q}}_h + \mathrm{Ad}^{-1}_{\boldsymbol{g}_h \cdots \boldsymbol{g}_i} \int_0^X \mathrm{Ad}_{\boldsymbol{g}_h(s)} \mathrm{ad}_{\boldsymbol{\eta}_h(s)} ds \boldsymbol{B}_h \dot{\boldsymbol{q}}_h \\
&= \sum_{h=0}^{i} {}^{i}\boldsymbol{S}_h \ddot{\boldsymbol{q}}_h + {}^{i}\dot{\boldsymbol{S}}_h \dot{\boldsymbol{q}}_h = \boldsymbol{J}_i \ddot{\boldsymbol{q}} + \dot{\boldsymbol{J}}_i \dot{\boldsymbol{q}} \,,
\end{aligned} \tag{2.42}$$

where the block elements of the i^{th} Jacobian ${}^{i}\boldsymbol{S}_{(\cdot)} \in \mathbb{R}^{6 \times n_{(\cdot)}}$ and its derivative ${}^{i}\dot{\boldsymbol{S}}_{(\cdot)} \in \mathbb{R}^{6 \times n_{(\cdot)}}$ have been defined. Note that this formulation applies directly to the motion submanifolds of any multi-DOFs lumped joint including Exp-submanifolds [42] and free-body motion.

2.3.1.2 Dynamics

Once a Jacobian is found, the generalized dynamics of the hybrid multibody system can be obtained by projecting the free dynamics of each body, including soft bodies, by virtue of the D'Alembert's principle. The free dynamic equations of a rigid body and a soft body (with its boundary conditions) are respectively:

$$\begin{aligned}
&\mathscr{M}_i \dot{\boldsymbol{\eta}}_i + \mathrm{ad}^*_{\boldsymbol{\eta}_i} \mathscr{M}_i \boldsymbol{\eta}_i = \mathscr{F}_{J_i} - \mathrm{Ad}^*_{\boldsymbol{g}_{ij}\boldsymbol{g}_j} \mathscr{F}_{J_j} + \mathscr{F}_{e_i} \text{ and} \\
&\mathscr{M}_i \dot{\boldsymbol{\eta}}_i + \mathrm{ad}^*_{\boldsymbol{\eta}_i} \mathscr{M}_i \boldsymbol{\eta}_i = \mathscr{F}'_{i-a_i} + \mathrm{ad}^*_{\boldsymbol{\xi}_i} \mathscr{F}_{i-a_i} + \bar{\mathscr{F}}_{e_i} \,, \\
&\mathscr{F}_{i-a_i}(0) = -\mathscr{F}_{J_i} \,, \mathscr{F}_{i-a_i}(L_i) = -\mathrm{Ad}^*_{\boldsymbol{g}_{ij}} \mathscr{F}_{J_j} \,;
\end{aligned} \tag{2.43}$$

where $\mathscr{M}_i(X)$ (respectively $\mathscr{M}_i$) $\in \mathbb{R}^{6\times6}$ is the screw inertia matrix of the cross-section (respectively the rigid body), $\bar{\mathscr{F}}_{e_i}(X)$ (respectively $\mathscr{F}_{e_i}$) $\in \mathbb{R}^6$ is the distributed (respectively concentrated) external load, $\mathscr{F}_{i-a_i}(X) \in \mathbb{R}^6$ is the internal wrench due to the distributed actuation [43] and the elasticity of the soft body, $\mathscr{F}_{J_{(\cdot)}} \in \mathbb{R}^6$ is the wrench transmitted across joint $(\cdot)$ and $\mathrm{ad}^*_{(\cdot)}$ (respectively $\mathrm{Ad}^*_{(\cdot)}$) $\in \mathbb{R}^{6\times6}$ is the co-adjoint (respectively co-Adjoint) map of the Lie algebra (respectively Lie group) defined in Appendix A. By Jacobian projection of the soft and rigid body in the system, we obtain the generalized dynamics in its classical form [13]:

$$\boldsymbol{M}(\boldsymbol{q})\ddot{\boldsymbol{q}} + \boldsymbol{C}(\boldsymbol{q},\dot{\boldsymbol{q}})\dot{\boldsymbol{q}} + \boldsymbol{K}(\boldsymbol{q})(\boldsymbol{q} - \boldsymbol{q}^*) = \boldsymbol{\tau} + \boldsymbol{F}(\boldsymbol{q},\dot{\boldsymbol{q}}) \,, \tag{2.44}$$

where $\boldsymbol{M} \in \mathbb{R}^{n\times n}$ is the generalized mass matrix, $\boldsymbol{C} \in \mathbb{R}^{n\times n}$ is the generalized Coriolis matrix (which may include also block-diagonal internal damping terms), $\boldsymbol{K} \in \mathbb{R}^{n\times n}$ is the block-diagonal generalized stiffness matrix, $\boldsymbol{q}^* \in \mathbb{R}^n$ is the vector of reference strain configurations, $\boldsymbol{F} \in \mathbb{R}^n$ is the vector of generalized external forces and and $\boldsymbol{\tau} \in \mathbb{R}^n$ is the vector of applied actuation forces.

2.3.2 Closed-Chain Dynamics

Following the approach of [37] for rigid-body systems, the closed chain dynamics of a hybrid soft-rigid system is obtained by applying the close-loop constrain wrenches to a spanning open-chain of the system, where the wrenches are parametrized by a vector of Lagrange multipliers $\boldsymbol{\lambda} \in \mathbb{R}^{n_c}$ (n_c being the total number of constrains). The crucial step to achieve this result is to express the constrain equations imposed by the close-loop joints in the Pfaffian form $\boldsymbol{A}\dot{\boldsymbol{q}} = \boldsymbol{0}$ ($\boldsymbol{A} \in \mathbb{R}^{n_c \times n}$), in order to obtain a basis for the constrain wrenches and close the system of equations for the unknowns $\ddot{\boldsymbol{q}}$ and $\boldsymbol{\lambda}$.

2.3.2.1 Closed-Loop Joints Pfaffian Constrain

The closed-loop joints impose that the relative velocity between the bodies connected by them has to be orthogonal (in the dual sense) to the subspace of constrain wrenches that the closed-loop joints generate. Let us define the relative velocity twist across the i^{th} closed-loop joint $\boldsymbol{\eta}_{Ji}$ and the basis for the constrain wrenches subspace ${}^{i}\boldsymbol{Z}_i^* \in \mathbb{R}^{6\times n_{ci}}$. Then, reminding that the motion subspace is spanned by ${}^{i}\boldsymbol{S}_i = \mathrm{Ad}_{g_i}^{-1}\mathrm{T}_{g_i}\boldsymbol{B}_i$, the closed-loop joint imposes that:

$$ {}^{i}\boldsymbol{Z}_i^{*T}\boldsymbol{\eta}_{Ji} = {}^{i}\boldsymbol{Z}_i^{*T}\,{}^{i}\boldsymbol{S}_i\dot{\boldsymbol{q}}_i = \boldsymbol{0}\,, \tag{2.45} $$

which yields

$$ {}^{i}\boldsymbol{Z}_i^* = \mathrm{Ad}_{g_i}^{*-1}\mathrm{T}_{g_i}^*\boldsymbol{B}_i^{\perp}\,, $$

where $\boldsymbol{B}_i^{\perp} \in \mathbb{R}^{6\times n_{ci}}$ is the basis orthogonal to $\boldsymbol{B}_i$ and $\mathrm{T}_{(\cdot)}^* = \mathrm{T}_{(\cdot)}^{-T}$ is analytically expressed in Appendix A. Note that we have considered only lumped closed-loop joints ($X = L_i = 1$) since all the soft bodies should be included in the spanning open-chain in order to account for the full kinetic energy of the system. Furthermore, it should also be noticed that the above formulation remains valid for any multi-dimensional lumped joint, even for the general case where $\mathrm{span}\left({}^{i}\boldsymbol{S}_i\right) \neq \mathrm{span}\left(\boldsymbol{B}_i\right)$ (*i.e.* $\left(\boldsymbol{B}_i\right)$ does not span a subalgebra of $\mathfrak{se}(3)$ [44]). However, for the majority of practical cases, $\mathrm{span}\left({}^{i}\boldsymbol{S}_i\right) = \mathrm{span}\left(\boldsymbol{B}_i\right)$ for a lumped joint [13], thus, ${}^{i}\boldsymbol{Z}_i^*$ may be replaced with $\boldsymbol{B}_i^{\perp}$ in (2.45).

Now, the constrain equation (2.45) can be expressed in terms of the open-chain kinematics as:

$$ {}^{i}\boldsymbol{Z}_i^{*T}\left(\boldsymbol{J}_{si} - \boldsymbol{J}_{pi}\right)\dot{\boldsymbol{q}} = \boldsymbol{0}\,, \tag{2.46} $$

where $\boldsymbol{J}_{si}$ and $\boldsymbol{J}_{pi}$ are respectively the Jocabians of the successor and predecessor body with respect to the closed-loop joint i (note that, for consistency, the two Jacobians have to point to the same body frame first considered attached to si then attached to pi). Collecting equations of type (2.46) for all the closed-loop joints of the system we obtain the desired Pfaffian constrain equation (with N_c the total number of closed-loop joints):

$$ \boldsymbol{A}\dot{\boldsymbol{q}} = \begin{bmatrix} {}^{1}\boldsymbol{Z}_1^{*T}\left(\boldsymbol{J}_{s1} - \boldsymbol{J}_{p1}\right) \\ \vdots \\ {}^{N_c}\boldsymbol{Z}_{N_c}^{*T}\left(\boldsymbol{J}_{sN_c} - \boldsymbol{J}_{pN_c}\right) \end{bmatrix}\dot{\boldsymbol{q}} = \boldsymbol{0}\,. \tag{2.47} $$

2.3.2.2 Dynamic Equations

Once a Pfaffian constrain equation is established, the open-chain dynamic equation (2.44) can be augmented with the additional constrain wrenches and closed for the unknowns $\ddot{\boldsymbol{q}}$ and $\boldsymbol{\lambda}$ [37]. In fact, the constrain wrenches, being orthogonal to the Null space of (2.47) (open-chain configurations that satisfy the new constrains), are spanned by $\boldsymbol{A}^T$ as a result of the fundamental theorem of linear algebra [45]. Furthermore, the time derivative of equation (2.47) provide the necessary supplementary equations to closed the system for the additional unknown $\boldsymbol{\lambda}$. Hence, we obtain

$$\begin{cases} \boldsymbol{M}\ddot{\boldsymbol{q}} + \boldsymbol{C}\dot{\boldsymbol{q}} + \boldsymbol{K}(\boldsymbol{q} - \boldsymbol{q}^*) = \boldsymbol{\tau} + \boldsymbol{F} + \boldsymbol{A}^T\boldsymbol{\lambda} \\ \boldsymbol{A}\ddot{\boldsymbol{q}} + \dot{\boldsymbol{A}}\dot{\boldsymbol{q}} = \boldsymbol{0} \end{cases} \tag{2.48}$$

Solving for $\boldsymbol{\lambda}$ [41], gives the desired closed-loop dynamic equation

$$\begin{aligned} \boldsymbol{M}\ddot{\boldsymbol{q}} = &\boldsymbol{P}\left[\boldsymbol{\tau} - \boldsymbol{K}(\boldsymbol{q} - \boldsymbol{q}^*) + \boldsymbol{F} - \boldsymbol{C}\dot{\boldsymbol{q}}\right] \\ &- \boldsymbol{A}^T\left(\boldsymbol{A}\boldsymbol{M}^{-1}\boldsymbol{A}^T\right)^{-1}\dot{\boldsymbol{A}}\dot{\boldsymbol{q}}, \end{aligned} \tag{2.49}$$

where $\boldsymbol{P} = \boldsymbol{I} - \boldsymbol{A}^T\left(\boldsymbol{A}\boldsymbol{M}^{-1}\boldsymbol{A}^T\right)^{-1}\boldsymbol{A}\boldsymbol{M}^{-1} \in \mathbb{R}^{n\times n}$ projects away joint wrenches that act on the constraints without doing any work on the system [46].

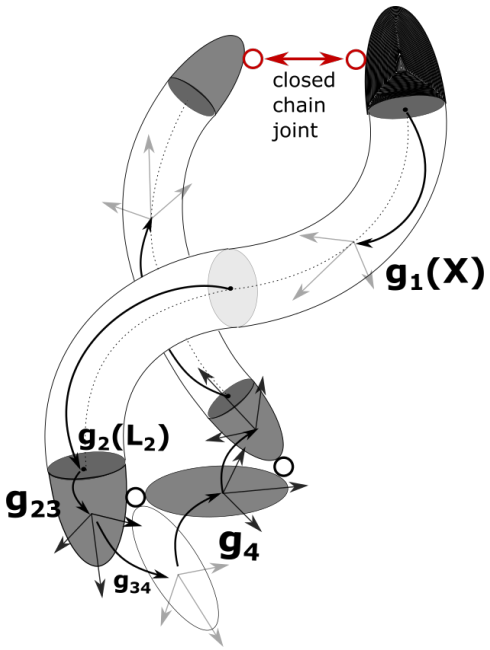

Fig. 2.10 Schematics of the proposed kinematics of a closed-chain soft-rigid multibody system

2.3.2.3 Constraint Stabilization

The closed-loop constrains expressed at the acceleration level, although theoretically correct, are not stable during numerical integration due to the finite machine precision [37]. Thus, a

Baumgarte stabilization is applied [47], which yields:

$$\boldsymbol{A}\ddot{\boldsymbol{q}}+\dot{\boldsymbol{A}}\dot{\boldsymbol{q}}+\frac{2}{T}\boldsymbol{A}\dot{\boldsymbol{q}}+\frac{1}{T^2}\boldsymbol{e}=\boldsymbol{0}\,, \tag{2.50}$$

where $T\in\mathbb{R}^+$ is the desired settling time constant and $\boldsymbol{e}\in\mathbb{R}^{n_c}$ represents a measure of the constrain error at the position level. For the latter, we can use the implicit formulation of the closed loop constrains at the position level by taking advantage of the logarithmic function in $SE(3)$ (defined in Appendix A), which yields to:

$$\boldsymbol{e}=\begin{bmatrix} {}^{1}\boldsymbol{Z}_1^{*T}\log\left(\boldsymbol{g}_{p1}^{-1}\boldsymbol{g}_{s1}\right)^{\vee} \\ \vdots \\ {}^{N_c}\boldsymbol{Z}_{N_c}^{*T}\log\left(\boldsymbol{g}_{pN_c}^{-1}\boldsymbol{g}_{sN_c}\right)^{\vee} \end{bmatrix}, \tag{2.51}$$

where $\boldsymbol{g}_{pi}$, $\boldsymbol{g}_{si}$ represent the configuration of respectively the predecessor and successor body and $^{\vee}$ maps $\mathfrak{se}(3)$ elements into $\mathbb{R}^6$ [41].

2.4 Mechanical Model of Fin Ray® Finger

In this section, we adapt the general formulation presented above to the case of the Fin-Ray finger. Furthermore, a new partition of the dynamics (2.49) is proposed to solve mixed (forward/inverse) dynamic and static problems.

2.4.1 Fin-Ray Kinematics

Taking advantage of the discrete Cosserat approach, the kinematics of the Fin-Ray finger can be outlined as follows. The base of the right side of the finger can translate vertically via a prismatic joint, while the rest of the finger is attached to this base through a revolute joint. The left base is fixed and also connected to the rest of the finger via a revolute joint. The V shape soft finger is naturally divided into sections by the tip cuspid and the interconnecting rigid bodies, which are linked to the soft part through revolute joints on both side. Each section of the soft finger is modeled with an inextensible Kirchhoff-Love rod (*i.e.* only torsion and bending are allowed). A schematic diagram of the Fin-Ray kinematics is presented in figure 2.11. Thus, the motion subspaces take the form:

$$\boldsymbol{B}_p=\begin{bmatrix}0\\0\\0\\1\\0\\0\end{bmatrix},\boldsymbol{B}_r=\begin{bmatrix}0\\0\\1\\0\\0\\0\end{bmatrix},\boldsymbol{B}_k=\begin{bmatrix}1&0&0\\0&1&0\\0&0&1\\0&0&0\\0&0&0\\0&0&0\end{bmatrix},\bar{\boldsymbol{\xi}}_k=\begin{bmatrix}0\\0\\0\\1\\0\\0\end{bmatrix}. \tag{2.52}$$

There are many possible spanning open-chains one could arbitrary chose to model the system. We decide to open the system at the revolute joints on the left side of the rigid bodies and at the tip cuspid connecting the two sides of the soft finger (see figure 2.11). Thus, the constrain wrenches subspaces are spanned by

$$\boldsymbol{B}_r^{\perp} = \begin{bmatrix} 1 & 0 & 0 & 0 & 0 \\ 0 & 1 & 0 & 0 & 0 \\ 0 & 0 & 0 & 0 & 0 \\ 0 & 0 & 1 & 0 & 0 \\ 0 & 0 & 0 & 1 & 0 \\ 0 & 0 & 0 & 0 & 1 \end{bmatrix}, \boldsymbol{B}_t^{\perp} = \boldsymbol{I}. \tag{2.53}$$

With this kinematics, if we consider, for example, three interconnecting rigid bodies, we obtain a total number of open-loop DOFs n = 1x1 (prismatic) + 1x5 (revolutes) + 3x8 (Kirchhoff-Love rods) = 30 and a total number of constrained closed-chain DOFs n_c = 5x3 (revolutes) + 1x6 (tip clamping) = 21, which leads to a remaining mobility of $n - n_c = 9$ independent DOFs (as the system has no redundant constrains).

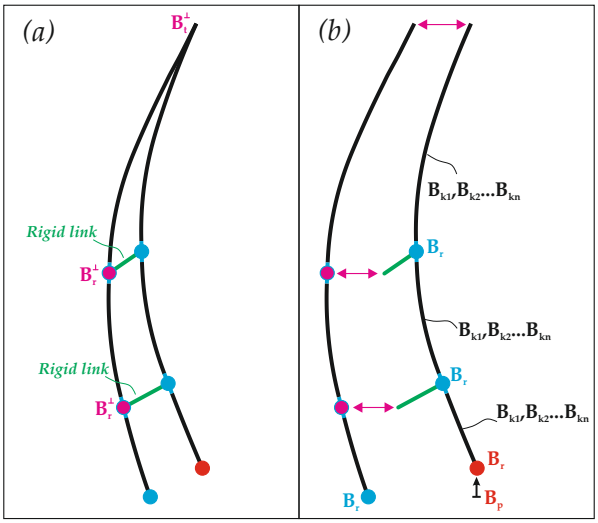

Fig. 2.11 Schematics of the proposed open and closed chain kinematics for a Fin-Ray finger system.

2.4.2 Fin-Ray Statics

The static formulation of equation (2.49) can be written as:

$$\boldsymbol{P}\left[\boldsymbol{\tau} - \boldsymbol{K}\left(\boldsymbol{q} - \boldsymbol{q}^*\right) + \boldsymbol{F}\right] = 0. \tag{2.54}$$

Equation (2.54) provides only $n - n_c$ independent conditions for its argument, with $n - n_c$ equal to the rank of $\boldsymbol{P}$. Thus, in order to solve the system for $\boldsymbol{q} \in \mathbb{R}^n$ (forward statics), $\boldsymbol{\tau} \in \mathbb{R}^n$ (inverse statics) or a mutually exclusive combination of them (mixed statics), additional n_c conditions

have to be given. These are conveniently provided by the implicit formulation of the closed loop constrains at the position level (2.51),which reads:

$$\begin{bmatrix} {}^{1}\boldsymbol{Z}_{1}^{*T} \log\left(\boldsymbol{g}_{p1}^{-1}\boldsymbol{g}_{s1}\right)^{\vee} \\ \vdots \\ {}^{N_c}\boldsymbol{Z}_{N_c}^{*T} \log\left(\boldsymbol{g}_{pN_c}^{-1}\boldsymbol{g}_{sN_c}\right)^{\vee} \end{bmatrix} = \boldsymbol{0}\,. \tag{2.55}$$

The system composed by (2.54) and (2.55) can then be solved by employing a nonlinear system solver.

2.4.3 Fin-Ray Dynamics

The dynamic equation (2.49) is given in its inverse dynamics form, *i.e.*, providing the kinematic motion of the system, the actuation force can be computed via a nonlinear system solver (although it will be always possible to add an element of the null space of $\boldsymbol{P}$). As usual, the symmetric positive definite mass matrix $\boldsymbol{M}$ can be inverted to give the forward dynamics model. On the other hand, in order to solve a mixed dynamic problem the elements of (2.49) need to be recombined. In particular, the known accelerations of $\ddot{\boldsymbol{q}}$ go, together with their respective columns of $\boldsymbol{M}$, to replace the unknown actuation forces of $\boldsymbol{\tau}$ and the respective columns of $\boldsymbol{P}$ (with a negative sign). Mathematically, this procedure provides the following dynamic equation:

$$\begin{aligned} \widetilde{\boldsymbol{M}}\widetilde{\ddot{\boldsymbol{q}}} = &\widetilde{\boldsymbol{P}}\widetilde{\boldsymbol{\tau}} + \boldsymbol{P}\left[\boldsymbol{F} - \boldsymbol{K}\left(\boldsymbol{q} - \boldsymbol{q}^{*}\right) - \boldsymbol{C}\dot{\boldsymbol{q}}\right] \\ &- \boldsymbol{A}^{T}\left(\boldsymbol{A}\boldsymbol{M}^{-1}\boldsymbol{A}^{T}\right)^{-1}\dot{\boldsymbol{A}}\dot{\boldsymbol{q}}, \end{aligned} \tag{2.56}$$

where $\widetilde{\boldsymbol{M}}$, $\widetilde{\ddot{\boldsymbol{q}}}$, $\widetilde{\boldsymbol{P}}$ and $\widetilde{\boldsymbol{\tau}}$ are the new components of the dynamics obtained as described above. Finally, matrix $\widetilde{\boldsymbol{M}}$ can be inverted at every time loop to solve for the unknowns $\widetilde{\ddot{\boldsymbol{q}}}$. An example of the results obtained from the simulation is reported in Fig. 2.12. It should be noted that, with the considered design, the overall shape of the finger is not changing significantly, but a quasi-rigid motion is observed.

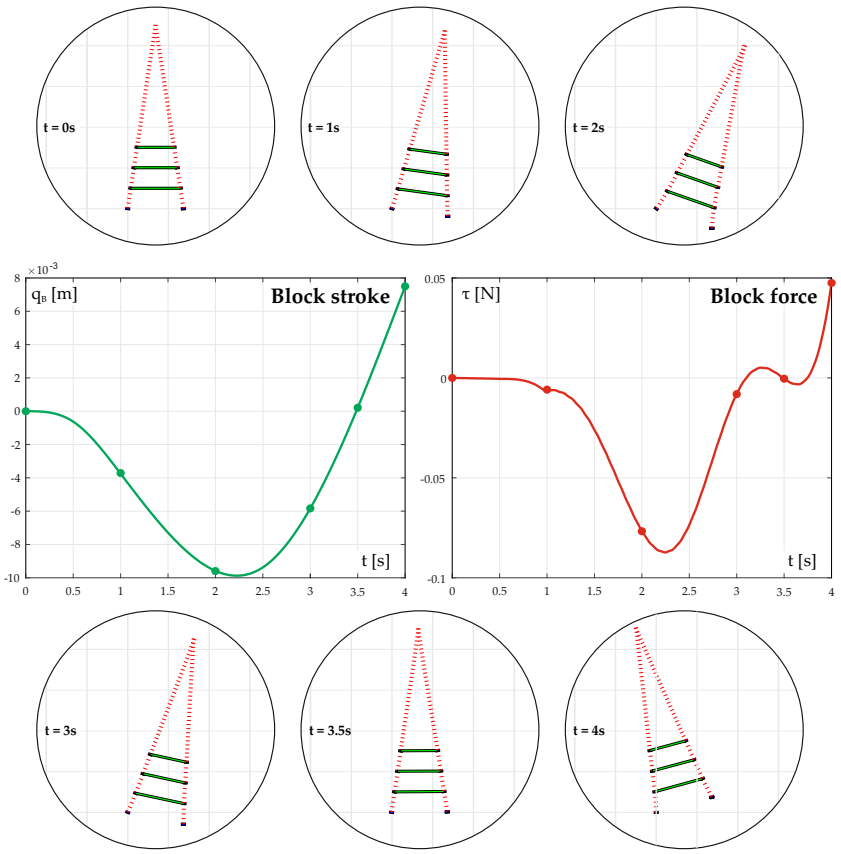

Fig. 2.12 Results obtained through a dynamical analysis: trends of the block stroke and (right) actuation force (left) over time. The dots correspond to the specific times at which the deformed shapes reported in the round circles have been obtained. It should be noted that, with the considered design, the overall shape of the finger is not changing significantly, but a quasi-rigid motion is observed.

2.5 Mathematical Model Validation

The theoretical model presented in Section 2.3 represents a general tool for the analysis of closed chain fingers and structures, such as Fin-Ray devices, as seen in Section 2.4. In order to validate its accuracy, in this section the model is employed to investigate the performance of the finger design previously presented in [36] and the results are compared with those obtained, first, through an FEM analysis and later through some experimental trials. Moreover, through the investigation, some conclusion are drawn on the performance of the proposed finger. The main features of the considered design [36] are reported in Figure 2.13: the flexible ABS fins are connected by two rigid links placed along their length.

The system is modeled using the mixed-static approach introduced in Section 2.4. In this case, in equations (2.54) the unknowns are one component of the actuation forces $\boldsymbol{\tau}$ and the complementary components of the configuration q. The system is solved thorough an iterative recursive method, where initially these unknowns are set, respectively, to zero and to q^*.

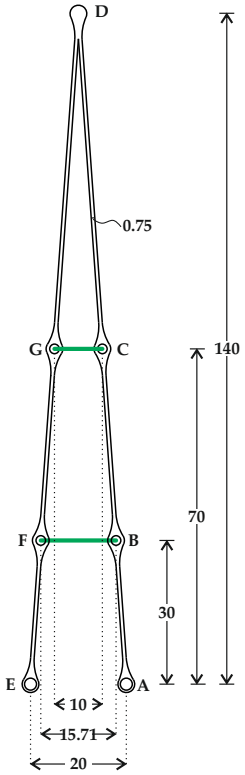

Fig. 2.13 Geometry of the considered finger design, previously presented in [36] and further investigated here. The finger is 18 mm deep, while the fins material is ABS, having Young's Modulus $E = 2250 \cdot 10^6$ MPa, Poisson's ratio $\nu = 0.3$. The ribs are considered as rigid elements. All the measures reported in the figure are in [mm].

The following loading conditions are considered:

- 2D - Concentrated force F_{py} laterally applied on the connector C. The considered force magnitudes are 0.5, 1.0, 1.5, 3.0 and 5.0 N.
- 2D - Distributed force F_{dy} laterally applied along the right tip $\bar{CD}$. The considered resultant forces applied are 0.5, 1.0 and 1.5 N.
- 3D - Concentrated force F_{py} on connector C and out-of-plane distributed load F_{dz} along the left tip $\bar{GD}$. The magnitude of the concentrated force F_{py} is $0.5N$, while the considered resultant loads F_{dz} are 1.0, 2.0 and 3.0 N.

In all the considered cases, the direction of the load is maintained orthogonal to the application points, following their deformations.

2.5.1 Finite Element validation

A finite-element analysis is performed to validate the results of the proposed mathematical model. The purpose of this comparison is twofold: being FE analysis one of the most powerful solutions for the numerical modeling of mechanical systems, we use the results to validate those obtained with the proposed model. At the same time, we want to prove that, even though

the proposed tool is simpler and characterized by a drastically reduced computational cost, it is able to provide accurate and reliable results.

Non-linear general static simulations are run in Abaqus, considering geometry, material and inertia representative of the device presented in Figure 2.13. The finger is freely meshed using tetrahedral elements, while the rigid links are modeled using a combination of *hinge* and *link* connectors, arranged in order to preserve the distances and the angles between the joints, allowing only in-plane rotations. It should be noted that the ribs could be modeled as rigid elements inserted in the connectors, in accordance to the real world physical model. However, this would require the modeling of the contact problem between these elements and the finger, drastically complicating the computational cost of the simulations. The finger is constrained at the lower part using displacement/rotation boundary conditions which simulates the prismatic and the revolute joints considered in the mathematical model. In order to facilitate the convergence of the simulations, the loads are applied using a sigmoidal amplitude curve and they are all simulated as pressure loads, to preserve their perpendicular direction with the applied elements.

The results of the comparison for the considered loading cases are reported in figures (2.14), (2.15) and (2.16). These comparisons show a good agreement between the theoretical and the finite elements results, as also demonstrated in table 2.2, reporting the errors obtained for each case. The errors have been evaluated as the sum of the mean differences between the joints positions resulting from the two analysis, weighted on the distances between the joints and the ground.

Table 2.2 Errors

Loading case	$\mathscr{E}(\%)$
2D Concentrated $F_y = 0.5N$	0.96
2D Concentrated $F_y = 1.0N$	2.73
2D Concentrated $F_y = 1.5N$	4.16
2D Concentrated $F_y = 3.0N$	7.11
2D Concentrated $F_y = 5.0N$	6.85
2D Distributed $Fd_y = 0.5N$	0.54
2D Distributed $Fd_y = 1.0N$	1.16
2D Distributed $Fd_y = 1.5N$	2.90
3D $F_y = 0.5N$ & $Fd_z = 1.0N$	2.01
3D $F_y = 0.5N$ & $Fd_z = 2.0N$	2.00
3D $F_y = 0.5N$ & $Fd_z = 3.5N$	1.71

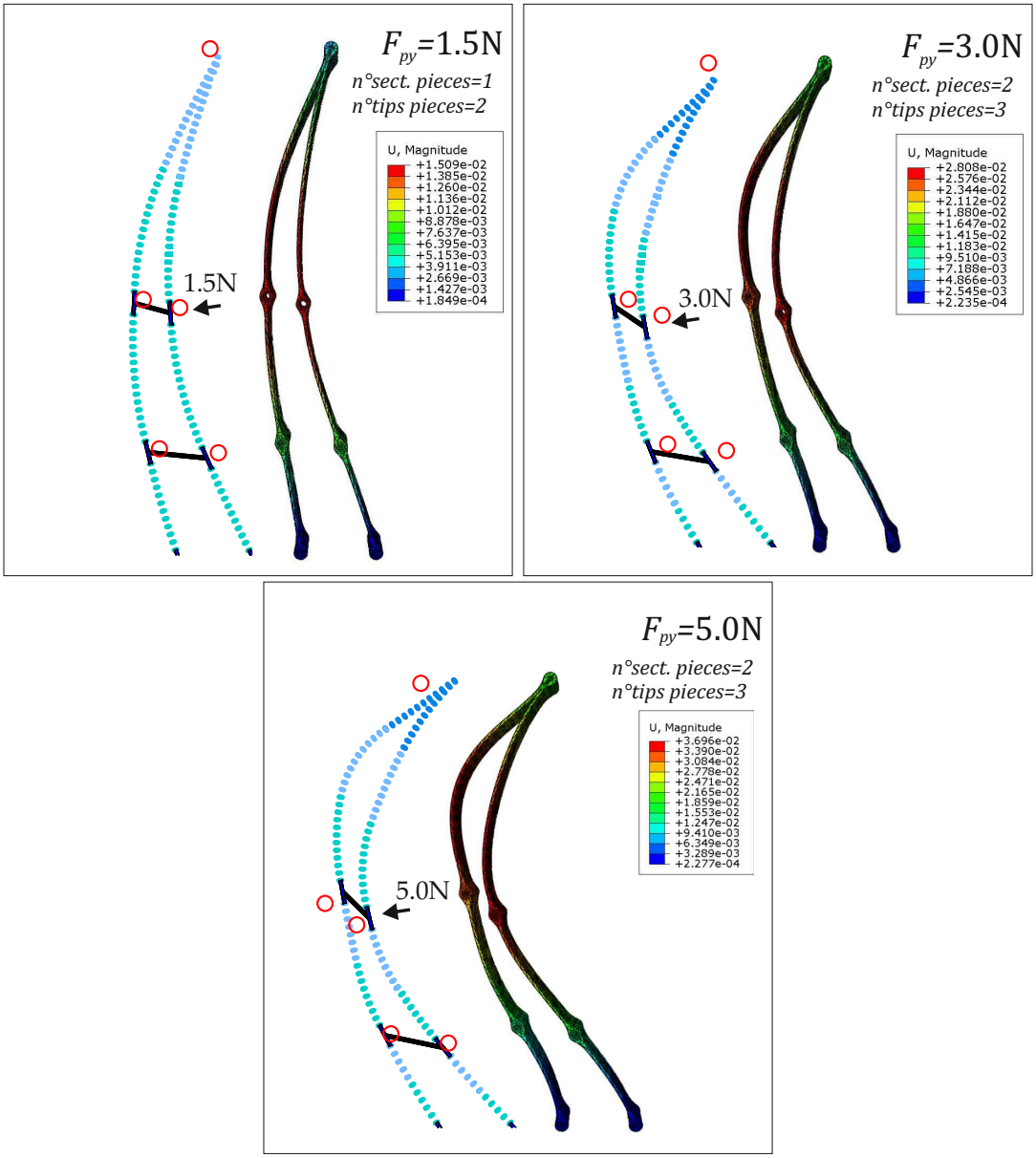

Fig. 2.14 Comparison between the proposed mathematical tool (left) and the FEM results (right), when a concentrated force F_{py} is applied at one node. In the figures, we reported the number of pieces which have been used in the mathematical model to discretize the sections and the tips composing the fingers.

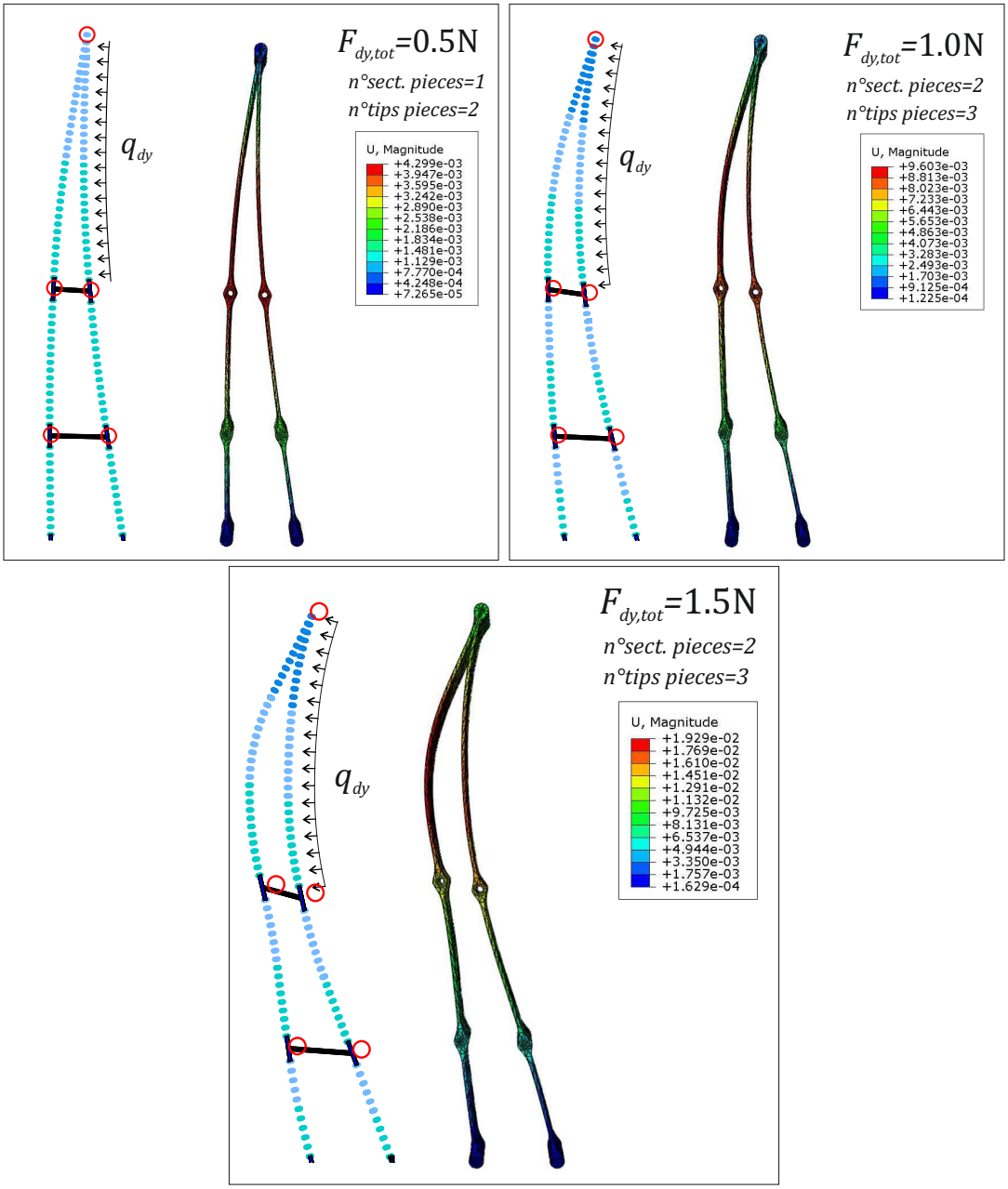

Fig. 2.15 Comparison between the proposed mathematical tool (left) and the FEM results (right), when a distributed force F_{dy} is applied on the right tip. It should be noted that, for higher loads magnitude, the numbers of constant strain pieces used to discretize the sections and the tips have been increased, in order to effectively model the higher deformations.

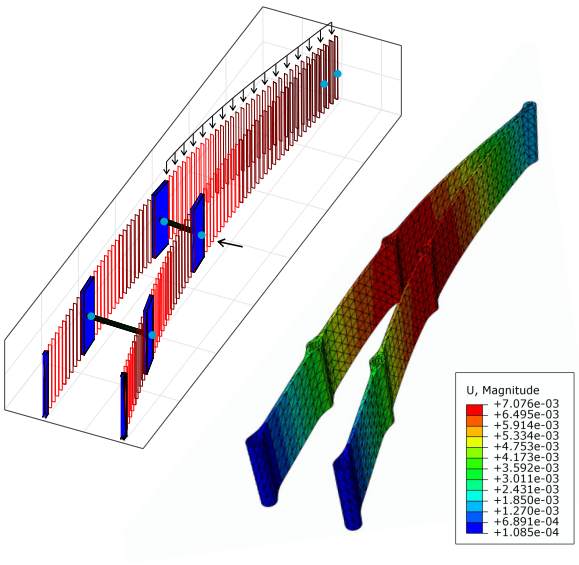

Fig. 2.16 Comparison between the mathematical model (left) and the FEM results, in a 3D case. A concentrated force F_y, acting along the y direction, is applied at node C, while an out-of-plane distributed force F_{dz} is applied on the left tip. The maximum out-of-plane displacement is 0.641 mm for the mathematical results and 1.21 mm for the FEM, measured at the tip of the finger (the displacements correspond to 0.46% and 0.86% of the total length at the tip, respectively).

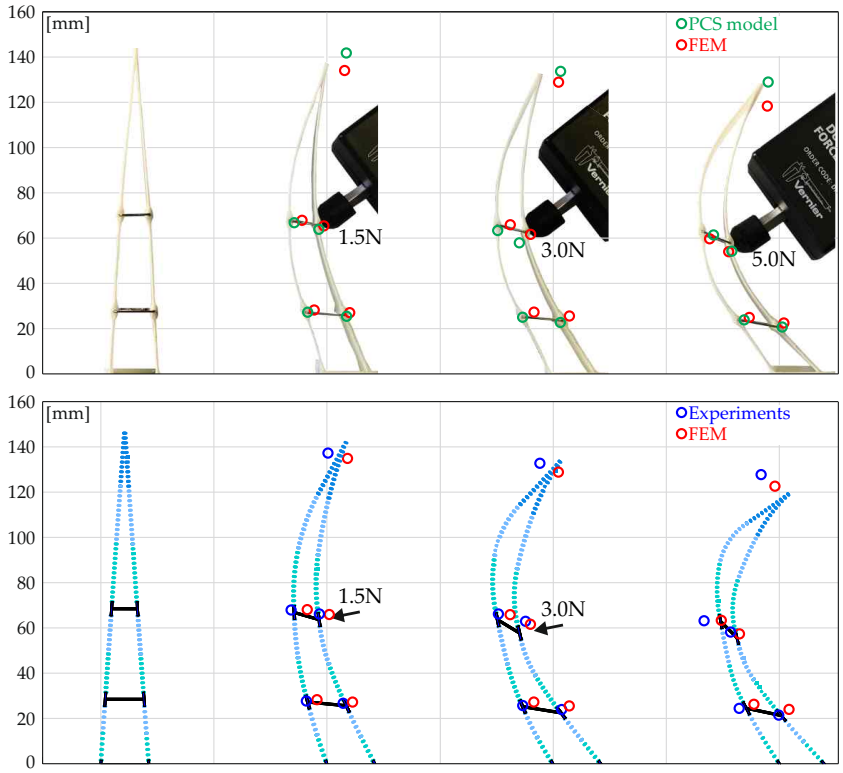

Fig. 2.17 Comparison between the experimental results and those predicted by the Piecewise Constant Strain model.

2.5.2 Experimental validation

The results obtained with the proposed theoretical model and with FEM are finally compared to those carried out experimentally. The finger's prototype is 3D printed using ABS material and the rigid links are obtained using steel ring elements inserted in the connectors. Grease has been used to reduce the friction between these elements and the finger. A concentrated follower force F_{py} is laterally applied on the connector C, figure 2.13. Only the higher values of the force, 1.5, 3 and 5 N, are considered here. The results of the comparison are presented in 2.17, where both the experimental and the modeled deformed shapes are reported. For the sake of completeness, the FEM results are also reported, with the red circles reporting the position of the connectors and the tip. Is it possible to notice the good accordance between the experimental and the theoretical results. In particular, comparing the deformed shapes obtained in 2.14, the proposed theoretical model provides more reliable results with respect to FEM. For the highest loading condition, even though the left part of the deformed finger is quite different with respect to the one predicted by the model, the right part, where the load is applied, shows a good accordance. During the experiments, when a load higher than $5N$ was applied, a buckling phenomenon was observed in the lower part of the left fin. This is due to the increasing inclination of the rigid ribs that provides an increasing compressive force resulting in the observed buckling. This phenomenon, which was also predicted by both the theoretical model and the FEM simulations, implicates that the maximum load that can be applied to the design presented in [36] is $5N$. Moreover, at the highest load condition, the overall deformed shape for the finger is not optimal for a gripper design, with a backward shape that is not able to properly wrap around an object. In order to overcome all the above mentioned limitations of the previous design, in the following section an optimization procedure is carried out to identify a new, improved design.

2.6 Optimization

One of the advantages of the proposed mathematical model is the opportunity to easily model different designs and materials, considering the loading condition imposed by the user case. Although an FEM analysis would allow the same process, as explained in Section 2.5, each considered case would require a longer process to set up the initial geometry and boundary conditions and the simulations would require longer time to be completed. Moreover, as proven by the results obtained in the previous section, FEM results presents some discrepancies with respect to the physical model, in some cases higher than those observed with the proposed approach.

In this section, we consider three different parameters for the optimization procedure:

- the number of rigid ribs place along the length of the finger;
- the inclination of the rigid ribs;
- the material used for the flexible finger.

In particular, the results will prove that, while the number and the inclination of the rigid ribs strongly affect the deformed shapes that can be obtained at increasing loads, this is no longer valid when a different material is considered. In fact, once the design is fixed, changing the material only affects the loads required to obtain a specific deformed shape, but these are the same for all the materials. This is particularly important from a gripper point of view, since the design can be investigated regardless of the material, which can be selected only once the loads are also defined.

2.6.1 Rigid ribs number

The first parameter that it's investigated for the optimization process is the number of rigid links used in the finger $n_{ribs} = \{2,3,4,5,6\}$, which have been equally distributed along the length of the finger. For all these cases, a concentrated load is applied to one of the connectors, approximately at the same height. The results of the comparison are shown in Figure 2.18. It can be noted that increasing the number of ribs strongly affects both the deformed shapes obtained and the maximum load that can be applied before instability arises. In particular, for a gripping purpose, an highly bent arch-like shape would be optimal to wrap and grasp objects having different sizes and shapes. This is not obtained using 2 or 3 ribs, where the final shape obtained is merely lightly bent. Moreover, reducing the number of ribs increases the sections length, thus anticipating the overcoming of instability.

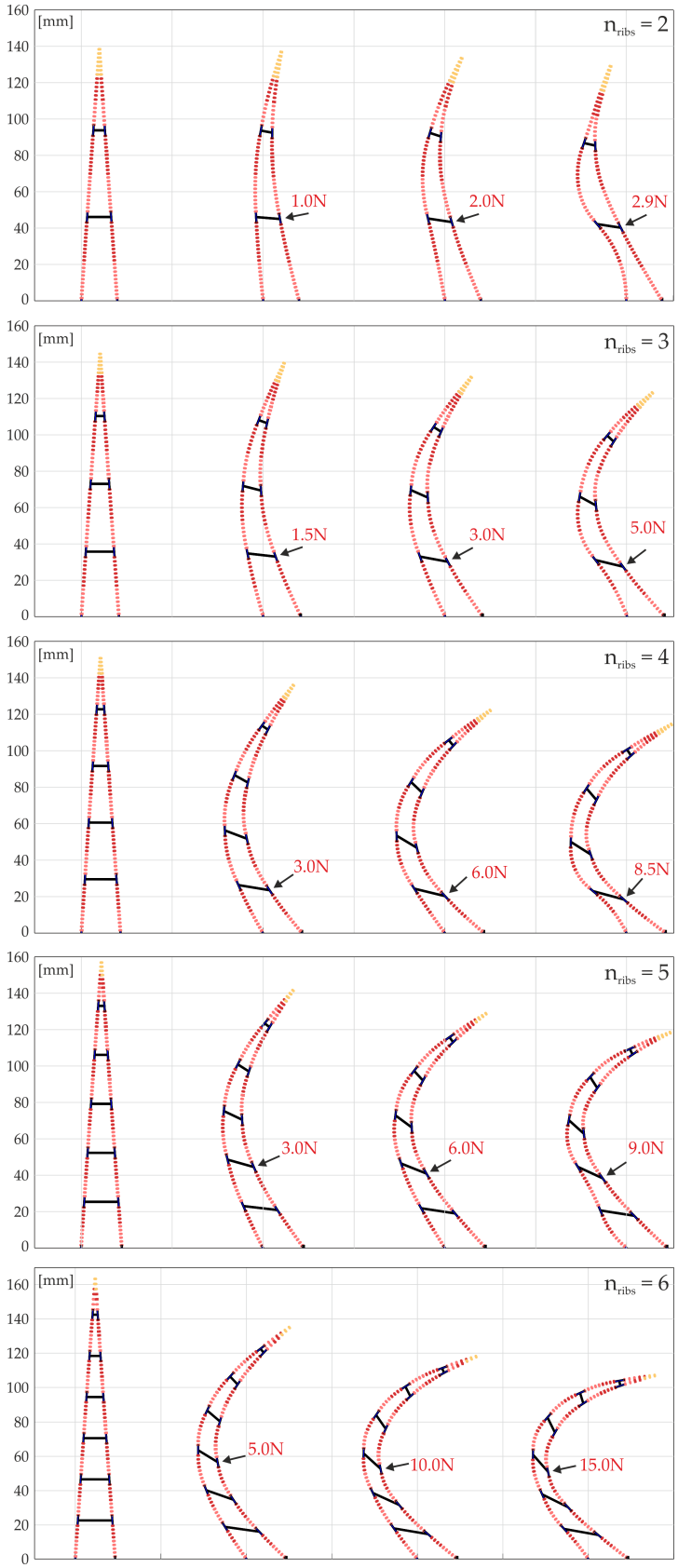

Fig. 2.18 Comparison between different fingers geometries, subjected to a concentrated load applied at one of the connectors. In particular, the number of rigid ribs is varied. For each design, the family of deformed shapes obtained at increasing the concentrated load is presented, until the buckling is reached.

2.6.2 Rigid ribs inclination

The second parameter that is inspected is the inclination of the rigid ribs. Following the results obtained in the previous section, we focus here on the design of the finger composed by 6 ribs placed along its length. The investigated designs are obtained decreasing/increasing the length of the first segment of the left part of the finger by $\{10, 30, 50\}\%$. Hence, the left tip length is increased/decreased of the same amount and the inclination of the ribs is kept constant along the length of the finger. The results of this investigation are presented in Fig. 2.19.

It is possible to notice that the inclination of the ribs strongly affects the overall behavior of the finger. In particular, for a -30% slope, the critical buckling load is drastically reduced and the final configuration shows the retreat and failure of the finger. Similarly, for a -10% slope, the lower part of the finger is collapsed, showing a 180 deg inclination of the revolute at the base. On the other side, the $+10\%$ slope appears as the most promising for the design of a gripper's finger, since the $+30\%$ incurs in the buckling of the sections for lower loads.

2.6.3 Material

While the previous results were obtained with a finger made out of ABS, here we investigate the influence of the material's property on the finger's behavior. In particular, we compare the results obtained with Semiflex, a flexible material commonly used in 3D-printing solutions. We present here the result obtained for a finger having 6 ribs with a $+10\%$ slope, which resulted as the optimal design from the previous investigation. The results obtained are reported in Figure 2.20.

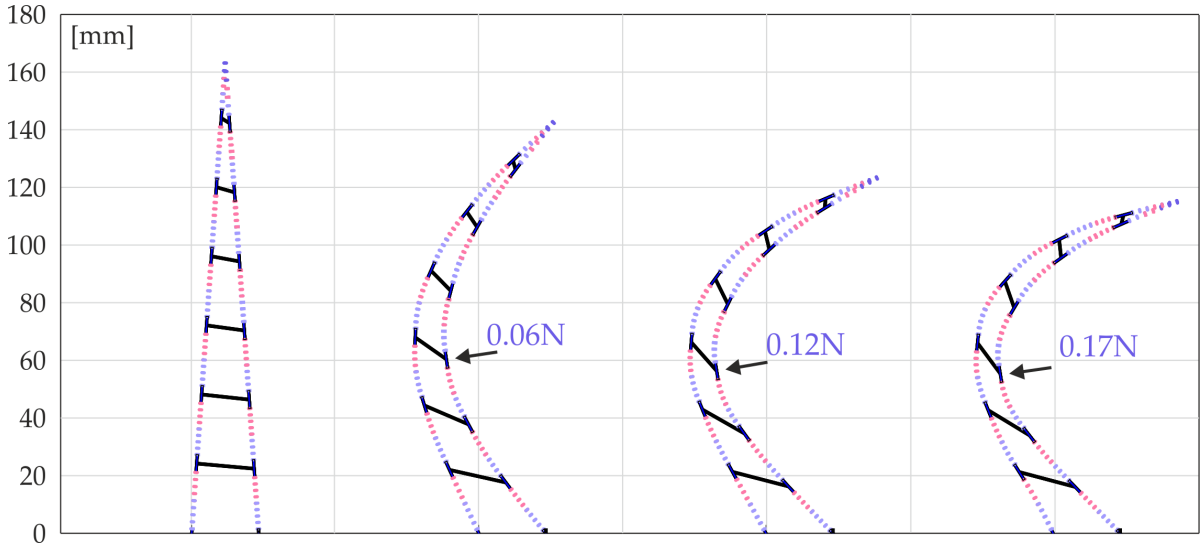

Fig. 2.20 Family of deformed shapes obtained with a Semiflex finger, composed of 6 rigid ribs with a $+10\%$ slope. It can be noted that the results are almost identical to those obtained with the same design with an ABS finger, but for lower values of the applied force.

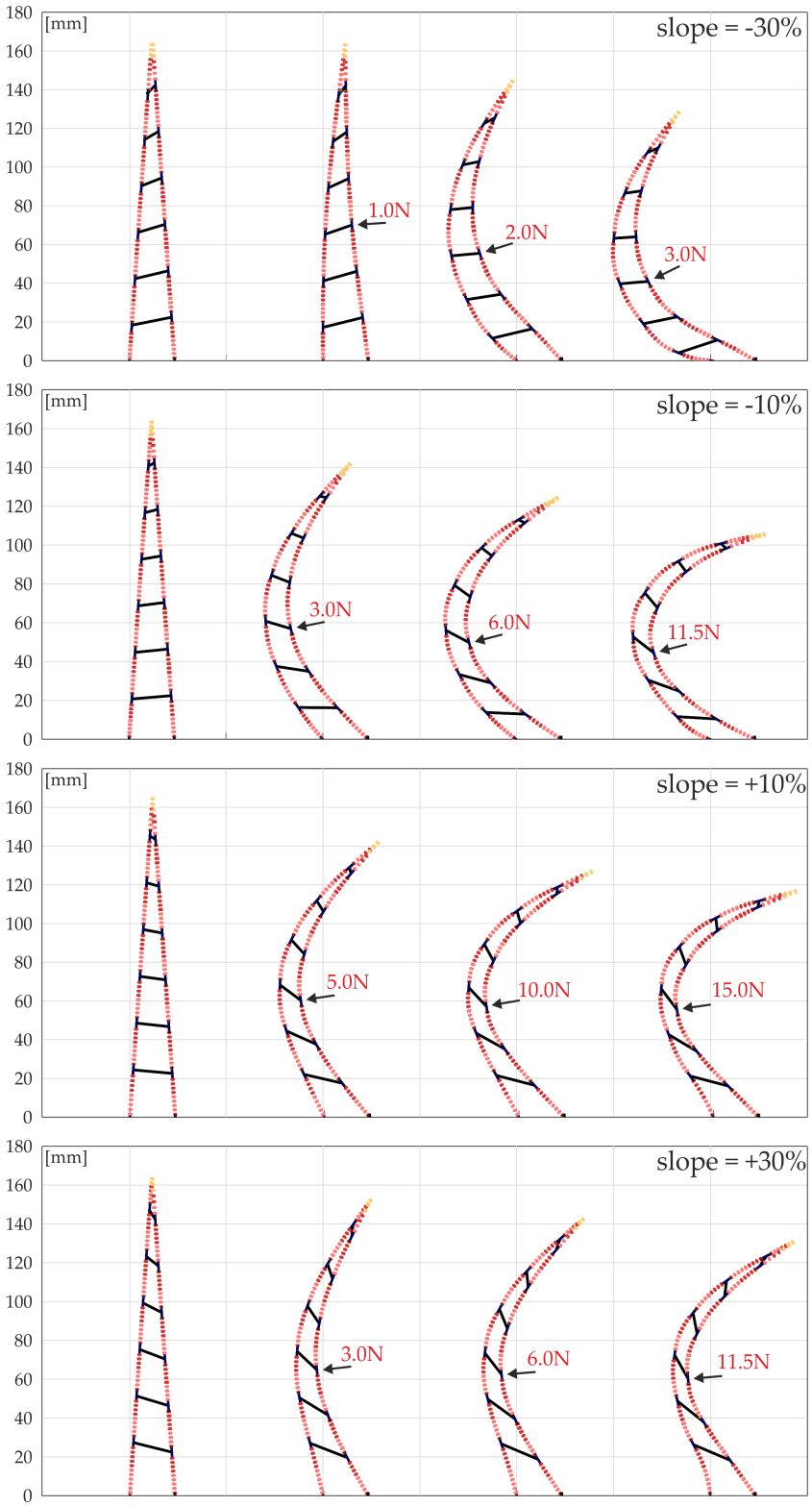

Fig. 2.19 Comparison between the family of deformed shapes that can be obtained at varying the slope of the rigid ribs. The concentrated load is increased until the onset of the buckling phenomenon. It can be noted that the highest load is attained with a slope of 10%, which also provides the optimal deformed shape for a gripper design.

It should be noted that the obtained deformed shapes resemble very closely those obtained with the ABS material, reported in Figure 2.19. Since Semiflex is characterized by a Young's Modulus $E = 26 \cdot 10^6$ Pa, 100 times lower than the ABS's one, the same deformed shapes are obtained for a drastically lower force. However, this result proves that, under the linear-elastic material assumption, a specific design provides a specific family of deformed shapes, regardless of the material employed. This is particularly important for an optimization point of view, meaning that it is possible to focus the investigation on the design, defining the material only once the entity of the load is defined.

2.7 New gripper design and experimental validation

Following the results obtained in Section 2.6, a new Fin-Ray finger is fabricated to improve the capabilities of the previous one. The optimal design, composed of 6 rigid ribs having a $+10\%$ slope, is adjusted following the restrictions posed by the $3D$ printing machining. In particular, the width of the finger is posed to 1 mm and thus the last, higher, rigid ribs is removed. The obtained design is presented in figure 2.21.

As previously mentioned, the prototype is $3D$ printed using ABS. The rigid ribs are obtained using steel rings placed inside the designated holes. Grease is used to reduce any friction between the ribs and the finger. To asset the new prototype's capabilities, a series of experimental tests is conducted, comparing the results with those obtained with the proposed mathematical tool. A perpendicular follower force is applied on node D, with increasing modules $F_y = \{5, 10, 15\}$ N. The results are reported in figure 2.22, together with the results from the theoretical predictions.

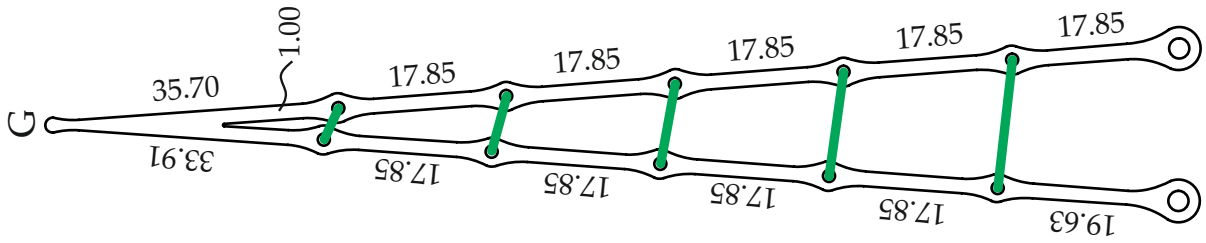

Fig. 2.21 Geometry of the new finger design. The finger is 18 mm deep, while the fins material is ABS, having Young's Modulus $E = 2250 \cdot 10^6$ MPa, Poisson's ratio $\nu = 0.3$. The ribs are considered as rigid elements. All the measures reported in the figure are in [mm].

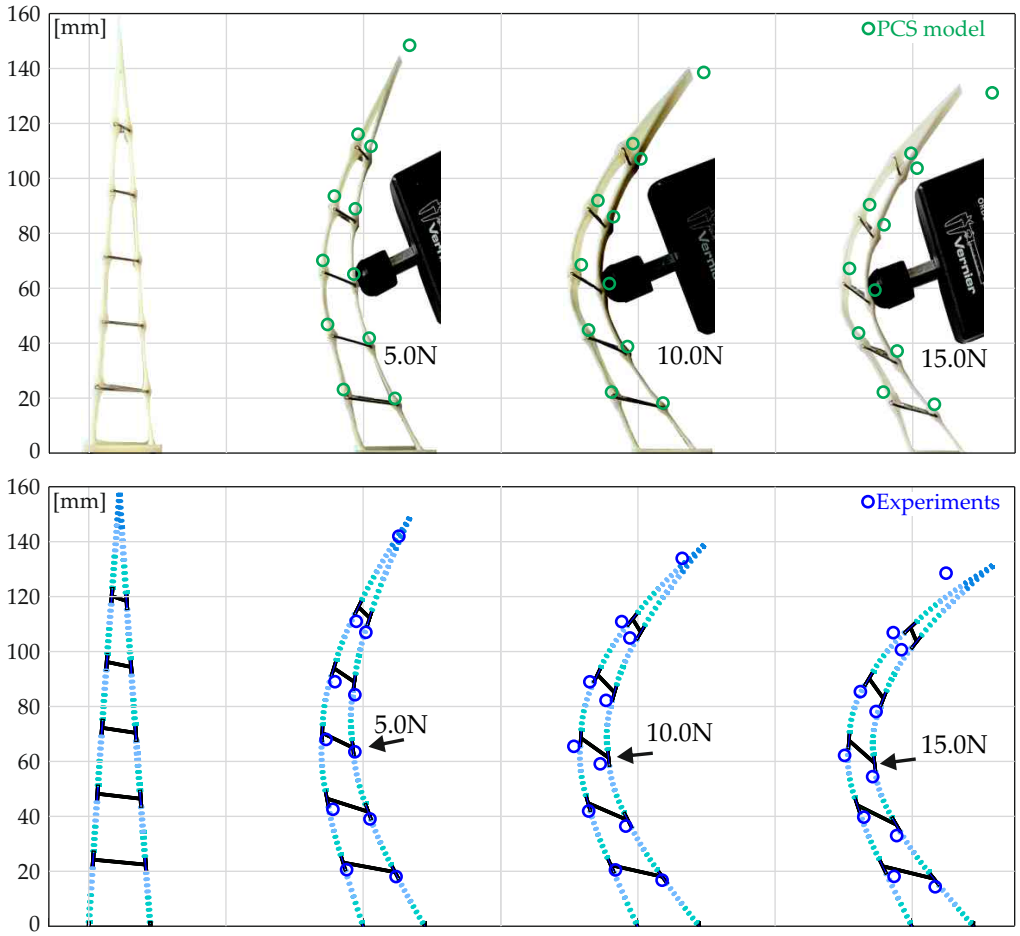

Fig. 2.22 Comparison between the experimental results and those predicted by the Piecewise Constant Strain model, for the new gripper design.

As predicted by the simulations performed, the new design is able to withstand a force up to 15 N and the overall deformed shape presents a 2D bent profile that perfectly fits the gripping purpose of the finger.

All of the following chapters will present devices designed by following the modeling principles discussed above.

Chapter 3

Design and Applications of Assistive Devices

"*it is not enough that we build products that function, that are understandable and usable, we also need to build products that bring joy and excitement, pleasure and fun, and, yes, beauty to people's* lives."

Don Norman, UX

3.1 Design of multiple wearable robotic extra fingers for human hand augmentation

Augmenting the human hand with robotic extra fingers represents an interesting research topic. It has many potential applications, in particular as a compensatory and rehabilitation tool for patients with upper limb pathologies and diseases. Devices composed of two extra fingers are preferred with respect to single finger devices when reliable grasps, resistance to external disturbance, and higher payloads are required. To reduce the device complexity and weight, maintaining the adaptability to different grasped objects, underactuation and compliance can represent a solution. When only one motor is adopted to actuate multiple fingers, a differential mechanism is necessary to decouple finger movements and distribute forces. In this work, the main features of a device composed of two wearable robotic extra fingers are described. Each finger is composed of modular phalanges and is actuated with a single tendon. Interphalangeal joints include a passive elastic element that allows restoring the initial reference configuration when the tendon is released. The stiffness of each passive element can be customized in the manufacturing process and can be chosen according to a desired closure movement of the fingers. Another key aspect of the device is the differential system connecting the actuator to the fingers: here, we present the design features of the solution that has been adopted, and we provide analysis in terms of kinematics, statics, and mechanical resistance.

3.1.1 Introduction

Robotic hands have represented a challenge for designers and engineers for at least three decades [48] due to the complexity involved in grasping and manipulation tasks. The devices have a lot of limits when compared to human hands and lack functionality. Although there are many solutions available, the challenge is still open. The solutions include anthropomorphic structure [49], [50] as well as some solutions following underactuation to gain adaptability to the grasped object [51]. Underactuation [52],[53],[54] and modularity [55] are aspects that are being investigated to reduce the complexity of the robotic hand while maintaining a considerable level for its performance output. The approach of using tendon driven mechanisms is common in articulated finger robotic hands.

3.1.2 Device Design

The dual finger device consists of two parts, the support base and two flexible fingers. The support base consists of the forearm part and actuator. While the flexible fingers consist of a modular structure comprising of rigid and flexible parts. Each finger has seven modules; each module constitutes a rigid part and a passively deformable flexible part. The dual finger device is shown in Figure 3.1.

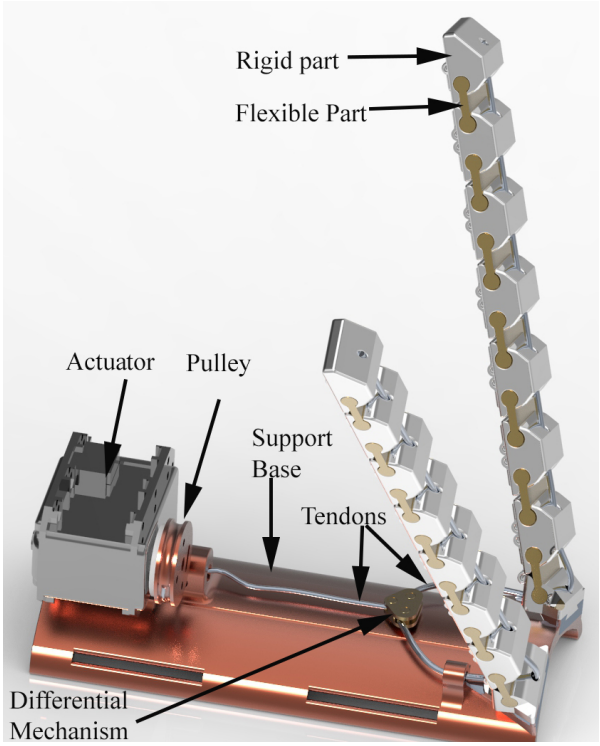

Fig. 3.1 CAD representation of the dual sixth finger device, depicting main components of the device.

The user can orient both the fingers in any desired orientation depending on the requirement of the task. Support base has been realized using Fused Deposition Modeling (FDM) technique.

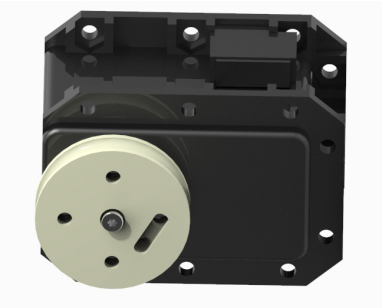

(a) Dynamixel MX-28AT Actuator

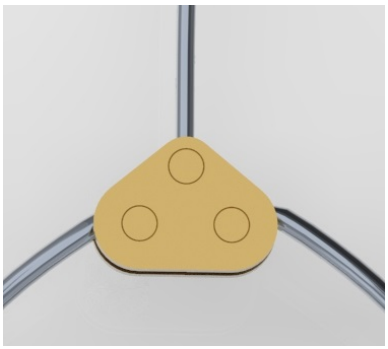

(b) Differential Mechanism

Table 3.1 Technical parameters of Dynamixel MX 28AT Actuator.

Technical Features	**Description**
Weight (including motors)	480 g
Max. actuator torque	3.1 Nm @ 12 V
Max. current	2.8 A @ 12 V
Continuous operating time	3.5 h @stall torque
Max. operating angles	300 deg, endless turn
Max. non-loaded velocity	684 deg/s
Dimension of Gripper	130 mm x105 mm x 85 mm

We used Acrylonitrile Butadiene Styrene (ABS) to 3D print the support base using Stratasys F170 3D printer. The support base as shown in Fig. 3.2.

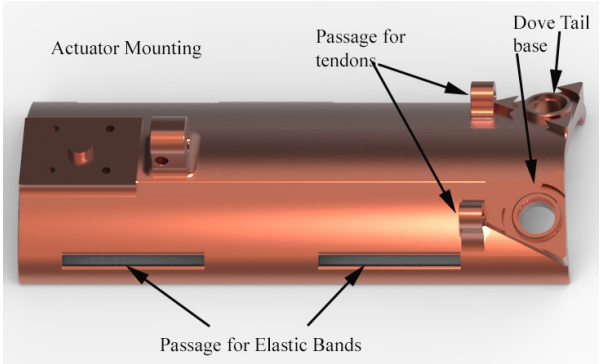

Fig. 3.2 Dual Sixth Finger Support Base

The support base contains an actuator that is fixed and provides the force for flexion and extension of both sixth fingers. The actuator used for this device is MX-28AT Dynamixel Servo motor as shown in Fig. 3.3a. The detail parameters of the actuator are listed in Table 3.1.

There are two bases for the dovetail mechanism that has also been integrated, which provide the assembly point of both sixth fingers. A differential mechanism as shown in Fig. 3.3b also resides on top of the support base, which is able to move freely. The actuation of the

device is carried out with the help of tendon driven approach. Where a single tendon on one side is connected to the differential mechanism while on the other side it is connected to the pulley attached firmly to the actuator shaft. Similarly, two more tendons are used to actuator fingers, where one side of each tendon is connected to a differential mechanism, and the other side is connected to the tip module of each of the sixth fingers. Furthermore, passages for easy insertion of the elastic band are also available on the support base. Elastic bands are used to allow the user for the easy wearing of the device. For the case of deformable passive interphalangeal elements (flexible parts), a certain material that bears the properties of high flexibility is required so that it can undergo high deformations when subjected to external forces. For passive elements, we employ Thermoplastic Polyurethene (TPU)30, a thermoplast that has the desired mechanical properties and is easily integrated in standard FDM techniques. The flexible parts are 3D printed using Lulzbot Taz 5 3D Printer. It is worth mentioning that by changing some manufacturing parameters like infill density percentage or pattern of printing or layer thickness *etc.*, it is possible to modify the mechanical properties of the end component.

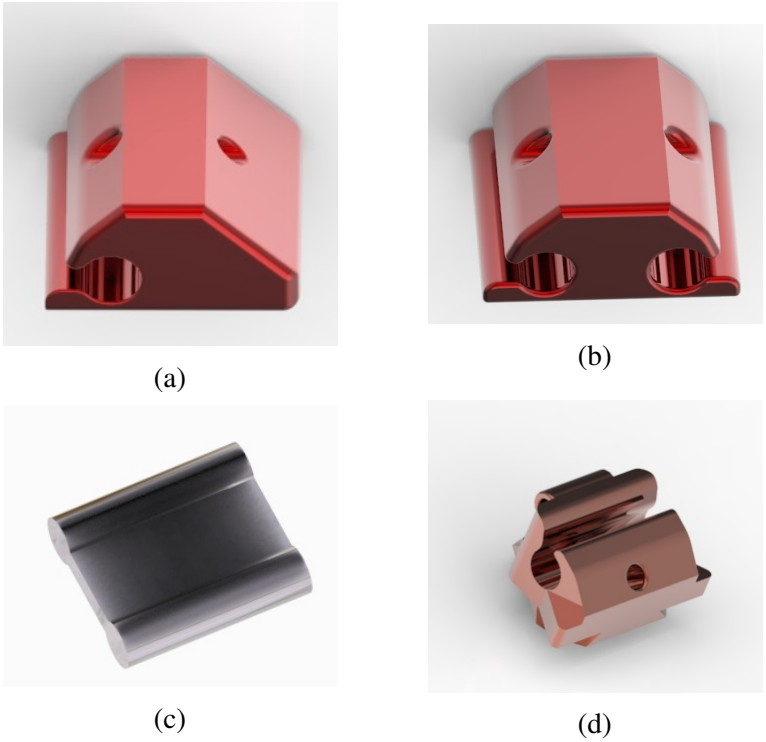

Fig. 3.4 Different part of Flexible Finger necessary to develop a finger. (a) Distal phalanx connected as tip of the sixth finger; (b) Intermediate Phalanx serving as middle phalanges; (c) Deformable interphalangeal element; (d) Proximal element connected to finger base and bearing dovetail assembly

The main element composing modular fingers, as described in Fig. 3.4, are stiff/rigid parts Fig. 3.4a, 3.4b 3.4d and Fig. 3.4c. As clear from the Fig. 3.4 three different rigid elements have been designed for the distal (Fig. 3.4a), middle (Fig. 3.4b) and proximal (Fig. 3.4d) phalanges. The complete structure of the finger has been kept modular, which allows the user to add as

many modules as we want to design a finger with different lengths. For this device, we consider both fingers having seven modules as shown in Fig. 3.5, each module consists of one rigid and one flexible part since we verified that this number of modules is an acceptable trade-off to guarantee wearability and suitable yet firm grasping capabilities of several objects used in activities of daily living (ADL).

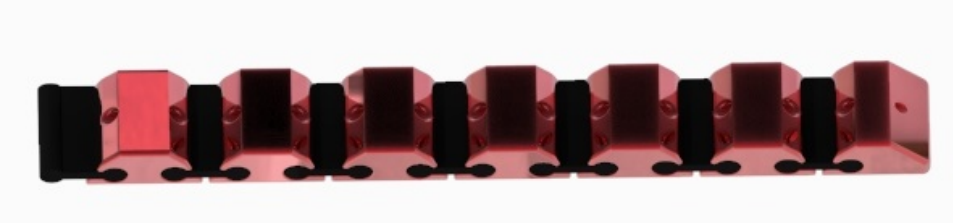

Fig. 3.5 Complete flexible finger consisting of rigid and flexible parts

Since each finger is actuated with a single tendon to the actuator via a differential mechanism, the motor actuator pulls the tendon; fingers close following the movement that depends on passive deformable elements stiffness, which will be described later in the text.

As the actuator and differential mechanism of the dual sixth finger is installed on the support base, see Fig. 3.1, the overall encumbrance of the motor, differential, and tendon routing system is 130 x 50 x 40mm. The size of the support base can be customized as per the user's specific requirements. Also, for more accurate modeling of the support base, systems [56],[57] like 3D laser scanners can be used to scan the forearm and reconstruct the user's forearm geometry to customize the design of the support base.

The actuator drives the pulley installed on its shaft. The tendon from the motor pulley connects to the sliding element hence pulls the fingers together. The main components of the device are shown in Fig. 3.1. As you can see, the whole device consists of two fingers, each having seven modules, each module consists of the rigid and flexible part, the assembly of rigid and flexible part is very simple, it can be achieved by sliding the flexible part through cylindrical guide inside the rigid part as depicted by Fig. 3.6. This removes the necessity of using a screw or any other fixing element.

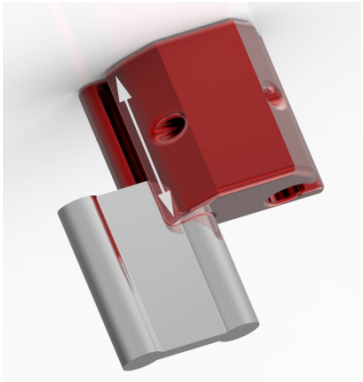

Fig. 3.6 Depiction of how the rigid and flexible parts are assembled

3.1.3 Analysis of different components of dual sixth finger

This section includes analysis of different components pertaining to the sixth finger, which includes design and analysis of soft and rigid parts of flexible fingers, differential mechanism *etc.*.

3.1.3.1 Passive elements

As introduced in the previous section, each finger is actuated by a single tendon and then, when actuated, can follow only one predefined closure motion. The characteristics of closure motion depend on both geometrical properties of finger components and the stiffness value of the passive element in the interphalangeal joints. Broadly speaking, when a pulling force is applied to the tendon, stiffer joints will bend less than softer ones. By properly regulating the stiffness of each of the passive elements, it is, therefore, possible to shape the closure motion. The modular structure of the finger allows to easily add, remove or substitute the passive interphalangeal elements to adapt the finger to different applications. The first step consists of choosing the closure motion that has to be followed by the extra finger, *i.e.*the relationship:

$$q = q(\Delta I) \tag{3.1}$$

when no external forces, except the tendon force, are applied to the finger elements. In other terms, in this phase, we do not consider any contact between finger elements and an object or the environment. In that equation, q represents a vector containing all the rotations of interphalangeal joints, and ΔI is a vector collecting the variation of tendon lengths with respect to the initial reference configuration. In general, in an underactuated system, such a relationship cannot be defined. However, in our case, it can be established since in the joints, there are passive elastic elements if the equivalent stiffness values of the passive elements are known, as detailed in [14]. To let the extra fingers be able to grasp a wide range of objects, cooperating with the human hand, it is important to choose the most suitable finger closure movement. The coordination between the human hand and wearable robotic extra fingers is an important issue, involving aspects of both grasp control and Human-Robot Interaction. In neurophysiology, the concept of synergies has been extensively studied in many contexts, including grasping [58, 59]. The concept of bio-artificial synergies was introduced in [56] to control wearable extra fingers. Synergies were derived, similarly to [60], by performing the Principal Component Analysis (PCA) on a set of grasps performed by the human hand augmented by two robotic extra fingers. In this work, we exploit the concept of synergies, but we could not extract directly the augmented hand synergy as in [57], since the methodology therein proposed is based on the analysis of a dataset of grasps that is not available in the design phase of the device. Here we extend the idea of mapping human hand synergies based on the definition of a virtual object, that we presented in some previous works. The method to map the human hand first postural synergy to robotic extra fingers has been previously introduced in [61]and in [14]. The output of the mapping procedure is the closure motion that we want to obtain when actuating the robotic extra fingers. As we introduced above, in an underactuated mechanism it is not possible

to define the relationship in Eq. (3.1), but it is possible to define its dual, *i.e.*

$$\Delta I = Mq \tag{3.2}$$

It is interesting to notice that this relation is linear, and the elements of the matrix M depend on finger geometrical properties [62]. By applying the Principle of Virtual Works to the fingers, it is easy to show that

$$\tau = M^T f \tag{3.3}$$

where τ is a vector collecting joint stiffness values, while f is the tendon force vector. Since in each joint a passive element is present, from the static analysis of the finger, it is easy to verify that

$$\tau - K_q(q - q_0) = 0 \tag{3.4}$$

where q_0 indicates the reference joint configurations. Once the desired closure motion $q_r = q_r(\Delta I)$ is defined, from eqs. (3.1) to (3.4) it is possible to find the stiffness matrix

$$K_q = K_q(q_r, q_0, f) \tag{3.5}$$

The second step of the procedure consists, therefore, in the definition of the stiffness value that each passive element of finger joints has to assume so to realize the desired closure motion. For a more detailed description of the procedure, the reader can refer to [14]. In this work, we report the results obtained by applying this process to three different configurations of human hand and extra fingers. For the evaluation, we realized the mathematical models of the hand augmented with the robotic extra fingers using SynGrasp [63], a Matlab toolbox for the simulation of robotic hand grasping and manipulation, that can manage synergy-actuated and more in general underactuated structures. The human hand biologically has 27 DoF, in this study, we adopted a model with 20 DoF, similar to the one described in [][38], in which we neglected the carpometacarpal (CMC) articulation of index, middle, ring, and little fingers. We choose this simplified model because we could apply to it the quantitative results, in terms of postural synergies, evaluated in [60] and available in the Hand Corpus repository [64].

Fig. 3.7a shows the kinematic structure of the hand augmented with two extra fingers, composed of seven modules. Fig. 3.7b shows the augmented hand configuration when the human fingers are actuated according to the first postural synergy evaluated in [60] and the motion of the robotic ones are evaluated with the mapping procedure reported in [61].

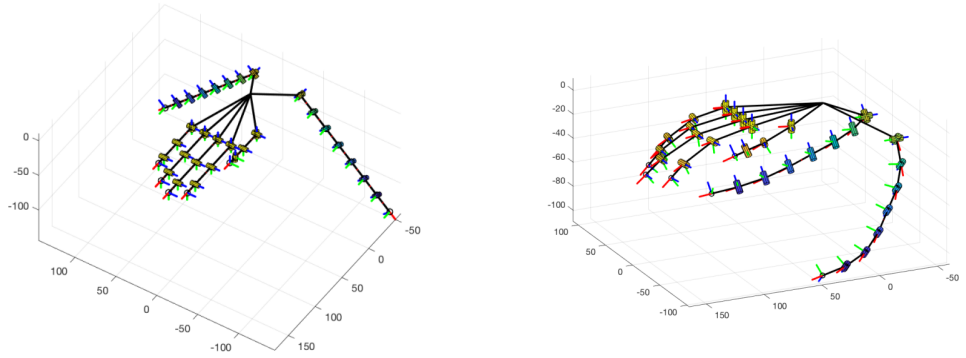

(a) (b)

Fig. 3.7 SynGrasp model of the human hand augmented with two robotic extra fingers. Black lines represent rigid links, cylinders represent revolute joints. The human hand is modeled as a 20 DoF system; augmented fingers have a modular structure with seven elements (a) reference initial configuration. (b) configuration of the hand when the first synergy is activated, in an intermediate configuration between the initial reference and the completely closed ones.

According to the procedure that we previously described, stiffness values of the passive elastic interphalangeal elements of robotic fingers depend on the trajectory that is mapped, but also on the structure of the robotic fingers and on the force applied on the tendons by the motor. Table 3.2 summarizes stiffness values obtained with extra fingers composed of 7 modules, in three configurations, shown in Fig. 3.8 single extra finger, opposite to human hand palm (Fig. 3.8a), double configuration, with two parallel fingers opposite to human hand palm (Fig. 3.8b), double configuration, with two opposite fingers, one close to human thumb and the other one close to the little finger (Fig. 3.8c). This last configuration has been considered in the analysis phase to verify the effect of finger configuration on closure motion and of the corresponding joint stiffness values. As previously introduced, the orientation of the fingers with respect to the hand can be manually regulated by the user to adapt to different objects and tasks. A configuration similar to the one described in Fig. 3.8c is the one described in [65]. Values in Table 3.2 have been normalized with respect to the stiffness of the proximal joint; in this way, it is possible to compare single and double finger configurations. As it can be seen, single and double parallel configurations present similar stiffness values, while the double opposite configuration presents some differences.

Table 3.2 Passive elements of interphalangeal joints, stiffness values normalized with respect to the first (proximal) element, evaluated for the three configurations shown in Fig. 3.9

Configuration	k_1/k_1	k_2/k_1	k_3/k_1	k_4/k_1	k_5/k_1	k_6/k_1	k_7/k_1
Single	1.00	1.17	1.39	1.74	2.32	3.50	6.98
Double, opposite to the palm	1.00	1.10	1.33	1.65	2.20	3.31	6.61
Double, aligned with the palm	1.00	1.43	1.71	2.14	2.85	4.28	8.57

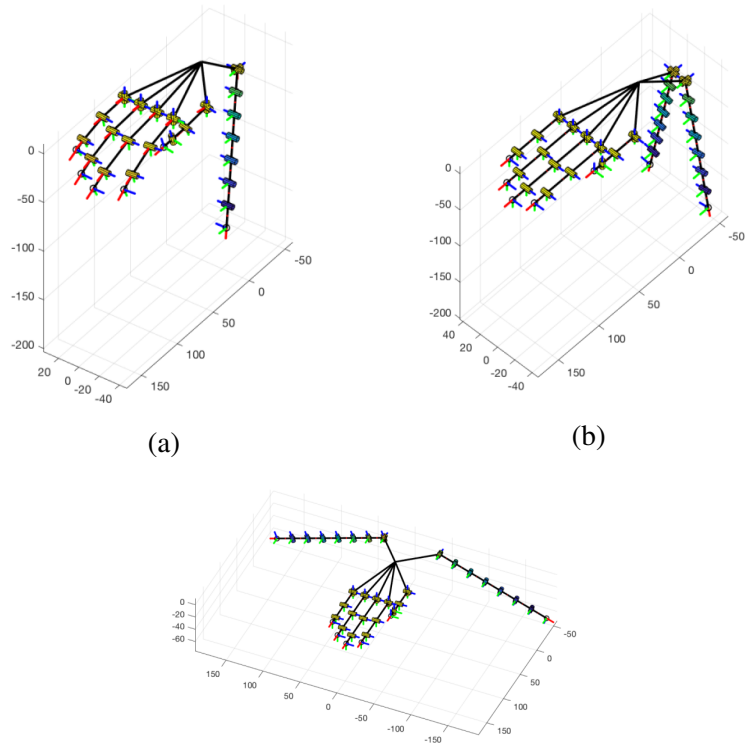

(a) (b)

(c)

Fig. 3.8 Configurations that we compared for the evaluation of passive joint stiffness with the mapping procedure applied to the first human hand postural synergy. (a) Single finger, opposite to human hand (b) Double configuration, fingers opposite to human hand palm (c) Double configurations, fingers are aligned with hand palm.

Fig. 3.9a shows, for one of the fingers of the configuration in Fig. 3.8b, the stiffness values of the passive interphalangeal elements K_q, that have been evaluated on the basis of the motion that we imposed on the fingers, plotted as a function of the variable z, describing synergy actuation ($z = 0$ in the reference configuration, $z = 1$ when the hand is closed). It is interesting to notice that:

- K_q values vary for the different joints: their values determine the closure motion of the fingers and are defined on the basis of the mapping procedure proposed in [57] and in [60].

- K_q values vary as a function of hand configuration. However, for the motion that we selected, such a variation is not very high.

To highlight the effect of stiffness value in the closure motion of the finger, in Fig. 3.9b we simulated, for one of the robotic extra fingers, the trajectory of the fingertips obtained with the variable stiffness values defined by the previously described procedure, exactly resembling the "ideal" desired trajectory, (blue curve), the one that we obtain if we consider, for each joint, the mean stiffness value (red curve), and the one that we would obtain if all the joints of the finger had the same stiffness value (magenta curve). As it can be seen, the difference between the blue curve and the red one is quite limited, compatible with the precision required for this type of device (few millimeters), so considering a stiffness value different for all the joints, but constant for each joint, does not introduce the significant difference between the closure motion that was planned and the one that can be obtained with the underactuated finger. On the other hand, the difference between the ideal fingertip trajectory and the one obtained with the same joint stiffness for all the modules (in the simulation, we assumed the mean stiffness value among all the joints) is very high.

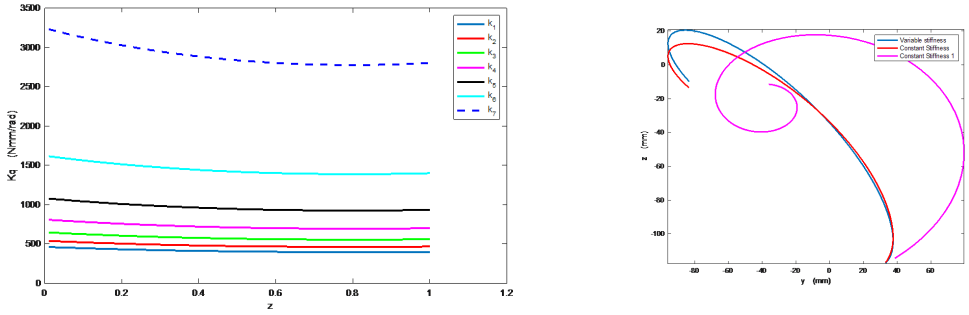

(a) (b)

Fig. 3.9 (a) Joint stiffness values for one of the extra fingers of the configuration in Fig. 3.8b, evaluated as a function of synergy activation. (b) For the same configuration, trajectories of one of the fingertips, during a finger closure motion, projected on a plane. Different trajectories are obtained by considering variable stiffness profile evaluated by means of the mapping procedure (blue curve), the mean stiffness value (constant) for each joint (red curve), the mean stiffness value for all the joints (magenta curve).

The third step consists of creating the passive elements so that their stiffness is the one calculated in the previous phase. We analyzed the possibility of tuning finger joint stiffness values by exploiting the potentialities of 3D printing fabrication methods that are nowadays rapidly improving and offering new opportunities. In particular, choosing a material as the Thermoplastic Polyurethane (TPU) for realizing the flexible parts, we can get different stiffness values while maintaining the same geometric shape by regulating the percentage of infill density. This parameter affects primarily material density, but also its mechanical properties [66]. As an example, Table 3.3 summarizes the variation of Young's modulus E of TPU as a function of the infill percentage density.

Table 3.3 Properties of TPU as a function of infill density percentage.

Infill density %	**E (MPa)**
10	1.07
30	1.38
50	2.07
70	6.53
90	9.45
100	10.5

In a more general framework, the overall passive joint stiffness k depends mainly on joint geometry and material structural properties, and, considering a linear elastic behavior, on Young's modulus E, *i.e.*:

$$k = k(\mathbf{d}, E) \tag{3.6}$$

where d is a vector containing all the parameters defining joint geometry (*e.g.*, for a parallelepiped joint, its length l, width w and thickness t). Young's modulus E depends on material parameters and fabrication methods, *i.e.*

$$E = E(p_1, p_2, ..., p_n) \tag{3.7}$$

Where each value p_i indicates one specific material property, in this work, we exploited the dependency of k with respect to infill density percentage to define robotic finger properties. Future developments of this study will consider other manufacturing parameters, as for instance the infill pattern profile and also composite materials.

3.1.3.2 Mechanical transmission and differential mechanism

Concerning the differential system, the solution proposed in this work to actuate a double extra finger device for human hand augmentation is inspired by Dollar's work on underactuated robotic hands [26], using a moving pulley system; in Fig. 3.10 a simplified and general scheme of this kind of differential is presented [67].

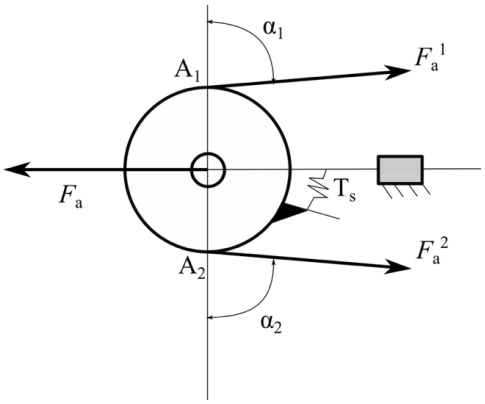

Fig. 3.10 Simplified scheme of a typical differential mechanism with moving pulley.

The motivation for this choice is the compactness and excellent adaptability to the human's forearm dimensions and, since the robotic fingers that are connected through the mechanism use tendons, the mobile pulley mechanism is the most effective system for force transmission. Spring is often used to keep the two outputs in the same reference configuration when the system is not actuated and the fingers are not externally constrained. The pulley has 2 DoF: it can translate along a sliding guide (realizing a prismatic joint), and it can rotate around an axis perpendicular to the plane of the figure. In this scheme, the input force is F_a and the output ones are F_1^a and F_2^a. The spring applies a torque T^s. In static equilibrium condition the following relationship holds:

$$F = [T^f]t^* \tag{3.8}$$

with

$$F = \begin{bmatrix} F_1^a \\ F_2^a \end{bmatrix} \qquad t^* = \begin{bmatrix} F_a \\ T^s \end{bmatrix} \tag{3.9}$$

where the transformation matrix $[T^f]$ is

$$[T^f] = \frac{1}{c}\begin{bmatrix} r & \sin\alpha_2 \\ r & -\sin\alpha_2 \end{bmatrix} \tag{3.10}$$

where c is the sum of the distances of A_1 and A_2 points from the sliding guide (or prismatic joint)

$$c = r\left(\sin\alpha_1 + \sin\alpha_2\right) \tag{3.11}$$

and α_1 and α_2 are the angles shown in Fig. 3.9 (that are the outputs angle between the tendon directions and the vertical). If the stiffness of the spring is negligible the relation is:

$$F_1^a = F_2^a = \frac{F^a}{\sin\alpha_1 + \sin\alpha_2} \tag{3.12}$$

An important property of this differential mechanism is that it is isotropic, and thus the two output forces are equal for any value of α_1 and α_2. The ratio F_i^a/F_a for $i = 1,2$ is significantly influenced by α_1 and α_2, and c must be positive for a proper device working.

The distance between the pin and the sliding has to be at least equal to the maximum distance that the pulley has to travel while both the fingers are completely closed from an initial extended configuration. Let us consider one of the fingers and let us indicate with Θ the generic rotation between the x_n axis, defined on the distal phalanx of one finger and the reference direction x_0 on the device base. Reference frames are defined so that $\Theta = 0$ in the initial extended configuration, while $\Theta = \Theta_c$ in the configuration corresponding to complete finger closure. Let us indicate with ϑ_i the rotation of the i-th joint so that

$$\Theta_c = \sum_{i=1}^{n} \vartheta_i \tag{3.13}$$

To obtain the rotation ϑ_i the tendon is pulled by the motor and its length variation is indicated with Δl_i (Fig. 3.11). When the joint is rotated, the elastic element bends, indicating with l its length and assuming that after the deformation, its profile is circular, its curvature radius can be evaluated as $r_i = \dfrac{l}{\vartheta_i}$. The corresponding arc cord can be evaluated as

$$a_i = 2r_i \sin\left(\frac{\vartheta_i}{2}\right) \tag{3.14}$$

and tendon length variation is therefore (Fig. 3.11)

$$\Delta l_i = l - \frac{a_i}{l}\left(r_i - h\right) = l - 2r_i \frac{\left(r_i - h\right)}{r_i} \sin\left(\frac{\vartheta_i}{2}\right) \tag{3.15}$$

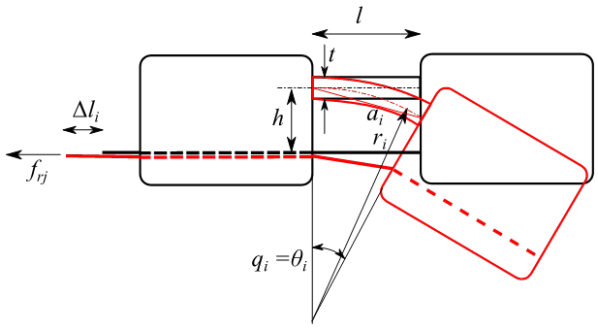

Fig. 3.11 Deformations of interphalangeal joints, scheme and main geometrical parameters,

To close the fingers, it is necessary to vary the length of the tendon by $\Delta\mathbf{l_{tot}}$, which can be evaluated as

$$\Delta l_{tot} = \sum_{1}^{n} \Delta l_i \tag{3.16}$$

Assuming $l_i = 17.3$ mm for all the elements, $h = 5$ mm and $\Theta_c = 2\pi$ we obtain $\Delta l_{tot} = 28$ mm: this is the maximum length variation of the tendon and corresponds to the maximum displacement of the sliding element. This result is necessary to define the minimum size of the box containing the differential mechanism.

Δl_{tot} also represents the maximum difference between fingers' tendon lengths when the differential is working, for example, when one of the fingers is blocked in its straight initial configuration, and the other one is free and can complete the closure.

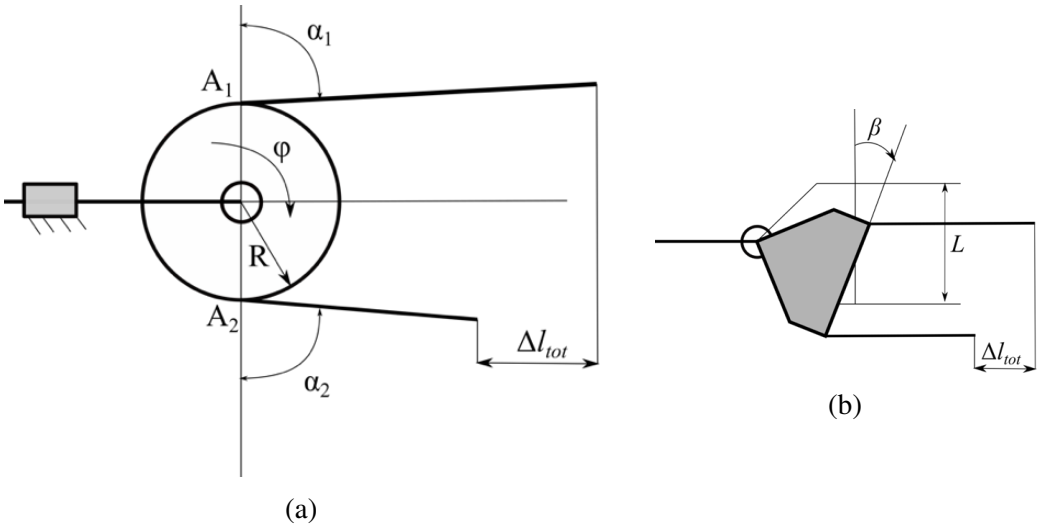

Fig. 3.12 Two different schemes for the differential mechanism. a) differential based on a pulley mechanism translating along a fixed direction; b) differential based on the tilting motion of an element.

Two possible solutions can be realized (Fig. 3.12): in the first one (Fig. 3.12a), the sliding element of the differential is constrained to move in one fixed direction by means of a prismatic joint, the two tendons are connected in a unique tendon that can slide over the element. In this case, at least one pulley is necessary to reduce the friction. In the second solution (Fig. 3.12b), the sliding element is able both to slide and to tilt inside the box, and the output tendons are connected directly to its edges, the differentiation between output motions is possible thanks to the tilting motion of the sliding element.

The first solution allows a more compact implementation; however, it requires that the sliding element is not a rigid body (at least one pulley, connected to the main body of the sliding element through a revolute joint, is needed).

Considering a single pulley, as shown in Fig. 3.12a, indicating with R its radius, when a differential motion Δl_{tot} is required, pulley rotation is simply given by

$$\varphi = \frac{\Delta l_{tot}}{R} \tag{3.17}$$

The second solution needs larger components but simpler from the mechanical and manufacturing point of view. In a preliminary design phase, we analyzed both the solutions; in the

Table 3.4 ABS main mechanical properties.

Property	**Value**	**Unit**
Density	1.03	kg/m^3
Elastic modulus	2000	MPa
Poisson's coefficient	0.394	
Yield stress	$45-60$	MPa
Specific heat	1386	$J/(kgK)$
Thermal conductivity	0.2256	$W/(mk)$

following prototyping phase, we realized the second solution because it resulted mechanically simpler and more robust. Indicating with L the width of the sliding element, *i.e.*the distance between the points in which fingers tendons are connected to it and with β its rotation generated by a difference Δl_{tot} between the deformation of fingers' tendons, it is easy to verify that (Fig. 3.12b):

$$\frac{\Delta l_{tot}}{L} = \sin\beta \tag{3.18}$$

assuming $L = 32$ mm we get $\beta = 64$ deg.

3.1.3.3 Structural analysis of rigid elements

For the realization of the prototypes, we exploited standard additive manufacturing techniques that allow to use of light materials at a quite low price and to easily adapt the design to specific user's needs. The differential mechanism was designed for a standard 3D printing considering generic ABS (Acrylonitrile Butadiene Styrene) material that has a limited density, good structural properties, good resistance to heat and impacts [68]. The main mechanical properties of ABS material are summarized in Table 3.4.

Considering the limited dimensions of the mechanical components and the loads that they have to resist, a static analysis of the most solicited elements was performed, testing their resistance by means FEM analysis.

Force Analysis When the motor applies the maximum torque (we considered a Dynamixel MX-28T - Robotis, South Korea- able to apply a torque of 3.1 Nm @ 12 V), assuming a pulley radius of about 11 mm, we get an equivalent force on the tendon equal to $F = 282$ N. In quasi-static conditions, the elements of the differential mechanism are subject to the forces sketched in Fig. 3.13.

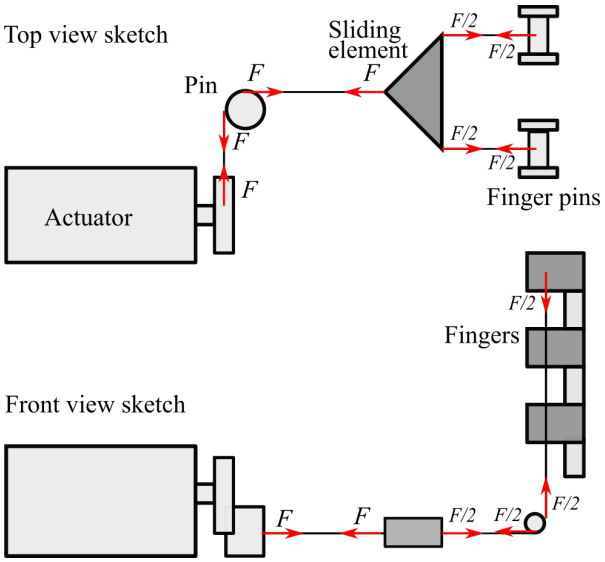

Fig. 3.13 Sketch of the forces acting on the main elements of the finger actuation and transmission system in quasistatic conditions. When the motor applies its maximum torque, 3.1 Nm @ 12 V, the force applied to the tendon driving the differential is $F = 282$ N. The forces applied to the tendons driven by the differential and connected to the fingers is therefore $F/2 = 141$ N.

Stress Analysis Results Given the previously introduced force distribution, we analyzed stress distribution on the main elements of the finger transmission. The more solicited element results to be the sliding element. The dimensions of the sliding element have been defined based on geometrical considerations summarized in the preceding sections. On the motor side, the central pivot is tied to the tendon connected to the driving pulley, which allows sliding. On the finger side, two tendons are connected to the finger pins. Fig. 3.14a shows Von Mises equivalent stress distribution. It can be noticed that the central pivot is the most stressed part of the sliding element. There are peaks of stress concentration in the edges that are not compatible with a standard ABS material. This drawback can be easily mitigated in the design and prototyping phase by increasing fillet radii. Since this is the most stressed element of the transmission system and it is not physically connected to other components, we can also consider different types of material to realize it, as for instance, ABS reinforced with carbon or metal fiber [30], or metal alloys. Rigid elements of finger phalanges have a quite robust shape; in Fig. 3.14b we report as an example the results of a FEM static simulation in which we applied a compressive loading of 40 N. As it can be seen, the overall stress level is low.

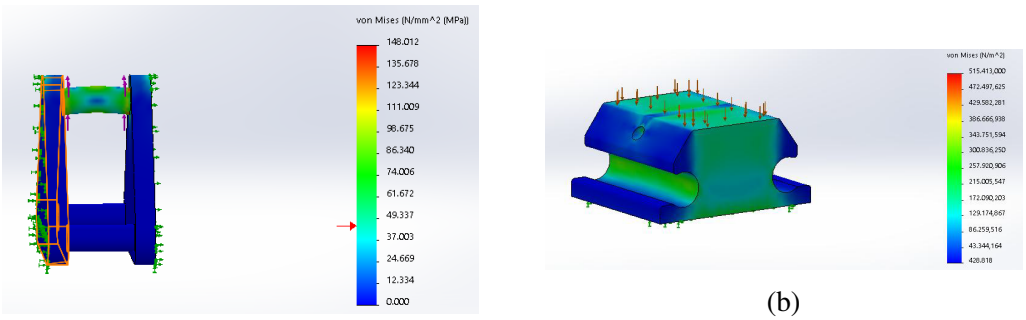

(a) (b)

Fig. 3.14 Main results of the static FEM analysis on some elements of the transmission and differential. Equivalent Von Mises stress distributions are reported. (a) Sliding element, (b) rigid element of finger phalanges.

3.1.4 Prototype Presentation

A simplified demonstrative prototype of the proposed double finger device is shown in Fig. 3.15. As previously explained, the device has been designed to be wearable, robust, and compliant to adapt to different object shapes. The device consists of two main parts, a support base, and two flexible fingers. The flexible fingers have a modular structure; each module is composed of a 3D printed ABS polymeric part that acts as a rigid link and a TPU part that realizes the flexible joint. Soft rubber pads are glued to the rigid links to increase the friction at possible contact areas. The modules are assembled by sliding the flexible part in the rigid one (Fig. 3.4). The support base of the finger is realized in ABS. It contains the actuator, the differential, and two elastic bands that allow the user to wear it on the forearm.

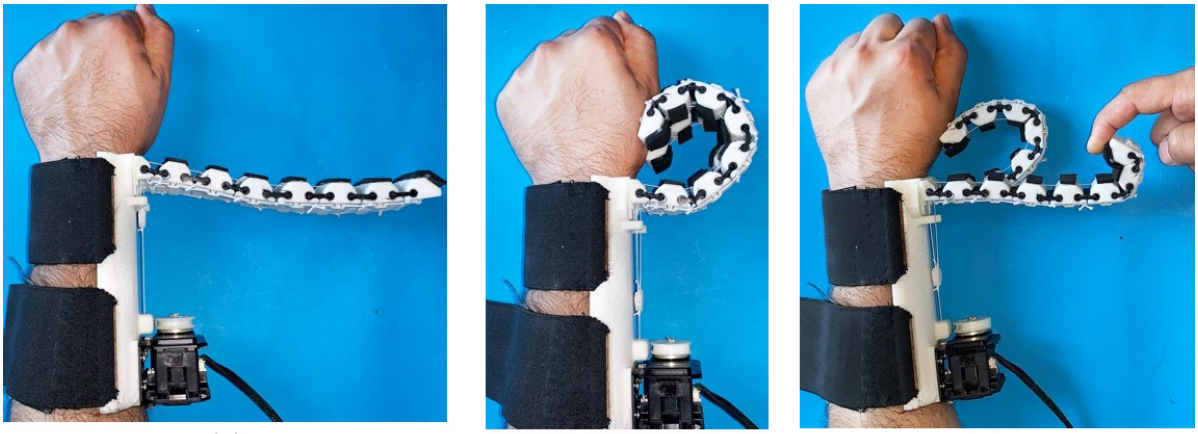

(a) (b) (c)

Fig. 3.15 The prototype of the wearable extra fingers worn by a user. (a) reference open configuration. (b) closed configuration. (c) the differential mechanism decouples the motion of the fingers so that the device can adapt to different surfaces and object shapes.

Table 3.5 Main technical properties of the prototype

Description	**Value**	**Unit**
Rigid module, dimension	20 x 31 x 12	mm
Flexible module, dimension	20 x 18 x 2	mm
Support base, dimension	170 x 50 x 40	mm
Actuator, dimension	71 x 71 x 45	mm
Actuator, weight	146	g
Max Torque @ 12V	3.1	Nm
Pulley radius	11	mm
Max current @ 12V	1.4	A
Operating angles	300	deg
Max unloaded velocity	684	deg/s
Max payload	2	kg
Total weight	210	g
Max force at the fingertip	12	N
Diameter of the smallest graspable object	17	mm
Diameter of the largest graspable object	110	mm

The actuator moves the fingers through a tendon connected to the sliding element that constitutes the differential. A hole in the rigid links allows the passage of a cable (Dyneema polyethylene fiber, Japan) which is used to realize the tendon driven actuation. The tendon wires run through the fingers and are attached on one side to the fingertips and on the other to the sliding element. Another tendon connects the sliding element to a pulley connected to the actuator. The actuator used, as previously introduced, is a Dynamixel servo AX12-A (Robotis, South Korea). Principal details on the motor and device features are reported in Table 3.5. We use ArbotiX-M Robocontroller to drive the Dynamixel motor. This control solution for Dynamixel motors incorporates an AVR microcontroller, Xbee wireless radio, and the motor driver.

Fig. 3.16 shows some examples of grasps realized with the wearable device. As it can be seen, even if the device is actuated by only one motor, the underactuated structure of the fingers and the differential system allow the device to adapt to different object shapes, realizing stable grasps of large objects, having a weight of up to 2 kg, and also to grasp multiple objects. Other grasp examples have been presented in the attached video.

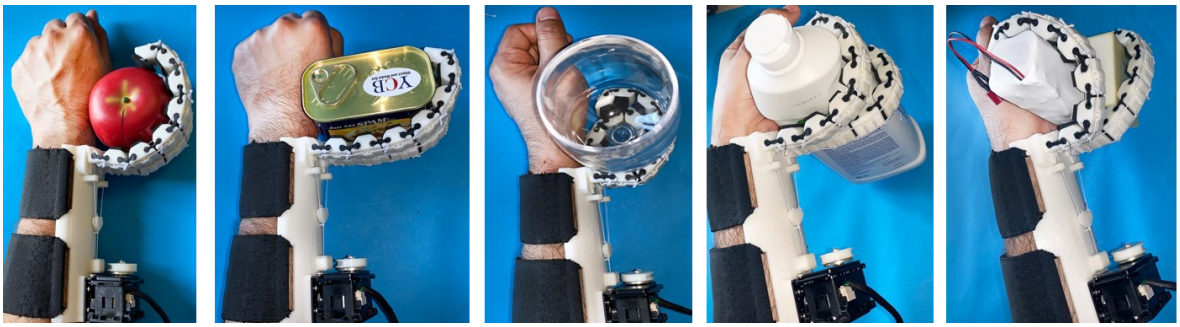

Fig. 3.16 Examples of grasps realized with the wearable device.

3.1.5 Discussion on potential applications, links

Wearable robots present interesting design challenges since they are expected to work closely and collaborate with users in an unstructured and dynamic environment. Wearable devices require additional design requirements concerning weight, adaptability to user's body specificity, safety, robustness, and easiness of use. A rather new research branch in wearable robotics deals with human body augmentation. In this work, we analyzed a device for human hand augmentation, focusing on its mechanical design, rather than on its control and interfacing with the human, that was the focus of other works [26]. Human hand augmentation by means of robotic extra fingers represents an interesting research topic involving engineering as well as ethical and philosophical challenges. With respect to other solutions available in the literature [69], [70], [65], the device that we propose presents the following features: • Actuation: while other devices available in the literature have rigid and fully actuated structures, in the device presented in this work, only one motor is necessary to actuate both the single and the double finger configurations. This feature limits the weight, complexity of the device and improves its wearability and user comfort. • Modularity: as discussed in Section 2, the structure of the fingers is modular at the phalanx level; the same modules can be used both for the single and double finger configurations. The device can be easily adapted to user's specific needs and features: for instance, a smaller hand would need a device with smaller dimensions that can be easily obtained, realizing fingers with fewer modules. • Robustness, safety for the user: in this type of device, the fingers are the elements more sensitive to unexpected contacts with the environment and shocks. Passive elements present in the interphalangeal joints of the fingers are realized by TPU, a material that presents a high resistance to impacts and elongation at break. As a result, the fingers are quite robust and can resist uncertainties and unpredictable impacts that may occur during Activities of Daily Living (ADL). At the same time, their compliance limits the risks for the user and for other people. • Costs: the simple but versatile mechanical structure, the choice of widely diffused and affordable manufacturing technologies and materials, and the modularity, lead to a cost of the device that is quite limited. We believe that the most impactful application of the device presented in this work is rehabilitation and assistance of patients with upper limb impairments, for example, after a stroke [71]. Stroke is a brain attack affecting 17 million people worldwide each year; it is the second most common cause of death and a leading cause of adult physical disability. Impairment of the hand, and in

particular of its grasping and dexterous manipulation capabilities, is one of the common deficits after a stroke. Approximately 60Different configurations for the robotic extra fingers, with one or two fingers, have been realized following the principles that we summarized in the previous sections and are now available for testing [35]. Double configurations allow more stable grasps and the possibility of carrying heavier loads. Besides rehabilitation purposes, supernumerary robotic fingers can increase patients' grasping capabilities, especially in object manipulation, thereby improving their independence in ADL, and simultaneously decreasing the need for compensatory unnatural motor strategies for solving everyday tasks. Supernumerary limbs will provide novel opportunities to recover missing abilities, resulting in improvements in patients' quality of life. The devices were tested with chronic stroke patients through qualitative experiments based on ADL, and preliminary results are widely discussed in [72], [73],[74]. The goal of the tests was to evaluate how quickly and easily the patients could learn to use the device in ADL. Different applications were considered (e.g., kitchen scenario, consisting in preparing breakfast and lunch, some tools activities, using the extra finger as an active hook, etc.). The initial tests gave encouraging results; users could complete the tasks reducing the time and with good success rates.

3.2 Fin-Ray® Effect based Supernumerary Robotic Finger (SRF)

"*It's not that we use technology, we* LIVE *technology.*"

Godfrey Reggio

In this section, we implement and fabricate a prototype of the proposed design, and we demonstrate an interesting application of the FRE finger as Supernumerary Robotic Finger (SRF).

3.2.1 Motivation and Design of Closed Chain SRF.

SRFs belong to an emerging field of robotics which aims at supplementing and augmenting the capability of natural limbs [75, 76, 73]. In this case study, we exploited the closed chain structure of the finger as shown in Fig. 3.17 to overcome the unwanted compliance in non-actuated directions.

In [77], we proposed one other version of a robotic finger, based on the flexure hinge based design. Flexure hinges allow efficient bending of joints while limiting bending of adjoining members, maintaining the rigidity of the structure under large deformation. In such a structure, the hinge-based soft joints play a critical role in guaranteeing the suitable contact force distribution [78] and stability of the grasp. An approach for designing flexible hinge joints with required bending stiffness using 3D printing technologies was also presented in [9, 14].

A CAD representation of the final prototype design is reported in Fig. 3.17. The final device is composed of three main parts: a flexible finger, a sliding mechanism, and a support base. The support base is housing for the linear actuator, the sliding mechanism, and the elastic straps mounting. The device can be worn on the human forearm using two elastic straps. The stroke of the linear actuator is attached to the front part of the finger. As the linear actuator pulls the front part, the sliding mechanism allows the back part of the finger to move along with it.

The sliding mechanism enables the finger to realize impactive grasp and to adapt to the shape of the grasped object as it moves towards it. The flexible finger consists of three main parts, a base part, the middle part having a set of intermediate modules, and the fingertip part. The base part is coupled with the actuator and the sliding mechanism; the finger is coupled at two positions where the front part is directly linked to the actuator while the back part is linked to a dowel pin constraint to move in the vertical direction, as the actuator pulls the front part of the finger, the back part starts to move up hence turning the finger downward, the middle part consists of truss-like structure and is designed as closed-chain modules. The specific flexible part is composed of two flat links connected to form a V-shape and reinforced by means of

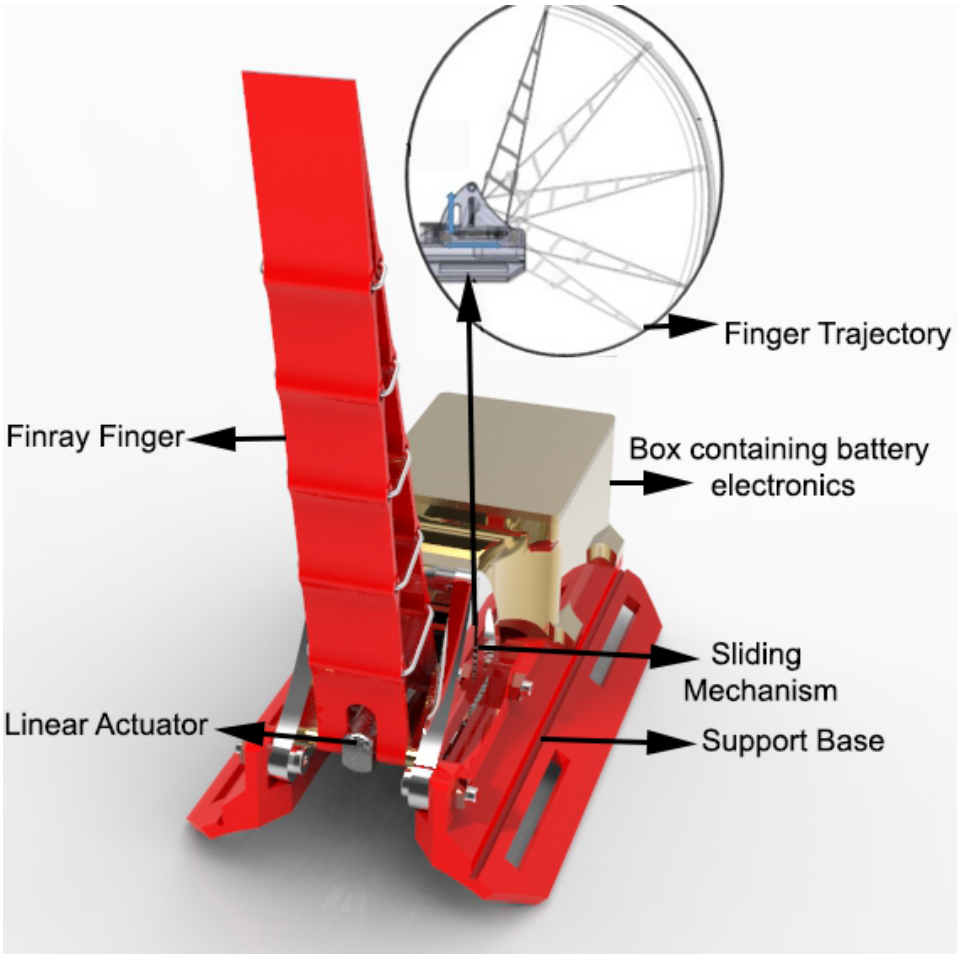

Fig. 3.17 The proposed design, inspired by Fin-Ray effect. The actuation mechanism allows the finger to move fully using the linear actuator.

parallel ribs. By applying a force to one of the links, in turn, cause the wall to converge towards the interference, resulting in conformity. A single linear actuator is used to drive the complete finger.

3.2.2 Prototype Development and EMG Interface

One of the main features of the proposed geometry is that it consists of a simple structure that can be easily fabricated.

The device is realized with a standard 3D printer, using ABS (Acrylonitrile butadiene styrene) plastic. The actuator used to drive the whole finger is a Micro Linear Actuator L12-P (Actuonix, Canada). The prototype of the device and block diagram of the complete system is shown in Fig. 3.18, while Table 3.6 reports the principal features of the device.

We used non-gelled reusable silver/silver-chloride electrodes for the EMG one channel interface, which present the lowest noise interface [79] and they are therefore recommended for biopotentials recording. The design and development of the EMG signal acquisition board are

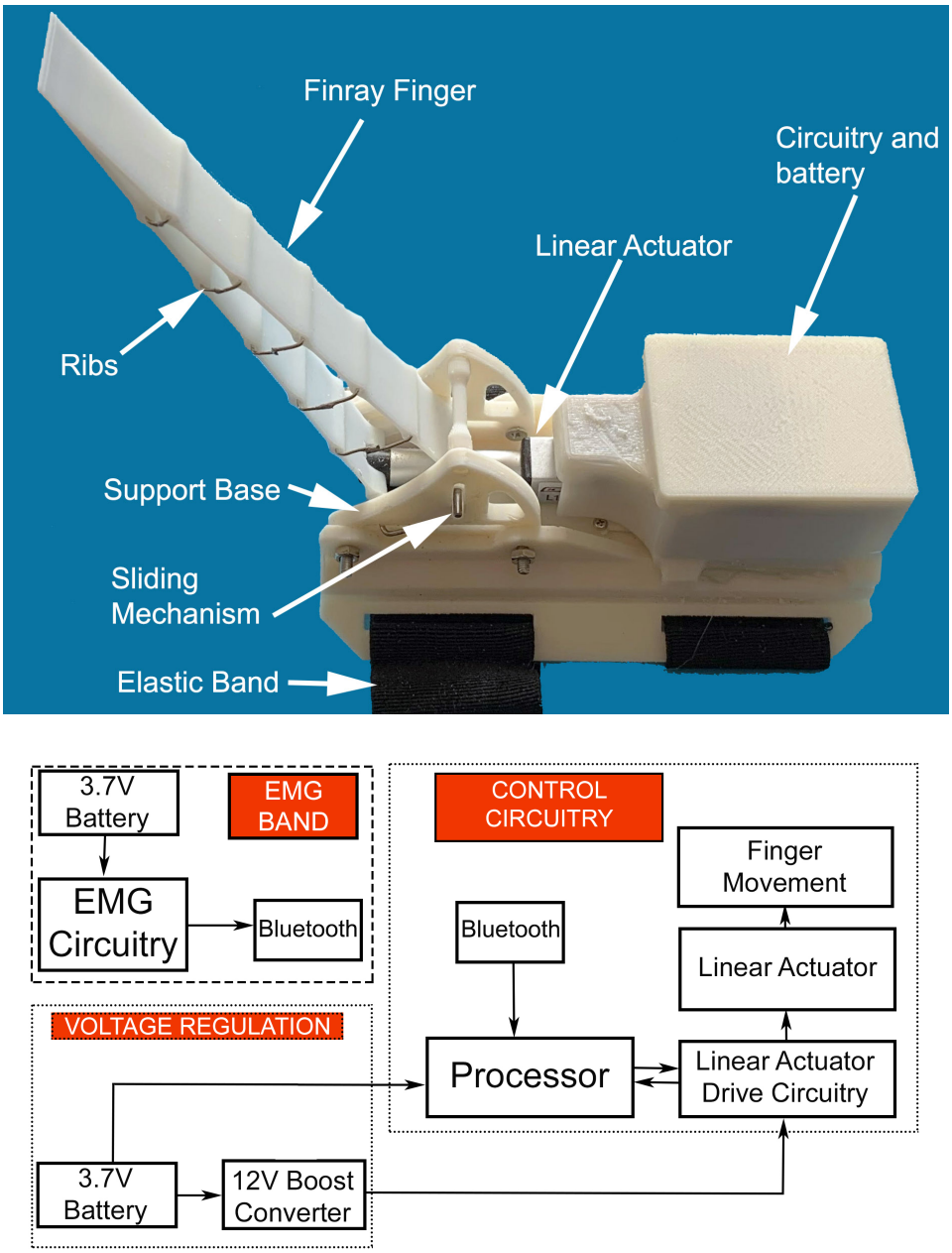

Fig. 3.18 The prototype of the finger (up) and the block diagram of the complete system (down).

Table 3.6 Summary of the performance and technical characteristics of closed-chain finger.

Characteristic	**Device Performance**
Max. payload (cylinder dia=85 mm)	approx. 50 N
Horizontal resistive force (cylinder dia=85 mm)	approx. 30 N
Finger Weight (including actuator)	0.175 Kg
Actuation Type	Linear Actuator
Material	ABS
The max. size graspable object	115 mm
The min. size graspable object	5 mm
Max. Power consumption	2.22 W (stall current 0.185 A @ 12 V)
No. of EMG electrodes	3
EMG principle	Differential voltage
EMG CMRR (common mode rejection ratio)	110 dB

Fig. 3.19 Frontalis muscle based EMG interface to control the motion of the device. The EMG interface is embedded in a head band to improve its wearability and easy to use.

carried out while considering the requirements associated with bandwidth, dynamic range, and physiological principles. The typical EMG waveform is characterized with a spectral content between 10 to 250 Hz with amplitude up to 5 mV, depending on the particular muscle [80]. The acquired EMG signal is sampled at 1 kHz (double EMG band) to avoid aliasing. The reference value of received EMG was normalized using the maximum voluntary contraction (MVC) technique [81]. This solution avoids the problems related to the high influence of detection conditions on EMG signal amplitude. Bluetooth modules RN42-i/rm are used to communicate between the headband (see, Fig. 3.19) and the finger. EMG data is collected using EMG control board, processed, and it is transmitted wirelessly using a Bluetooth module installed within the headband. This data is received by the Bluetooth module installed on the robotic finger, and the Arduino microcontroller operates the finger accordingly by generating the required motion signals for the linear actuator hence activating the bending and extension of the finger.

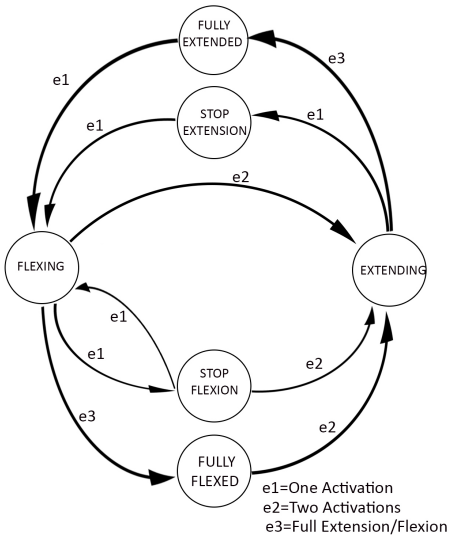

Fig. 3.20 Finite State Machine implemented to control the bending and extension of the finger

The strategy used to control the robotic supernumerary robotic finger by using EMG interface is depicted in Fig. 3.20. A single upward motion of the frontalis muscles means single activation, which is represented as e1, while a double upward motion of the frontalis muscles in a time window of 1.5 sec means a double activation and is represented as e2. The full extension or full bending of the robotic finger is represented as e3. When the user does a single activation, the robotic finger starts flexing and will continue to flex until the fully flexed position unless stopped by the user. After bending is started, another single activation can stop the finger from further bending. Now the user has two options either to keep on flexing or start extending. Another single activation will start the further bending of the finger, and a double activation will start the extension of the finger. As the finger is extending, the extension can be stopped by doing a single activation. In the stop position again, the user can either continue extension or can change the direction and start flexing. Also, if the user doesn't intend to stop the motion and switch to extension from bending or bending from the extension is possible by doing double activation.

3.2.3 The Performance Characterization

Besides the mathematical modeling and design guidelines reported in the previous sections, the device performance was confirmed through experiments (see, Fig. 3.21) similar to ones presented in [82]. In order to quantify and measure stable grasp and manipulation capabilities, we used a dynamometer (Vernier, USA). In particular, we recorded the maximum load lifting capability of the device and the maximum horizontal force that it can resist. The results of the experiments are given in table 3.6.

Fig. 3.21 Experimental setup for measuring the maximum payload and horizontal grasp resistive force.

3.2.4 Evaluation of grasping ability of device

The grasping ability of the device was observed through qualitative experiments consisting of different objects from the YCB object set [83]. The YCB toolkit is designed for the benchmarking of grasping in rehabilitation, prosthesis design, and robotic manipulation. The objects are chosen from daily life activities to have various shapes, sizes, and weights to involve many aspects of the manipulation problem. The aim was to confirm the capability of the finger to adapt to objects having various shapes and sizes, realizing a stable grasp. The devices work together with the impaired hand to grasp the objects and allow the healthy hand to perform manipulation if needed. The patients can wear the device at the wrist using elastic straps. During all the tests, we simulated the paretic hand and the device position on the arm as supposed to be used with the patients. Fig. 3.22 shows the snapshots of the experiments with some of the different objects that were used. The proposed robotic device was an effective aid in completing the ADL bi-manual tasks.

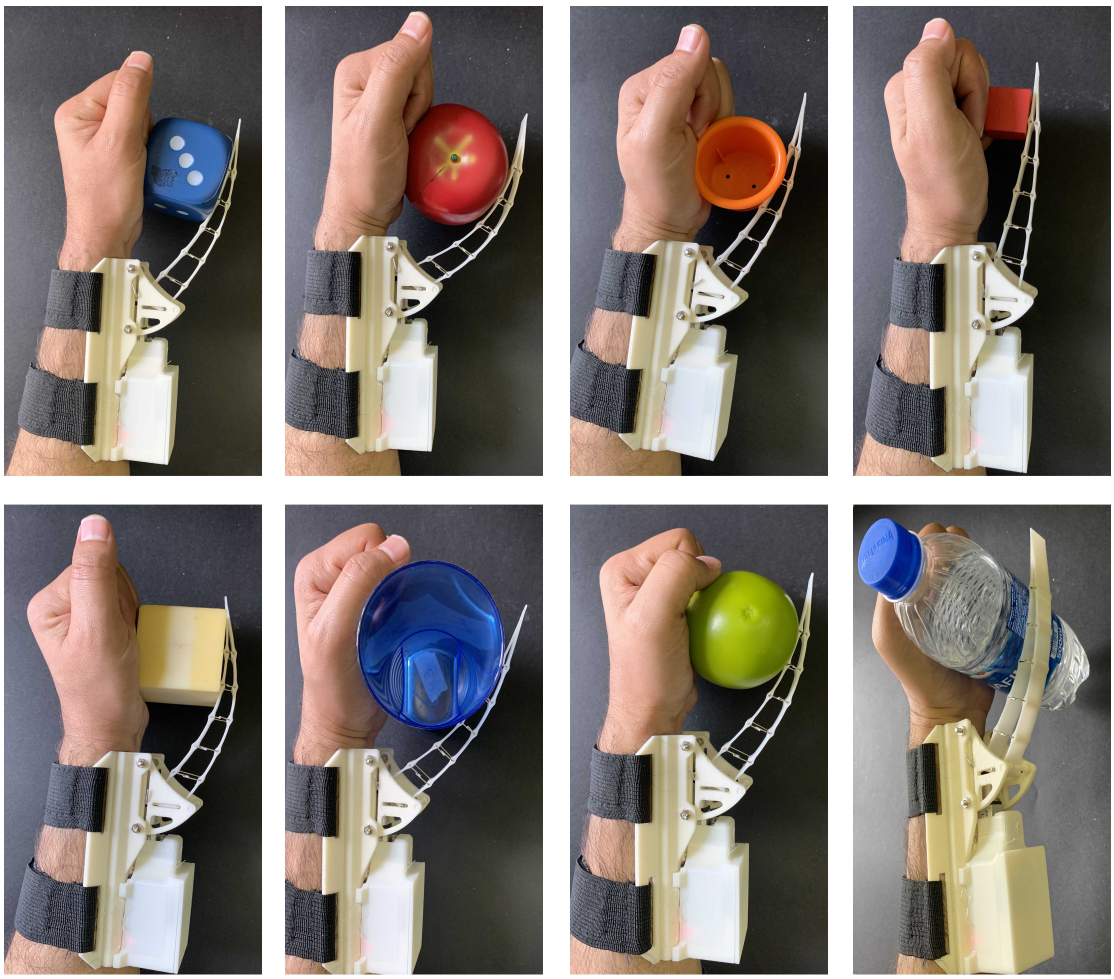

Fig. 3.22 Grasping various objects of different sizes and shapes.

3.2.5 Conclusion

In this work, we presented a general mathematical tool for the modeling of closed-chain geometries composed of both soft and rigid elements. In particular, we applied the formulation to Fin-Ray fingers, and we validated the results through some Finite Element simulations. A specific design has been proposed, and a prototype has been fabricated. The FRE structure's ability to conform to an external force while maintaining rigidness out of its grasping plane inspired us to exploit its use as supernumerary robotic fingers to meet their ergonomics, and functional requirements [35]. We evaluated the device's ability to grasp various ADL objects having different shapes and sizes, proving that the proposed device can improve the autonomy of patients. We believe that the presented work represents the first step towards a more effective design of FRE fingers and, more in general, closed-chain manipulators, allowing the optimization of these devices for specific tasks which have not yet been explored.

3.3 Design, Development, and Control of a Hand/Wrist Exoskeleton for Rehabilitation and Training

> "*For a person without disability, technology makes things easier. For a person with disability, technology makes things* possible."
>
> Mary Pat Radabaugh

Robotic devices for patients' rehabilitation and training is a promising and challenging research topic with a potentially huge social impact. The availability of tools for autonomously performing physiotherapy exercises increases their intensity and efficiency, provides supplementary information about results and progress, reduce s physiotherapist's efforts and the need for their physical presence during exercise sessions, and encourages autonomy and independence in people with disabilities. Nevertheless, supportive technologies developed without the inputs and feedback of the end-user throughout the design process, are less likely to be adopted for its intended purpose and use case. In this work, we propose a modular hand/wrist exoskeleton that actuates the wrist's flexion/extension and adduction/abduction motions and hand fingers' flexion/extension motions. It is designed to be wearable and easy to control and manage and can be used by the patient in collaboration with the therapist or autonomously. A user-centered design perspective has been employed in all the design and development phases. The work introduces the main features of the device and presents some tests conducted with a user having limited hand and wrist mobility.

3.3.1 Introduction

Nowadays, most people are living a longer and healthier lives than in the past, as the mean age of the population increases and, as a consequence, the overall social impact of chronic diseases related to the musculoskeletal and nervous system becomes more important. The World Health Organization (WHO) statistics show that nearly one billion people worldwide are suffering due to neurological and musculoskeletal diseases [84]. On the other hand, the spreading of technology in everyday life is playing an important role in preserving and guaranteeing a high quality of life also in the presence of temporary and/or permanent diseases [85].

At the beginning of 2020, the COVID-19 pandemic dramatically modified most of our habits, including medical and rehabilitation practices, that necessarily had to be delivered remotely, through audiovisual technology. Orthopedic and rehabilitation also shifted from face-to-face visits to audiovisual-guided sessions. In the immediate future, telerehabilitation could further spread and become more common. Despite some limitations, there are evident advantages in distance rehabilitation, whether synchronous (real-time) or asynchronous (store-

and-forward). The implementation of telehealth rehabilitation, which was initially considered difficult or even impossible, now has been forced to be utilized widely [86].

In particular, robot-augmented therapy is a clinically verified path forward to improving rehabilitation outcomes for several neuromuscular conditions, such as cerebrovascular and spinal cord injuries [87]. Technology advancements in the medical and assistive field allow people with disabilities and diseases to have a life that, in many cases, is almost completely autonomous. Devices and supports can help in the autonomy of activities of daily living (ADLs), in communication, study, learning, and more in general, in the whole process of integration. In this context, the use of robotic rehabilitation aids to provide motor therapy has shown great potential since they combine the high intensity, the long duration interventions needed for regaining motor function, and quantitative metrics for tracking therapeutic outcomes [88]. The capacity of performing precise and repeatable therapeutic exercises, reducing the physical burden of therapists, embedding virtual reality systems, and collecting quantitative data that can be used to optimize therapy sessions and assess patient outcomes are the main advantages offered by rehabilitation robotics.

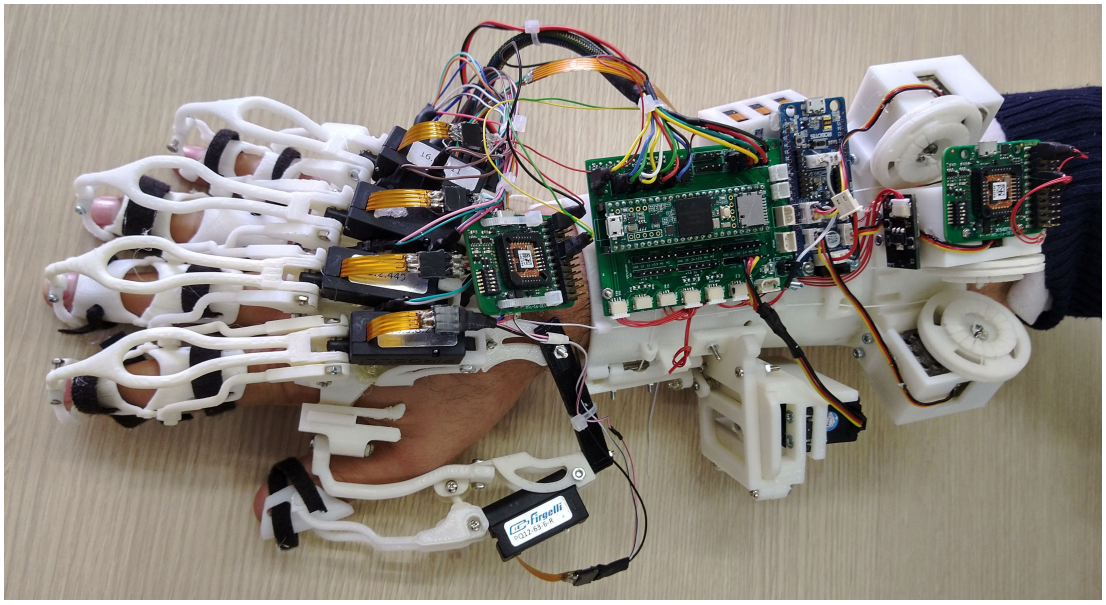

Fig. 3.23 Prototype of the hand/wrist exoskeleton for rehabilitation and training worn by a user.

Many researchers focused on developing devices designed to retrain impaired upper limbs [89], *e.g.*An exoskeleton arm having seven degrees of freedom wrapped around the arm and supported by the shoulder [90]. However, regaining the 'pick and place' and 'grasping' ability allows patients to perform the majority of ADLs, providing both functional improvements and regained independence. Therefore, successful upper arm therapy requires focusing not only on the arm but also on the wrist and the hand. Indeed, hand therapy via exoskeletons, and more in general, rehabilitation robotics, has received growing attention in the last decades. Lately, a number of robots have been developed to provide hand motor therapy. All these devices have similar goals: to develop a training platform that helps patients regain hand range of motion

and the ability to grasp objects, ultimately allowing the impaired hand to partake in activities of daily living.

These devices widely vary in terms of cost, design philosophy, actuated Degrees of Freedom (DOFs), and range of motion. In [91], the authors present HandCARE, an exoskeleton for the hand that uses cable loops attached to the ends of each digit. A motor and pulley system applies forces to the digits, and a clutch design allows individual actuation of the fingers and thumb. The Rutgers Hand Master II proposed in [92] is a force-feedback glove powered by pneumatic pistons positioned in the the palm of the hand.

A different design philosophy was exploited by Lambercy *et al.* in [93] where a parallelogram structure that presents two movable surfaces squeezed by the subject was presented. The hand module developed in [94] uses a double crank and slider mechanism driven by an electric motor. The operation of the motor controls the radius of the cylinder and guides grasping motions. A common disadvantage of the aforementioned devices is limited control of the proximal joints of the fingers, which may lead to physiologically inaccurate joint kinematics.

Cable-driven devices have been developed that allow for individual control of the fingers and thumb with pulley systems that rest on the dorsal surface of the hand [95, 96]. Bowden cables allow the motors to be remotely located, reducing the overall weight so these devices can be used in conjunction with arm movements. In [97] tendons are replaced with an air chamber and channels that run along the palmar side of the hand digits. An electro-pneumatic servo valve is used to regulate air pressure to provide assistance in digit extension.

Another class of devices is represented by robotic exoskeletons. In this type of devices, the exoskeleton joints are aligned with the anatomical ones, allowing for proper interjoint coordination between anatomical joints. Several solutions have already been developed as support tools for the upper part of the body [98–100]. For what concerns the hand and wrist, Krebs *et al.* in [101] presented a robot for wrist rehabilitation designed to provide three rotational DOFs. Similarly, in [102] authors present the RiceWrist. It is a high fidelity four DOFs wrist exoskeleton for training and rehabilitation purposes. The RiceWrist is intended to provide kinesthetic feedback during the training of motor skills or rehabilitation of reaching movement. A soft wrist orthosis exoskeleton that is able to actively assist users in all degrees of freedom is detailed in [103]. Considering only the hand, in [104] the Hand Wrist Assistive Rehabilitation Device is presented. The exoskeleton directly controls finger rotation about the metacarpophalangeal (MCP) joint, thumb abduction/adduction, and wrist extension/flexion. The Hand Mentor (Kinetic Muscles Inc., Tempe, AZ) is a commercially available exoskeleton device that uses an artificial muscle to simultaneously extend and flex the fingers and wrist, but the thumb is not actuated [105]. Finally, a system based on 3D printing technology for assisting stroke patients in performing rehabilitation exercises was developed in [106]. The interested reader is referred to [107] for a more comprehensive review on hand exoskeletons.

Notwithstanding all the technological developments just described and the presented evidence of clinical effectiveness of robotic technologies for upper-limb neuro-rehabilitation, there are still some limits in their diffusion [108]. Technological and economic barriers, together with communication biases between the producers of the technologies, are still open issues.

Supportive and rehabilitative technologies that are developed without the inputs of the end-user throughout the design process or without knowledge on how the technology will be

used are less likely to be adopted for its intended purpose and use case. This approaches the risk that the developed technology may be designed to meet requirements that are irrelevant for the intended user and use case. Rather, the design of technology has to meet the needs of the user engaged in the relevant activity across necessary contexts, including the utility needs, the usability, occupational, and social requirements factors [109].

In this work, we propose an exoskeleton for hand and wrist motion assessment and training (Fig. 3.23). Differently from the majority of the available device, the one here presented has been designed starting from the user's point of view, to be easily and independently wearable, easy to control and manage, modular and versatile. The proposed device can be used by the patient in collaboration with the therapist or autonomously and is composed of two independent and modular elements: the wrist actuation and the hand actuation systems. To the best of our knowledge, the proposed device represents the first attempt to realize a wearable hand/wrist exoskeleton able to record and playback motions and, at the same time, store data for further analyses.

The work is organized as follows. Section 3.3.2 describes the proposed devices, focusing in particular on their hardware and actuation part. Section 3.3.3 focuses on device tracking system, control and user interface. In Section 3.3.4 the results of a set of tests are presented and discussed. Finally Section 3.3.5 concludes the work.

3.3.2 Device description

Preliminary studies and first prototypes of the device have been introduced in [110] for the wrist and in [111] for the hand. First user feedback from the tests with these devices revealed that one of the main requirements to be addressed is providing the possibility, also for the users with limited motion capabilities of the upper limb, to wear and use it without the need for external support. Another important aspect that patients asked to be considered is the adaptability of the device to user's specific characteristics (i.e., anthropometric measurements). The proposed solution for the wrist consists of a tendon actuated module comprising two main elements worn on the hand and on the forearm, respectively. Opening/closing motion of the hand is actuated by means of five finger modules with one actuator per module. The CAD representations of the hand and wrist modules developed in this work are shown in Fig. 3.24. In what follows, before tackling the algorithmic development and experimental evaluation, we describe in detail all the mechanical parts comprising the exoskeleton.

3.3.2.1 Wrist Actuation

The wrist preliminary prototype [110] consists of a forearm part and a simple hand structure which was realized in thermoplastic material. It was developed to fit on the user as depicted in Fig. 3.25b. The arm part is fastened by using Velcro belts wrapped around user's forearm. Although the above mentioned system was simple and low cost, it was not suitable for users with limited motion capabilities, and the Velcro based closure system could result in undesired (or infeasible) relative motions between the device and the forearm.

In the version here presented, the wrist module has been significantly improved, in particular the part connected to the forearm. The most relevant upgrade is represented by an automatic

closure system, designed for easy and fast wearability and actuated by two servomotors. The complete forearm CAD is shown in Fig. 3.24b. The structural parts of the wrist module, both on the hand and on the forearm, have been realized in Acrylonitrile Butadiene Styrene (ABS) material through Additive Manufacturing (AM) technologies, and it can be customized according to users' specific anatomical characteristics (*e.g.*size of the forearm) and requirements.

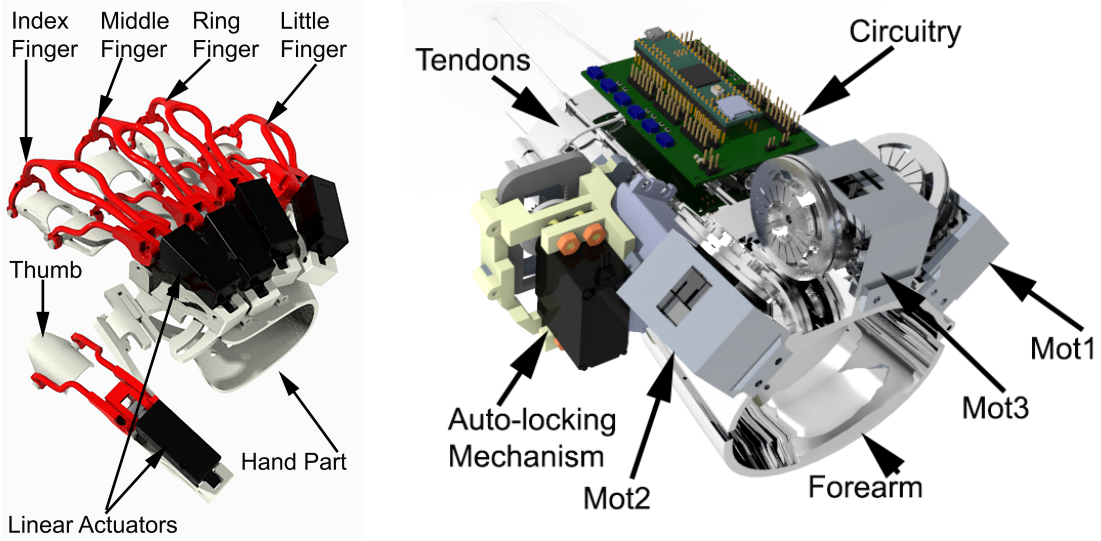

(a) (b)

Fig. 3.24 Exoskeleton prototype. (a) hand module; (b) hand/wrist integration CAD representation.

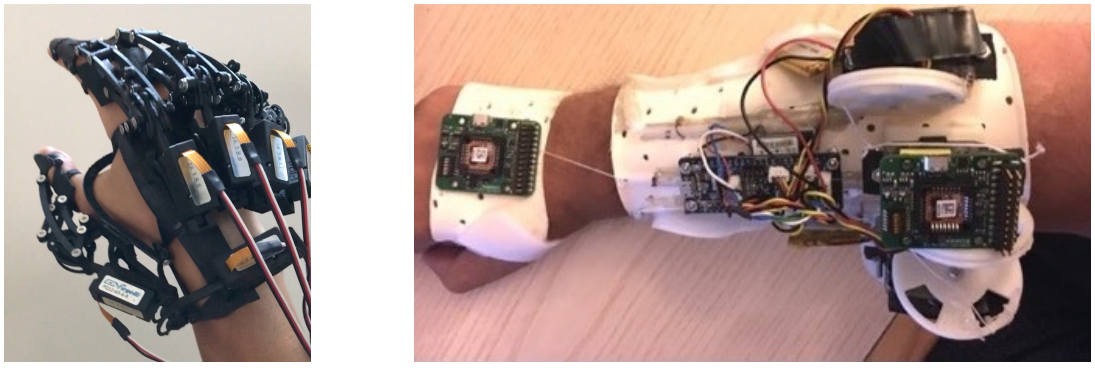

(a) (b)

Fig. 3.25 First versions of wrist and hand modules. (a) wrist module introduced in [110]; (b) hand module introduced in [111].

Regarding wrist joint actuation, in the forearm, the main principles introduced in [112] have been maintained, even if the design of this part has been consistently modified to make it more wearable and fitting to the arm. User's wrist movement during exercise execution is guided

and supported by a 3DoFs tendon system actuated by three servo motors (Dynamixel XL-320): two motors are used for the upward (extension) motion (indicated in the following with *Motor1* and *Motor2*), and the third motor is used for the downward (flexion) motion (namely *Motor3*). Rotation of *Motor1* and *Motor2* with opposite directions realizes the actuation of the radial/ulnar deviations. In the new version of the device, wrist pronation and supination motions are not activated. The position of the actuators on the forearm and tendon routing was selected, taking into account that flexion motion is easier for the user than extension, also due to the role of the weight of the hand in standard exercises where the palm side of the hand is facing down. For the choice of the position of the tendons and actuators on the forearm, therefore, we assumed that the effort necessary for the extension is higher than for the flexion. Furthermore, pulleys connected to motor shafts have been redesigned and optimized with respect to the ones presented in [112].

One of the novelties introduced in this work is the automatic closure system of the forearm module, needed by the user to Easily and autonomously wear it. For this purpose, a rack and pinion mechanism, actuated by a servo motor (HS-422, Hitec RCD Inc., USA), has been designed. A pinion gear driving the rack is connected directly to the output shaft of the motors. The pinion gear is designed to provide a rack stroke suitable for device closure and to provide enough strength to withstand the torque applied by the motor. The maximum rotation angle range of the motor is limited in the range $10° - 170°$; the corresponding rack stroke is 20 mm. The mechanism[1] is depicted in Fig. 3.26a.

The rack and pinion mechanism is coupled to the lower part of the arm support by means of a rigid link, allowing minor adjustments in the rotation around the axis of the lower arm support during opening and closing. The lower part of arm support is connected to the forearm part via a hinge joint that can move freely about its axis. The rack movement allows for pulling and pushing the lower arm support part of the forearm resulting in opening and closing motion, which provides a firm and solid connection with the arm.

(a) (b) (c)

Fig. 3.26 (a) The rack and pinion mechanism used for ensuring a tight closure saving batteries lifetime. (b) CAD model of single finger part. (c) CAD model of thumb part.

[1] A short video showing the working principle is available at http://sirslab.dii.unisi.it/exoskeleton/latch.mp4

Table 3.7 Main Characteristics of Linear Actuator

Technical Features	
Mass	15 g
Max. Force (lifted)	45 N
Stroke	20 mm @
Feedback Potentiometer	5 kΩ
Stall Current	550 mA @ 6V
Max Duty Cycle	20 %
Max Speed (no load)	15 mm/s

The user can control the opening and closure of the forearm fastening mechanism from the software Graphical User Interface (GUI) that has been developed to control the exoskeleton, and that will be detailed in the following sections. The developed system ensures a comfortable device opening and closure that can be autonomously controlled by the user.

3.3.2.2 Hand actuation

Hand actuation system is composed of one module per finger, and each module can be controlled independently. The modules for index, middle, ring and little fingers have the same mechanical structure, with different dimensions, while the thumb module has a different mechanism due to its particular kinematic structure [113]. In Fig. 3.26b and Fig. 3.26c we report the rendered CAD models of the fingers and thumb, respectively. In exoskeletons, actuators are the elements that usually have the highest impact on the overall device weight and encumbrance. Thus, to reduce the weight and inertial loads that may fatigue the user, we positioned the actuators on the back of the hand, and the motion is transmitted to the joints through a mechanical linkage system Fig. 3.26a.

One linear actuator, PQ12-63-6-R from Actuonix, has been used for each finger that actuates both the proximal and intermediate phalanges and is able to apply bi-directional forces. The main characteristics of this linear actuator are summarized in Table 3.7.

The mechanical transmission has been developed to implement the simplifying concept of postural synergies, introduced by the neuroscientific studies presented in [60]. In particular, the position and dimension of the exoskeleton linkages have been defined to reproduce the first postural synergy. At the same time, in the hand module, we maintained the fingers independently. In other words, for each finger, the transmission mechanism is designed to replicate the same coordination between the proximal and intermediate interphalangeal joints observed in the first postural synergy, but each finger can be independently controlled. This choice allowed us to reduce the number of actuators per finger down to one, maintaining, at the same time, a good versatility thanks to the independence between the fingers. Automatic synthesis procedures allow to properly define linkage dimensions on the basis of user hand anthropometric measurements. The kinematic structure of the finger actuation system and, in particular, the mechanism for coupling the Metacarpophalangeal (MCP) and Proximal

interphalangeal (PIP) joints has been changed with respect to the one presented in [111], to improve its lightness and adaptability to user's fingers.

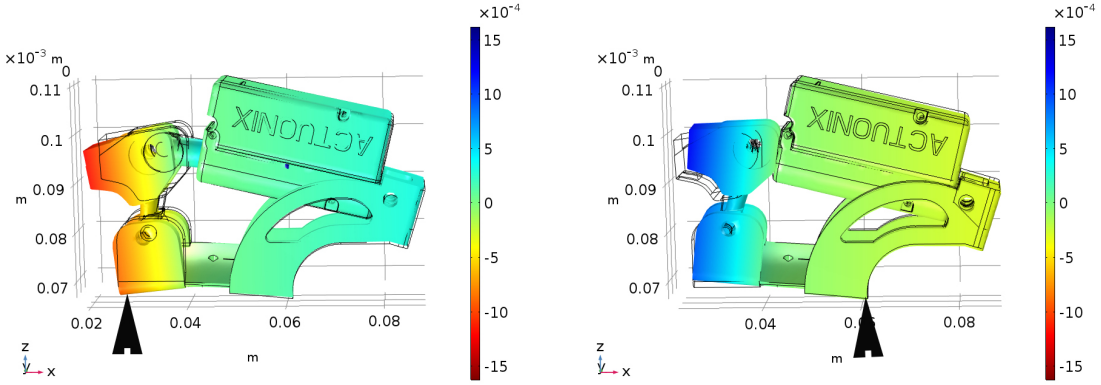

(a) (b)

Fig. 3.27 Results of FEM analysis on finger module support to evaluate force distribution generated by physiotherapist pulling and pushing action on the fingertip. (a) result generated by a pulling force applied on the fingertip of the index finger. (b) result generated by a pushing force applied on the middle finger pulp.

Linear actuators, due to their nature, are not back-drivable; this means that a physiotherapist cannot freely open or close the hand (i.e., flex or extend the fingers) while the patient wears the hand exoskeleton. To overcome this limitation, we provided the exoskeleton with a system for making the linear actuator back drivable in a transparent mode to the user. We conducted a stationary structural analysis based on the Finite Element Method (FEM) on the CAD model of one of the finger modules, simulated by means of external forces applied on the fingertip standard physiotherapist exercises. Forces for opening and closing the hand and finger were separately and jointly considered. Results of representative tests are visually depicted in Fig. 3.27 in terms of overall displacements. Outcomes of the analyses highlighted how the physiotherapist force is transmitted through the different elements of the exoskeleton and in particular how it can be measured with force sensors on the back part of hand palm. Further analysis results highlighted that pulling and pushing forces can be measured by means of force sensors placed on two different points of exoskeleton support (Fig. 3.27). We exploited this result for controlling the linear actuator in both directions, following the desired motion guided by the therapist. For each finger, two small FSR (Force Sensitive Resistors) sensors (Ohmite FSR04, active area diameter 5.60 mm) are placed at the points identified with the FEM analysis, between the motor support and the hand shell. A detail of prototype view showing the embedded sensors is reported in Fig. 3.28. Considering a single finger, ideally, when no forces are applied on top of the fingertip, both sensors' output is zero. It means that no pressure is detected in these points. On the contrary, pushing and pulling forces applied by the physiotherapist on the distal phalanx generate different compression of the sensors, from which an output proportional to the force can be estimated. Thus, a PD controller has been realized that seeks to keep the forces measured by the sensors to zero. In this way, the fingers gently

follow the desired motion, and the position of each joint can be measured from actuator stroke thanks to the kinematics structure of the mechanism.

Furthermore, as a preliminary experimental test devoted to device kinematic validation, we evaluated the capability of the proposed fingertip actuation mechanism in following the first synergy trajectory. Firstly a kinematic simulation was conducted for each finger, in Fig. 3.29 we report a plot of the index finger for different values of the MCP rotation angle, varying from 1° to 45°. Then, once the theoretical feasibility was assessed, we validated the accuracy of the prototype by means of an optical tracking system. We exploited a Vicon tracking system consisting of 10 Bonita cameras and 6.4 mm retro-reflective markers to track the motion of the exoskeleton. For the sake of comparison, in Fig. 3.30 we report a representative trajectory obtained by the index finger only.

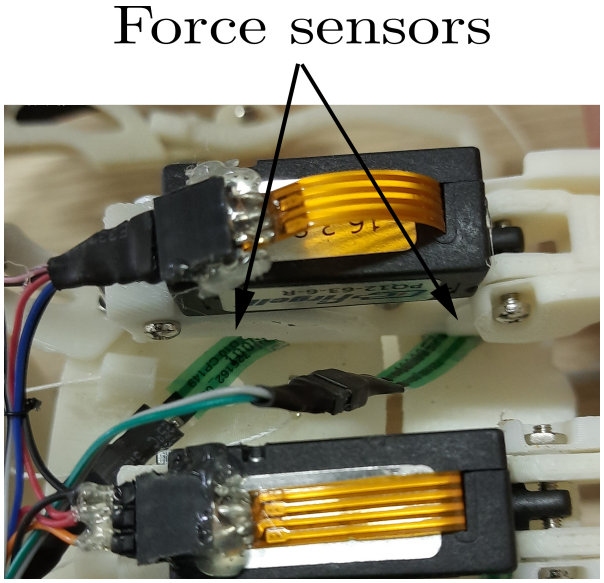

Fig. 3.28 Force sensors positioning in the index finger module.

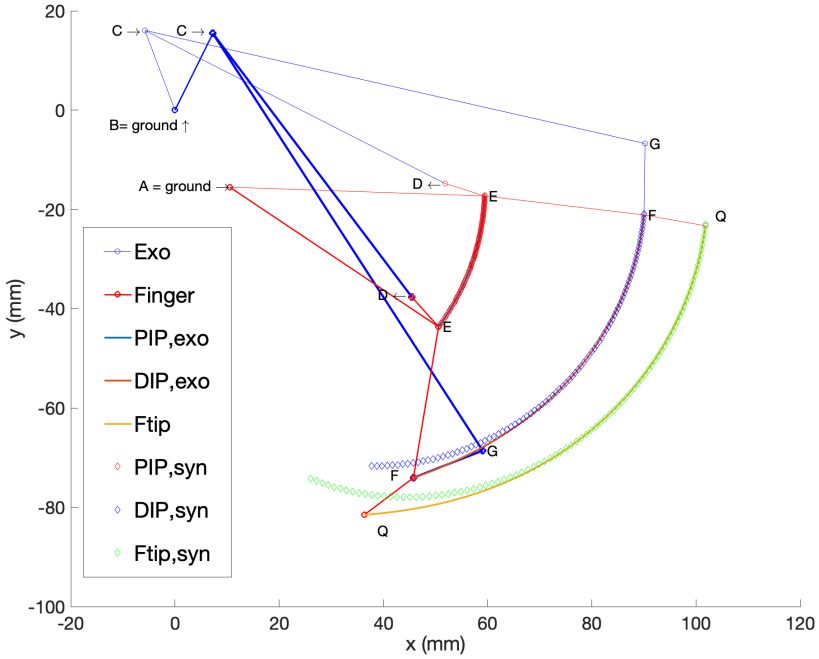

Fig. 3.29 Kinematic simulation of the index finger module for different values of the MCP rotation angles, varying from from 1° to 45°. The PIP joint is represented by point E trajectory while the DIP joint is represented point F trajectory.

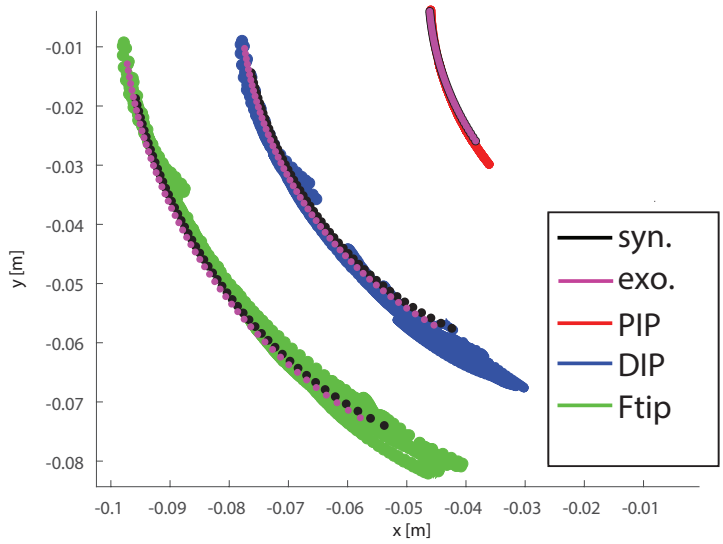

Fig. 3.30 Representative trajectories comparison: in red trajectories of points E (corresponding to the PIP joint position) in blue F (corresponding to the DIP joint position), and in green Q (corresponding to the fingertip position) for different values of MCP angle. Trajectories are acquired using the optical tracking system. Black dots represent the theoretical exoskeleton trajectory, while magenta dots correspond to the first postural synergy [60].

3.3.3 Device control

3.3.3.1 Tracking

In the hand modules, finger configuration is related to actuator stroke through the direct kinematics relationship. On the contrary, regarding the wrist module, since the two parts of the proposed exoskeleton (i.e., hand and wrist modules) are connected by flexible tendons and therefore are not mechanically constrained, a key aspect for controlling the device is represented by the tracking hand and wrist motions. The adopted solution relies on multiple Inertial Measurement Units (IMUs), low-cost electronic devices embedding an accelerometer and a gyroscope on a single board. This solution is the optimal trade-off between the accuracy of the estimation, wearability, and lightness. More in detail, we developed data acquisition and processing software capable of translating online IMU measurements into biomechanical information (i.e., the orientation of the hand with respect to the forearm). The resulting algorithm is able to: *i)* record the user's motion (e.g., wrist exercises suggested and guided by the physiotherapist); *ii)* monitor/control exercises played back by the exoskeleton; and *iii)* analyze patient's wrist articulation range of motion and consequential improvements.

To this end, we exploited two Xsens Mi-3 (Xsens, NL) embedding an accelerometer, a gyroscope, and a magnetometer in a single chip. For the purpose of this work, we decided not to use readings provided by the magnetometer since the magnetic flux in the surrounding of the exoskeleton is not reliable. The orientation of the hand with respect to the forearm (i.e., the wrist angles) is computed by means of two sensors board. An IMU is placed on the back of the hand exoskeleton structure, whereas a second one is firmly attached to the forearm exoskeleton support (as visible in Fig. 3.23).

To estimate the orientation of each board, we adapted the algorithm presented in [114]. The algorithm computes, for each sensor board, the actual orientation with respect to its initial pose. Raw data from the sensors is collected and processed by the worn microcontroller in charge of all the mathematical computations. The update rate for the system is 1 kHz. In what follows, we briefly summarize the procedure required to calibrate the sensors, and we outline the tracking algorithm. Each IMU board requires an initial calibration, which consists of two steps. In the former, the user is asked to maintain the hand stable for a second, e.g., displace the hand on a flat surface. In this phase, each IMU board collects 500 samples to estimate the gyroscope bias. In the second step, we compute the offset quaternion between the hand and the forearm.

In this work, we use quaternions to estimate the orientation of a single IMU sensor. Using quaternion allows us to overcome the problems introduced by the Euler angles, for instance, the gimbal lock problem and the issues related to the trigonometric functions.

Let ${}^{S}q_{H}(t)$ and ${}^{S}q_{F}(t)$ be the quaternions that express the orientation, with respect to the sensor reference frame Σ_S, of the frames associated to the hand and to the forearm, respectively. Let ${}^{F}\hat{q}_{H}$ be the offset quaternions between the hand and the forearm, estimated during the aforementioned calibration phase. At a certain time instant t, the orientation of the hand referred to the forearm can be computed as

$$ {}^{F}q_{H}(t) = {}^{F}q_{S}(t) \otimes {}^{S}q_{H}(t), $$

where ${}^{F}q_S(t)$ is the conjugate quaternion of ${}^{S}q_F(t)$. As a final step, the resulting quaternions are converted into *Euler Angles*.

3.3.3.2 Actuators' control

The complete control scheme for the wrist and hand module is depicted in Fig. 3.31. The user can select different options listed in the software Graphical User Interface (GUI). The data from the user interface are sent to the device via Bluetooth. Two Bluetooth modules RN42 are used for the communication between the PC and the device. The data from PC are received by the Bluetooth on the device and is fed directly to a Teensy 3.6 microcontroller which acts as the main control and processing unit. Teensy microcontroller controls the movement of the motors and the autonomous closure mechanism. It can also receive the data related to wrist exercises, in this case it generates a set of commands for Open CM 9.04 control board to actuate the three XL-320 motors.

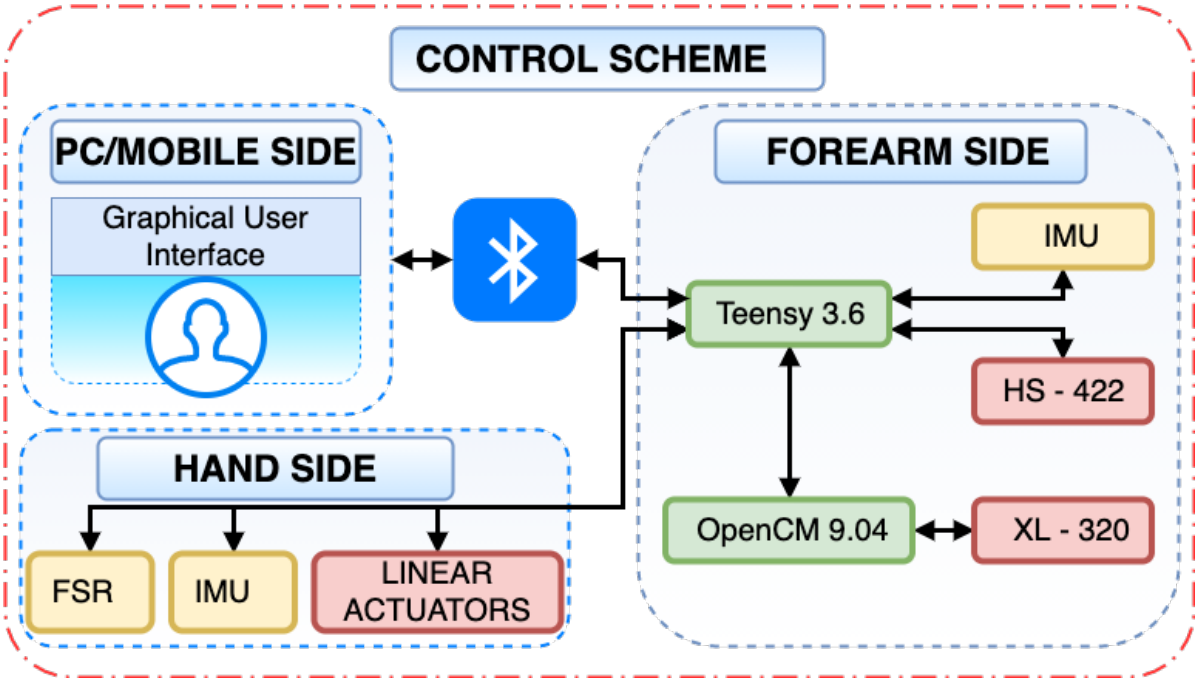

Fig. 3.31 Control scheme for wrist and hand exoskeleton modules.

Regarding the control of the hand actuation system, since finger motion is constrained by exoskeleton mechanical structure, hand configuration is directly related to actuator displacements by means of standard forward kinematics relationships. Both the hand and the wrist actuators are position controlled. The proportional gain can be selected in a predefined range to regulate the stiffness of the device. The input for the control scheme is the desired movement $\boldsymbol{\theta}_{des}$ that can be assigned by the user through the graphical user interface or previously recorded by the tracking system. $\boldsymbol{\theta}_{des}$ is a 7×1 vector, i.e., two rotation angles for the wrist and one rotation for each of the fingers. $\boldsymbol{\theta}_{des}$ values can be recorded, for example during the execution of an exercise in which the exoskeleton is not actuated, and the hand and wrist motions are manually

guided by the physiotherapist or can be loaded from an exercises database by means of the user interface. Through inverse kinematic analysis, desired configurations are transformed in references for the actuators control systems $\boldsymbol{q}_{des}$. $\boldsymbol{q}_{des}$ is an 8×1 vector (3 motor rotation angles for the wrist module and five linear actuator strokes for the hand). Actual hand and wrist movements $\boldsymbol{\theta}$ are monitored by the IMU-based tracking system and by linear actuator encoders during exercise execution, displayed on the GUI, and logged.

3.3.3.3 Graphical User Interface

Together with the hardware design and prototyping, a Graphical User Interface has been developed for managing the exoskeleton and fully exploiting its features.

The main objective of the GUI is to provide the user a simple and easy way to manage the device. Secondary, the interface makes available the opportunity of storing and playing backhand motions for training and rehabilitation purposes. Stored data can be further exploited for monitoring the effectiveness of the rehabilitation treatment. A cross-platform Python-based application connects the exoskeleton system via a Bluetooth and displays the user the options to record/replay wrist and fingers motions. A screenshot of the GUI is reported in Fig. 3.32.

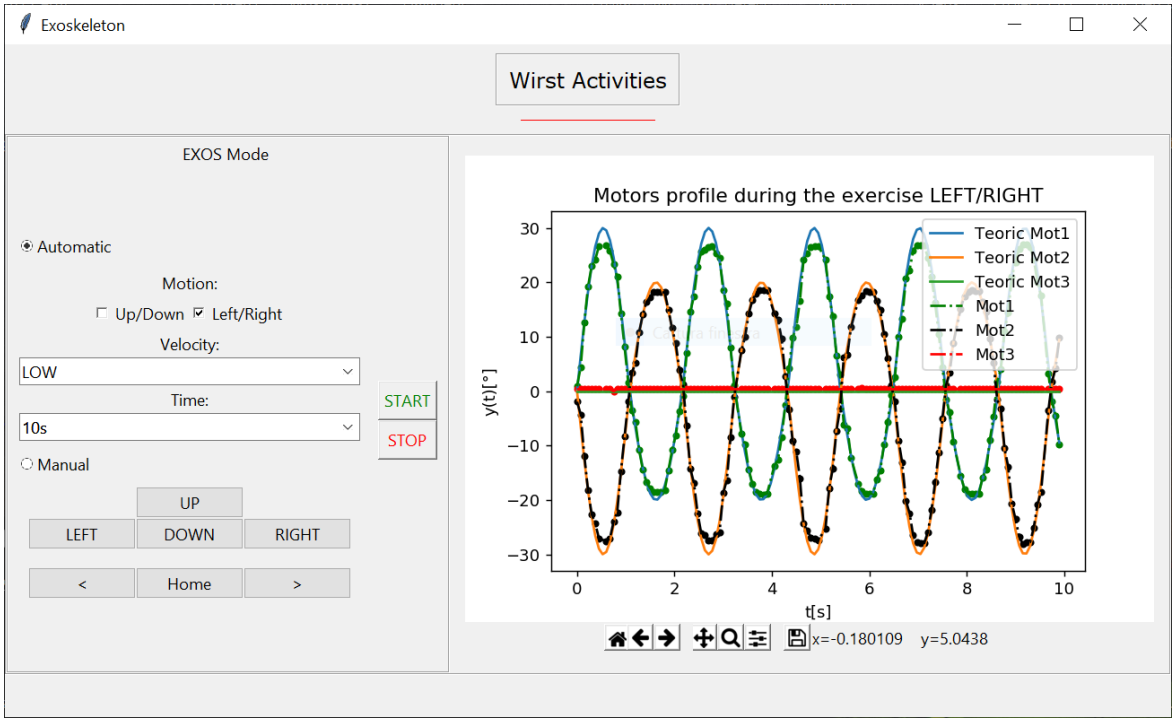

Fig. 3.32 Graphical User Interface display during an Automatic Exercise layout for wrist abduction/adduction.

Three main pages help the user in selecting the desired feature:

Activities for Hand: The aim of this page is to control the hand-exoskeleton. Two modalities are available: *Motion* and *Grasp*. The former allows to control and moves one finger at a time (selectable via

The *Grasp* option lets the user control all the fingers by moving only the index finger and exploiting the first postural synergy. Both modalities can be recorded and played back on demand.

Activities for Wrist: Here the user is allowed to select two modes of use: *automatic* or *manual*. The *manual* modality enables four buttons for controlling the motion of the wrist: DOWN for flexion, UP for extension, LEFT for ulnar adduction, and RIGHT radial abduction. Conversely, the *automatic* mode allows the user to perform some typical exercises for the wrist, such as abduction/adduction and flexion/extension movements. Paradigmatic exercises are already available in the interface. For each exercise, the user can select a running time and three different speeds (high, medium, and low). Moreover, the GUI allows also to set a specific time span and a certain speed value for the exercise manually.

Learning Mode: The aim of this page is to learn exercises, performed for example by a physiotherapist and then playback them. During the Learning phase, wrist exoskeleton motors are disabled. In this way, the specialist can freely move the wrist while the exoskeleton takes care to record these movements and the GUI saves them in a file. In Reproduce mode, a saved profile is loaded from the archive and played back. The learning mode feature is also available for fingers. In fingers learning mode, the linear actuators are moved, exploiting the FSR-based approach detailed in Section 3.3.2.2.

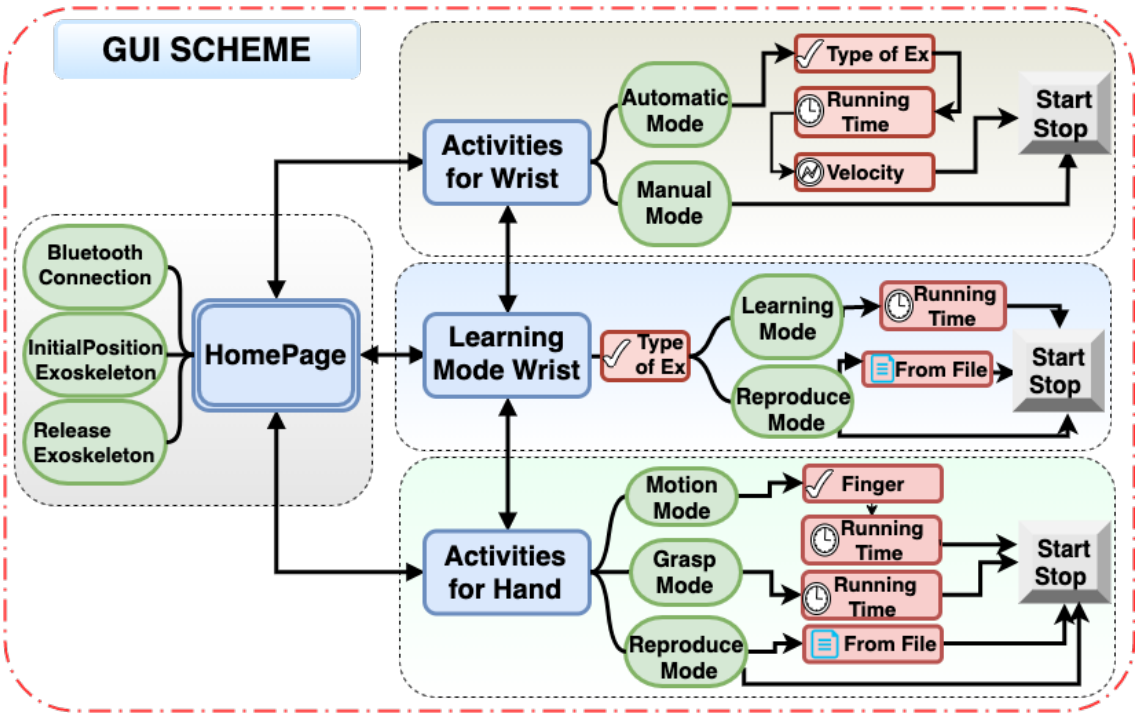

Fig. 3.33 Graphical User Interface flow chart for Wrist and Hand exercises

A flowchart reporting all the GUI components is depicted in Fig. 3.33.

3.3.4 Tests and evaluation

Since the modules of the exoskeleton are designed according to user's specific characteristics and needs, in the testing and evaluation phase, a single patient was involved, according to the "Single- Case-Design (SCD)" methodology, a procedure that is often employed in the clinical field in which an individual is the only unit of data analysis and which is capable of providing rigorous experimental evidence [115].

The tests were aimed at verifying the performance of the device in terms of accuracy in the execution of specific exercises. Different typologies of exercises suggested by the physiotherapist, involving both the hand and the wrist, were considered.

The study was approved by the local Institutional Ethics Committee. The subject gave her/his written informed consent to participate and was able to discontinue participation at any time during experiments. The experimental evaluation protocols followed the declaration of Helsinki, and there was no risk of harmful effects on subjects' health. Data were recorded in conformity with the European General Data Protection Regulation 2016/679, stored locally, and used only for the post-processing evaluation procedure. Please note that no sensible data were recorded.

A step-wise validation was conducted. In the former step, we focused on wrist tracking and actuation, whereas in the second, fingers were considered. Finally, wrist and hand were evaluated together. The system was evaluated on a subject with severe limitations in extension motion (movement in flexion are with reduced problems), some limitations in radial adduction and ulnar abduction, and severe limitation in opening/closing the hand.

3.3.4.1 Wrist Evaluation

To evaluate the proposed exoskeleton in wrist-based exercise performance, we conducted three different experiments. Precision in following the desired profile was considered as a metric and measured by means of the Root Mean Square Error (RMSE). Similarly to [116], for each trial we define this quantity as $RMSE_t = \sqrt{\frac{1}{N}\sum_{i=1}^{N}(y_{t,i} - y_i)^2}$, where N is the number of samples in a trial, y_i is the actual value, and $y_{t,i}$ is the corresponding target value. The mean among the ten RMSE values was used to analyze the tracking performance throughout the whole experiment. Notice that the tracking RMSE is a suitable metric to evaluate the rapidity and the accuracy of the robot motions. This is due to the fact that $RMSE$ increases both if the exoskeleton is slow in updating the control variable and if it does not reach the target value.

Wrist test 1: flexion/extension The first set of tests were carried out to evaluate the system's accuracy in following a specific desired motion. A predefined set of movements was generated with the aim of covering the entire patient's wrist range of motion.

Wrist flexion/extension is obtained by setting the same profile to actuators *Motor1* and *Motor2*, and the opposite to actuator *Motor3*. To simulate a realistic flexion/extension exercise performed by a physiotherapist, the following reference values were set to the actuators:

$$\varphi_{1,des} = \varphi_{2,des} = \alpha \sin(\omega t), \ \varphi_{3,des} = -\alpha \sin(\omega t)$$

with $\alpha = 50°$, $\omega = 2.9$ rad s^{-1} and $0 < t < 10$s. The internal encoder of the motors was used to record the actual angular value. Twenty trials were repeated, each one lasted 10 s. Desired and measured values of rotation angles of a representative trial are reported in Fig. 3.34. The figure shows how the actuators are able to follow the profile for the entire duration of the exercise.

Results We observed that the average RMS errors in following the reference were 6.70°, 8.45° and 7.51° for *Motor1*, *Motor2*, and *Motor3*, respectively.

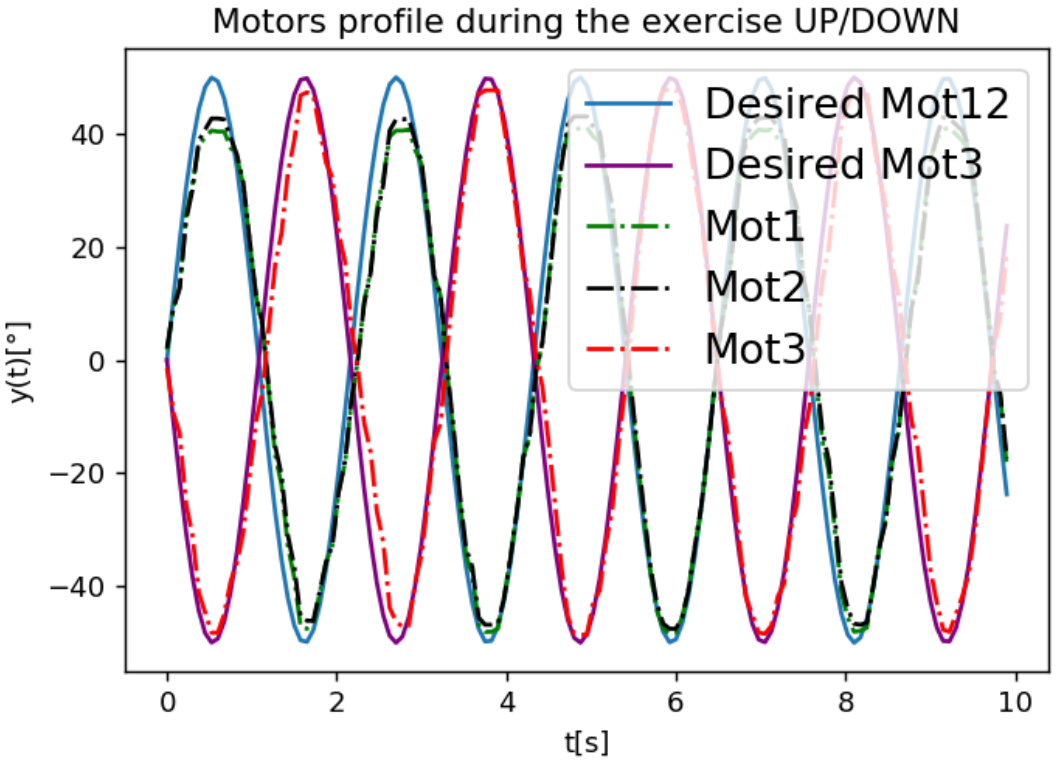

Fig. 3.34 Wrist test 1: automatic wrist flexion and extension. Reference and actual motor rotations during one of the trials.

Wrist test 2: adduction/abduction Then we simulated the ulnar adduction and radial abduction. To reproduce this behavior, *Motor3* was maintained steady, whereas motors *Motor1* and *Motor2* pulled their tendons in opposite directions. As in the previous experiment, with the aim at evaluating the exoskeleton in the whole range of motion of the wrist, the following reference profiles were used as motors control input:

$$\varphi = \alpha \sin(\omega t),\ \alpha = \begin{cases} 30° \text{ if } \sin(\omega t) > 0 \\ 20° \text{ if } \sin(\omega t) < 0 \end{cases}$$

$$\varphi_{1,des} = \varphi,\ \varphi_{2,des} = -\varphi,\ \varphi_{3,des} = 0$$

$\omega = 2.9$ rad s^{-1} and $0 < t < 10$s. Twenty consecutive trials were repeated. For each repetition desired rotation angle and real motor value were recorded.

Results We observed that the average RMS errors in tracking the requested profile were 2.36°, 2.10° and 0.50° for *Motor1*, *Motor2*, and*Motor3*, respectively .

Wrist test 3: record/playback An additional test was conducted for verifying the capability of recording an exercise performed by a physiotherapist and reproduce it with the exoskeleton. A physiotherapist and a patient with severely limited wrist mobility were involved in this test. We asked the physiotherapist to gently move for ten seconds the hand of the patient while the system was recording the hand orientation with respect to the forearm (i.e., the wrist angles). Ten adduction/abduction and ten flexion/extension exercises were carried out. A representative trial for this type of trial is reported in Fig. 3.35. The figure shows that the system is able to record hand motion with respect to the forearm through the tracking system and playback motions through the exoskeleton. Ten consecutive trials were performed by using the same profile recorded by the physiotherapist. For each repetition, the real values of the motors' rotation angles were recorded.

Results The average RMS errors in tracking the trajectory previously recorded by the physiotherapist were 1.88° for *Motor1*, 2.65° for *Motor2*, and 0.76° for *Motor3*.

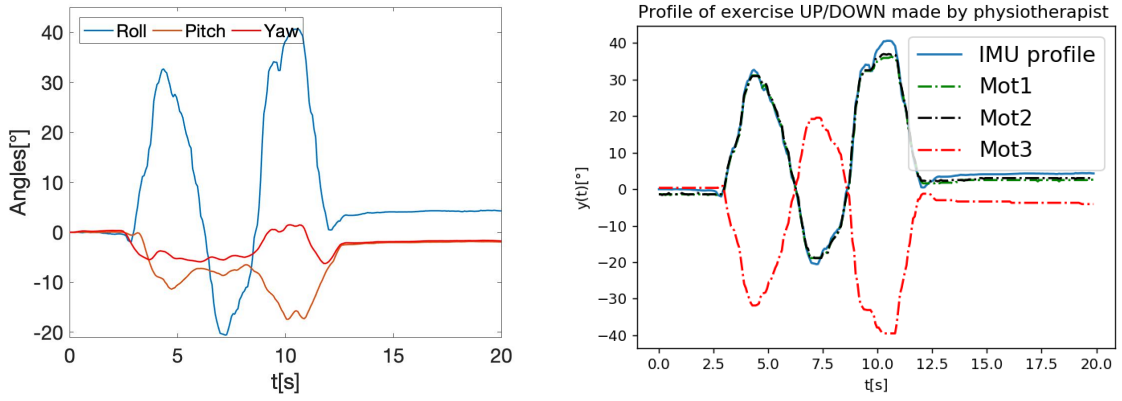

(a) (b)

Fig. 3.35 Wrist test 3: record/playback. (a) Roll, pitch, yaw angles measured by the tracking system. (b) Learning Mode: Flexion and extension angles as recorded by the physiotherapist and corresponding motor rotations.

3.3.4.2 Hand evaluation

In the second stage, the performance of the hand part of the exoskeleton has been considered.

Hand test 1: single finger We started the evaluation of the hand module, considering the capability of the exoskeleton in following therapeutic exercises through four fingers. The first

experiment consisted of an exercise of individual fingers carried out by the physiotherapist. In this exercise, the physiotherapist moved the individual finger (i.e., index, middle, ring, little finger) by either pulling the finger down or pushing the finger up. The FSR sensors installed under the base of the finger (see Figures 3.27 and 3.28) recognized this movement, and the linear actuator moved accordingly. This movement was recorded, and when the physiotherapist was done with the exercise, all the data related to the exercise were saved and available for future therapies. Fig. 3.36a shows the data acquired in the recording phase; the red curve represents the FSR reading when the physiotherapist push and pulls the fingertip, while the blue curve represents the position of the actuator. The trial started with the finger in normal position, where both FSRs recorded no force at all; as soon as the physiotherapist pressed the fingertip upward, the FSR installed under the back end of the finger base measured a force that triggers the movement of the linear actuator to move in the backward direction resulting in finger moving up as depicted by the plot with the first blue slope down. Similarly, when the physiotherapist presses the fingertip downward, the FSR installed under the front end of the finger base detected the force, and the linear actuator started to move forward, which result in the finger moving downward, as can be seen by the upward slope of the blue line in the plot. The physiotherapist can stop pressing up or down at any stage to generate a variety of motions. Fig. 3.36b shows the profile recorded by the physiotherapist in moving the finger up and down by means of pushing down or pulling up the fingertip. The blue curve represents the recorded data, while the red plot represents the trajectory followed by the linear actuator. It can be seen that the linear actuator followed the recorded trajectory perfectly.

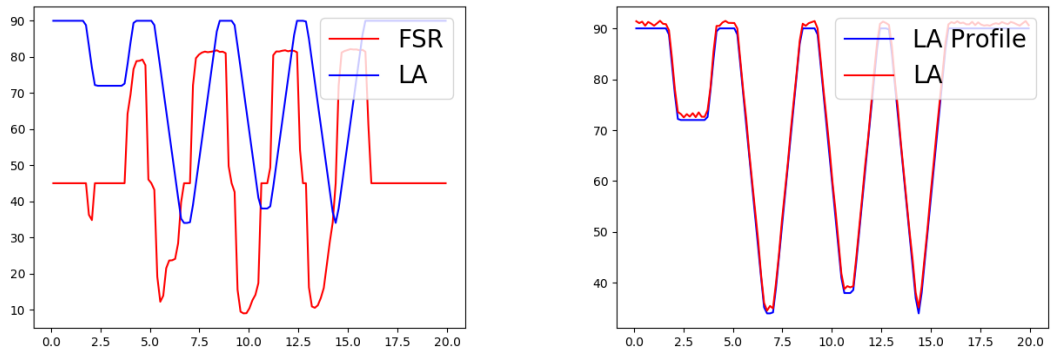

(a) (b)

Fig. 3.36 Hand test 1: single finger. (a) Single finger physiotherapist exercise, FSR sensor measure and corresponding linear actuator reference. (b) Desired vs followed trajectories of the linear actuator stroke.

Hand test 2: synergy based hand motion In this experiment, the physiotherapist moved the finger of the patient like in the case of single finger motion, but here the difference is in the actuation; instead of a single finger moving, this time the whole hand (all fingers and thumb) moved in accordance with the first synergy. The data were saved and reused later for standalone exercises. Fig. 3.37a shows the plot for this exercise. As it can be seen, as

soon as the physiotherapist push down or pull up the finger, the FSRs measured the force, and consequently, all the linear actuators moved forward or backward to move the finger down or up, respectively. The red line in the plot (Fig. 3.37a) shows the FSR data, whereas the other five lines depict the movement of the fingers. Similarly, Fig. 3.37b shows the stroke profile followed by the linear actuators as recorded by the physiotherapist.

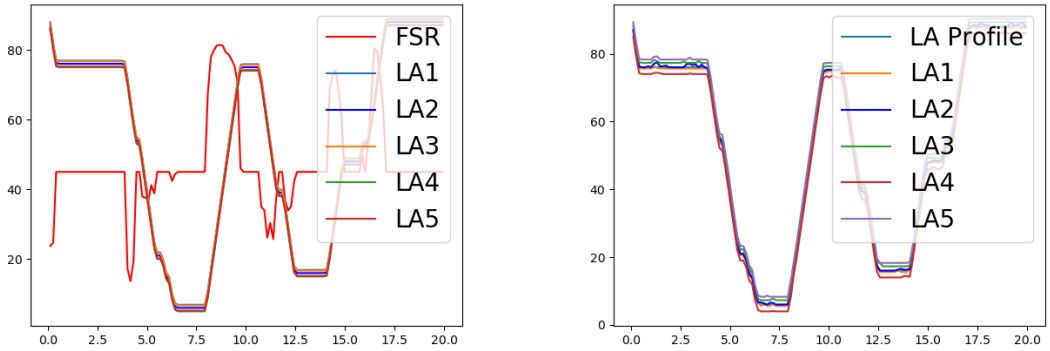

(a) (b)

Fig. 3.37 Hand test 2, synergy based actuation of all the fingers. (a) FSR measure during an exercise guided by the physiotherapist and linear actuator strokes for all the fingers. (b) Desired vs followed trajectory for all the fingers.

Hand Test 3: Grasping Task This experiment replicated a real scenario in which a physiotherapist helps the patient in grasping an object, like a bottle. The physiotherapist started moving a single finger by following the above-mentioned approach and stopped it at the desired position. In this experiment, the physiotherapist was able either to move all the fingers individually to establish a grasp or to exploit the first synergy (i.e., moving a single finger for controlling the whole hand). Also, in this case, at the end of the exercise, all the data were recorded to be reproduced in future therapy sessions. Fig. 3.38a showed the FSR measures when the physiotherapist formed a stable grasp, and the blue line shows the resulting linear actuator position. Similarly, Fig. 3.38b reports the comparison between the desired trajectory and the one followed by all the linear actuators to playback the physiotherapist movement. Finally, Fig. 3.39 shows the act of grasping a bottle carried out with the exoskeleton using the physiotherapist recordings. It is worth noticing that the patient without the exoskeleton would not have been able to grasp the object due to the hand muscles limitations.

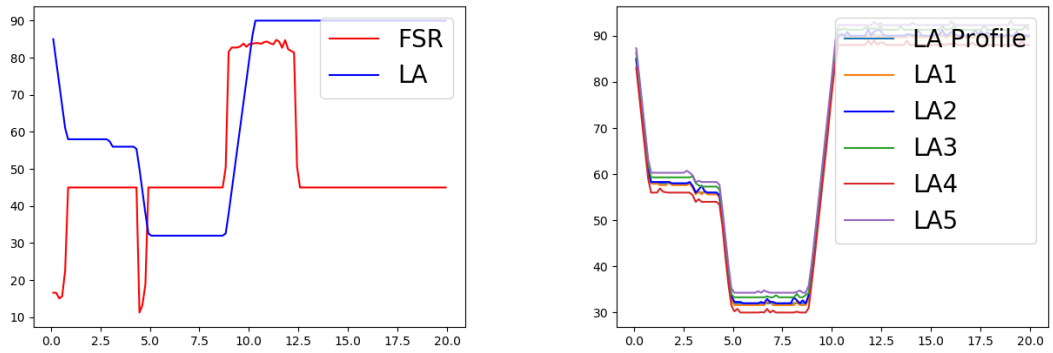

(a) (b)

Fig. 3.38 (a) Grasp exercise perfomed by physiotherapist (b) Grasp exercise reproduced without physiotherapist

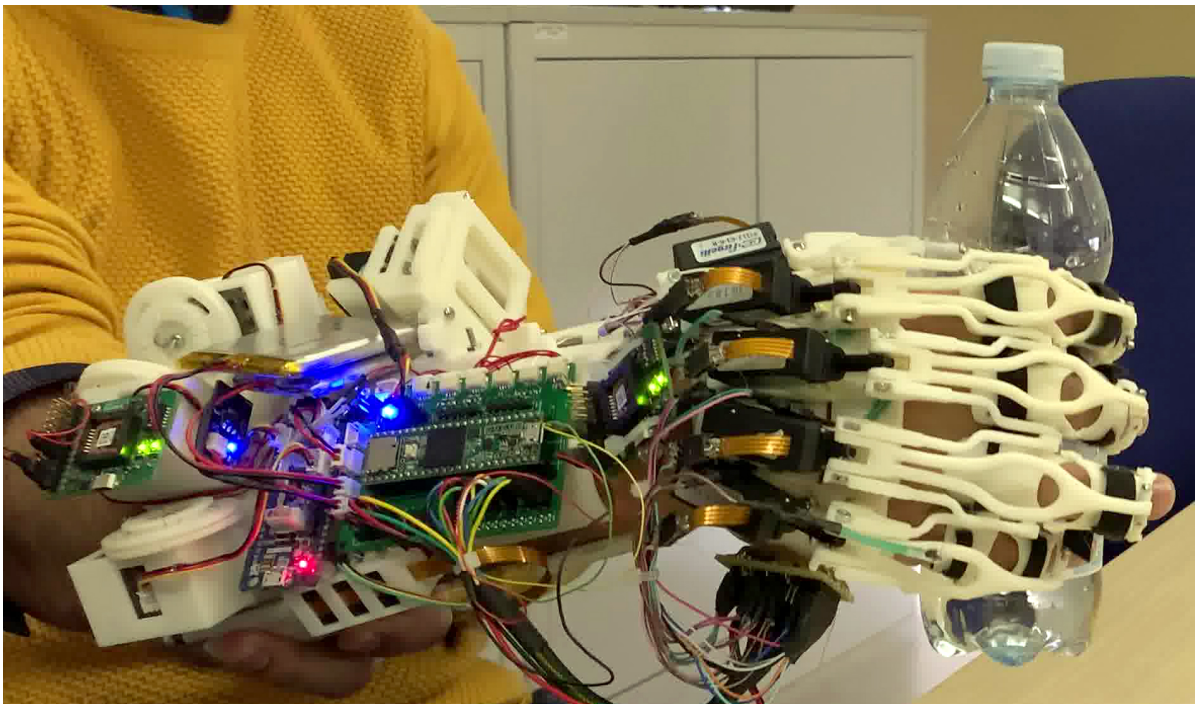

Fig. 3.39 Grasp exercise autonomously reproduced by the patient without physiotherapist.

3.3.5 Conclusion

In this work, we presented the main features in terms of the design and control of a hand/wrist exoskeleton for rehabilitation and training. The device has been developed to enhance patient independence and autonomy in the rehabilitation and training phase, reducing the time and the efforts needed by a physiotherapist or an external trainer.

This main objective was pursued by developing a device that can be easily worn also by a patient with limited arm and hand motion capabilities. This design criterion guided the realization of the locking mechanism that automatically fix the wrist support to the patient's forearm and the wireless connection to the PC. Another way to increase patient's autonomy is represented by the possibility of recording exercises guided by the physiotherapist by means of device sensors and replay them any time in other sessions.

The proposed device could represent a useful tool in the telerehabilitation context, whose importance has become very relevant in the past few months. The possibility to load personalized exercises and to record and replay an activity guided by the physiotherapist allows reducing the need for face-to-face interaction between the patient and the physiotherapist.

In the work, we showed some rehabilitation exercises for the wrist, for the single finger, and for the whole hand, in which exoskeleton motion was defined by means of specific mathematical functions or recorded by a demonstration realized by a physiotherapist and then autonomously reproduced.

It's worth underlining that in this work, end-users, *i.e.*patients suffering from upper limb disabilities and motion limitations, have been continuously involved throughout the different phases of the project, from the very preliminary design steps to the prototype development and testing.

In a successive phase of the work, the design of finger modules will be further developed to reduce their size, an *ad-hoc* App for the most common smartphones or tablets will be developed and released to further improve the accessibility for the users.

Chapter 4

Design and Applications of Industrial Devices

"*Technology is nothing. What's important is that you have a faith in people, that they're basically good and smart, and if you give them tools, they'll do wonderful things with them.*"

Steve Jobs

4.1 The Co-Gripper: a Wireless Cooperative Gripper for Safe Human Robot Interaction

In this work, we introduce a set of guidelines for the design of grippers suitable for a safe human robot/interaction in cooperative tasks.

Modularity, adaptability, robustness, intuitive control, limited weight are some of the key elements that could allow the effective spread of these devices in industrial and service applications. Following such guidelines, we present the prototype of the Co-Gripper: a robotic device for cooperative manipulation tasks with humans. The gripper is composed of two pairs of fingers, actuated with two motors, that can be controlled in a coordinated way or independently. Each finger has a modular underactuated structure, composed of three phalanges connected by passive joints. The gripper is wireless, so it can be easily connected both to the robotic arms and on passive structures. We designed a wearable wireless control interface composed of a ring and a bracelet allowing a simple and intuitive activation of the gripper without limiting the human operator's manipulation capabilities. We performed a set of tests to quantify gripper performance and to exploit its potentialities in human-robot cooperation tasks.

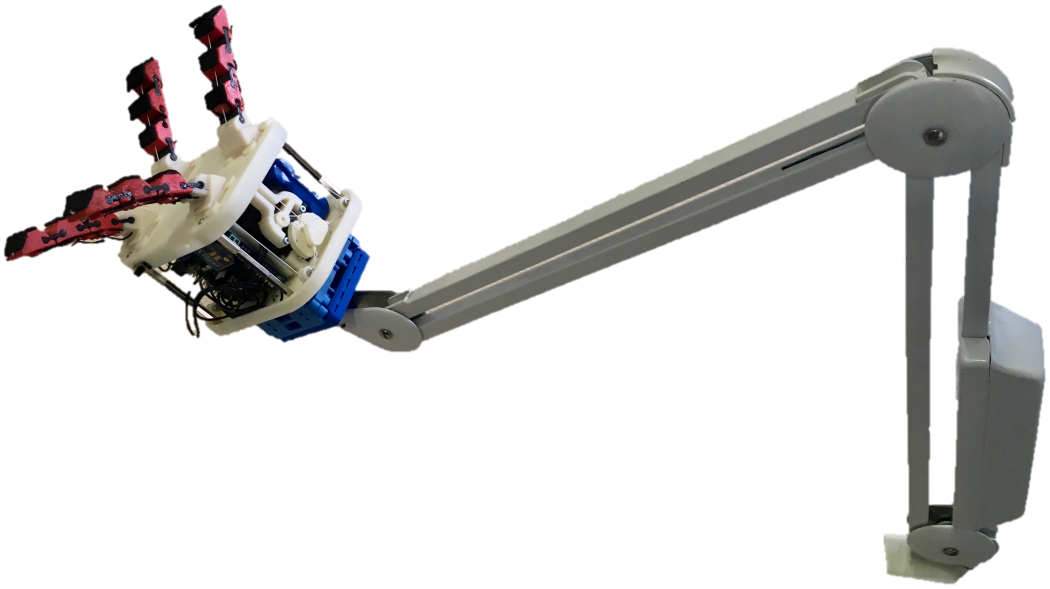

Fig. 4.1 The Co-Gripper. The device is completely wireless and can also be used with a passive arm support.

4.1.1 Introduction

Applicative scenarios envisaged in the Industry 4.0 framework present closer cooperation between humans and robots. The automated solution will be spread not only in large productive realities but also in SME (small medium enterprises) [117]. This new perspective effects also design requirements for robotic systems: from the maximization of the merely dynamical performance needed in a completely automated reality to more complex constraints necessary to assure a suitable level of adaptability to uncertainties, robustness, safety in the physical interaction with an unstructured environment and with humans [118]. Most of the work on collaborative robots (cobots) and more in general on physical human robot interaction have focused on robotic arm design and control. This has led to a novel generation of collaborative robots that can safely interact with a human operator. Commercial examples of these new robots are the LBR iiwa (KUKA, Germany), the Sawyer (Rethink Robotics, USA), and the FRANKA (FRANKA EMIKA, Germany), just to name a few. A concept common to these robots is the possibility to compliantly react to a collision, in opposition to the stiff behavior of classical industrial robots.

Exploiting compliance and environment constraints with underactuated compliant hands is also a lively research branch [119] for robotic end-effectors. Remarkable examples of soft grippers are available in literature, e.g., the Yale OpenHand Project [120], the 3-Finger Adaptive Robot Gripper [121], the Jamming Gripper [122], the underactuated grippers presented in [123], etc, In all these works, however, the attention was mostly devoted to analyzing hand/gripper manipulation capabilities and adaptability, rather than specifically evaluating the interaction with humans.

Although robot end-effectors are most of the time the part of the robot more proximal to the human partner in collaborative scenarios, only a few works have been dedicated to the design and the control of collaborative grippers. The Schunk Co-Act Gripper [124] is an example of a gripper designed for collaborative robotics, even if it still needs a complex system to be safe and can deal with a limited type of object's geometries. Another example of a plug–and–play gripper is represented by the RG6 Collaborative Gripper [125], however, can be controlled only through the robotic arm interface thus limiting its applicability in many collaborative contests. In this work, we present some design guidelines and propose a prototype of a soft–gripper explicitly devoted to easy and safe interaction with human operators in cooperative tasks. The key ingredient of the soft-grippers is the intrinsic softness of the devices, i.e., their embodied ability to comply and adapt to features of the objects and of the environment. The proposed device, that we named the *Co-Gripper* (see Fig. 4.1), is a wireless underactuated tendon-driven gripper, with four flexible fingers composed of three soft-rigid modules each. A wireless implementation allows to easily integrate the gripper both on actuated arms and on passive structures. Also, its control interface is extremely simple and can be used both in industrial and more general service applications, without the need for specific knowledge or training for the user. Nevertheless, we managed to obtain suitable adaptability and robustness properties, thanks to a tendon based actuation and flexible finger structure, in which joint stiffness is evaluated according to the methodologies proposed in [126]. The gripper has been realized using rapid prototyping techniques, in which we can manage material's mechanical properties by properly regulating 3D-printing parameters, and it can easily be reconfigured, due to its modular structure at a finger level. The rest of the work is organized as follows. In Sec. 4.1.2, design guidelines for collaborative soft-gripper are outlined. In Sec. 4.1.3 a prototype realized according to the proposed guidelines is presented and evaluated as well as the interface designed for its control. Sec. 2.1.2 deals with the experiments performed to evaluate the proposed system and its usability, whereas in Sec. 4.1.5 conclusions and future work are outlined.

4.1.2 Design guidelines

In this section, we report the main design guidelines for the collaborative gripper. As we introduced in Sec. 4.1.1, in this work we delineate which are the main features of a novel generation of grippers explicitly designed to interact with a human operator. Together with the automation standards detailed in the ISO/TS 15066 [127] and more in general in the ISO/TS 10218 [128, 129], we identified four main principles that a co-gripper should have with respect to foster human robot cooperation: *i*) intrinsic safety and adaptability, *ii*) easy reconfigurability, *iii*) portability and *iv*) easy interface with the human operator. In the rest of the section, we detail how each of these principles impacts human robot cooperation.

4.1.2.1 Intrinsic safety and adaptability

Safety is a crucial aspect to take into account in workplaces where humans are directly assisted and supported by robots, improving product quality, productivity, and worker's comfort. Using robots in an unstructured environment and the presence of humans needs specific requirements in terms of sensory perception, mobility, dexterity, planning, and management of uncertainties

and disturbances [130]. Robustness, adaptability, flexibility, and changeability of assembly processes, especially in an unstructured environment with human presence, need a close linkage between the worker and the robot: the human operator controls the process, while the robot provides support and assistance [131]. The whole robotic system should comply with the above mentioned issues, including the end-effector. In this view, an interesting solution can be sought in the novel generation of underactuated compliant hands that is growing in the robotics community in the last years, upgrading the preliminary attempts pioneered by Hirose et al., at the end of the seventies [132]. These devices are usually referred to as "soft hands" since they embed intrinsically passive compliant elements often at the joint level. Passive elements guarantee a safe interaction with the human co-worker. Moreover, compliant elements consent to store elastic energy, avoiding tendon slackness, distributing forces over a large contact area, and overcoming the indeterminacy of configuration problem typical of an under-constrained mechanical system [4]. Finally, this type of underactuated hands has the desirable adaptability to shapes which allows them to easily perform grasps of several objects. Underactuation is usually implemented using differential and elastic elements that allow the motion of other joints to continue after contact occurs on a coupled link so that the hands can passively adapt to the shape of the grasped object [123]. Another advantage of passive adaptability is the reduction of requirements on engineering the environment of the manufacturing facility since the passive adaptation to different object shapes is less demanding for accurate perception [25]. Such extended capabilities also lead to a reduced effort in programming the manipulation system enabling to drive the device with a reduced number of control parameters. Both of these factors significantly reduce set-up costs and shorten set-up times.

4.1.2.2 Easy reconfigurability

Human-robot collaborative environments are intended to be highly dynamic if compared with classic industrial production chains where specific areas are devoted to the production of a specific item. Such flexibility can be obtained if it is possible to quickly change the gripper configuration. Flexibility refers to the various types of operations that the machine can perform without requiring a prohibitive effort in switching from one operation to another [133]. Reconfigurable manufacturing system aims at achieving cost-effective and rapid system changes, as needed and when needed, by incorporating principles of modularity, integrability, flexibility, scalability, convertibility, and diagnosability [134]. When flexibility and reconfigurability concern grippers, this usually refers to devices that can rearrange the position and orientation of their fingers [135] or that can adapt the number of DoFs to the task at hand [136]. In Co-Grippers this reconfiguration should be easy to be performed by the human operator while performing a cooperative task.

4.1.2.3 Portability

The Co-Gripper envisaged in this work is intrinsically safe thanks to the embedded passively compliant elements and thus does not need a complex perception system to detect human presence. This can also be exploited to use the gripper detached from a robotic arm. In Fig. 4.1, the co-gripper is attached to passive arm support (in this case a simple table lamp support)

and can be used by a worker without the necessity of a robotic arm. This can be possible if the gripper can be used in a completely wireless solution, i.e., if it has batteries for the power supply onboard. This solution opens interesting scenarios where the co-gripper can be used in a broader context than in manufacturing scenarios, e.g, by other types of workers such as plumbers, electricians, etc. The passive arm support and the portable co-gripper may be valid support to hold pipes, pass cables, and so on. Within an industrial environment, portability may also be exploited to use the gripper both as the end effector of a robotic arm to perform pick and place and other common operations, and together with a passive arm as an advanced third hand support system on the worker's desk.

4.1.2.4 Ease of the interface

One of the characteristics of collaborative robots is their intuitive as an easy interface. Different solutions have been proposed to control grippers of collaborative robots that mainly involve displays or buttons embedded in the gripper themselves or the supporting robotic arm, see as an example the interface proposed for the gripper of the Rethink Robotics Sawyer robot [137]. However, we do believe that co-grippers should also be used detached from a robotic arm. The portability requirements should be extended also to the interface, which should be light and easily wearable. Simple interfaces are sufficient to provide basic operative commands, like the opening and closure of gripper fingers. More complex, still wearable, interfaces could be adopted also to haptically render to the user specific operating conditions [138]. Moreover, the interface should require a minimal cognitive effort to be used by the operator and it must not prevent the user's hand to perform a collaborative task.

4.1.3 The Co-Gripper system

the device In this section, we introduce the Co-Gripper, a soft tendon driven modular gripper that has been designed following the guidelines reported in Sec. 4.1.2 and a possible wearable interface to control it. The CAD model of the gripper is shown in Fig. 4.2, whereas the 3D printed prototype is reported in Fig. 4.4. Its overall weight is 480 g and, as we will detail later, it can resist forces up to 4.75 kg.

4.1.3.1 The Co-Gripper

The proposed device is intrinsically compliant, modular, underactuated, and cable driven. Each module consists of a rigid 3D printed link realized in ABS (Acrylonitrile Butadiene Styrene, ABSPlus, Stratasys, USA) and a 3D printed thermoplastic polyurethane part (Lulzbot, USA) that acts as the flexible joint. We selected polyurethane for soft parts because the high elongation of this material allows for repeated movement and impact without wear or cracking proving also an excellent vibration reduction.

The main technical features and material/geometric parameters of the soft modular gripper are summarized in Table 4.1. The mechanical properties of 3D printed materials, like polyurethane, depend on manufacturing processes and can be controlled. We exploited this property in [126] to design the stiffness of passive joints to realize a robotic underactuated

finger whose fingertips follow a given trajectory when the finger is actuated. This approach can easily be applied also to the co-gripper described in this work, in which passive joints can be realized with stiffness values defined to obtain a given closure strategy, for example, suitable to grasp large objects or perform pinch grasp of small objects. The modules are connected by sliding the thermoplastic polyurethane part into the ABS part. This method makes the assembling process easy without using any screws or passive elements to combine the modules. The holes in the rigid links allow the passage of a cable (realized with polyethylene Dyneema fiber, Japan), which realizes the tendon driven actuation.

The device actuation is achieved by using two actuators and four tendons running in parallel through the modules of the fingers. The actuators are two Dynamixel MX-28T (Robotis, South Korea), each having a maximum torque of 3.1 Nm and a maximum angular speed of 684 deg/s. The main technical features of the Co-Gripper and its actuation system are summarized in Table 4.1. Each actuator along with a differential mechanism [139] is used to control the motion of two fingers. The differential mechanism is necessary to adapt fingers' configurations to the specific geometric features of the grasped object, if one of the fingers contacts the object or any surface, the other one can continue its closure motion until a firm grasp is achieved. In Sec. 4.1.4 we will report some examples where the Co-Gripper is conforming to irregularly shaped objects. Tendon wires run through the fingers and are attached on one side to the fingertips and on the other to the differential mechanism which in turn is connected with a pulley rigidly attached to the actuator shaft. When the motor is actuated, the tendon wire is wound on the pulley reducing the length of the wire and producing the closure/flexion of connected fingers. The opening/extension of the fingers is achieved thanks to elastic force stored in the flexible parts of the modules.

The fingers are connected to the palm of the grippers through a Dovetail joint that allows to completely rotate the finger along the direction perpendicular to the palm plane. This feature can be exploited to reconfigure finger orientation according to the object to be grasped. Fig. 4.3 shows some of the possible fingers' configurations. We named them perpendicular, parallel and circular configurations. In the first configuration, the fingers are perpendicular to the longest side of the gripper. The two pairs of fingers are at the maximum distance, which allows grasping relatively big objects. Instead, the configuration where fingers are oriented parallel to the long edge of the palm can be exploited to grasp objects with a dimension much higher than the others, e.g., pipes. Finally, the circular configuration may be exploited for objects with a circular section. These three are only examples of the high number of possible achievable configurations.

The combination of the modularity, possible finger trajectory design through stiffness, and finger configurations meet the requirements for easy reconfigurability of the system. The soft structure and the tendon driven actuation satisfy the requirements for safety and adaptability.

4.1.3.2 The wearable interface

The control interface of the Co-Gripper is based on a remote ring, whose prototype is shown in Fig. 4.4. The ring configuration has been chosen to obtain an interface highly wearable and portable. The ring is realized in a flexible material which allows the ring to comfortably adapt to different finger sizes. It includes two push buttons to remotely control Co-Gripper motion.

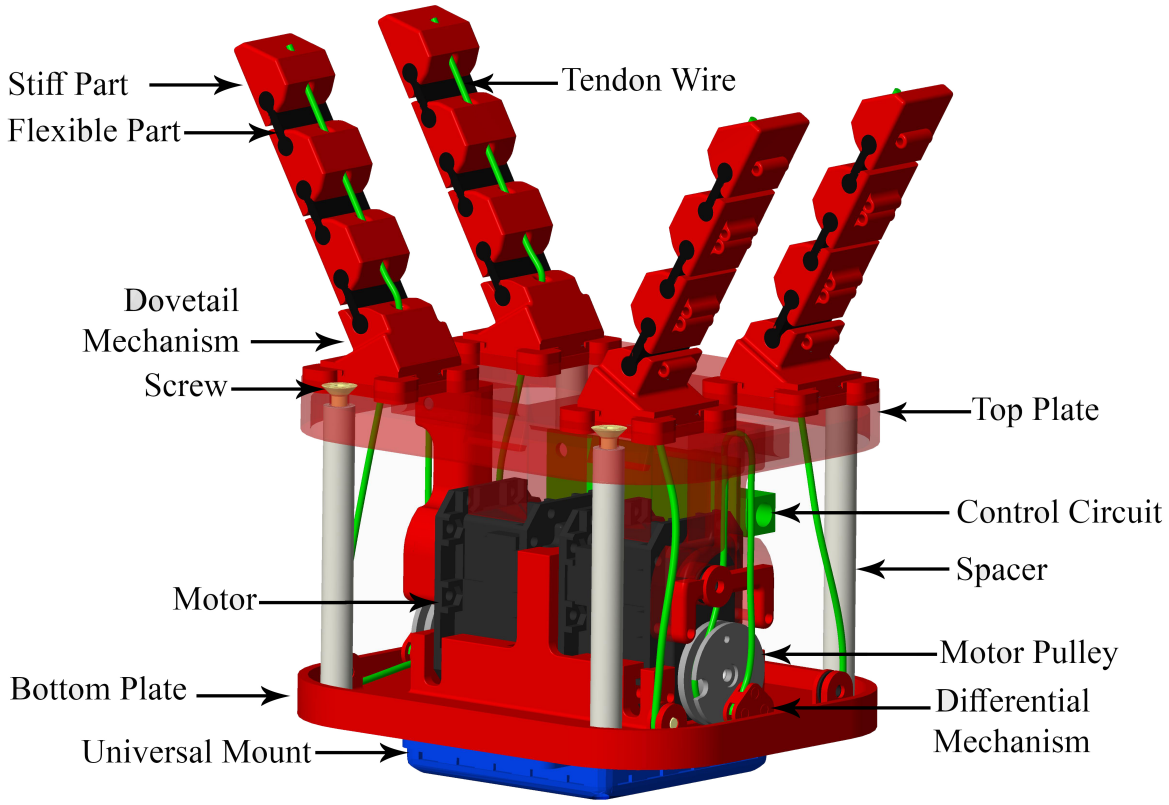

Fig. 4.2 The Co-Gripper: A wireless underactuated tendon-driven gripper with four flexible fingers composed of three soft-rigid modules each. Modules can be assembled with different stiffness values at flexible joint level, obtained changing 3D-printer parameters during manufacturing.

The user wears the remote ring on the index finger, its controller box housing is included in a bracelet that can be worn on the wrist, (see, Fig. 4.4). The ring controller receives the activation signals from the pushbuttons and sends them to the actuator's controller through a wireless transmission, which in turn controls the motion of the gripper according to the high-level control strategy summarised in Table 4.2.

The Arbotix-M controller (Robotis, South Korea) is used to control the Dynamixel actuators of the soft gripper. This control solution for Dynamixel motors incorporates an AVR microcontroller, a socket for a XBee wireless radio, and the motor driver. The wireless communication between the remote ring and the gripper controller is realized through the XBee modules.

The soft gripper can be operated in two different modes of operation: four finger mode and two finger mode depending on the nature of the task to be performed. In the case of the former, the four fingers are moved simultaneously to grasp relatively big size objects. The fingers can be oriented in different configurations depending on the size and shape of the object to grasp. In the case of the latter, the gripper has two different two fingers' gripper configurations where

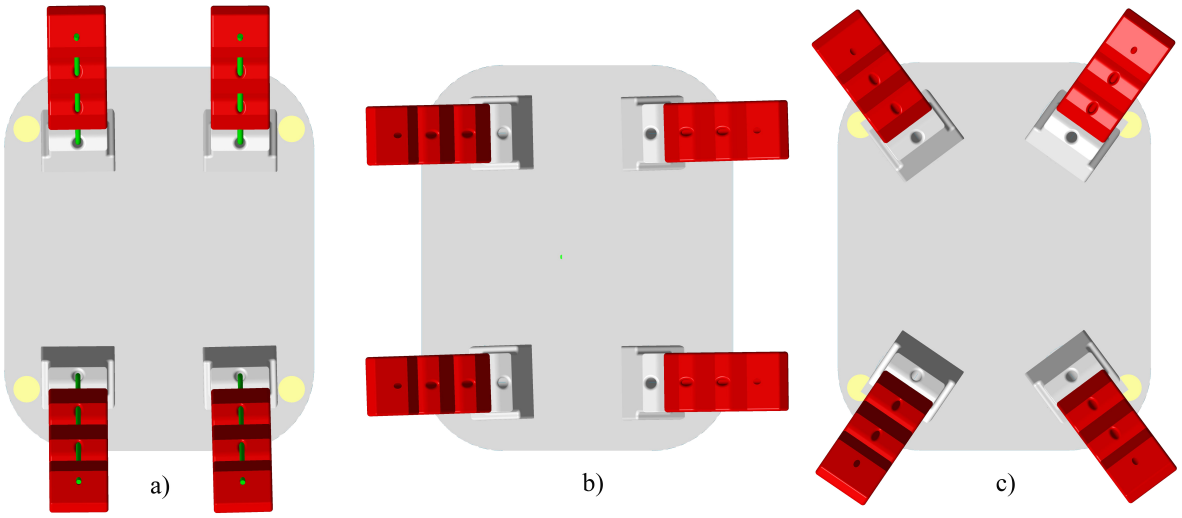

Fig. 4.3 Possible configurations of fingers achieved through Co-Gripper. a) perpendicular b) parallel and c) circular configurations.

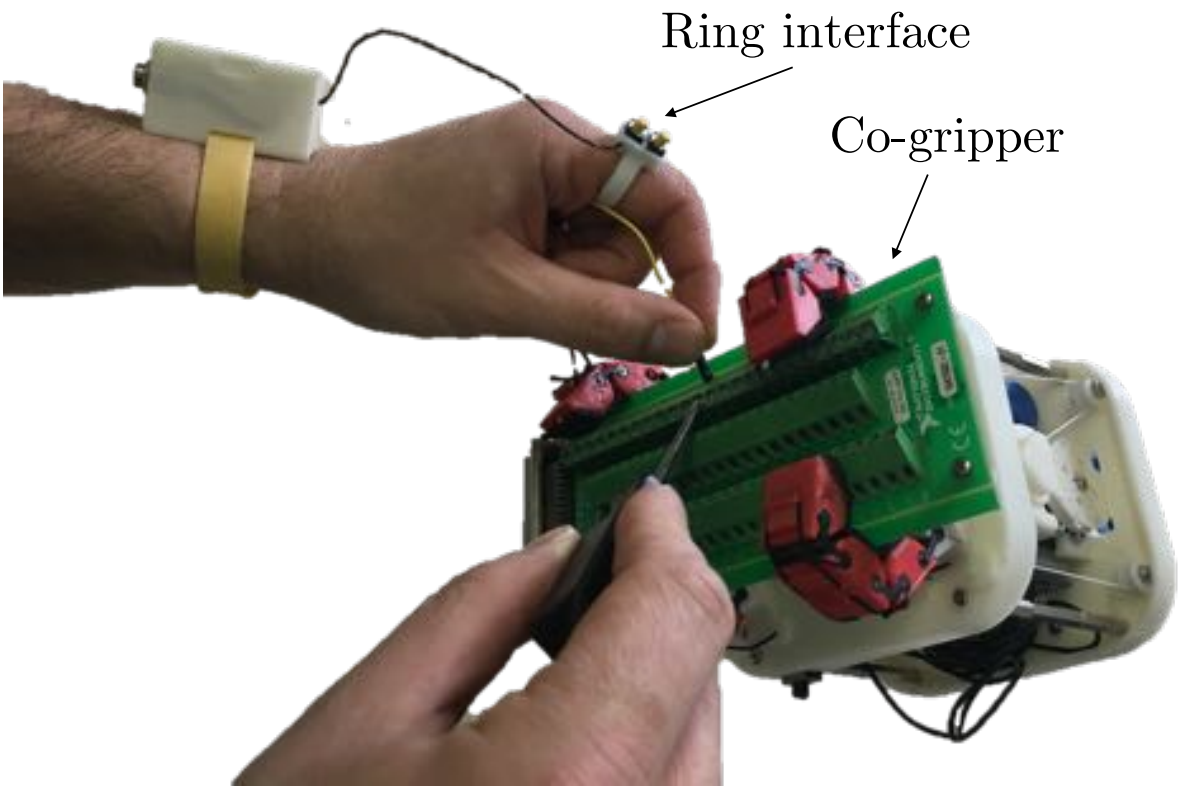

Fig. 4.4 The remote ring interface and Co-Gripper.

each pair of the fingers is controlled separately enabling the grasp of multiple objects at the same time.

Table 4.1 Technical features of the Co-Gripper.

Technical Features		
Weight (including motors)	480 g	
Max. actuator torque	3.1 Nm @ 12 V	
Max. current	2.8 A @ 12 V	
Continuous operating time	3.5 h @stall torque	
Max. operating angles	300 deg, endless turn	
Max. non-loaded velocity	684 deg/s	
Dimension of Gripper	130 mm x105 mm x 85 mm	
Material Parameters	**Flexible Part**	**Stiff Part**
Material type	Thermoplastic polyurethane (TPU)	Acrylonitrile Butadiene Styrene (ABS)
Modulus of elasticity (E)	15.2 MPa	40 MPa
Shore Hardness	85A	70D
Density	1200 kg/m^3	1070 kg/m^3
Geometric Parameters		
width	25 mm	23 mm
length	23 mm	30 mm
height	3.5 mm	15 mm

Table 4.2 Finite State Machine Table

Push Button (PB) trigger signal	**Associated actions**
Simultaneous trigger (both PB)	Mode change (two–fingers/four–Fingers and vice-versa)
Four–fingers mode	
Single trigger (first PB)	flexion/stop and vice-versa
Two triggers (first PB)	flexion/extension and vice-versa
Two–fingers mode	
Single trigger (first PB)	flexion/stop and vice-versa (first pair of fingers)
Two triggers (first PB)	flexion/extension and vice-versa (first pair of fingers)

Fig. 4.5 Gripper's performance characterization experiments. a) Evaluation of vertical grasp resistive force. b) Evaluation of horizontal grasp resistive force

As a default condition, four–fingers mode is selected: when one of the pushbuttons is selected, the flexion/extension motion of all the four fingers is initiated. With a single button pressure, the user switch between the motion/stop of the fingers. When the fingers are stopped, two trigger signals within a time window of 1s, switch the motion direction from flexion to extension and vice versa. Switching between the modes (four fingers and two fingers) can be achieved by pressing both pushbuttons simultaneously. The switch is possible at any state of the gripper. In two finger mode, the gripper behaves like two independent grippers that can be separately controlled. A LED on the board is used to provide visual feedback of the selected modes of operation and activation of the trigger signal. The wireless communication and battery onboard together with the ring interface for gripper control meet the requirements for portability and ease of interface.

Table 4.3 Main performance of the Co-Gripper.

Technical Features	**Value**
Max. payload	4.75 kg
Max. horizontal resistive force	64.0 N @(cylinder diameter 95 mm)

4.1.3.3 Performance characterization

The performance of the gripper was evaluated through a subset of the tests proposed in [82]. In particular, we measured the maximum payload and maximum horizontal grasp resistive force in the case of power grasp. The experimental setup is shown in Fig. 4.5. To compute the maximum payload of the gripper in power grasp configuration, a cylindrical object (diameter 95 mm, weight 130 g) was slowly pushed down by using a dynamometer's bumper (Vernier, USA) as shown in Fig. 4.5-a. The maximum force was recorded when the object started to slip from the gripper. The maximum payload of the device is the sum of the grasp object's weight and the force applied to the point of slippage. It was observed to be 46 N, which resulted in a maximum payload of 4.75 kg. To measure the maximum horizontal grasp resistive force, the gripper was fixed on the table and the hook of the dynamometer was attached to the object by using a small thread. The object was slowly pulled in the horizontal direction by using the hook of the dynamometer as shown in Fig. 4.5-b. It was observed that the gripper hold on to the object till 64 N. It is pertinent to mention that in all of the above summarized tests the gripper was actuated at the maximum motor torque, the results obtained are summarized in Table 4.3.

4.1.4 Experiments

We first evaluated the capability of the Co-Gripper to adapt to different shapes of objects. We selected 10 common objects with different shapes and we exploit the characteristic of our prototype to achieve stable grasps. Two fingers were assembled so to perform a pinch grasp by selecting the stiffness of the soft joints as reported in Sec. 4.1.3. The obtained results with the relative chosen fingers' configurations are reported in Fig. 4.6. After this evaluation of the device capabilities, we evaluated the whole system (gripper + interface).

Ten subjects (7 male, average age 28) tried the system wearing the ring interface on the non dominant hand to control the open/close motion of the device. Four different objects were presented to the subjects (small cube, pipe, ball, and electronic board, see Fig. 4.6). The subjects were instructed on the functioning of the ring interface and the possible reconfiguration of the fingers, but no suggestions on fingers' positioning according to the object shape were given. After the explanation of the system working principle, subjects were asked to grasp the objects with the device, open again the gripper fingers, and put the objects back on the table. Each subject was left free to rearrange the orientation of the fingers to achieve the grasp. After the task was completed, subjects were asked to fill the System Usability Scale (SUS), a simple, ten-item scale giving a global view of subjective assessments of usability [140]. SUS yields a single number representing a composite measure of the overall usability of the system being studied. It is a Likert scale where it is possible to answer each item with a mark ranging

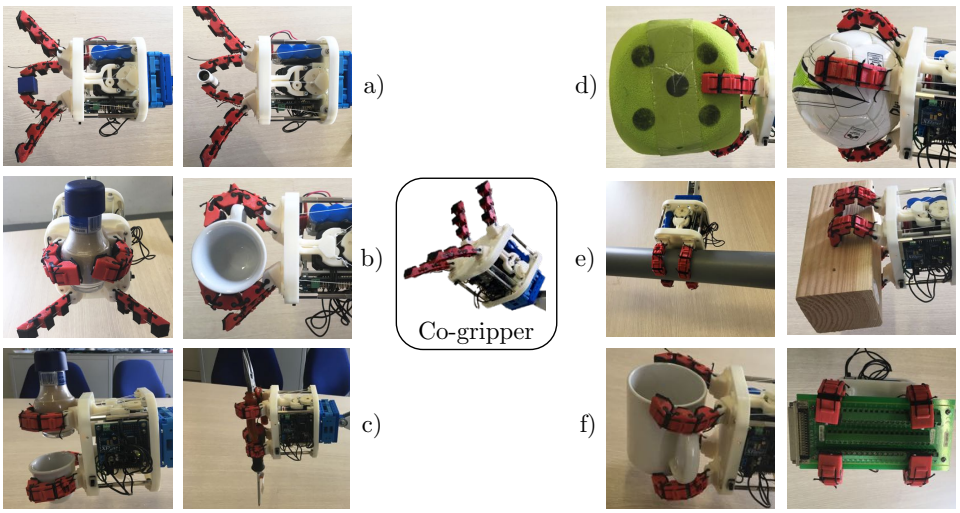

Fig. 4.6 Possible grasps achieved with the Co-Gripper. a) two fingers in a pinch grasp configuration. b) grasping of small size objects achieved with the two fingers. c) each of the two finger grippers controlled separately so to achieve the grasps of two objects with the same gripper. d) grasp of big size objects achieved with a circular configuration. e) grasps obtained with the perpendicular configuration. f) grasps obtained with the parallel configuration.

from 1 "strongly disagree" to 5 "strongly agree". Items of the SUS are reported in Table 4.4. To calculate the SUS score, it necessary to sum the score contributions from each item. Each item's score contribution ranges from 0 to 4. For items $1, 3, 5, 7$, and 9 the score contribution is the scale position minus 1. For items $2, 4, 6, 8$ and 10, the contribution is 5 minus the scale position. The sum of the scores is then multiplied by 2.5 to obtain the overall value of SU. SUS scores have a range of 0 to 100. The Co-Gripper used together with the ring interface got an average score of 92.25 with a standard deviation of 4.92. This result confirms how the system is easy to use also without specific training. Note that 9 out of 10 subjects chose the circular configuration for the ball, 10 out of 10 chose the pinch grasp gripper for the small cube, 6 out of 10 used the perpendicular configuration both for the pipe and the cup, while the other 4 chose the parallel.

4.1.5 Conclusions

In this work, we presented the design guidelines and a possible device realization of a soft collaborative gripper. Soft-manipulation technology imposes fewer requirements on engineering the environment of the manufacturing facility since the passive adaptation to different object shapes is less demanding for accurate perception. The extended capabilities also lead to a reduced effort in programming the manipulation system. Collaborative grippers inherently address aspects of safety, preparing robotic systems with the ability to forcefully interact with their environment while being safe in proximity to the human. This facilitates the co-manipulation

Table 4.4 Items of the System Usability Scale

I think that I would like to use this system frequently
I found the system unnecessarily complex
I thought the system was easy to use
I think that I would need the support of a technical person to be able to use this system
I found the various functions in this system was well integrated
I thought there was too much inconsistency in this system
I would imagine that most people would learn to use this system very quickly
I found the system very cumbersome to use
I felt very confident using the system
I needed to learn a lot of things before I could get going with this system

applications making the soft-grippers ideal candidates for a possible technology transfer to the industry.

We are currently working on the gripper interface so to display to the user the grasp force measured on the gripper. We are also testing novel possible finger configurations so to enhance the possible gripper dexterity.

4.2 Bilateral Haptic Collaboration for Human-Robot Cooperative Tasks

This work aims to introduce the concept of bilateral haptic cooperation as a novel paradigm for human-robot cooperative tasks. The approach is demonstrated with a system composed of a soft gripper and a wearable interface. The soft gripper, called CoGripper, has been designed to guarantee a safe interaction giving the possibility to the operator to reconfigure the device according to the object to be grasped. The wearable interface is used to control the open/close motion of the gripper and to feedback information about important task parameters, e.g., the grasp tightness. The result is a bilateral haptic collaboration where humans and robots bidirectionally communicate through the interface. The user interaction with the system is extremely intuitive and simple. We performed three user studies to prove the effectiveness of bilateral haptic collaboration involving ten subjects. Results confirmed that the use of the wearable interface reduces the time to accomplish a cooperative task and enables better control of the grasp tightness.

4.2.1 Introduction

Automation of production processes has revolutionized manufacturing over the last fifty years. However, there are still many manufacturing tasks that are tedious or strenuous for humans to perform. Some of these tasks are difficult to automate because they require robots and workers to collaborate in close proximity and adapt to each other's decisions and motions [141]. Rather than fully automating such tasks (which may not be possible and/or cost-effective), human-robot collaboration may enable safe and effective task execution, while reducing tedium and strain of the human. Collaborative robots, also called cobots, have been thus designed to share the same workspace with a human operator [142]. This has led to a novel generation of robotic arms that can safely interact with a user. Remarkable examples of these commercially available robots are the Panda (FRANKA EMIKA, Germany), the LBR iiwa (KUKA, Germany), and the Sawyer (Rethink Robotics, USA). A unifying concept among these robots is the capability to compliantly react to a collision, as opposed to the stiff behavior of classical industrial robots. More recently also collaborative robot end-effectors have been proposed since, most of the time, these are the parts of the robot that interact with the human partner. In [143], we introduced design guidelines for soft cooperative grippers and we proposed a preliminary version of a cooperative gripper that we called CoGripper. Also, few commercial products are designed for collaborative robotics, see e.g., the Schunk Co-Act Gripper [124] and the RG6 Collaborative Gripper [125].

However, to achieve effective collaboration, the robots should not only be safe and respond to a human command but should also be able to communicate with the human collaborator, as this is an important feature for human dyads [144]. The way humans and robots communicate is an important issue to solve when designing a human-robot collaborative architecture [144]. Among the possible solutions available in the literature, we do believe that the sense of touch can be the primary channel of communication between the worker and his/her artificial mate. One of the main reasons to support this choice is the robustness of the sense of touch. Such

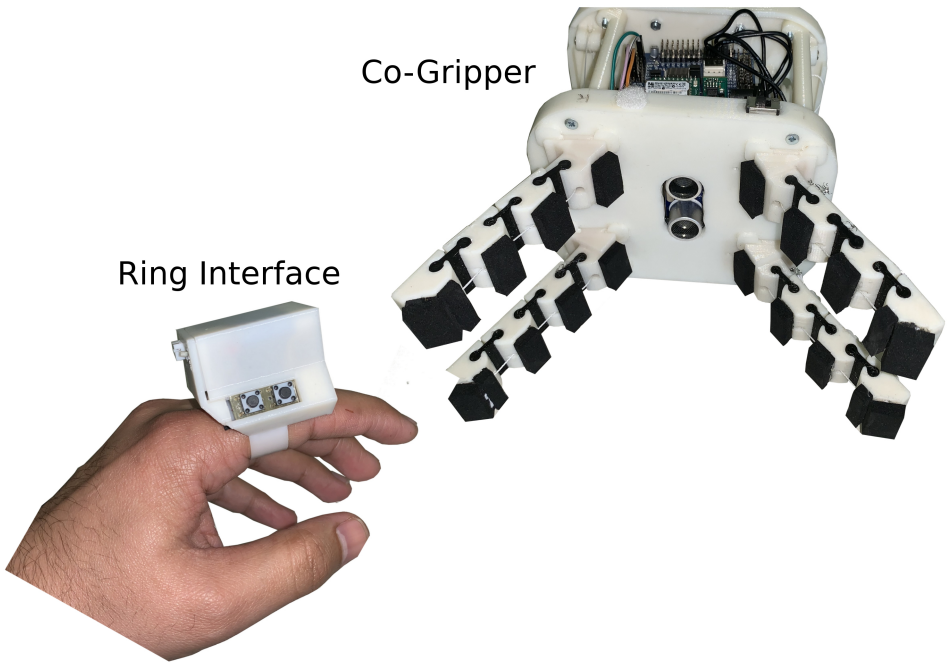

Fig. 4.7 The CoGripper and its ring-shaped interface. The ring provides vibrotactile haptic feedback about the grasp information coming from the gripper.

robustness comes from the full distribution on the human body of the skin, the organ where the receptors of touch reside, that consents to position an interface in different parts of the body leaving free the other important organs (e.g., ears and eyes) for the task execution. This aspect may be of particular interest in a factory scenario where acoustic communication may be impaired by personal protective equipment whereas visual displays may not always be on the field of view of the worker during different task execution phases. Recent results on wearable haptics [138, 145], have strongly reduced the form factor of haptic displays making it possible to wear it on hand.

First attempts to let the robot communicate with the human companion through haptics are available in the literature. For instance, Casalino et al. presented in [146] a wearable vibrotactile device used to improve the operator awareness during a human-robot collaborative assembly task. A vibration acknowledged to the operator that the robotic system had predicted over certain confidence the next action of the operator. In [147], wireless vibrotactile displays were designed to inform the operator about excessive overloading of body joints and to suggest a more ergonomic posture. In both these examples, the haptic interfaces are used to inform the human that the robotic system detected a certain behavior of its collaborator. The concept of bilateral haptic collaboration introduced in this work goes beyond the simple communication of intention or posture detection. The interface we propose can be used both to control the robotic gripper motion and to haptically display information related to the tasks that are measured by the robot. As a paradigmatic example, we propose the collaborative gripper system reported in Fig. 4.7. A ring-shaped interface can be used to control the open/close motion of a collaborative

gripper through two embedded switches. The ring embeds also a vibrotactile motor that can be used to feedback information about the cooperative task execution, e.g., the grasp tightness measured by the gripper. In [148], we introduced the idea of a vibrating ring for the interaction with a wearable assistive device designed for stroke patients. Differently from [148], in this work we use the ring-shaped interface both for the control of the open/close motion of a gripper and for the communication of important tasks related parameters, e.g. grasp tightness and acknowledge of a gripper status.

We conducted three user studies to investigate the possible usage of the system in human-robot cooperative tasks. In the first, we evaluated whether the presence of haptic feedback from the gripper would reduce the time to complete a collaborative hand-over task and better regulate the grasp tightness. In the second study, we evaluated the perceived system usability when the interface is used to display task information. We consider the case where the gripper can autonomously detect the presence of an object through a proximity sensor embedded in its palm and the ring interface is used to display the acknowledge of a gripper status, i.e., of the start of the closing motion and the reaching of a predefined level of grasp tightness. Finally, in the third example, we compared in terms of completion time the usage of the ring interface with the usage of a button interface at the end-effector for a mockup of a human-robot collaborative task.

The rest of the work is organized as follows. In Section 4.2.2 the collaborative gripper system is described in detail. In Section 4.2.3 the three user studies and their relative results are reported. Section 4.2.4 reports a discussion on the possible use of bilateral haptic collaboration, whereas in Section 4.2.5 conclusion and future work are outlined.

4.2.2 The Collaborative Gripper system

In this section, we briefly recall the main features of the CoGripper and we introduce a novel wireless ring-shaped interface that is used to control the gripper and to display vibrotactile feedback. With respect to its preliminary version, the novel gripper includes a proximity sensor (sonar) located on the palm to detect the presence of an object in the gripper workspace. The novel wearable interface is a completely redesigned ring-shaped device, which embeds a vibrotactile motor that enables bilateral haptic collaboration. A Bluetooth communication protocol between the interface and the gripper allows a bilateral data flow.

4.2.2.1 The CoGripper

The CoGripper is a soft tendon-driven modular gripper that has been designed following the guidelines reported in [143]. Exploiting compliance with underactuated soft hands is an active research branch for the design of novel robotic end-effectors that has led to interesting solutions and prototypes, like the Pisa-IIT hand [4] and the SDM hand [26].

The CoGripper has four soft fingers, each made up of soft and rigid modules, connected to a palm. The CAD model of the gripper is shown in Fig. 4.8, whereas the 3D printed prototype is reported in Fig. 4.7. Each finger has a modular structure where each module consists of a rigid 3D printed link realized in ABS (Acrylonitrile Butadiene Styrene, ABSPlus, Stratasys, USA) and a 3D printed thermoplastic polyurethane part (Lulzbot, USA) that acts as the flexible

joint. Following the approach presented in [126], it is possible to regulate the stiffness of the flexible joints to achieve the desired closing trajectory for each finger. In [143], we regulated the stiffness to obtain different behaviors for the two pairs of fingers in the gripper. In this version, all four fingers have the same closing trajectory designed for power grasps. A tendon-driven approach is used to actuate the fingers. Two Dynamixels MX-28T (Robotis, South Korea) are used for the actuation. Each motor moves a pair of fingers. A differential mechanism [139] is embedded on the gripper base to adapt fingers' configurations to the specific geometric features of the grasped object. All the fingers can be manually rotated to any configuration. The Arbotix-M controller (Robotis, South Korea) is used to control the Dynamixel actuators of the soft gripper.

We have added an ultrasonic (HC-SR04) sensor module in the middle of the palm in the version of the CoGripper proposed in this work, see Fig. 4.8. The sonar sensor provides a detection range from 2 to 40 cm. The sensor exploits the concept of ultrasonic waves. The transmitter sends a burst of ultrasonic waves. When the waves encounter an object these are reflected and received by the receiver. The receiver converts the ultrasonic waves into an electrical signal to be read by the main controller. The distance is calculated by measuring the time difference between sending a signal and receiving its echo. The sensor can detect when an object enters a predefined grasping area and can provide this information to the main controller triggering the closure of the gripper.

The main technical features of the CoGripper and its actuation system as well as an experimental evaluation of the payload and the maximum horizontal resistive force are detailed in [143].

4.2.2.2 The wearable ring-shaped interface

The control interface of the CoGripper is a ring-shaped device, whose CAD exploded view is shown in Fig. 4.9. The proposed prototype is shown in Fig. 4.7. The ring configuration has been chosen to obtain an interface highly wearable and portable [148]. The user wears the remote ring on the index finger. The position of the buttons allows using the interface simply moving the thumb. Although the ring is realized in ABS material, the thickness of the ring shape is chosen to provide enough flexibility to fit on different finger sizes. The remote ring consists of a very compact structure containing all the electronics. It has two push-buttons currently being used to control the gripper. The ring controller (ATtiny45) receives the activation signals from the push-buttons and wirelessly transmits them to the actuator main controller, which in turn controls the motion of the gripper according to the "high level" control strategies summarised in Table 4.5. Bluetooth (RN42-i/RM) module is used to transmit and receive all the relevant information. A coin type shaft-less vibratory motor (Precision drive, USA) with a diameter of 10 mm is installed in the ring for tactile feedback. A reduced dimensions Li-Ion 3.7 V rechargeable battery is used to power up the remote ring.

4.2.2.3 High-level control

The soft gripper can be operated in two different modes both actuating all four fingers. In the first mode, called *ring-controlled mode*, the remote ring is used to control the activation of the

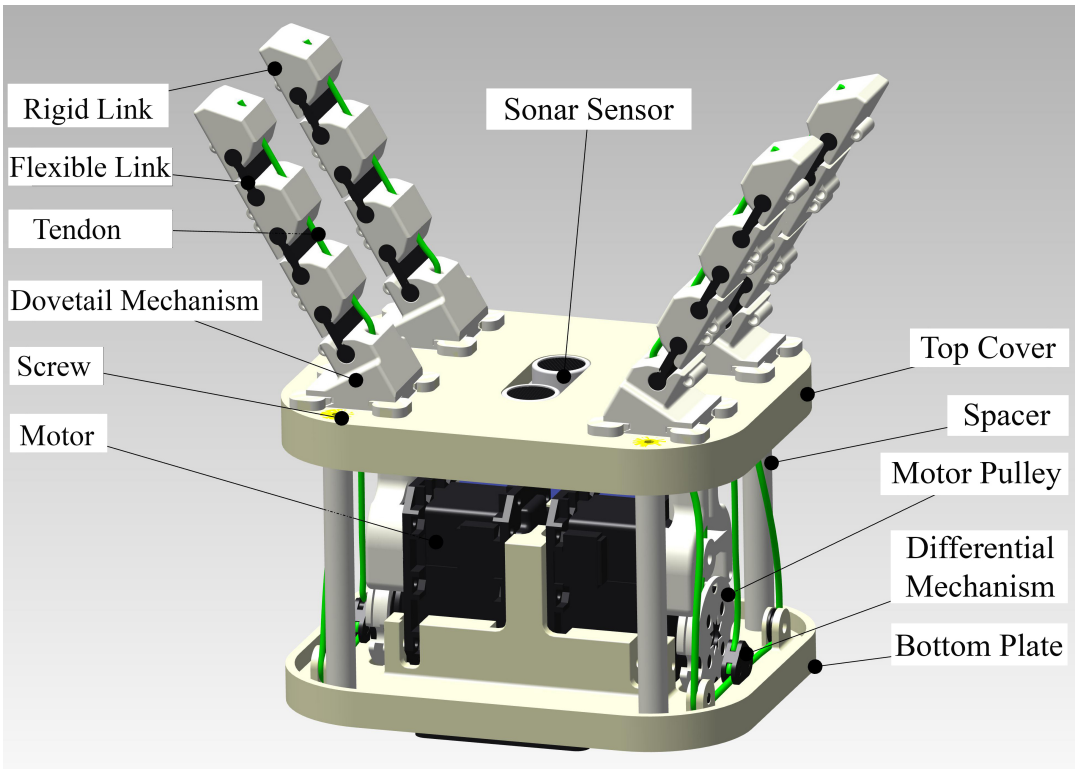

Fig. 4.8 The CoGripper: A wireless underactuated "tendon-driven" gripper with four flexible fingers. Modules can be assembled with different stiffness values at flexible joint level, obtained changing 3D-printer parameters during manufacturing.

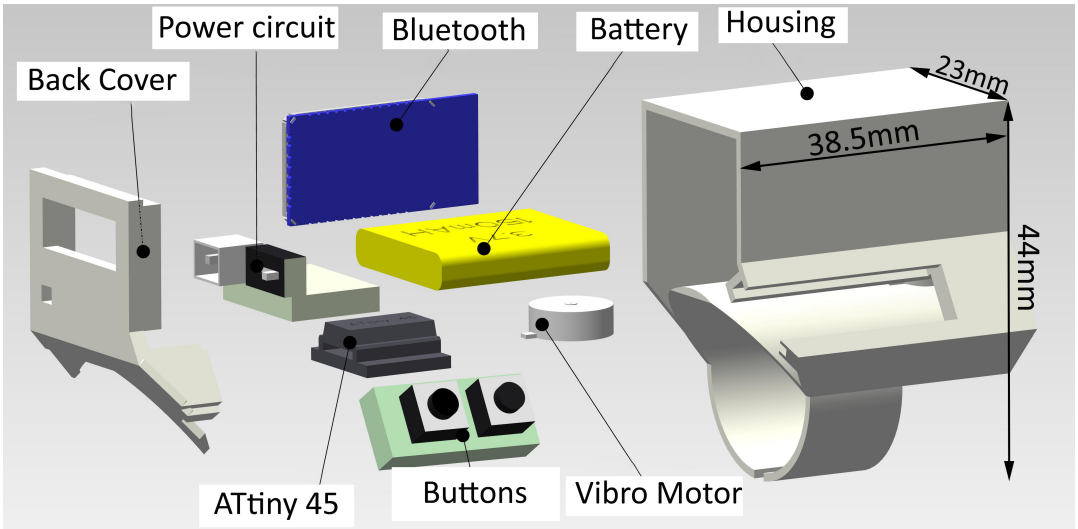

Fig. 4.9 CAD exploded view of the remote ring interface for the CoGripper.

gripper. The user pushes a button to activate the flexion of the gripper. When the flexion motion is initiated the gripper starts to close by increasing the torque of the actuators. The user can stop the closure of the fingers at any moment by pressing the same push-button again. Once

contact is detected thanks to the torque sensors available in the servomotors, the remote ring provides vibrotactile feedback to the user, proportional to the force exerted on the object.

To relate the variation of a signal to the variation of vibration there are several techniques mostly focusing on the modulation of amplitude or frequency of the generated vibration [145]. Considering the vibrating motor installed in the ring, we decided to generate different perceivable levels of vibrations by regulating the frequency of consecutive active vibrations. The feedback consists of a train of vibratory bursts whose frequency increases proportionally to the increase of the measured torque at motors. Controlling the time of vibration and the time between two consecutive vibrations, it is possible to generate different patterns of stimuli that can be perceived by the user, as demonstrated in Sec 4.2.2.4. extension of the gripper's finger is activated. The extension of the fingers can be activated with a single click of the second push-button.

The gripper can also work in the *self-closing mode*. In this modality, the sonar sensor in the palm is used to trigger the closing motion. When the object enters the predefined graspable area defined in the workspace of the fingers of the gripper, a single burst of vibration (1 s) is displayed to the user through the ring interface. This alerts the user that the gripper is automatically initiating fingers' flexion. When the motor torques reach a predefined threshold, the gripper automatically stops the closing motion and a longer vibration (2 s) is provided to the user. The extension of the gripper's fingers can be triggered by the push button.

In self-closing mode, the vibrotactile feedback is used to alert the user about the current state of the gripper, whereas in ring-controlled mode the vibrotactile feedback is used to display the tightness of the obtained grasp. Note that, when using the self-closing mode, it is possible to disable the sonar detection by simultaneously pressing both buttons for more than 2 sec. This option can be used for finger reconfiguration. When the sonar is disabled, the user can re-orient the fingers in different configurations according to the size and shape of the object without triggering the closure of the fingers. It is possible to switch from ring-controlled mode to self controlled mode by simultaneously pressing both push-buttons installed on the ring interface for a duration lasting less than 1.5 sec.

Note that these two modalities represent a subset of all the possible controllers that can be implemented with the CoGripper system. In general, it is possible to define a finite state machine with different gripper states and navigate through the machine states using a button or a combination of the buttons.

4.2.2.4 Perceptual thresholds for the vibrating ring

We ran three experiments to understand how to drive the vibrotactile ring to evoke the most effective cutaneous sensations. This preliminary study is necessary to correctly model the vibration feedback proportionally to the torque/force exerted on the object by the actuators installed on the gripper. The motor we use is a shaft-less vibrotactile motor. In this type of motor, it is not possible to separately control the amplitude and the frequency of vibration. For this reason, we decided to generate a signal where the pulse frequency can be modulated. For pulse frequency we mean that is possible to turn off and on the vibrating motor for a certain period to produce a different type of stimuli. By regulating the length of this period we regulate the pulse frequency. The vibration intensity was fixed at 50% of the maximum PWM intensity,

Table 4.5 High-level control of the system

Control mode	Fingers' motion	Type of feedback
Ring-controlled		
Right PB, single trigger	flexion/stop	vibration proportional to measured motor torque
Left PB, single trigger	extension	no feedback
Self-close mode		
Sonar detection	flexion	vibration burst on flexion starting and when motor torque reaches a predefined threshold
Left PB, single trigger	extension	no feedback

that corresponds to the starting voltage of the vibration motor. Subjects were required to wear the vibrotactile ring on their left or right index proximal phalanx. Moreover, to avoid any additional cues, subjects were blindfolded and wore noise-canceling headphones.

Absolute thresholds Absolute threshold provides us information about the smallest stimulus length of the vibration that can provide a perceivable sensation to the user. An experimental setup involving ten subjects (five female, average age 34.3) was carried out. The subjects were asked to wear the ring on their non dominant hand index finger and tell the experimenter when they were perceiving a single vibration. The absolute threshold was evaluated using an up-down approach as defined in [149]. The starting stimulus duration was 100 ms. At every reversal, the stimulus duration was reduced by a step size whose duration started from 16 ms and was reduced by half every reversal. We considered the task completed when five reversals occurred. Each subject was asked to repeat the experiment five times. The mean value of minimum stimulus duration required to produce a perceivable perception was recorded to be 40 ms. Below this value, the users were not able to perceive any vibration.

Differential thresholds For the case of the differential threshold, the same up-down approach was followed. The experimental setup was similar to the absolute threshold with vibration intensity fixed at 50 percent of the maximum PWM intensity. In this case, the subjects were asked to report when they perceived two distinct vibrations. This is important in our application since we modulate pulse frequency. If the user perceives the train of vibration burst as a single vibration, he/she cannot recognize a variation of the stimulus. Again a step size of 16 ms was used with half on every reversal, upon five reversals the task was considered completed. The mean value evaluated was 100 ms. This value tells us that if the stimulus length is less than 100 ms the user perceives a single vibration rather than perceiving two distinct vibrations.

To demonstrate that more precise regulation of grasping tightness can be achieved by using vibratory feedback, we carried out an experiment where the participant was provided with three

(a) (b)

Fig. 4.10 User study on ring-controlled mode. (a) shows how objects were hand over to the gripper. The thumb of the left hand is used to control the gripper. (b) The five objects used for the study. From the left: a cleaner bottle ($\sim$ 1 kg), a chips tube ($\sim$ 200 g), a coffee jar ($\sim$ 400 g), a mustard bottle ($\sim$ 600 g) and a wood block ($\sim$ 800 g).

different level of stimulus intensity: weak (pulse period 3 Hz), medium (pulse period 6 Hz), and strong (pulse period 10 Hz). Each participant tested five stimuli for each intensity level. The stimuli were provided randomly and the participants were asked to differentiate between different stimuli. Prior to the experiments each participant was trained for three raw trials and was provided with the necessary information. Upon receiving the vibratory feedback the participant has to announce two things: if there was feedback or not and if there was feedback, whether it was weak, medium or strong. The total number of stimuli was fifty in each case. Out of 50 stimuli, the successful perception of weak, medium and strong stimuli was 86%, 88% and 96% respectively as shown in Fig. 4.11.

4.2.3 User studies

The main goal of this work is to introduce the concept of bilateral haptic cooperation as a novel paradigm for human-robot cooperative tasks. The wearable haptic interface plays a major role since it allows both to control the gripper and to perceive robot action through vibrotactile feedback. We conducted a user study involving ten subjects (four females, average age of 28.3 years) to prove the effectiveness of bilateral haptic cooperation. All participants were students or employees of the University of Siena and participated voluntarily. At the beginning of the experiment, all participants gave informed consent where the potential risks during the experiment were mentioned. The study was approved by our departmental Ethical Committee. All participants were naive to the specific design of the study focusing on the influence of haptic feedback modalities on cooperative tasks. In the following, we describe the three user studies and we report the results.

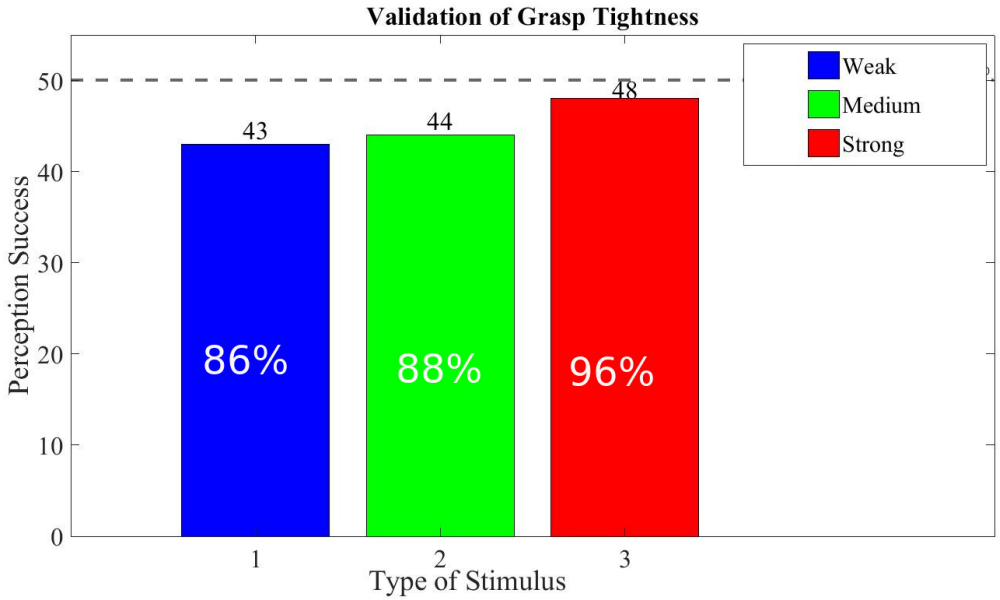

Fig. 4.11 Perception of weak, medium of strong vibration feedback. Number on the top of the columns report the success answers of the participant of a total of 50 trials.

The first study focuses on controlling the gripper using the wearable ring while being provided with continuous feedback about the grasp tightness. The second study focuses on the possibility of using the ring to display information about the gripper status when the self-closing mode is activated. In the third study, we considered a mockup of a human-robot collaborative task, where the robot picks an object, moves it to a location where the user performs an operation on the object, and eventually leaves the object in a predefined position. The user study is based on evaluating the completion time using the wearable ring compared to buttons at the robot arm end-effector.

4.2.3.1 Ring-Controlled mode and grasp tightness feedback

The goal of this study is to test whether a feedback signal proportional to the force exerted by the gripper on the grasped object can improve the gripper usage. To this aim, the user perceives a vibration on the ring interface that is proportional to the torque exerted by the servomotors. The open/close motion of the gripper is controlled by the user through the two buttons available in the ring. The right button is used for finger flexion and the left button is used for the extension of the fingers, see Table 4.5. It is possible to stop the motion by pressing again the same button. All four fingers are actuated at the same time. The torque is measured through the control board of the servomotors. The average torque between the two motors is computed and then mapped into a value of pulse frequency (period of active vibration) for the Vibro motor and sent to the interface via Bluetooth. According to the results reported in Sec. 4.2.2, the torque values are mapped into a range of pulse frequency going from 2 to 10 Hz.

The participant tested the interface to get familiar with the controller and the feedback for a total of five minutes before the starting of the experiment. After this testing period, the

participants were asked to hand over five objects to the CoGripper. The CoGripper was fixed to passive support, see Fig. 4.10-(a). The five objects were selected among those available on the YCB set [83] and are shown in Fig 4.26-(b). The objects were chosen to have different weights ranging from about 200 g of the chips tube to the kilogram of the cleaner bottle. Participants were instructed to use the ring to start the closing motion and to stop the motion as soon as they felt confident about grasp stability. The closing velocity of the motors was set to 8 mm/s to provide enough time for the user to recognize a torque variation. For each object, the hand over task was repeated six times. Haptic feedback was randomly provided for half of the time. In total, each subject performed 30 hand over grasps, 15 of them being provided with the haptic feedback. We compared the torque reached by the motors for each object with and without the force feedback. Results are reported in Fig. 4.12. As expected, for lighter objects less torque was commanded to execute the grasps. For all the objects, the torque commanded when the vibrotactile feedback was activated resulted lower. A paired T-test analysis [150] revealed a statistically significant difference between the average torques obtained with tactile feedback and with no feedback condition ($p < 0.001$) for each object.

We also considered the time to achieve every single grasp. As the user initiates the closing motion of the gripper, a timer was activated and run until the motion of the gripper was stopped. Average completion times for each object are reported in Fig. 4.13. Lighter objects were grasped more quickly since they required less torque to be firmly grasped. A paired T-test analysis revealed a statistically significant difference between the average time needed to grasp an object when tactile feedback was activated with respect to the no feedback condition ($p < 0.001$) for each object.

4.2.3.2 Self-closing mode and haptic communication of gripper status

The goal of the second experiment is to show the possibility of using the ring interface as a means to inform the user about relevant task parameters. We considered the CoGripper controlled using the self-closing mode (see Table 4.5). In this control mode, the gripper autonomously detects the presence of an object in its workspace and starts to close the fingers. The flexion of the fingers is automatically activated when the object is detected through the sonar sensor at a distance of 3 cm from the palm. The user may not be sure about the correct distance for activating the closure or may not be sure about a correct object detection by the sonar sensor. To help the user understand the gripper status, a vibration burst lasting for 1 s is generated at the ring side at the starting of the fingers' flexion. Grasp tightness is another parameter that could be difficult to visually understand in this control mode since the gripper keeps closing until motor torques reach a predefined value (2 Nm in our experiment). For this reason, once the torque limit is reached, a vibration lasting for 2 s is provided to the user through the wearable interface and the user can safely leave the object.

We asked the participants to perform five hands over grasps of the coffee jar using the system. Then, we asked the participants to answer the ten questions of the system usability scale (SUS) [140] to evaluate the utility of the feedback in the proposed task. The SUS is used to evaluate the subjective assessments of usability. SUS yields a single number that represents a composite measure of the overall usability of the system being studied. It is a Likert scale where it is possible to answer each item with a mark ranging from 1 "strongly disagree" to 5

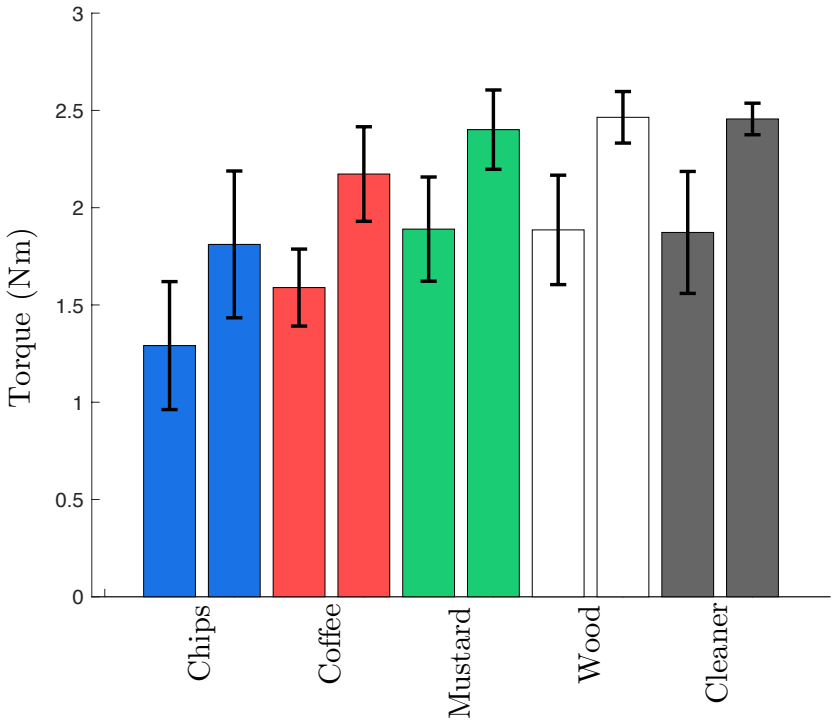

Fig. 4.12 Motor torque. Means and standard deviations of the commanded motor torque are plotted for the two conditions (feedback of the grasp tightness and no feedback) for the five considered objects. The first bar for all objects shows feedback and the second one is without feedback

"strongly agree". Items of the SUS are reported in Table 4.6. SUS scores range from 0 to 100, where 0 means awful and 100 represents excellent. A SUS score above 68 is considered above average. Details on how to compute the final mark can be found in [140]. The bilateral haptic collaborative system got an average score of 97.25 with a standard deviation of 4.15.

4.2.3.3 Mockup of a human-robot collaborative task

The goal of the third study was to prove the potential of bilateral haptic communication in a mockup of a human-robot collaborative task involving a collaborative manipulator, the Sawyer arm (Rethink Robotics, USA). We tested two possible scenarios. In one case, the interface was worn on the hand in its ring position allowing also the possibility of haptic feedback. In the other case, the interface was placed next to the end-effector to resemble the location of the button already available in the robotic arm for the control of the standard Sawyer gripper. The task was separated in three main phases: *i)* object grasping, *ii)* human operation and *iii)* object deposit, see Fig. 4.14. In the first phase, the CoGripper approached the object, a 2 cm diameter pipe, in a predefined location. The self-closing mode was used and the CoGripper started to close once the object was close enough to the palm. Note that with the ring interface

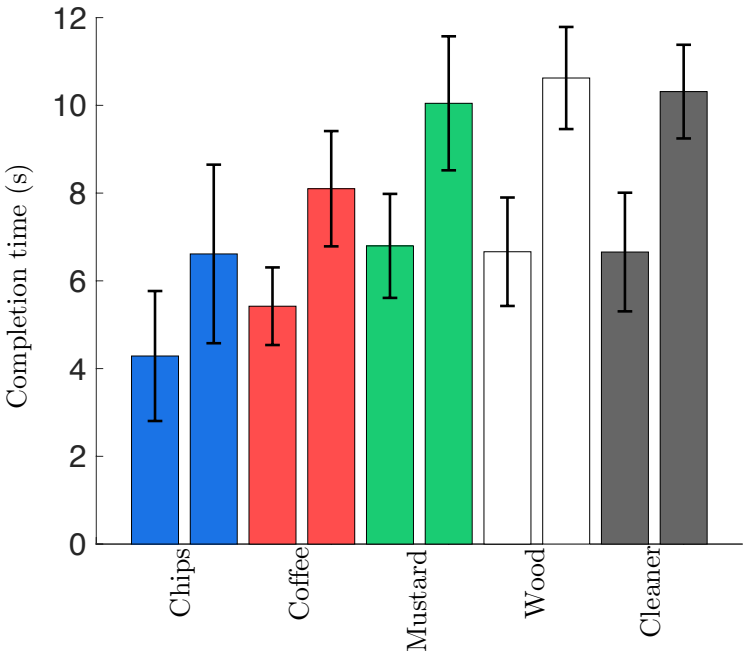

Fig. 4.13 Completion time. Means and standard deviations are plotted for the two considered conditions (feedback of the grasp tightness and no feedback) for the five considered objects. The first bar for all objects shows feedback and the second one is without feedback

Table 4.6 Items of the System Usability Scale

I think that I would like to use this system frequently
I found the system unnecessarily complex
I thought the system was easy to use
I think that I would need the support of a technical person to be able to use this system
I found the various functions in this system was well integrated
I thought there was too much inconsistency in this system
I would imagine that most people would learn to use this system very quickly
I found the system very cumbersome to use
I felt very confident using the system
I needed to learn a lot of things before I could get going with this system

it would have been possible to remotely control the grasp whereas it would not be possible to

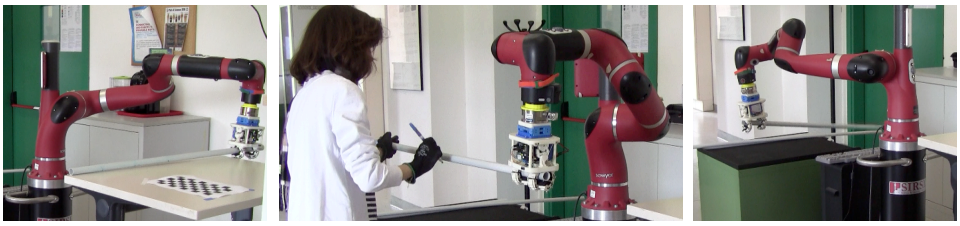

Fig. 4.14 Collaborative task. On the left side, the first phase of the task when the robot autonomously grasps the pipe. In the center, the second phase when the human operator draws the three circles on the pipe. On the right side, the last phase where the object is deposited.

press the button on the arm due to the table. The robot grasped the pipe and moved toward the human operator. In phase two, the operator had to draw three circles around the pipe, in correspondence of three marked dots, see Fig. 4.15. Drawing circles is representative of possible manual processing on the object. The three semicircles on the upper part of the pipe can be drawn starting from the object configuration at the beginning of phase *ii*. To complete the circles, the object has to be rotated by roughly 180 degrees to show what previously was the bottom part and allow the operator to finish the circle drawing. The operator had to open the CoGripper using one button on the interface and reposition the pipe close to the palm to activate the self-closing procedure and thus complete the pipe rotation.

Once the three circles were completed, the participant pressed one button on the interface and activated the next phase. In phase three, the robot arm waited 10 seconds in the initial position to allow the paint to dry and then moved toward the final deposit position. Once the robot reached the final position, the operator opened the CoGripper using the interface. Screenshots of the three phases are reported in Fig. 4.14. In Fig. 4.15, we report two interesting particulars of the task execution. On the left side, it is reported the configuration of the CoGripper fingers used for grasping the pipe. This orientation of the fingers allows to grasp relatively small diameter pipes and was easily achievable thanks to the reconfiguration capabilities of the CoGripper. On the center, we report the operator's hand while performing the second phase. When the interface is worn as a ring, it is possible to activate the gripper keeping the object grasped. The position of the button on the ring can be easily accessible with the thumb and leave the possibility to keep the object with the remaining part of the hand.

Each task was repeated five times. We evaluated the time to complete all the three phases for the two proposed scenarios, ring-worn interface, and buttons at the end-effector. Results are reported in Fig. 4.16. The task was completed with an average time of 57.8 s and 66.4 s using the ring and the button at the end-effector, respectively. A paired T-test analysis revealed a statistically significant difference ($p < 0.01$) between the average time needed to complete the task using the ring interface and the button at the end-effector interface.

4.2.4 Discussion

Bilateral haptic collaboration is a novel concept that indicates the possibility of bidirectional communication between the human and robot through the sense of touch. In this work, this concept is introduced considering a collaborative grasping system that consists of a collaborative

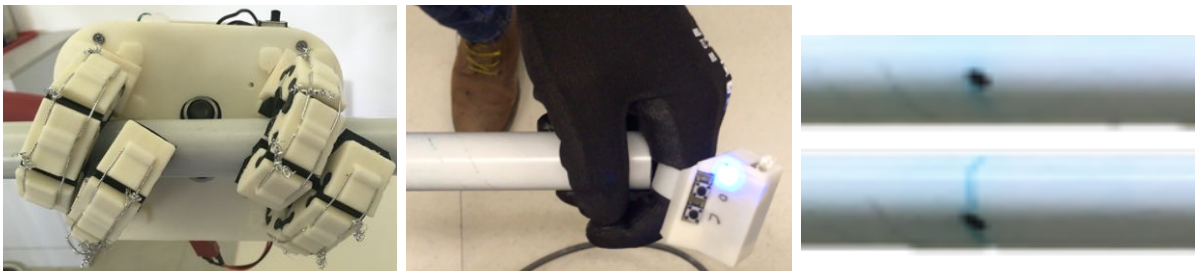

Fig. 4.15 Particulars of the collaborative task. On the left side, how the object is grasped using the reconfigurability of the fingers. On the center, the hand of the human operator together with the ring interface is shown. On the right hand side, the pipe before (up) and after (down) the operator drawing.

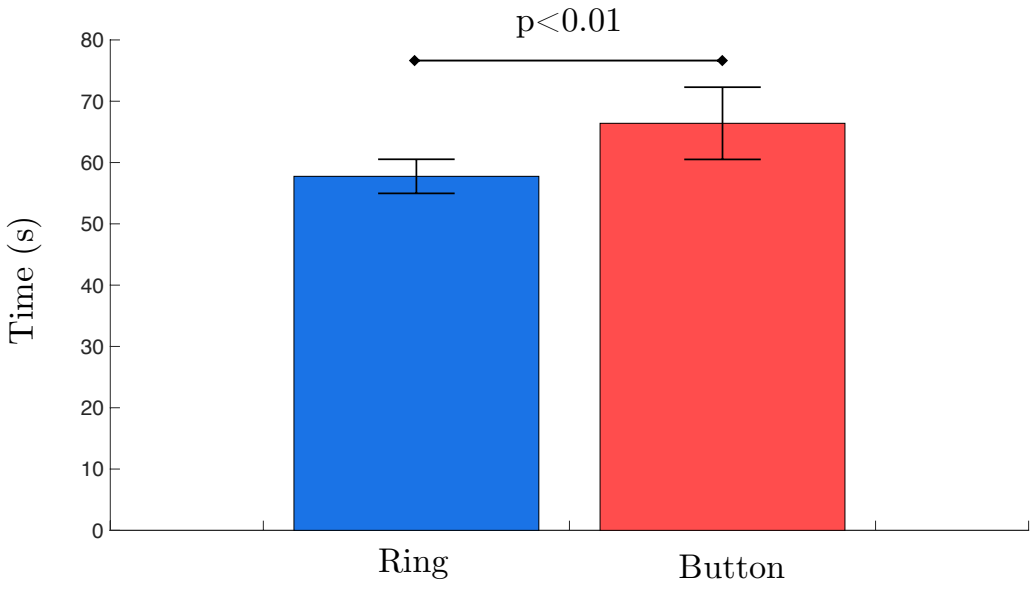

Fig. 4.16 Completion time. The blue column represents the average time needed when using the ring interface, whereas the red column represents the average time used to complete the task using the button interface at the end-effector.

gripper and a ring-shaped interface. We do believe there is a broad class of cooperative tasks that may benefit from the proposed system. For instance, the wearability of the interface allows to hold the object with both hands during hand over, a feature that may result important for long objects or fragile objects as it was showed in Sec. 4.2.3. The feedback of the grasp tightness is intuitively important when fragile objects are manipulated. However, as we demonstrated in Sec. 4.2.3, information about the grasp tightness reduces the time to fulfill a handover task and reduce also the necessary torque. Using less torque, and in general, more efficient control of the motor torque is beneficial beyond the manipulation of the fragile object. A reduction of torque results also in a reduction of battery consumption that may be an important issue when using the CoGripper with passive supports since only batteries are used as a power supply.

The use of the interface as a means for acknowledging gripper status has been also very positively evaluated by the participants as demonstrated by the high value of the SUS. The need for awareness in human-robot interaction is a well know concept in the literature [151]. Solutions based on visual or acoustic signals [152, 153] may not be the preferable solutions in industrial scenarios where auditory and visual modalities might be not available to accomplish a task since the human is focusing his view on finding and picking objects or may be impaired due to personal protective equipment, e.g., a worker wearing noise canceling headphones. Our proposed solution resulted in efficient, simple, and intuitive to use. The possibility of feedback continuous signals as the grasp tightness measured while grasping and also discrete events such as the reaching of a torque threshold is a unique feature of the proposed vibrotactile ring.

Observing users testing our system, we also collected interesting information about the limitations of the current setup. For instance, some users needed to look at the interface before pressing the correct button (left or right). Although this may be solved after a period of training, this distraction may reduce the effectiveness of the system. Two female participants with relatively small hands needed additional foam parts to better fit the ring at the index finger. In the long term, the interface could be directly integrated into a glove to reduce possible fit and wearing problems. At the moment, if a gripper reconfiguration is needed, the user has to leave the object, re-arrange the finger orientation and then take again the object and perform the handover. If finger reconfiguration could be directly controlled with the ring interface acting on dedicated motors on the CoGripper there would not be any necessity to leave the object.

It is also worth observing that the evaluation of the effectiveness of the communication between robots and humans is still at the beginning and no standard guidelines are available at the moment. Different cooperative tasks may present different results, as well as different working conditions, which may influence the reliability of tactile feedback. However, we do believe that the results reported in this work are the first step toward the study of a possible bilateral communication in cooperative tasks where haptics may play a central role.

In the proposed application to collaborative tasks, the possibility of sending haptic signals to the operator could also be exploited to optimize productivity. As an example, the operator could use machine working time (e.g., in the proposed experiment the time need for the paint to dry) to perform another task. When needed, the operator could be alerted with a vibrotactile signal to come back closer to the robot arm. Using tactile signals, it is not necessary to have eye contact with the robot arm, and thus the operator could concentrate on the parallel task. Moreover, wearing the interface reduces the total movements of the operator that can control open/close motion just using the thumb as shown in the completion time reduction reported in Sec. 4.2.3.

4.2.5 Conclusions

This work introduces the concept of bilateral haptic collaboration. A novel system including a CoGripper having a sonar sensor to detect the proximity of the object and a new remote ring-shaped interface embedded with a vibrotactile motor are presented as a testing system for a user study involving ten subjects. This work sheds light on the importance of bilateral communication between the worker and the collaborative robot. We carried out three different

user studies emphasizing the importance of haptic feedback during human-robot collaboration. The user is provided with continuous as well as discrete vibration feedback pertaining to the gripping force and state of the gripper respectively. This novel interface is a first step towards bridging the communication gap between humans and robots.

The proposed model of human-robot communication could be exploited by the robotic community to investigate the role of the human and the role of the robot in hybrid dyads. For instance, it will be possible to focus on the way the human can communicate his/her intention to the robot. As an example, it will be possible to study for which tasks it is preferable to explicitly declare an intention to the robot using the switch button and for which tasks it is better that the robot implicitly understands the human intention by using the sonar sensor.

Currently, we are evaluating different kinds of acknowledgment that can be of great importance in a working scenario. Another important feature that we are embedding in the interface is a design of tactile buttons with haptic cues, e.g. different sizes, different roughness *etc.*, for better user recognition. As future work, we are planning to make the re-configuration of the gripper automatic providing the user with ease to reconfigure the gripper using the same remote ring interface.

4.3 Soft Hands with Embodied Constraints: The Soft Scoop-Gripper

The design of robotic grippers requires the accomplishment of several contrasting requirements. Research in under actuated soft hands is a lively topic, with several potentialities and challenges. Soft hands are simple, robust, and able of adapting to the uncertain environment and operative conditions, how ever, their intrinsic compliance and underactuation reduce control capabilities and precision. Recent studies attempted to compensate this limitation by wisely exploiting environmental constraints and considering them as supports to accomplish the task rather than an obstacle to avoid. The development of grasp primitives taking into account environment features led to interesting and encouraging results. In this work, we propose to embed on the hand the positive aspects of studies on environmental constraints exploitation. We present a modular under actuated soft hand in which we added a scoop as a feature of the palm, which simplifies object grasping. The scoop allows to grasp objects in narrow spaces, augments the possible contact areas, allows to obtain more robust grasps, with lower forces. The work illustrates the main design principles, a prototype, and experimental results

4.3.1 Introduction

This work proposes a novel design of a robotic hand with two soft fingers and a flat surface (Fig. 4.17). The concept is much deeper than it appears. The main idea behind is a novel approach to the design of soft hands which includes not only the soft fingers but also the constraints, such as flat surfaces. In soft manipulation, robotic hands are compliant to adapt to the shape of the object to grasp [4, 25, 26]. Soft hands are largely underactuated and do not usually have enough dexterity to execute a precision grasp. Most of the grasps are of power grasp type [19] and the grasp planner is enriched with the exploitation of the environmental constraints to adjust the object position and then grasp it [154]. The environment, such as a planar surface, represents a constraint able to reduce the uncertainties that can be exploited by the robotic hand [155]. This concept is in contrast with classic grasp planning for rigid hands where the environment is treated as a disturbance to avoid. Such enabling constraints are typically considered as part of the environment and to the best of our knowledge, no one proposed to include a constraint, such as a planar surface, into the design of the gripper to grasp an object in combination with the soft fingers. Embodying the constraint in the design of the hand is novel and allows the design of primitives of soft manipulation that are independent of the environmental constraints, at least to a certain extent, since the constraint is available and does not need to be detected in the environment.

The idea is described in Fig. 4.18. On the left, a robotic hand pushes the sphere on the flat surface to constraint it to the corner and then grasp it. On the right, the robotic gripper is designed to embed the constraint in the design of the hand. In this case, the robot hand does not need to exploit the environmental constraints that are already in the design of the hand. Of course, this is one of the many possible primitives that can be designed on a soft hand embodying the constraints.

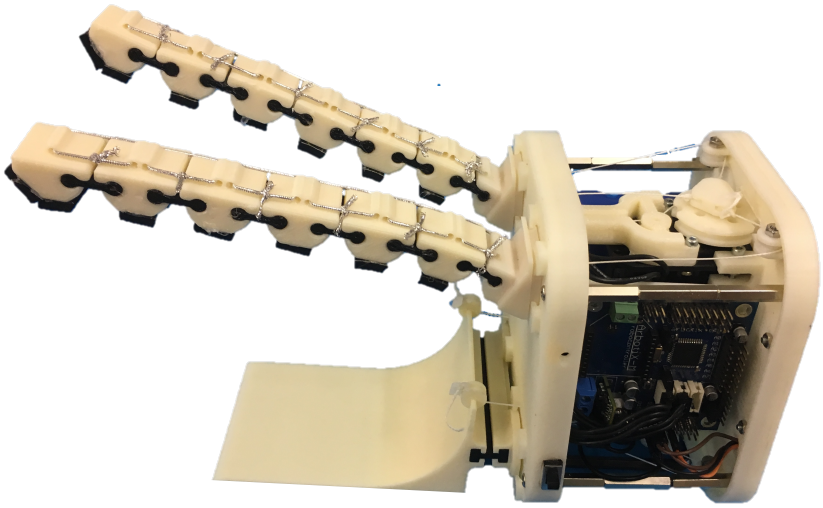

Fig. 4.17 The Soft ScoopGripper

Fig. 4.18 The main idea of soft hands with embodied constratins.

Regarding dexterous in-hand manipulation, one might observe that one of the limitations of including constraints such as a planar surface, might reduce the dexterous manipulation of the robotic hand. This is certainly true, but it is not a limitation in soft robotics. Soft hands are mainly designed to firmly grasp an object more than implementing a dexterous in-hand manipulation [156]. One of the main issues of soft hands, as designed up to now, is that the enabling environmental constraints not always are reachable or detectable by the grasp planning system making difficult to exploit the primitives of grasping developed for soft hands [157].

In this work, we propose to include the environment by design in the robotic hand. The constraint is embedded in the robotic hand. The Soft ScoopGripper is composed of two soft modular fingers actuated by a single tendon through a differential system, similarly to the fingers designed for the gripper proposed in [158]. Flexible joints connect rigid links so to build a deformable structure able to adapt to the shape of the grasped object. The scoop, representing the constraint, is connected through a flexible hinge to the hand palm. This allows to easily adapt the scoop orientation to the surface where it slides. The soft hinge also allows actuating the scoop to move toward the fingers increasing grasp stability as it will be better explained in Sec. 4.3.2. The solution proposed with the Soft Scoop Gripper may outperform classical soft grippers when dealing with uncertain contacts, complex shape, grasping flat object without exploiting edges or flip motion, soft deformable objects, objects that can be damaged, and slippery objects.

4.3.2 Design guidelines for soft hands embedding constraints

This section provides details about the design guidelines of the Soft ScoopGripper. The CAD model of the gripper is shown in Fig. 4.19, whereas the 3D printed prototype is reported in Fig. 4.17. The device consists of two modular fingers and a scoop connected to the gripper wrist by a flexible hinge. Each module of the fingers consists of a rigid part 3D printed using ASA material (Acrylonitrile Styrene Acrylate, Stratasys, USA) and a flexible part 3D printed in thermoplastic polyurethane (Lulzbot, USA). Polyurethane is used for flexible parts considering the high elongation property of this material allowing repeated movement and impact without wear and cracking proving also an excellent vibration reduction. Table 4.7 summarises the main technical features and material/geometric parameters of the ScoopGripper. The rigid and flexible parts of each module are connected by sliding the thermoplastic polyurethane part in the ASA part. This approach enables an easy assembling process by eliminating the use of any kind of fastener or passive elements to link modules. The rigid parts contain holes to allow the passage of a cable (polyethylene Dyneema fiber, Japan) that provides the tendon driven actuation. The actuation of the device is achieved by using two actuators and four tendons running in parallel, each pair of tendons connected to one actuator with two tendons running through the modular fingers and two running through the scoop.

The actuators used are two Dynamixel MX-28T (Robotis, South Korea), each having a maximum torque of 3.1 Nm and a maximum angular speed of 684 deg/s. An Arbotix-M controller (Robotis, South Korea) is used to control the actuators of the ScoopGripper. This control solution for Dynamixel motors incorporates an AVR microcontroller, a socket for a XBee wireless radio, and the motor driver. Each actuator is linked to a differential mechanism [139] to control the motion of both fingers as the bending of the scoop. The differential mechanism plays an important role in the adaptation of fingers' configurations to the specific geometric features of the grasped object. It works in a way that if one of the fingers comes in contact with the object, the other finger can continue its flexion motion. Tendon cables run through the fingers and are attached on one side to the fingertips and on the other to the differential mechanism which in turn is connected with a pulley rigidly attached to the actuator shaft. The actuation of motors results in the winding of the tendon cable on the pulley reducing the length of the wire and producing the closure/flexion of connected fingers. The opening/extension of the fingers and the scoop is achieved thanks to elastic force stored in the flexible parts of the modules.

The two fingers are connected to the palm of the grippers through a dovetail joint that allows complete rotation of the fingers about their axis (perpendicular to the wrist). This feature can be exploited to reconfigure finger orientation according to the object to be grasped. Fig. 4.20 shows possible configurations of the fingers. In the rest of the section, we will explain how the scoop and the finger flexion trajectory can be designed in a soft hand embedding a constraint.

4.3.2.1 Design of the scoop

Hand palm in robotics is an important element since it is the base on which the fingers are connected, but is not often studied from the functional point of view. Typically its main role is to host fingers' actuators and transmission elements and to be the mechanical interface

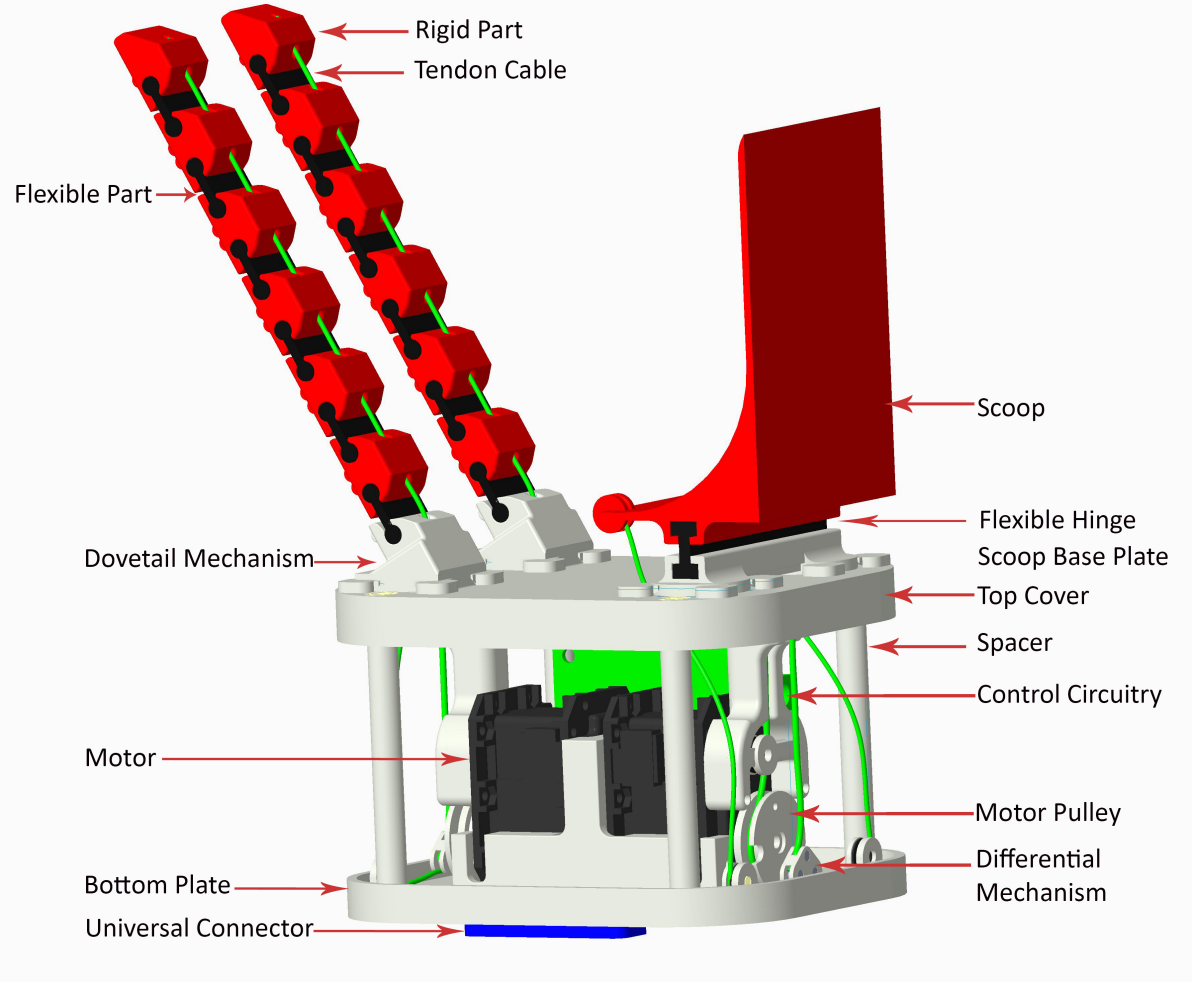

Fig. 4.19 The Soft Scoop Gripper: An underactuated tendon-driven gripper with two flexible fingers composed of six soft-rigid modules each and a scoop. Modules can be assembled with different stiffness values at flexible joint level, obtained through changing 3D-printer parameters during manufacturing.

that connects the hand to the wrist of the robotic hand. Nevertheless, hand palm can provide additional contacts with grasped objects, contributing to overall grasp stability. A clever design of a hand palm could improve hand dexterity and manipulation capabilities. The main difference of the proposed hand with respect to the existing ones is that we integrated the palm with an element, the scoop, that enhance its grasping capabilities.

The scoop is connected to the palm through a joint at his base, so we can reduce its thickness towards the tip to the minimum necessary to realize it and to resist structural solicitation.

According to the modular approach that we have followed in the design of underactuated compliant hands [126], we can connect the scoop to the palm in three different ways. The first one consists of a fixed connection, that locks the scoop on the palm. This connection is the stiffest and more robust and is suitable when the hand has to lift weight objects, or when precise positioning is necessary. In the second solution, the scoop is connected to the palm with

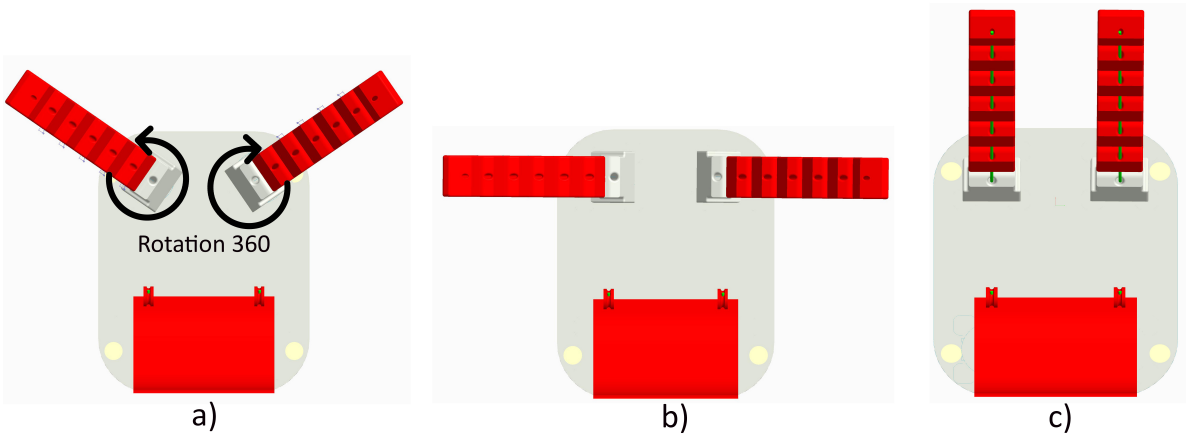

Fig. 4.20 Possible configurations of fingers achieved acting of the dovetail joint at fingers' bases.

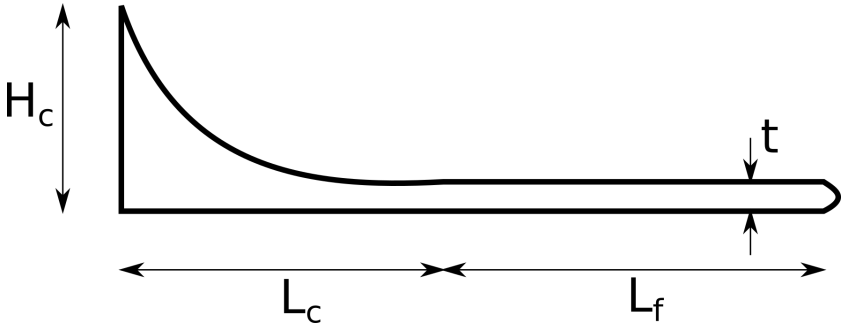

Fig. 4.21 Lateral view of the scoop and main geometrical parameters.

a compliant joint similar to the one used to build the finger joints. In this case, the scoop has a rotational degree of freedom with respect to the palm, that is not actuated, so its position with respect to the palm is not fixed and depends on the external forces acting on it. This solution reduces the stiffness of the scoop but increases its adaptability to uncertain situations. Finally, it is possible to actuate the passive joint connecting the scoop to the palm with a motor and a tendon system, in this way its configuration can be adapted to improve grasp capabilities.

In this work, we assumed for the scoop a linear extruded profile whose section is sketched in Fig. 4.21. The thin end allows the scoop to access narrow spaces, for example, the small backlash between adjacent objects packed in a box. The part of the scoop close to the tip is flat so that it constitutes an additional surface providing support and additional contacts to the grasped object. In Fig. 4.21, we indicated with L_f the length of the flat part. Its definition depends on the dimension and the weight of the objects that have to be grasped.

If the scoop is maintained horizontal, in quasistatic conditions it can hold in equilibrium any object without the use of the other fingers if the vertical direction through the object center of mass is within the scoop profile. In this configuration, hand fingers are not necessary to maintain the grasp (Fig. 4.22a). The hand can move the object without applying supplementary internal grasp forces [159], and this is an advantage when manipulating fragile or highly deformable objects that could be damaged by the application of locally high forces. Furthermore, hand fingers, not necessary to maintain the grasp in this situation, could be potentially used to realize

Table 4.7 Technical features of the Soft ScoopGripper

Technical Features		
Weight (including motors)	500 g	
Max. actuator torque	3.1 Nm @ 12 V	
Max. current	2.8 A @ 12 V	
Continuous operating time	3.5 h @stall torque	
Dimension of the wrist	130 mm x105 mm x 85 mm	
Dimension of a finger	144 mm x20 mm x 15 mm	
Dimension of the scoop	101 mm x70 mm	
Material Parameters	**Flexible Part**	**Stiff Part**
Modulus of elasticity (E)	15.2 MPa	29 MPa
Shore Hardness	85A	80D
Density	1200 kg/m^3	1070 kg/m^3
Geometric Parameters		
width	20 mm	20 mm
length	17.5 mm	23 mm
height	2.5 mm	15 mm

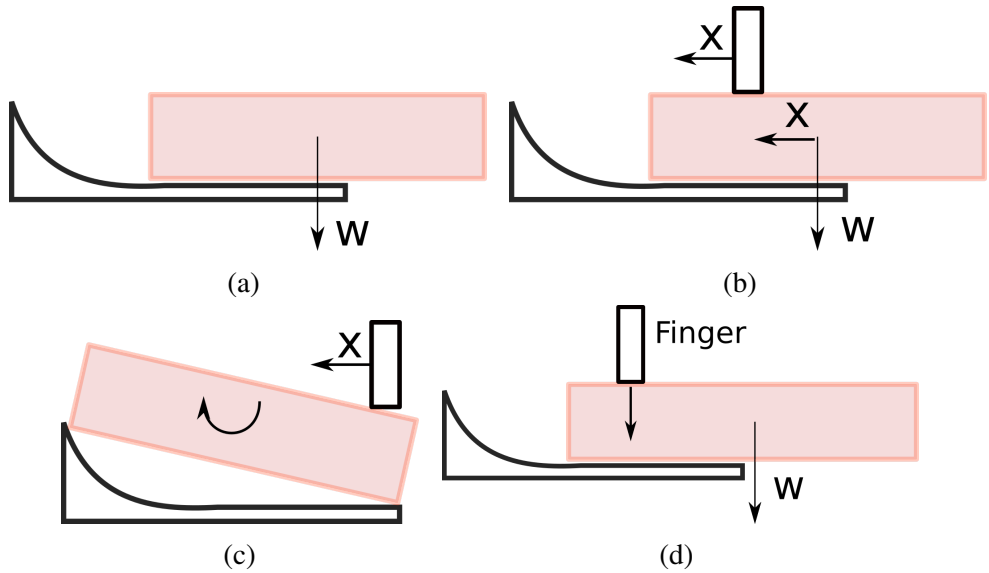

Fig. 4.22 How the scoop helps the hand to grasp and manipulate an object. (a) The scoop can hold the object when the vertical direction passing through its center of mass is included in the flat surface of the scoop. (b) The fingers can be used to reposition the object on the scoop surface. (c) The curved surface of the scoop can be used to reorient the object in the hand. (d) If the object center of mass falls outside the flat surface, the grasp can be maintained if the fingers provide support, by applying a force on the object.

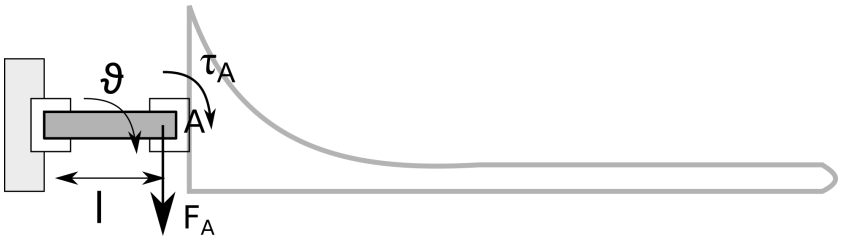

Fig. 4.23 When a force is applied to the scoop, the flexible joint undergoes to a deformation. F_A, τ_A are the equivalent bending force and torque evaluated at point A, and θ indicates the corresponding rotation.

in-hand manipulation of the object more safely and robustly (Fig. 4.22b). Scoop thickness increases close to the connection with the palm and its profile becomes curved. In this case, the object can be easily and safely rotated within the hand. The maximum rotation that can be obtained depends on object dimension and geometry (Fig. 4.22c). When the object center of mass falls outside the scoop (Fig. 4.22d) the grasp can be still maintained by applying a force with the fingers.

The thickness of the scoop in the flat hand has to be defined so to resist the external loads and accidental impacts. It is also influenced by the manufacturing technique that we use to produce it. We realised our prototype with ASA material, [1] with $L_f = 60$ mm, $L_c = 38.5$ mm, $H_c = 40$ mm, $t = 2$mm. Printing direction was set perpendicular to the lower flat surface. In this condition, the scoop can resist a load on its tip up to 100 N.

When the scoop is connected to the palm with an elastic joint, the application of a load on the scoop causes a rotation, that can be evaluated as

$$\theta = \frac{l}{E_j I_j}\left(\tau_A + \frac{F_A l}{2}\right) \tag{4.1}$$

where F_A and τ_A are the force and torque at the point A of the loads applied on the scoop, E_j is the Young's modulus of flexible joint material, TPU, I is the moment of inertia of joint cross section, and l its length. If the load on the scoop is not centred, the joint will have a torsional deformation. Indicating with $\tau_{t,A}$ the equivalent torsion evaluated in A, the corresponding torsional deformation can be evaluated as

$$\theta_t = \frac{\tau_{t,A} l}{I_t G} \tag{4.2}$$

where I_t is the polar moment of inertia of joint cross section and G is the shear modulus.

4.3.2.2 Design of the finger flexion motion

The two fingers of the ScoopGripper have been designed so to adapt to the different shapes of grasped objects. Such adaptability is obtained thanks to the flexible joints and the tendon

[1] Young's modulus, $E = 2.6$ GPa, elongation at break 6%, shear modulus $G = 0.8$ GPa, ultimate tensile strength, $\sigma_{UTS} = 55$ MPa.

driven actuation. Flexible joints and the modular structure of the ScoopGripper also allow to design the flexion trajectory of the finger. In fact, differentiating the stiffness of the soft joints, and in particular the stiffness ratio between two consecutive joints it is possible to reproduce the desired fingertip trajectory while closing the fingers. Given a certain desired trajectory, we need a procedure to compute the stiffness values of the joints so that, once the tendon is pulled to close the finger, the fingertip reproduces such course. In the following, we report the main equations of this procedure. More details can be found in [126]. Choosing a suitable movement for finger flexion is important both to ensure that the objects can be correctly grasped together with the scoop and to constrain object motion to favor the sliding of the scoop under the object itself.

Let us consider the gripper with two fingers and with n_q joints, actuated by a series of n_t tendons. For the sake of simplicity, we model the soft joints as revolute joints, considering other possible deformations negligible with respect to a rotation axis, so that the variable q_i describing the i-th displacement is a rotation. A complete three-dimensional analysis of flexible joint deformation has been recently presented in [160]. We define the vector containing hand joint rotations as $\mathbf{q} = [q_1, \cdot, q_{n_q}]^{\mathrm{T}} \in \Re^{n_q}$, whereas $\mathbf{d} \in \Re^{n_t}$ represents tendon displacements. The equation

$$\mathbf{d} = \mathbf{M}\mathbf{q}, \tag{4.3}$$

relates tendon displacements $\mathbf{t}$ to hand joint configuration $\mathbf{q}$. $\mathbf{M} \in \Re^{n_t \times n_q}$ is a transformation matrix independent from hand posture and defined by the size of finger pulleys and by the topology of tendon routing [123].

The hand joint torques $\boldsymbol{\tau} \in \Re^{n_q}$ and the vector containing tendons' pulling forces $\mathbf{f} \in \Re^{n_t}$ can be computed with the dual static relationship

$$\boldsymbol{\tau} = \mathbf{M}^{\mathrm{T}}\mathbf{f}, \tag{4.4}$$

by applying the principle of virtual work to the gripper. If the fingers are moving without interacting with external surfaces or objects and no external forces are applied on them, the following relationship between gripper status and joints torques can be set

$$\boldsymbol{\tau} + \mathbf{K}_q \Delta\mathbf{q} = \mathbf{0}, \tag{4.5}$$

where $\mathbf{K}_q \in \Re^{n_q \times n_q}$ is joint stiffness matrix, symmetric and positive definite, and $\Delta\mathbf{q}$ indicates a variation of the configuration w.r.t. a reference rest position of the gripper $\mathbf{q}_0$, i.e., $\Delta\mathbf{q} = \mathbf{q} - \mathbf{q}_0$. We assume $\mathbf{q}_0 = \mathbf{0}$ for the sake of simplicity.

If the joints are independent, matrix $\mathbf{K}_q$ is diagonal and Eq. (4.5) can be rewritten as

$$\boldsymbol{\tau} + \Gamma\mathbf{k}_q = \mathbf{0}, \tag{4.6}$$

where $\Gamma \in \Re^{n_q \times n_q}$ is defined as $\blacksquare = \mathrm{diag}(\mathbf{q})$, while $\mathbf{k}_q \in \Re^{n_q}$ is a vector collecting joint stiffness. The system can be solved taking into account eq. (4.4) as

$$\mathbf{k}_q = \Gamma_r^{-1}\mathbf{T}^{\mathrm{T}}\mathbf{f}_r. \tag{4.7}$$

The solution of the system contains the values of the stiffness for the flexible joints that allows to obtain a given configuration $\mathbf{q}_r$ of the gripper when a force $\mathbf{f}_r$ is applied through the tendons. The vector $\mathbf{k}_q$ can be normalized to obtain a base for the subspace of possible stiffness combinations that can be used to track the desired trajectory. The trajectory shape depends on the stiffness ratios between two consequent joints, rather than on their actual value. However, to obtain a complete trajectory, we need to evaluate a sequence of configurations that lead to a sequence of k_q values. We demonstrated in [126] that for several closing trajectories, the values in k_q have little fluctuation in the sequence necessary to complete the flexion motion. This allows to consider an average value for k_q with a reduced error on the trajectory tracking. We then leverage the possibility of tuning finger joint stiffness values exploiting the potentialities of 3D printing. It is possible to use, for instance, thermoplastic polyurethane (TPU) as a material for realizing the flexible joints. Once a geometry for the joints is defined, it is possible to regulate their stiffness values by selecting the percentage of infill density. This parameter affects primarily material density, but also its mechanical properties. Infill density can be regulated during the extrusion process in 3D printers using the standard technique of Fusion Deposition Modelling (FDM). Mechanical properties for the TPU can be found in [161].

4.3.3 Experiments

4.3.3.1 Experimental setup

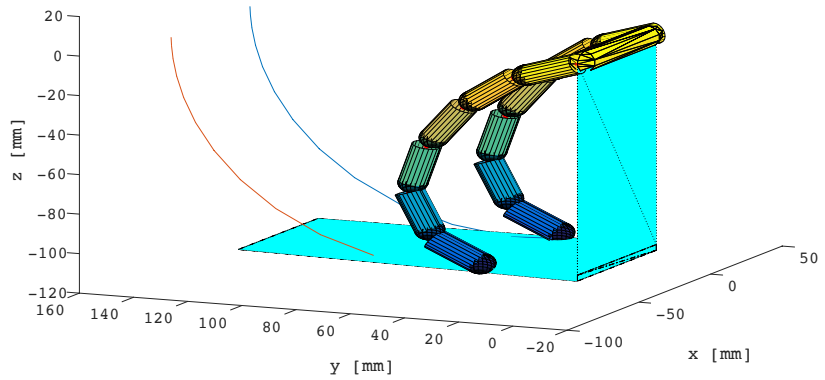

Fig. 4.24 Simulation to design the flexion trajectory of the gripper's fingers.

In this section, we report the experimental results that we obtained with the Soft ScoopGripper prototype. The fingers have six modules which allow a sufficient length to reach the scoop. We have designed using the Syngrasp toolbox [63] a suitable trajectory for the finger flexion, Fig. 4.24. The idea was to have a trajectory that could push big objects toward the scoop and push small objects toward the palm by sliding on the scoop. The resulting ratio vector $rv \in \Re^5$ between the joints computed as in reported in Sec. 4.3.2.2 is $rv = [0.84\, 0.83\, 1.15\, 2\, 1]$.

To fully exploit the gripper capabilities, we designed a handle and we move the gripper manually to achieve a grasp, see the top-left figure in Fig. 4.26. The handle embeds also the control interface of the gripper that is realized with two pushbuttons so to guarantee easy use.

However, the ScoopGripper can also be installed on a robot arm and wireless controlled using the XBee module installed on the gripper control circuit. The handle consists of two parts, a connector plate for the assembly with ScoopGripper and a two button interface to implement the control scheme. It is 3D printed in ASA material. Fig. 4.25 represents the Finite State Machine (FSM) for the control scheme of the device. The handle contains two pushbuttons, where one button is used to control the flexion and extension of the modular finger and the second one is used to control the bending of the scoop. This finite state machine is duplicated for the fingers and the scoop. A single press of a button activates the event "e1" which initiates the "flexion" of the fingers, as soon as the fingers come in contact with the object flexion is stopped and the fingers enter a new state "contact/torque control". In this mode, we can regulate the torque/force exerted on the grasped object by continuously pressing the button. Another single activation will again start the "flexion" of the fingers/scoop unless it reaches the state of "fully flexed". The fingers or the scoop can be open/extended by a double activation of the button in any of the states of the finger/scoop. The extension of the finger/scoop can be stopped upon a single activation during extension.

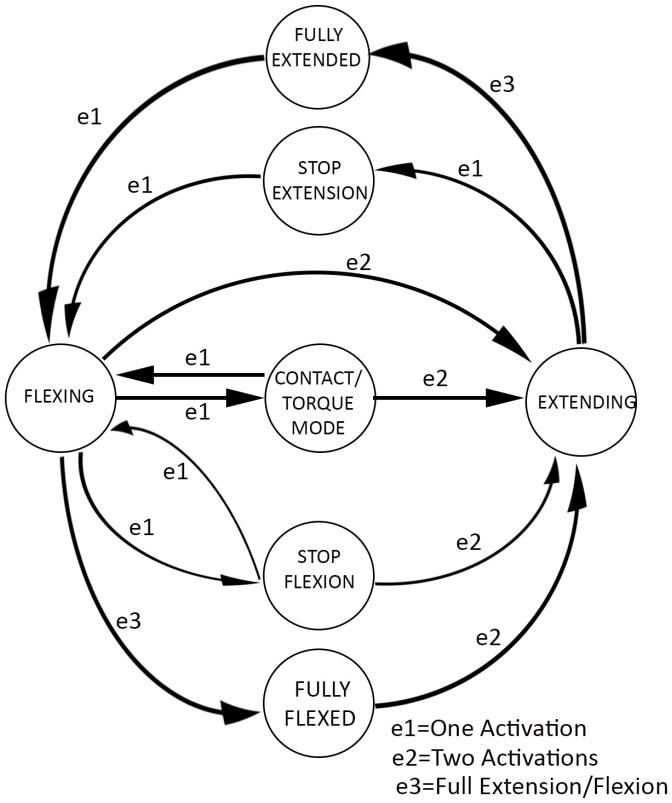

Fig. 4.25 Finite State Machine for Soft ScoopGripper control

4.3.3.2 Grasping of different objects

We performed a series of grasping with the device assembled as reported in Sec. 4.3.3.1. The main goal of these experiments is to show the potentialities and versatility of the gripper. In

particular, we selected objects with different shapes, weights, and stiffness. Some of the objects are included in the YCB object set [83]. The obtained grasps are reported in Fig. 4.26. The approach direction and all the grasping phases have been controlled by the user handling the gripper. For the grasp of smaller objects, i.e. the banana, the lemon, and the apple, also the scoop is bent so to increase the grasp robustness. For bigger objects, i.e. the coffee machine, the jug, and the box, the scoop is left in its straight position. Note that for the jug and the box the fingers have been rotated so to close parallel to the scoop. This is an important feature of the ScoopGripper that also allows to grasp objects with a cylindrical symmetry without rotating the whole gripper and sliding the scoop under the objects. Two examples are reported in the last row of Fig. 4.26.

4.3.3.3 Comparison of grip force needed for a grasp

The scoop can also help to improve the robustness of the grasp reducing the force that the finger needs to exert on the object. Consider the ball grasped on the top-left side of Fig. 4.27. The fingers are only used to cage the ball with the help of the scoop and of the gripper palm. In the bottom-left of Fig. 4.27, the ball is only grasped using the two fingers as it usually happens in classic two-finger grippers. We evaluated the grasp tightness by measuring the torque exerted by the servomotor in these two different cases. We performed 10 time the two different grasps asking the operator to stop closing the finger when it was possible to lift the object. After that, the operator should place the object in a target point 50 cm on the right with respect to the initial grasp position so to test the robustness of the grasp. For the case of the ball grasped with the help of the scoop, the average measured torque for the motor was 0.90 Nm with a standard deviation of 0.21 Nm. When the ball was grasped only by the fingers (basically the gripper was rotated of 180 degrees), the average torque measured at the motor was 2.08 Nm with a standard deviation of 0.15 Nm, which is more than double of that required using the scoop. This feature may be very important when handling fragile objects such as fruit or vegetable that may be damaged by an excessive force exerted in a reduced area. We repeated the experiment also with soft dice, see the right side of Fig. 4.27. In this case, the average exerted torque was 1.05 Nm with a standard deviation of 0.25 Nm, whereas when the dice was grasped only by the fingers the average torque measured at the motor was 2.25 Nm with a standard deviation of 0.27 Nm,

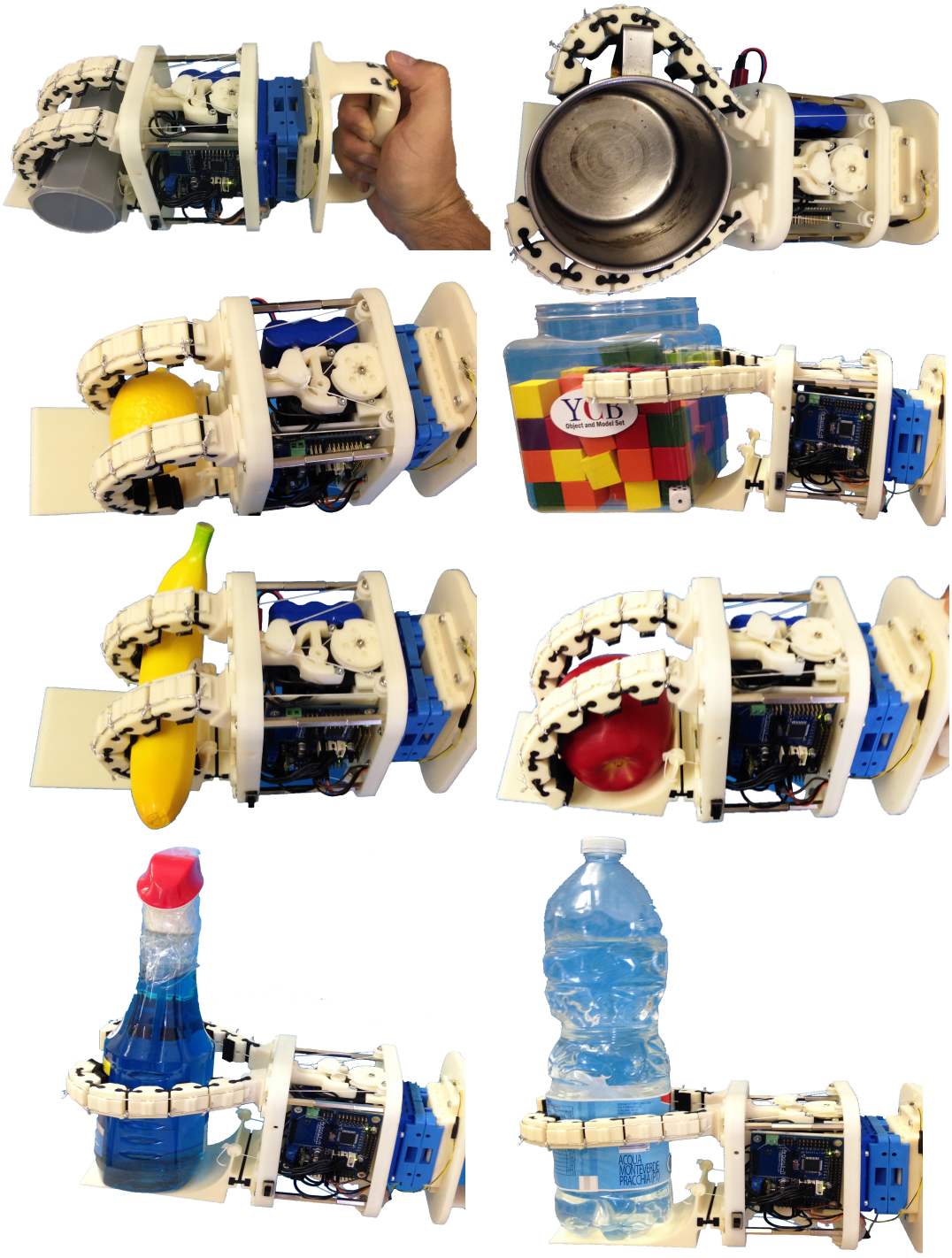

Fig. 4.26 Different objects grasped with the ScoopGripper. Starting from the top left: a toy coffee machine, a jug, a lemon, a box with toy cubes, a banana, and an apple. Note that the object has very different shapes and weights. For the case of the jug, the box of cubes, the water bottle, and the glass cleaner bottle the scoop is slid under the bottom and the fingers closed in parallel to the scoop.

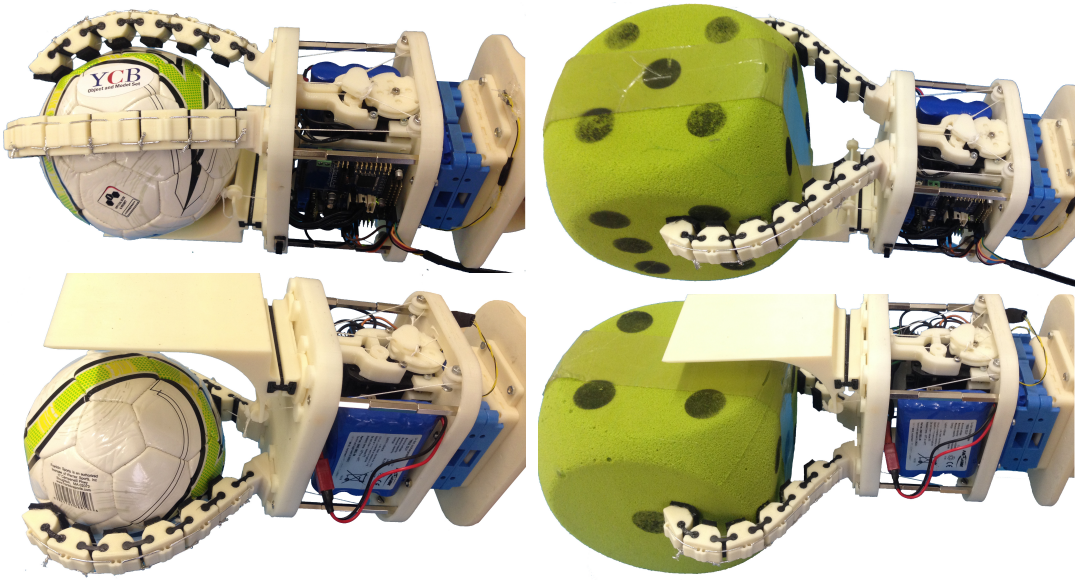

Fig. 4.27 Grasps exploiting the scoop and grasps only with the fingers.

4.3.3.4 Strategies to achieve the grasp exploiting the scoop

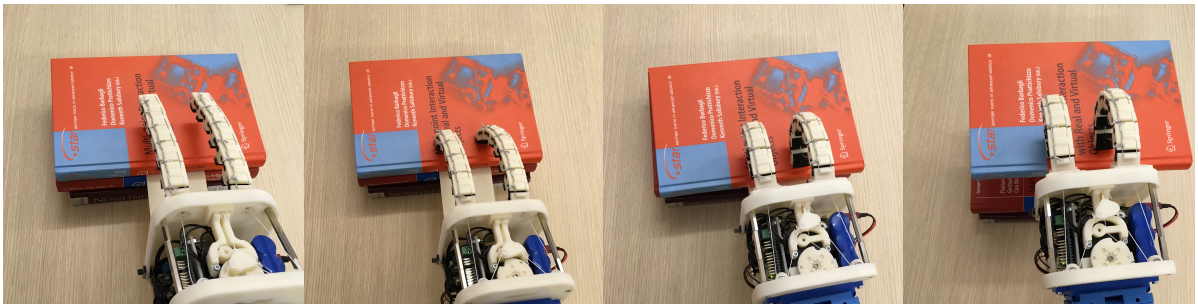

(a) (b) (c) (d)

Fig. 4.28 Possible strategy to grasp a book form a pile exploiting the scoop.

This experiment aimed to show how the Soft Scoop gripper can be used in a situation where simple grippers would fail or would require a complex manipulation strategy to achieve a stable grasp. Consider, for instance, the case reported in Fig. 4.28-a. The goal is to grasp the first book from a pile. We asked ten subjects to try to grasp the book using the ScoopGripper. All the subjects were able to grasp the book. Fig. 4.28 represents the most used strategy (7 out of 10 subjects). In Fig. 4.28-a the scoop is placed between two books. The fingers are then closed so to reach the book, Fig. 4.28-b. Later, the finger closure is used to help the scoop slide underneath the book, Fig. 4.28-c. Finally, the fingers' torque is increased, and also the scoop is bent toward the fingers so to increase grasp robustness, Fig. 4.28-d. Another observed strategy consisted of first pushing the scoop below the book and then activate the fingers. However, this approach resulted in a bit slower since the book tended to move forward together with the scoop.

4.3.4 Conclusion

In this work, we presented a novel soft gripper that embeds a flat surface able to scoop objects. We demonstrate that in several grasping problems, the presence of the scoop allows to reduce the squeezing force required to grasp increasing the grasp robustness. The idea of embedding a scoop may open to the study of a novel generation of soft-rigid gripper that brings the idea of environmental constraints exploitation inside the device. This mainly means that the capability of soft grippers, and more in general of soft hands, to comply with the environment to achieve stable grasps using a reduced set of control inputs may be fully exploited also when the constraint is not available. The Soft ScoopGripper itself contains environmental constrain. Advantages of this solution may be: i) large contact area, ii) compensate uncertainties in contact, iii) lower grip force necessary to maintain the grasp, and iv) the possibility to achieve grasp not possible from the top, due to object dimensions or position in the environment.

Currently, we are focusing on the design of more advanced scoops that may help increase grasp robustness. We are also working on exploiting the ScoopGripper as an end-effector of a robotic arm for autonomous grasp planning.

4.4 The Mag-Gripper: A Soft-Rigid Gripper Augmented with an Electromagnet to Precisely Handle Clothes

This work introduces Mag-Gripper , a novel robotic gripper specifically designed for autonomous clothing manipulation. It is capable of improving grasp repeatability and precision, compensating uncertainties in the target grasping locations. We propose to approach the autonomous clothing manipulation challenge by involving a suitable magnetic force. For this reason, Mag-Gripper is equipped with an electromagnet capable of interacting with small metal parts properly placed on the garment to be grasped. Electromagnet exploitation is not a novelty in literature, but our design innovation consists of embedding the electromagnet in the structure of a jaw gripper. In so doing, we revisit a classic end-effector type, corresponding to the simplest representation of a hand capable of opposability, allowing easily controllable devices to perform grasps similar to the human pinch grasp. Mag-Gripper can find applications either in Research labs investigating Machine Learning-based clothing manipulation techniques either in companies having to manage a large number of returns, either in home setting scenarios.

4.4.1 Introduction

4.4.1.1 Motivations

Continuously evolving robot generations are spreading out in factories and home settings as service robots. Today, small robots embedding some intelligent skills are taking the first steps in dwelling our homes, and in the next future, a much wider diffusion is expected, both as assistants for housework and physically impaired people. The capability of interacting in a dynamic environment requiring fine sensory perception and dexterity will play a fundamental role since robots will be expected to perform some tasks autonomously (at least partially). Adapting robots to perform tasks requiring complex dexterity (*e.g.*, to manipulate deformable objects) poses new challenges. In particular, deformable objects cannot be grasped according to classic grasp planning methods [162], and their manipulation strategy strongly depends on the object configuration. Clothes are extremely deformable objects, whom configuration is significantly affected by the trajectory performed by the handling arm. Therefore, clothes are challenging because of their difficult perceivability and manipulation, due to the potentially infinite configurations they can assume. To bring clothes in the desired configuration, the sequence of the intermediate movements is paramount: Each sub-movement, along with the points where the cloth is grasped, causes a cloth configuration. Due to the deformable nature, relatively small changes in the grasping points location can produce a significant change in the final configuration assumed by the grasped garment. This variation of configuration can influence the outcome of the task, potentially causing a failure. On the contrary, grasping the garment in proper locations leads to a fast and effective task accomplishment, as shown in the video reported in [163] by a popular garments producer. As such, properly designed assistant robots could be able to fold our garments in the near future. To this aim, we propose a novel approach to the problem, exploiting both grippers and garments specifically designed to allow autonomous manipulation by robots. In the following, we detail the rationale and specifications of Mag-Gripper , a novel type of jaw gripper augmented with an electromagnet. Small metal

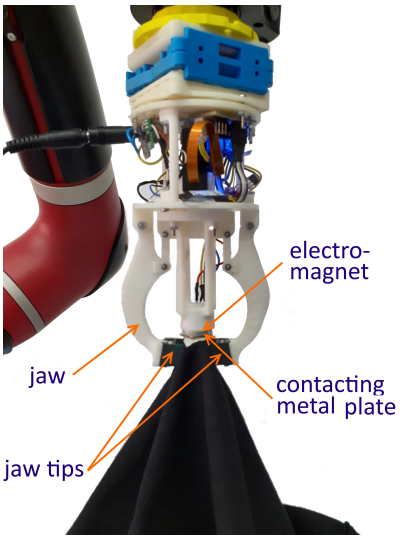

Fig. 4.29 Mag-Gripper : a novel gripper to manipulate clothes

parts embedded in the garment as ornamental or brand elements are involved in the attractive gripper-clothing approach. Our long-term vision involves cooperation between researchers in robotics and garments producers, so to realize clothes that can be easily manipulated by our gripper. In the meanwhile, Mag-Gripper features an immediate field of application in the robotic community: It is meant to be a support tool for the research in Machine Learning-based garment manipulation, where high repeatability in grasp location is required during the

4.4.1.2 Previous Work on Cloth Manipulation

In the last decade, research on autonomous cloth manipulation has received a great boost. This task can be decomposed into two sub-tasks: unfolding and folding. The former being aimed at bringing the cloth from a random configuration to a known one (usually corresponding to have the garment lying flat on a table), while the latter is aimed to accomplish the required manipulation starting from that known configuration. Typically, the cloth pose is not known *a priori* and a perception system is needed. Regarding the unfolding task, the most popular approach consists of re-grasping the object until the target configuration is reached. In [164], a geometric approach is proposed, consisting of identifying two grasping points on the garment outline capable of generating a half-folded cloth configuration, to which shape analysis techniques are applied to estimate the novel re-grasping points. In [165], a 2D perception and a Markov Hidden Model are used. In [166], 3D perception and fiducial markers located on the garment are used to compute a mesh of the object, and a Support Vector Machine is employed to implement a greedy policy for the next grasping point estimation. In [167], a data-driven approach joint with Random and Hough forests is used for garment recognition and to estimate the grasping points in a probabilistic planning framework taking into account uncertainties related to the estimation process. In [168], a simulation environment is used to compare the synthetic data in it with a reconstructed mesh of the physical garment to grasp, and mapping the re-grasping points on the synthetic mesh to the physical garment. The main difficulties

encountered in the above-cited works are: *i)* the time required to accomplish the task; *ii)* the uncertainties on the estimate of the final grasping point; *iii)* the risk of losing the object during multiple re-grasping. In a more recent work [169], a hierarchical structure of Convolutional Neural Networks is used to recognize the garment category and grasp it directly in two points, avoiding multiple grasps and decreasing the required completion time.

Regarding the folding task, early works proposed geometric approaches [170] relying on the gravity-based folding: in [171], the cloth is assumed to be representable as a simple polygon, and the task is accomplished by moving a portion of the garment over another one, having a segment termed *g-fold* as separation line. Following this approach, in [172] the garment-polygon matching was improved, and in [173] the garment flexibility taken into account. In [174], a complete pipeline from picking up a garment to folding it exploiting the *g-folds* is presented. More recent works arise from the synergy between Machine Learning and Robotics, relying on Deep Learning, Learning from Demonstration (LfD), and Reinforcement Learning. In those works, the robot is taught to learn the folding task by means of a set of demonstrations provided by a human operator. In [175], a deep convolutional autoencoder joint with a deep time delay neural network is used to process data acquired via teleoperation. In [176], an LfD with Deep P-Network is used to learn a T-shirt folding. In [177], Dynamic Motion Primitives are exploited with LfD and RL. When dealing with Machine Learning techniques, it is well-known that to achieve a good learning process (*i.e.*, good generalization capabilities), a large and consistent dataset has to be provided to the machine. In particular, when a given cloth manipulation task has to be learned by means of human demonstrations, the multiple demonstrations have to start all with the same initial garment configuration [177]. To this aim, grasping the cloth always in the same points is fundamental, since clothes are extremely deformable objects and relatively small changes in the grasping points can cause significant errors in the initial configuration. This is why in [177] the gripper maintains contact with the garment during the entire learning process.

4.4.1.3 Previous Work on Grippers for Cloth Manipulation

In [178], a taxonomy of the grippers that have been used in works on deformable object manipulation is presented. As highlighted in the work, usually those grippers are not specifically thought for interacting with clothes, which are extremely deformable objects. Indeed, the most commonly used tools are the parallel-jaw grippers, whose surface tips are supposed to contact the object have a rectangular shape. The gripper can then interact with the object by taking the longer or the shorter rectangle side parallel to the table on which the cloth lies, depending on the desired closing motion. Multi-fingered hands (such as those used for instance in [179]) allow to exploit in a more complex way the abduction motion and can allow a more dexterous manipulation (*e.g.*, to identify the boundary of clothes [180]). Few hands are designed to establish specific interactions with clothes: in [181], force sensors are placed on the tips to perform garment classification according to the material roughness. In [182], an underactuated three-fingered hand capable of generating human-like grasping movements exploiting environmental constraints [183] is presented. However, when these tools are used to manipulate clothes, the grasping task is mainly performed by sliding on the table surface and enclosing a portion of the garment between the jaws. This approach: *i)* restricts the cloth

manipulation to occur on a tabletop; *ii)* requires that enough portion of the fabric is constrained between the tips to avoid undesired slippage. However, *i)* cloth manipulation can be performed also in the air [166, 177], and this is important also in the light of the growing need for assistive robotic tools; *ii)* grasping by sliding the fabric on the table surface introduces unpredictable variations in the configuration taken by the garment after the grasp has occurred. This is due to the fact that the portion of the tissue actually constrained by the tips is the consequence of the interaction between the garment, the robot, and the environment, and the related changes are difficult to face for vision-based Machine Learning techniques.

4.4.1.4 Contribution

In this work, we want to suggest a novel approach to the execution of autonomous clothing manipulation, by exploiting the presence of an attractive magnetic force established between the gripper and the garment. As a suitable tool, we present Mag-Gripper , an augmented jaw gripper embedding an electromagnet. As it will become clear in the following, this design choice allows to achieve a repeatable extended point-like grasp: Since the location where clothing is grasped causes its configuration after the grasp has occurred, having a repeatable grasping capability results in having repeatable clothing configuration. Hence, Mag-Gripper wants to be a possible solution to cope with the issues mentioned in Sec. 4.4.1.2 and 4.4.1.3. To the best of our knowledge, no grippers exploiting the magnetic force so far have been exploited for clothing manipulation. Moreover, the difference with commercially available grippers exploiting the presence of a magnet [184] is that we want to exploit the magnetic force only to establish the contact between the gripper and the garment, whereas the presence of a permanent magnet would need an opposite magnetic field to allow the object detachment any time the grasp has to be released. After the extended point-like grasp has occurred, the magnetic force is no more needed: the electromagnet is deactivated to avoid overheating and secure grasp maintenance is achieved by exploiting the gripper jaws.

In our approach, the garment has to embed a metallic part. During data acquisition for Machine Learning-based approaches, these parts can be easily inserted by researchers in the desired locations to meet grasp precision requirements. However, the implementation of autonomous garment manipulation applications for the general public will be possible only by establishing a synergy between companies and researchers, and such synergy will be encapsulated in novel clothing production lines specifically thought to allow autonomous manipulation. These novel garments will have the needed metal parts embedded as ornamental or brand elements, such as buttons and small plates.

4.4.2 The Mag-Gripper

Mag-Gripper has been designed to be lightweight, modular, and with a limited encumbrance. The prototype has been designed via CAD and realized with additive manufacturing techniques (the material used is ABS M30), which allowed small production costs and short production time. The gripper is similar to a jaw gripper, but the novelty we propose consists in having realized an *augmented* jaw

gripper: in its central part, there is an electromagnet mounted on the top of a linear actuator. By activating the electromagnet, a magnetic field is generated, which causes a magnetic force attracting the metal part attached to the cloth. Due to the attractive motion of the metal part, a collision between the end-effector and the cloth occurs and is detected by a small resistive force sensor (FSR), which is located near the electromagnet. The contact is deemed to be occurred when the force measured by the sensor exceeds a given threshold, triggering the closing motion of the jaws. The proposed gripper exploits the advantages of both the electromagnet and the parallel-jaws: the former allows to grasp the cloth at the desired point, while the latter allows secure grasp maintenance during the cloth manipulation. In other words, the uncertainty brought by the soft fingertips of the jaws are tamed by the action of the electromagnet.

4.4.2.1 Components

The Mag-Gripper is an augmented jaw gripper, a sketch of which is shown in Fig. 4.30a. In the gripper central part, between the jaws, there is a linear actuator (PQ12-30-12-P by Actuonix), at the top of which an electromagnet (KS0320 by Keyestudio) is mounted. Thanks to a set of pin joints and connecting links, the motion of the actuator allow both to approach the electromagnet to the cloth, and to open/close the jaws. Thus, the proposed gripper has one degree of actuation, which allows the gripper to be lightweight (181 g, including all the electronics) and with the limited encumbrance, taking into account the considerations in [178]. The closed structure width is 9 cm. The maximum opening size of the jaws is 13 cm. When the jaws are at the maximum opening distance allowed by design, the most prominent part is the electromagnet and the distance between the electromagnet and the base is 15.3 cm. When the jaws are completely closed, the most prominent part is given by the jaw tips, and the distance between the tips and the base (bottom plate in Fig. 4.30a) is 15.5 cm. The circular base has a 5 cm diameter, and the links connecting the two circular surfaces enclosing the electronics are 5 cm long. To have a robust structure, the gripper base, the jaws, and the locations assigned to the actuator and the electromagnet are 3D-printed in ABS. Conversely, the jaw-tips are hollow and realized in TPU, to ensure a more compliant interaction with the cloth. The tips are designed with grooves (see Fig. 4.30b) to increase the friction during contact with the objects, thus reducing undesired slippage.

The gripper microcontroller is an Arduino Pro Mini with an ATmega328P (running at 16MHz, 5V input voltage). Gripper control is achieved via position control, by exploiting the actuator feedback position and the polarity inversion through the L293B motor drive. The electromagnet is activated or deactivated through a logic input (H/L), which is a function of the actuator position and sensor measurements (see also Sec. II-B). The gripper receives commands through a Bluetooth connection (RN42 module by Microchip) and its working voltage is 12 V.

4.4.2.2 Working principle

In Mag-Gripper , the electromagnet plays a fundamental role during the approach to the object, while the jaws allow secure grasp maintenance. As soon as the central cart moves, two orthogonal motions are generated: the first one, along the direction of the actuator, corresponds to the electromagnet approaching direction, the second one lies on the plane orthogonal to that

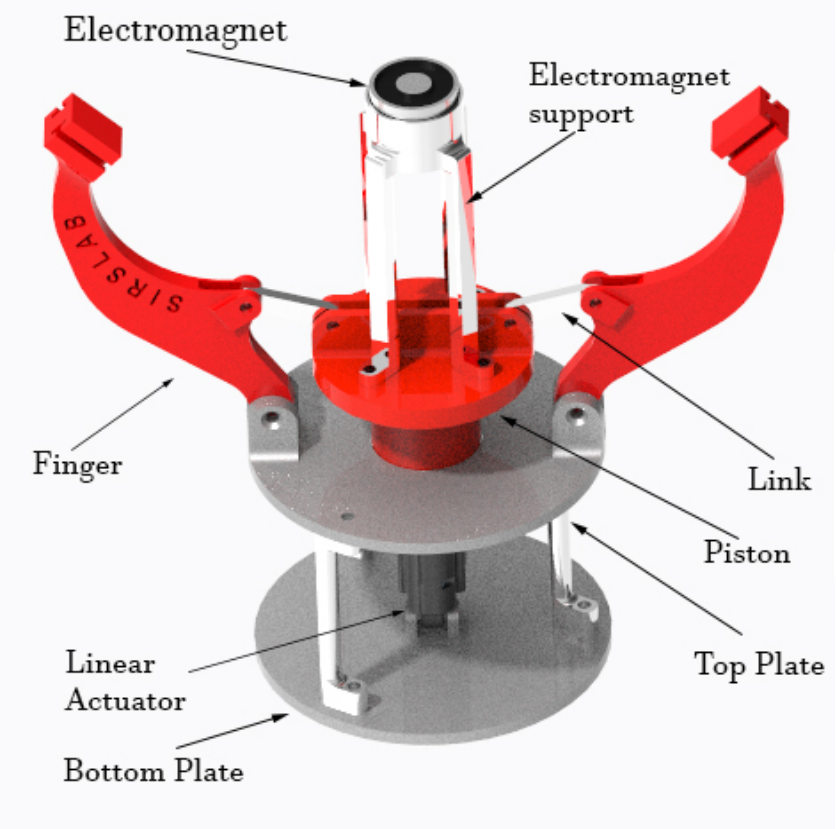

(a) Mag-Gripper CAD

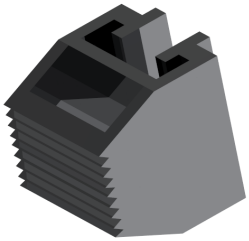

(b) Jaw-tips

Fig. 4.30 Sketches of the Mag-Gripper . (a) isometric view. (b) zoom on the jaw tips which are slided at the end of the fingertip; notice the grooves and the hollow structure, where the grooves provide friction to avoid slippage.

direction, and corresponds to the motion of the jaws. To avoid unwanted collisions between the jaws and the object during the approaching phase, and collisions between the jaws and the electromagnet, three working configurations have been defined: pre-grasping, grasping and release. The working configuration can be seen as a function named *conf* of three independent variables: *ae*, which stands for activation of the electromagnet, *sr*, i.e., sensor reading, and *at* i.e., translation of the actuator,

$$conf(ae, sr, at) = \begin{cases} pre-grasping \\ grasping \\ release \end{cases} .$$

As mentioned in Sec. 4.4.2.1, during the *pre-grasping* phase, the distance between the jaws is the maximum allowed and the electromagnet is the most prominent part of the gripper. This allows the electromagnet to approach the cloth without collisions between the cloth and the jaws. This configuration is reached as soon as the electromagnet is activated, the force sensor starts sending the measured values and the motion of the linear actuator has not yet started.

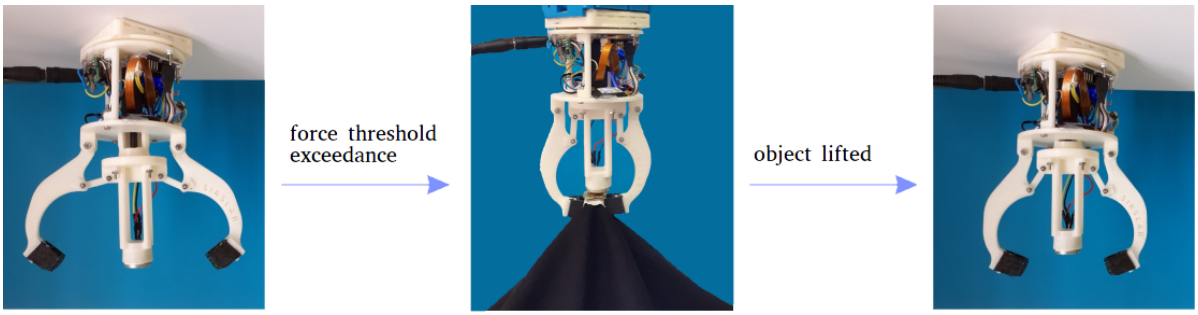

Fig. 4.31 Mag-Gripper working configurations. During the pre-grasping, the electromagnet slot is the most prominent part of the structure, to allow the attractive motion of the metal plate without undesired collisions between the jaws and the cloth.

After the gripper has entered the pre-grasping phase, the actuator starts translating to approach the object. The contact is considered to have occurred when the force sensor measures the exceedance of a given threshold. This allows the gripper to enter in the *grasping* configuration: the jaws close and the electromagnet is deactivated (no more needed). The motion of the linear actuator is prevented through a position control until the release command is sent and the gripper enters in the *release* configuration: the electromagnet is still deactivated, the sensor readings are discarded and the linear actuator is commanded to move so to allow an opening distance between the jaws equal to one half of the maximum allowed (see Fig. 4.31). Notice that the jaws closing motion relies on the force sensor measurements. This is why, in principle, Mag-Gripper can work also without the electromagnet (see also Sec. 4.4.3.3).

4.4.2.3 Finite Element Modelling

Finite Element Analysis and Dynamic Analysis of the gripper have been carried out using COMSOL Multiphysics Software. A boundary load of 18 N (Linear Actuator maximum force) was applied in the y-axis direction. The gripper was cut in half to simplify the geometry and the symmetric constraint was applied to compute the solution. Tetrahedron elements were used for meshing. A mesh convergence test was also carried out based on maximum element size, which suggested that when element size is between 0.00180 m to 0.00375 m the results are almost similar. Hence, a maximum element size of 0.00218 m was selected. The result of FEM is depicted in Fig: 4.32. The maximum stress experienced is 5.29 MPa and it is exerted on the link between finger and piston, showing it as the most vulnerable part. For the case of dynamic analysis, a constant force of 18 N was applied and the corresponding velocity and acceleration plots of the jaw tip are shown in Fig. 4.33.

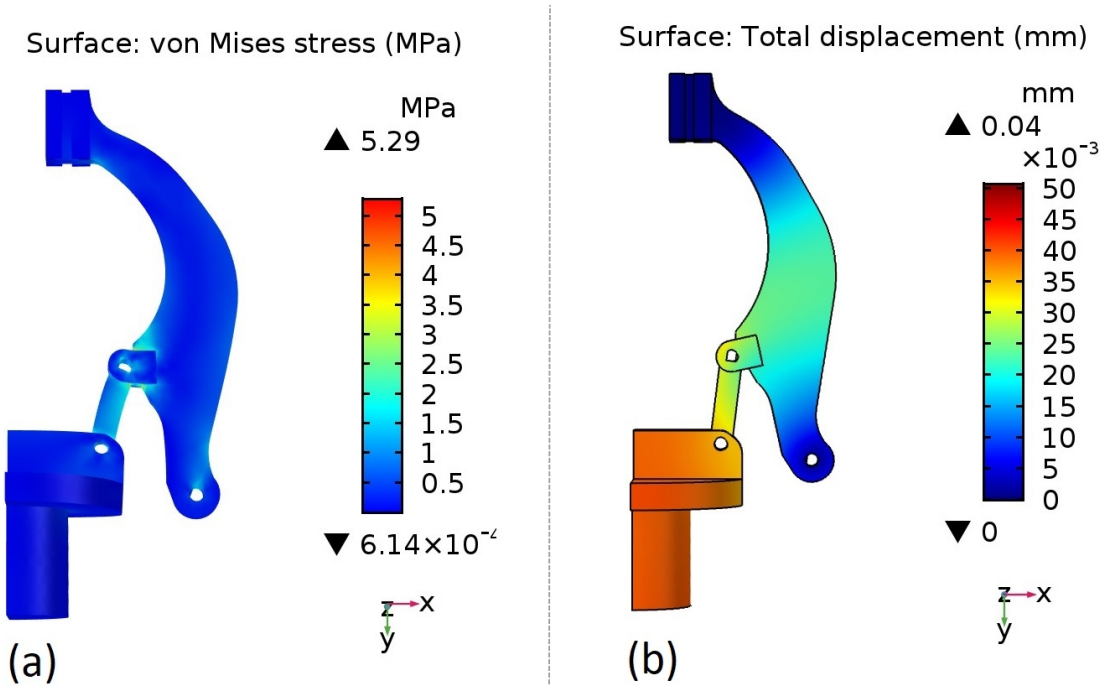

Fig. 4.32 FEM: (a) Stress Von Mises (MPa), (b) Maximum Displacement (mm).

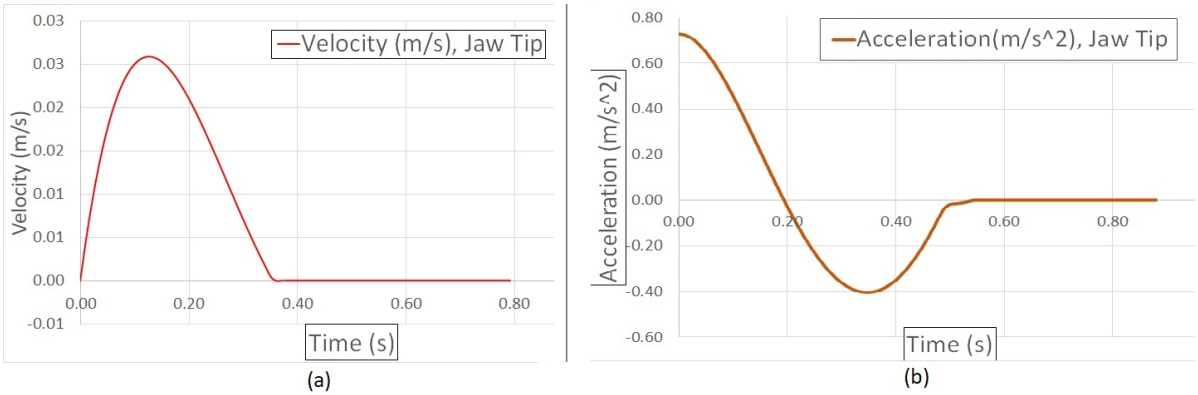

Fig. 4.33 Dynamic analysis: (a) Velocity and (b) Acceleration plot of the jaw tip (F = 18 N).

4.4.3 Experiments

We propose Mag-Gripper as a tool for autonomous manipulation of clothes, by exploiting the presence of a small metal part on the garments. Grasping the object in the desired points is the first condition to be met to achieve the required manipulation. Experiments with a Sawyer collaborative robotic arm (by Rethink Robotics) were performed to test the actual capabilities of the proposed gripper. To this aim, we investigated: *i)* how the performance is related to the size of the metal plate and the cloth weight; *ii)* which is the role played by the electromagnet on the configuration taken by the cloth after the grasp has occurred; *iii)* how to compensate possible

uncertainties on the estimate of the grasping points. For the sake of simplicity, we assumed the desired location of the grasping point to be fixed on the garment (*i.e.*, on a shoulder), and a fiducial marker located in that position had been used to retrieve an estimate of the desired pose with respect to the robot base. The cloth was located on a tabletop and an overhead camera (ASUS Xtion) was used during the marker detection phase. The trajectory planning was implemented in the *MoveIt* framework [2], and it was decomposed in three different steps: *i)* go 4 cm over the estimated location; *ii)* go down until the contact between the gripper and the metal part has been detected; and *iii)* lift the garment for 20 cm.

Communication between the devices (robot, gripper, PC) run via ROS (Robot Operating System). In the following, five different sets of experiments are described. For the sake of simplicity, the gripper orientation was fixed to have a not occluded view of the scene from our desk. However, it can be chosen arbitrarily. Unless otherwise stated, the garment to grasp was the T-shirt included in the YCB dataset [185], and the square metal plate had a side of 1.8 cm.

4.4.3.1 Dependency on the metal plate dimensions

By means of this set of experiments, we investigated two aspects related to the metal plate size: *i)* how the number of successful grasps changes by varying the plate dimensions and *ii)* the repeatability of the grasp execution. Regarding the former issue, we termed *successful* a detected grasp occurred in correspondence of the metal plate and maintained without appreciable changes during the lifting phase. Regarding the second investigated aspect, we meant to have a measure of repeatability by estimating the area of the garment contacted by the electromagnet when multiple grasp attempts were performed with the same target. To have this measure, we covered that extremity with a thin rubber layer and put a thin layer of tempera colors on it. During the contact with the metal plate, the color is laid down on the plate, leaving a mark of the executed trial. After 10 grasp attempts, we estimated the radius of a circumference containing all the color marks on the plate by measuring the distance between the two furthest points with a caliper. After each trial, the rubber was cleaned to avoid a dry color layer which would have reduced the magnetic force. The usage of the thin wet tempera color layer did not reduce appreciably the attraction up to 0.5 cm of distance between the plate and the electromagnet. Three different metal plates were used. They had a squared shape with a side of 1.0 cm, 1.8 cm, and 2.5 cm, respectively. Results are reported in Table 4.8. Notice that in the bimanual clothing manipulation presented in [165], a grasp configuration is termed successful if both the left and the right grasp occurred within 5 cm from the estimated most likely grasps.

4.4.3.2 Dependency on the cloth weight

To have an insight on how the performance of Mag-Gripper is influenced by the cloth weight, 4 different garments were used to be autonomously grasped 5 times: the YCB T-shirt, a mid-season pullover, an old bib, and a terry guest towel. Objects weight and thickness are reported in Table 4.9. Besides the number of successful attempts, we report also the mean distance that was required between the electromagnet and the garment to allow the magnetic force to cause the desired attractive motion of the cloth towards the electromagnet.

[2] https://moveit.ros.org/

Table 4.8 Number of successful grasps on the YCB T-shirt and radius of the estimated contacting area between end-effector and plate when the grasping attempts are repeated 10 times. Results are related to the size of the metal plate.

Square side	Success	radius [mm]
1.0 cm	8/10	15.1
1.8 cm	9/10	21.2
2.5 cm	9/10	24.5

Table 4.9 Objects used to have an insight on how the Mag-Gripper performance is related to the weight and thickness of the objects. The number of successful grasp attempts and required distance between the electromagnet and the plate is reported. The metal plate with a side of 1.8 cm was exploited.

Object	Weight	Thickness	Successes	Distance
T-shirt	125 g	0.4 mm	5/5	6 mm
Pullover	266 g	0.7 mm	5/5	5 mm
Bib	43 g	1.3 mm	5/5	3 mm
Towel	148 g	2.5 mm	4/5	2 mm

4.4.3.3 Dependency on the electromagnet (gripper opening size)

Using these kinds of experiments, we investigated which is the role played by the electromagnet on the configuration taken by the cloth when the grasp has already occurred. To this aim, we compared the area involved in the grasp with and without the exploitation of the electromagnet. In other words, we performed 10 attempts providing the garment with the metal plate (E experiments) and then more than 10 attempts after removing it (WE experiments). In both sets of experiments, the gripper closing motion started when the contact between the gripper and the cloth had been detected by the force sensor. In both, the set of experiments, a thin layer of tempera colors was added on the jaw-tips to mark the areas involved in the grasp execution. In Fig. 4.34, the green marks correspond to the areas contacted without exploiting the presence of the electromagnet, while the blue colored marks are the areas of interaction when the grasp execution relies on the force of attraction between the gripper and the cloth. In the first case, the distance between the corresponding centers of the marks is about 10 cm (avg), while in the second case the same distance is about 5 cm (avg).

Fig. 4.34 Estimate of the fabric portion involved in the grasp, with and without the electromagnet exploitation (blue and green marks, respectively). A smaller portion produces fewer wrinkles, increasing the grasp precision.

When the metal part is lifted by the electromagnet, the portion of the fabric involved in the grasp is smaller than the one involved without the electromagnet exploitation. This reduces the possibility of wrinkling the fabric, increasing the grasp precision and repeatability.

4.4.3.4 Target uncertainties compensation

When dealing with vision-based grasp planning, it is common to have to cope with pose errors due to the camera calibration process. Usually, several transformations are needed to retrieve the desired grasping point in the reference system used for the trajectory planning. This causes the propagation of the estimation error. To this aim, we introduced by purpose an error of 1 cm on the x and y coordinates of the estimated grasping point, and 10 grasping attempts were performed. During 7 grasps trials the electromagnet was still capable of attracting the cloth. However, in 3 out of these experiments, the force sensor did not detect the occurred contact, since it had happened in a lateral location not involving the sensor (the sensor radius is about 3 mm).

4.4.3.5 Common small objects with metal parts

This set of experiments was aimed at testing the Mag-Gripper capability in grasping small objects different from clothes. Two small boxes, a comb, hair barrettes, and paper clips have been used. On the top of the boxes and the comb handle the squared metal plate with a side 1 cm (used also in Section 4.4.3.1) was located. The other objects were already provided of metal parts. The heavier object (box) weighed 25 g. The size of the objects spanned between

0.1 cm x 4.5 cm (paper clip) and 4.5 cm x 6.5 cm (box). An overall of 12 grasp attempts has been performed, achieving a success rate of 100%.

4.4.4 Discussion

4.4.4.1 On the dependency on metal plate dimensions

This set of experiments was aimed at investigating the role played by the metal plate size in the grasp execution. In all the failures, the contact between plate and electromagnet occurred but was not detected by the force sensor, since it occurred in a location not involving the sensor. Hence, the garment lifting phase was not triggered and the robot remained stuck. In respect to the estimate of the actual contacting area between the end-effector and the plate, as it can be foreseen, the larger is the plate, the larger is the contacting area. That area could be represented as a circle enclosing the plate, since the contact between the plate and the electromagnet can occur everywhere on the plate, as long as there is a superposition of the two surfaces. The location variability is due to the manual collocation of the marker on the plate, but also errors related to the camera calibration.

Interestingly, one successful grasp related to the plate with a side of 1 cm allows further consideration. During that attempt, contact between the end-effector and plate occurred. However, suddenly the plate fell before the electromagnet deactivation. The magnetic force generated was capable of re-establishing the contact in time and the gripper successfully lifted the T-shirt. This suggests that by properly managing the electromagnet deactivation time, Mag-Gripper could be used to cope with the possibility of losing contact with the object, ending up in a successful grasp.

4.4.4.2 On the dependency on the cloth weight

Experiments aimed at having insights on how much the Mag-Gripper performance relies on the cloth weight revealed that the thickness of the garment is more relevant than the overall object weight. As it can be noticed by looking at the fourth column of Table 4.9, the thicker the garment is, the smaller the distance required to attract the metal part is. This is because changing the thickness results in varying the local mass the electromagnet has to attract. If the local mass increases, the electromagnet needs to be closer to the plate to cause the attractive motion of the metal part.

These results suggest that the electromagnet should be chosen either to grasp specific clothes or in a conservative manner, by considering a set of interesting objects and ensuring to be capable of grasping the thicker one. However, this gives us the possibility to remark that the choice should be context-related: in some cases, an unnecessary strong magnetic field can introduce some disturbances in other devices which are present in the robot workspace. Moreover, we want to stress the importance of having an attractive motion between the gripper and the cloth without the need of getting in contact with the environment to grasp the garment. This capability allows an intrinsically safer robot-environment interaction, besides the possibility of performing aerial grasps [186].

(a) WE experiments (b) E experiments

Fig. 4.35 Grasps performed with and without electromagnet exploitation, left and right subfigures, respectively. The electromagnet exploitation allows a more repeatable cloth configuration, without wrinkles.

4.4.4.3 On the dependency on the electromagnet (gripper opening size)

Regarding this set of experiments, as it can be seen in Fig. 4.34 when the grasp execution relies on the presence of the electromagnet (E experiments), the distance between the jaws during the grasp is smaller than the case where the electromagnet is not exploited (WE experiments). This is because the closing motion of the gripper starts as soon as the contact between the end-effector and the cloth is detected. However, in the WE experiments, the gripper needs to reach the table before detecting the occurred contact. As a consequence, when the jaws start closing, the distance between the jaws is close to the maximum allowed (13 cm by design). On the other hand, in the E experiments, the magnetic force attracts the plate before the gripper reaches the table, and the cloth takes a somehow conic shape. This is the reason why the distance between the jaws is smaller in the E experiments than in the WE experiments.

Moreover, a qualitative consideration should be done. As it can be seen in Fig. 4.35, when the WE experiments are performed, the part of the cloth located between the jaws is significantly crinkled. This is due to the fact that the grasp is executed by sliding the jaws on the table. The contact points between cloth and jaws do not change and the minimum distance between these points (*i.e.*, the distance without considering the wrinkles) is gradually smaller and smaller, but there is still a portion of fabric constrained to lie between the jaws.

If the aim is to grasp the cloth in the desired location, so to let the cloth assume a configuration that is easy to manage with vision-based Machine Learning techniques, the exploitation of the electromagnet seems to be a good way to proceed. Indeed, the conic-like shape taken by the cloth after the grasping allows to achieve a sort of pinch grasp, which results in a less disturbing configuration of the points located near the actual grasping point. This sort of extended point-like grasp allows a more predictable configuration of the cloth, which is a high deformable object with potentially infinite ways of deforming.

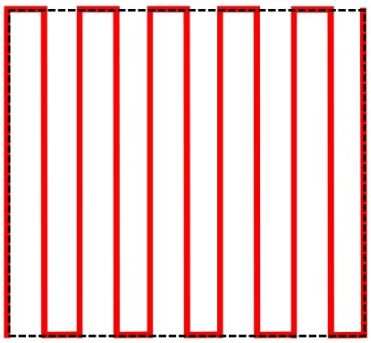

Fig. 4.36 Example of possible motion pattern (in red) for a *blind grasp*: it spans a small area (delimited with the dashed line) around the estimated grasping point to cope with pose estimation errors.

4.4.4.4 On the target uncertainties compensation

The artificial introduction of uncertainties in the estimate of the grasping point pose was aimed at investigating to what extent the exploitation of the magnetic force can allow grasping the object in the target location, thus realizing a compensation of the position estimation error. Disturbances of 1 cm acting simultaneously along the x and y coordinates result in a noised goal location actually about 1.4 cm far from the desired point. The fact that 7 grasps over 10 allowed the electromagnet to attract the plate is encouraging (with respect to a target error of 1.4 cm), yet not exciting.

However, the presence of the electromagnet suggests the possibility of performing a sort of *partially-blind grasp*. A blind grasp is meant to be a strategy to be applied when the vision system is not particularly reliable. According to this strategy, the robot is first commanded to reach the estimated grasping point and, if the contact between the object and the gripper is not detected, the robot starts following a predefined pattern inside a square of the known side, similar to the one shown in Fig. 4.36. The basic idea is to span a small area around the estimated grasping point to exploit the magnetic attraction to cope with pose estimation errors due to a non-ideal vision system calibration. This motion pattern corresponds to a planar motion occurring at a given height with respect to the metal plate, so it can allow to successfully compensate uncertainties on the xy plane. However, the success of blind grasping is highly dependent on the distance between electromagnet and garment. That distance, in turn, depends on the thickness of the cloth. To get a more generalized planning strategy, further investigations are needed. Notice also that if the plate dimensions are not sufficiently small and the attraction occurs near the borders, the grasp might be unstable.

In principle, the blind grasp could be taken to extremes to perform a *totally-blind grasp*, when the vision system is not present at all and a minimal *a priori* knowledge of the environment is given (*i.e.*, size and pose of the table where the cloth is located).

4.4.4.5 On common small objects with metal parts

This set of experiments was aimed at having insights on the Mag-Gripper capabilities of grasping objects different from clothes. We proposed Mag-Gripper as a tool for service robots suitable in home settings or assistive robotics. In this respect, it could be useful to have a robot capable of grasping small objects of common usage. In particular, we considered objects (*i.e.*, comb, hair barrettes, and paper clips) difficult to grasp either with a parallel-jaw gripper either with a more complex robotic hand, usually needing environment exploitation [183]. The challenging nature of these objects relies on the fact that they are flat and thin. The electromagnet was capable of generating a visually appreciable attractive motion, that allowed the grasps without the end-effector needed to reach the tabletop. As a note, we want to point out that the metal part located on the object could be small and lightweight, depending on the object: in a hair barrette, it consists of a spring of length 5 mm.

4.4.5 Conclusions

In this work, we have proposed Mag-Gripper , a novel augmented jaw gripper designed for autonomous clothes manipulation. The only working assumption is to deal with garments provided with small metal parts. Mag-Gripper is equipped with an electromagnet: The electromagnet is exploited to establish an extended point-like contact with the garment, while the jaws allow secure grasp maintenance during the manipulative motion. Experiments performed with a collaborative robotic arm showed that the exploitation of the magnetic force allows to perform a repeatable grasp execution and to compensate vision-related planar uncertainties on the estimated pose of the target grasping point. Moreover, the extended point-like contact caused by the electromagnet allows to perform grasp without unnecessary wrinkles, achieving clothing configurations more suitable to vision-based Machine Learning techniques for autonomous manipulation. Future work will focus on testing the gripper in robotic setups for bimanual autonomous clothes manipulation. Moreover, the proposed *blind grasp* strategy will be further investigated, as a method to be applied when the vision system is not sufficiently reliable.

4.5 Grasping with the SoftPad, a soft sensorized surface for exploiting environmental constraints with rigid grippers

A common trend in robotic manipulation is to build compliant hands that can exploit environmental constraints to perform robust grasps. However, in large-scale industrial applications, end-effectors are mostly rigid. How can we exploit environmental constraints using rigid industrial grippers? We propose to add compliance to the environment, thanks to a soft modular pneumatic surface: the SoftPad. Pressure sensors connected to its modules allow to estimate the object pose and center of mass and to detect the contact between the gripper and the SoftPad during a grasping task. A new grasp strategy that exploits such information for top-grasping objects, without using cameras or force sensors, is presented. It was tested with objects having a wide range of sizes, shapes, and weights. The SoftPad design can easily be adapted to the set of objects that are used in a certain application.

4.5.1 Introduction

The field of soft robotics has greatly changed researchers' perspective on robotic grasping, introducing new hands and grippers [187] that allow grasping and manipulation strategies that were inconceivable with rigid hands. Differently from classical rigid robotic hands, soft hands can safely interact with constraints present in the environment [188]. Thus, grasp planning with soft hands does not rely on exact models and precise positioning of contact points, but aims at using the direct physical interaction with the environment to constrain and grab the object (Fig. 4.37-(left)) [189, 190]. This is not possible with rigid grippers (Fig. 4.37-(center)). Rigid robots, however, still have important features that are difficult to obtain with soft robots, such as the precision and repeatability of movements, as well as the possibility of having accurate measurements through sensors. The different features of soft and rigid hands make them suitable for distinct applications. Soft hands are more used in collaborative and assistive robotics [191], while industrial picking still relies mainly on rigid grippers [192].

In this work, we propose a novel solution to take advantage of the strengths of both soft and rigid robotics approaches. We propose to use rigid robotic grippers while adding compliance to the surface laying beneath the objects to be grasped (Fig. 4.37-(right)). In other terms, we shift the focus from the gripper to the environment. This is achieved by introducing a grasping strategy that exploits the *SoftPad*, a matrix of silicone pneumatic modules connected to pressure sensors that, when placed beneath an object, can be used to detect object pose, shape, and center of mass based on pressure variations. Given the estimated center of mass, a planner computes the center and the direction of the grasp that can be used by a robotic gripper to pick the object up. Thanks to the SoftPad, grasps can be performed without the need of a camera to locate the object and without prior knowledge on its mass distribution or its shape. Besides, the gripper can safely interact with the soft surface, coping with uncertainties on the object pose and achieving more robust grasps thanks to environmental constraints exploitation strategies [188]. Our approach goes beyond classical vision-based object detection strategies [193, 194], as it allows to estimate the center of mass of the object, not only its pose and shape. Besides, there

Fig. 4.37 Soft hands, like the RBO Hand 2 [196], can easily interact with rigid surfaces for grasping objects (left), rigid grippers, instead, cannot safely exploit the environment (center). We propose a soft sensorized surface (right) that allows rigid grippers to exploit the environment to pick objects up and provides a grasp planner with information on object pose and weight distribution.

is no need to add force sensors to the robot [195, 189], as the sensorized modules can detect the contact between the gripper and the SoftPad.

Previous work showed that pneumatic devices can effectively be used for force and pressure sensing. In [197], for example, pneumatic chambers are used to detect obstacles with a robotic cleaner, whereas in [198, 199] pneumatic cushions are used to measure forces exchanged between a human and a robotic system in two different scenarios. More recently, pneumatic sensors were developed for manipulation [200] and for robotic surgery [201]. All previously presented works focus on adding softness and sensing capabilities to robotic devices themselves. Here we show that pneumatic sensing is a viable solution to create compliant and sensorized inclusions to instrument the environment for facilitating grasping tasks with rigid grippers.

In principle, combining an elastomeric layer with an array of tactile sensors could lead to a device comparable to the SoftPad. Nonetheless, we have preferred the pneumatic solution, which has several advantages with respect to other technologies. First, the size (width, length, and thickness) of pneumatic modules is completely customizable. This feature is shared with other sensing technologies like soft sensors based on liquid metals or pressure sensitive conductive sheets (*e.g.*, Velostat). However, their use still presents some challenges. In liquid metals sensors, none of the patterning methods is yet high-throughput, the interface between soft and hard materials within the device is still an issue, and studies should be performed on the effect of the oxide presence [202]. Using conductive sheets, common problems include the large crosstalk between adjacent cells and low accuracy [203].

Moreover, we chose to rely on pneumatic technology because it allows to create soft devices that can be used both as sensors and as actuators [204]. In our case, for example, the possibility of inflating more or less the pneumatic chambers is fundamental, as it allows to adapt the stiffness of the modules to support and sense objects with different weights. This would not be possible by simply placing a matrix of tactile sensors under a soft passive layer. In [205], soft actuation and soft sensing are combined for body pressure sensing but are obtained with

different technologies. Another advantage of using pneumatic systems is that the electronics can be delocalized [201], ensuring a high-temperature resistant and washable device in the work-space.

The work is organized as follows. The SoftPad design is described in Section 4.5.2, where also a comparison between the real device and its Finite Element model (FEM) is carried out. Section 4.5.5 introduces the grasp planning algorithm taking advantage of the pressure readings from the SoftPad which is then tested with several experiments in Section 4.5.8.

4.5.2 The SoftPad

In this section, the SoftPad structure and its manufacturing processes are described. Then, a FEM simulation framework to study the device behavior is introduced. Here we will focus on the specific SoftPad that was built to test the grasping strategy described in Section 4.5.5 and that is shown in Fig. 4.38a, but the device features (size, material, stiffness, *etc.*) can be customized depending on the specific application.

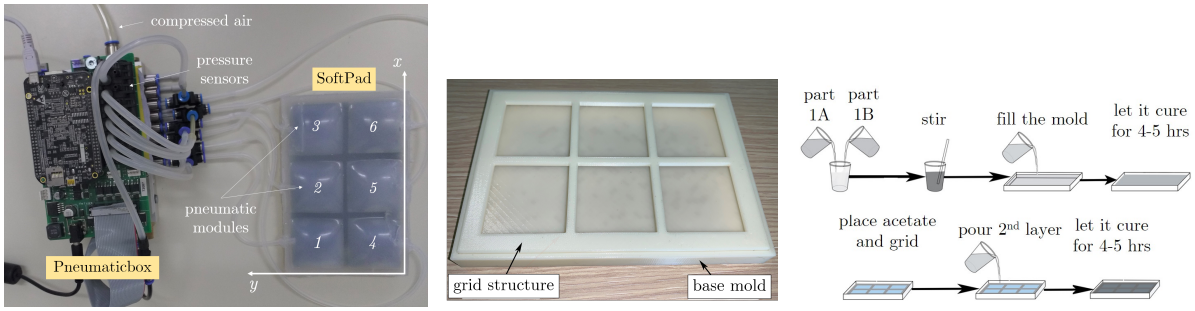

(a) (b) (c)

Fig. 4.38 (a) SoftPad and Pneumaticbox used in the experiments. (b) 3D printed mold and grid structure for building the SoftPad. (c) Complete process flow to develop a SoftPad.

4.5.3 Device description

The proposed device consists of a 2×3 matrix of pneumatic modules. Each module is 45×45 mm, with a total height of 10 mm, of which 1.5 mm constitute the inflation layer. The overall size of the SoftPad is $165 \times 115 \times 10$ mm. The size of the module can be chosen according to the required spatial resolution and to the size of the objects. Smaller objects, for instance, require smaller modules to well detect their shape. For developing the SoftPad, we followed similar guidelines as that described in [206]. The process starts by designing a mold consisting of a base and a grid both realized in ABS material, as shown in Fig. 4.38b. The material used for the SoftPad is the EcoFlex silicone with a shore hardness of 00-30[3].

The Ecoflex silicone is a platinum-catalyzed silicone that is versatile and easy to use. It comes in two parts: A and B. The optimal mixing ratio (weight or volume) to achieve a smooth and well cured elastomer is $A/B = 1$. The molding process is shown in Fig. 4.38c. The first

[3] https://www.smooth-on.com/tb/files/ECOFLEX_SERIES_TB.pdf

layer, which serves as a base for the SoftPad, is cast with silicone as per the predefined height. Once the filling is completed, the elastomer is left to cure for 4-5 hours. The next step is to divide the structure into a number of small squares (which will serve as soft modules) by using the grid part. To define a pneumatic channel in each square, a 45×45 mm piece of acetate is placed on top of the first layer. The purpose of acetate is to allow the silicone elastomer to flow around it without adhering, establishing an inner channel. Lastly, the second layer of silicone is cast on top of the acetate and the mold is filled as per the required height, 1.5 mm in our case. Again, the second layer has to cure for 4-5 hours. To avoid bubble formation, the two parts must be mixed and stirred very thoroughly for at least 3 minutes, and the curing phase must occur in a heating chamber. The height difference between the base and the upper layer of the SoftPad enables the modules to be very soft on the top and considerably rigid on the other side, hence, minimizing the downward inflation. To further reduce downward inflation and enable smooth upward inflation, a sheet of neoprene was embedded inside the base layer. High strength silicone tubes SPX-60 FB Versilon were placed in each module by inserting them through a small hole made with pointed end tweezers at the level of the acetate. Liquid silicone was put around the circumference of the tubes to avoid air leaks.

The tubing was connected to the Pneumaticbox, which was used to control the inflation and deflation of the modules. The Pneumaticbox is a control system developed to enable fast, real-time control of pneumatic systems. It can provide up to eight independently controlled channels, each equipped with two discrete valves for inflation and deflation, and a differential pressure sensor. All sensors and valves are connected to a BeagleBone Black embedded computer which is the main processing unit for the Pneumaticbox.

4.5.4 FEM simulation

A Finite Element Method (FEM) simulation has been set up to analyze the main structural properties of the SoftPad. Comsol Multiphysics® software was used for the simulations.

For the sake of clarity, only one pneumatic module was considered. The geometrical model of the SoftPad consists of a mesh with 5106 tetrahedral elements. A surface pressure loading p is applied to the lower surface of the pneumatic module, while its external boundaries are blocked with a fixed constraint.

We assumed a hyperelastic material, nearly incompressible with quadratic volumetric strain energy [207]. Since the main properties of the material vary in a wide range and the manufacturing process may be affected by some uncertainties, the first set of simulations were realized to identify material properties (Young's modulus, Shear Modulus, Poisson's ratio, bulk modulus, and mass density). In these simulations, a constant pressure value varying from 0.5 to 2.8 kPa was applied and the overall displacement in the center of the pneumatic module was evaluated. Pressure values varying in the same range were applied to the real SoftPad and the corresponding physical deformation was measured. Results are shown in Fig. 4.39a. In the same figure, also the results obtained by applying an external force in the center of the module, with different force magnitude values, are reported. The indicated minimum and maximum pressure values were chosen by observing the SoftPad behavior, as explained in Section 4.5.8. Other simulations were conducted to study how the sensitive area of a module changes with

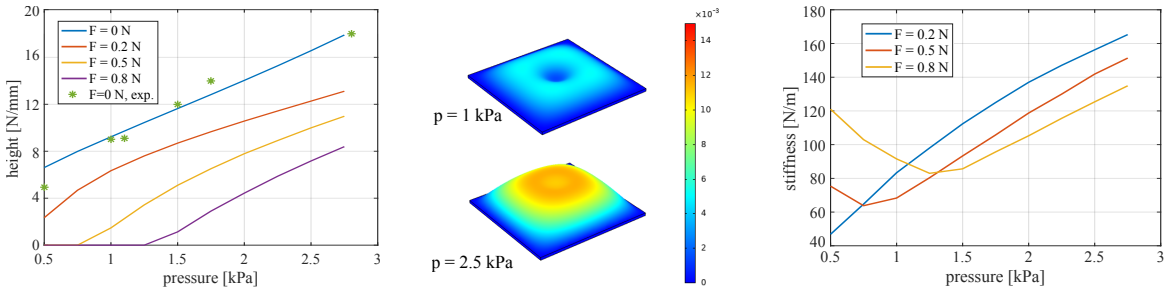

(a) (b) (c)

Fig. 4.39 FEM model of the SoftPad. (a) Height of a module as a function of inflating pressure, comparison between simulation results (continuous curves) and experimental measurements (green dots). (b) Deformation (in m) of the module for different inflating pressures (1 kPa, 2.5 kPa), and an external load $F = 0.5$ N applied in the center. (c) Equivalent mean stiffness of a module as a function of inflating pressure: simulation results for different external forces.

respect to the inflating pressure. The sensitive area of a module approximately corresponds to the 3D surface of a spherical cap with a square basis having side l.

For the analyzed configuration, l varies from ≈ 20 mm for low pressures (0.5 kPa) to ≈ 45 mm for higher pressures (2.8 kPa). Fig. 4.39b shows the module deformation (in m) obtained for two different inflating pressures ($p = 1$ and $p = 2.5$ kPa) when simulating the application of an external normal force $F = 0.5$ N in a central circular area with radius $r = 5$ mm. Note that the deformation around the borders is limited.

The second set of simulations was carried out to estimate the mean equivalent stiffness in the vertical direction of each pneumatic module. To this aim, a vertical force was applied on a circular area with a radius $r = 1$ cm in the center of the module, with an equivalent resulting magnitude $F = \{0.2, 0.5, 0.8\}$ N. We measured the corresponding deformation of the module, for different inflating pressure values, and compared the displacement in the vertical direction of the module center h_{load} with the value obtained without external forces, h_{free}. We, therefore, evaluated the equivalent stiffness as $k = F/(h_{free} - h_{load})$. Obtained results are reported in Fig. 4.39c. For low force values, k increases as p increases, as expected, while for high force and/or low pressure, the overall module deformation caused by force application is such that the upper silicone layer contacts the lower one and the corresponding stiffness is therefore higher. A decrease in the equivalent stiffness as the applied force magnitude increases can be furthermore observed.

From the sensing point of view, varying the inflating pressure allows to change the measurement range and sensitivity of the device. For high inflating pressures, for example, modules are less sensitive to external deformations, because they are stiffer, but they can resist higher forces and thus detect heavy objects without collapsing.

4.5.5 Grasping with the SoftPad

This Section describes a grasping strategy that allows a rigid gripper to perform top-grasps of objects placed over the SoftPad. Pressure readings coming from the SoftPad are used in the

grasp planning phase to estimate the pose and the center of mass of the object to be grasped, and during grasp execution to detect the contact between the robotic gripper and the SoftPad. In both phases, the algorithm is based on the evaluation of the pressure increments ΔP_i in each module i.

4.5.6 Grasp planning

When an object is placed on the SoftPad we assume that there is a contact between the object and the modules in which we detect an increment of pressure with respect to the initial inflating value higher than a threshold t_o.

Note that when a variation of pressure occurs in a module, it is not possible to

estimate the exact location of the object over the module itself from the sole pressure measurement. For the same pressure variation, there could be a lighter object covering the whole module surface or a heavier object covering a smaller portion of it: since the only information we rely on is given by pressure measurements, we cannot distinguish these two cases. Thus, the size of the module should be chosen on the basis of the size of the objects that have to be grasped in a certain application. If the objects are too small and cover just one module, most of the benefits of using the SoftPad would be lost.

The outcomes of the grasp planning phase are the center and direction of the grasp for a rigid parallel-jaw gripper. To compute them, first all the modules are inflated to the same pressure, to ensure that they all reach the same height, and then the center of mass of the object is computed.

4.5.6.1 Initial inflating procedure

Before starting to use the SoftPad, it should be inflated to a desired initial pressure. By changing the value of the inflating pressure it is possible to change the compliance of the SoftPad according to the set of objects that must be grasped. A highly compliant SoftPad detects lighter objects that generate variations of pressure which would not be detected by more rigid modules. For heavy objects, modules inflated at a low pressure would collapse, hence, it is preferable to use considerably higher inflating pressures (see the simulation results in Fig. 4.39a: for high force magnitudes and low pressure values, the pad crashes on the lower layer and its height drops to zero).

To guarantee the proper functioning of the algorithm and the repeatability of the experiments, it is important that each module is inflated at the same initial inner pressure. This ensures that the heights of the six modules are the same, and thus the object is not tilted when placed on the SoftPad.

If before the placement of the object the pressure in one or more modules differs from the selected initial pressure of a value greater than a certain tolerance t_{adj}, an automatic procedure will inflate/deflate it accordingly. Tolerance should be chosen as a compromise between accuracy and length of the adjustment phase. After the adjustment procedure is finished, the current pressure of each module is measured and saved as a reference value. Then, an object can be placed over the SoftPad and its center of mass can be evaluated starting from the new pressure readings, as explained in the following.

4.5.6.2 Estimation of the center of mass

We consider the object as a discrete system composed of as many masses as the number of modules in contact with the object, each of them placed in the center of the corresponding module (see Fig. 4.40a). The center of mass of the object is estimated by computing a weighted average of the variations of pressure ΔP_i, $i = 1, \ldots, N$, where N is the number of modules in contact with the object.

The resulting point is called *Pressure-based center of mass*, or *PCOM*, and is computed as:

$$x_{PCOM} = \frac{\sum_{k=1}^{N}(\Delta P_i x_i)}{\sum_{k=1}^{N}\Delta P_i}, y_{PCOM} = \frac{\sum_{k=1}^{N}(\Delta P_i y_i)}{\sum_{k=1}^{N}\Delta P_i}. \tag{4.8}$$

Considering the reference frame shown in Fig. 4.40a, x and y range in a discrete set of values: $x_i = \{0.5, 1.5, 2.5\}$ and $y_i = \{0.5, 1.5\}$.

Note that, from these assumptions, the two objects in Fig. 4.40b have the same *PCOM*, even if they have different shapes. In Fig. 4.40b-(3), module 1 is only partially covered by the object, and this information is taken into account thanks to the fact that most of the pressure variation is sensed in module 4, as the object is shifted towards it. In Fig. 4.40b-(4), the object is equally placed over the two modules but has a mass distribution that generates a higher pressure variation in module 4.

4.5.6.3 Computation of center and direction of grasp

To identify the grasp, two parameters are required: a point on the object over which the gripper's center should be aligned (*center of grasp* or *COG*) and an angle θ identifying the orientation of the gripper (*direction of grasp*). Angle θ ranges from $-\pi/4$ to $\pi/2$, considering that it is equal to 0 when the direction of grasp is parallel to the SoftPad x-axis.

As a first step, the planner counts the number N of modules touched by the object. If the N modules are not adjacent (not even in diagonal), the algorithm assumes that there are at least two objects on the SoftPad, since bridge-shaped objects are not taken into account. In this case, the algorithm treats them separately, to grasp them in sequence. Depending on the value of N, *COG* and θ are evaluated with different procedures. The SoftPad that we designed has six modules, this is why in the following we describe six different cases. However, the described computations can easily be extended to more modules, as more complex cases can be treated, with some adjustments, as simpler cases.

• **N = 1.** The *COG* corresponds to the center of the module, *e.g.*, (0.5, 1.5) for module 1. The direction of the grasp can be chosen by default, *e.g.*, $\theta = 0$. Note that the 1-module object is a limit case of our algorithm, because, as we wrote at the beginning of this section, we cannot retrieve information about its shape.

• **N = 2.** The algorithm detects if the object is horizontal, vertical, or diagonal. As shown in Fig. 4.40c, the *COG* corresponds to the *PCOM*, which is always on the major axis of the object (dashed red line). The direction of the grasp is perpendicular to the major axis. For example, if the object is vertical, $\theta = 0$ and *PCOM* have the same x of the center of the two modules, while the y depends on the weight distribution of the object.

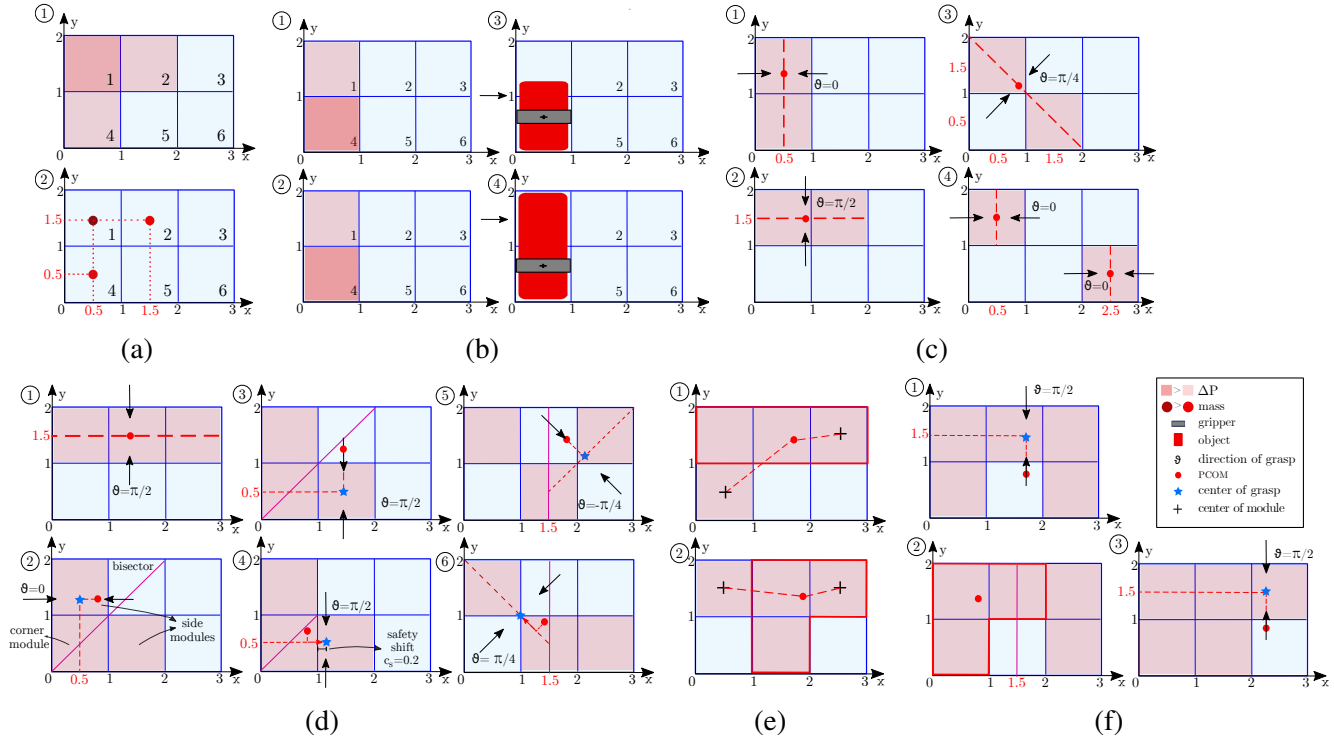

Fig. 4.40 Illustration of the working principles of the SoftPad based grasp planning strategy, from simpler to more complex cases. Note that while in (a) and (b) different shades of pink are used to denote different ΔP to let the user familiarize with the *PCOM* computation, this detail is omitted in other figures for the sake of clarity.

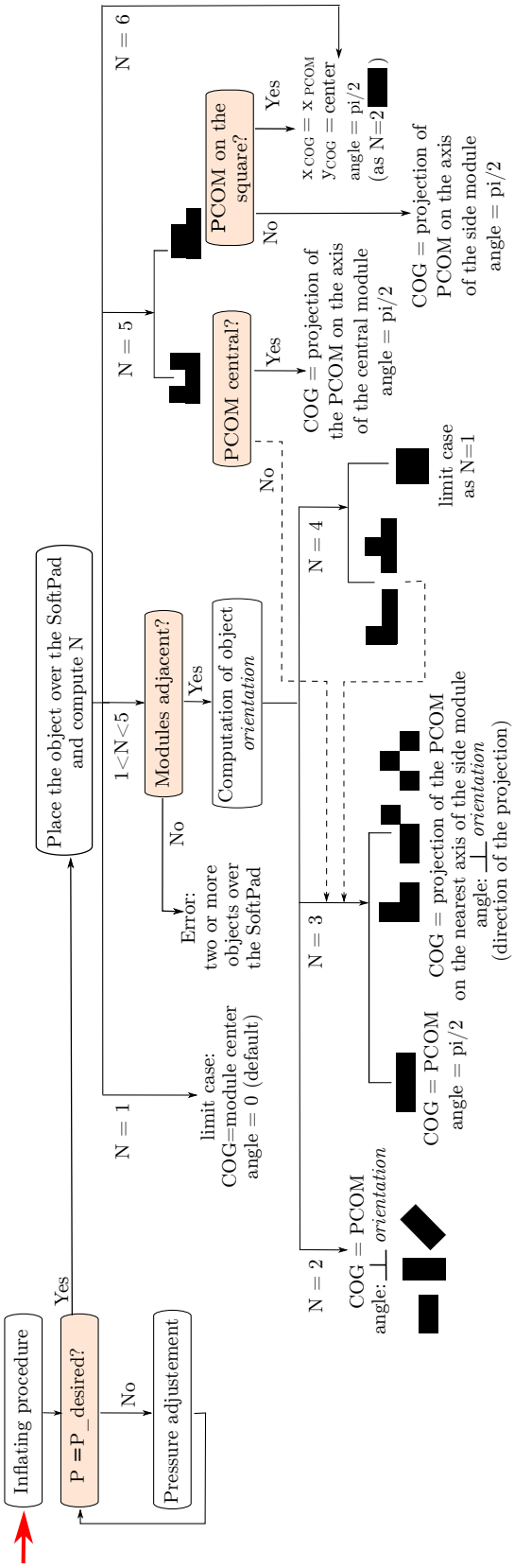

Muhammad Zubair Iqbal
30.08.2021
23:25:19
GMT+01:00

Fig. 4.41 Diagram of the grasp planning algorithm that outputs center and direction of grasp. The red arrow shows the starting point. Pink squares represent if-statements. Dotted lines indicate that one case can be simplified and treated as if it involves a lower number of modules.

• ***N* = 3.** As shown in Fig. 4.40d-(1), if the object is horizontal, the *COG* corresponds to the *PCOM* and the direction of the grasp is vertical ($\theta = \pi/2$). If the three modules are in a "1" configuration as in Fig. 4.40d-(2)(3)(4), the *COG* may not coincide with the *PCOM*. Since we are considering a discrete system of masses, when they are not aligned, the *PCOM* can also fall outside of the involved modules. The *COG*, instead, has to be on the axis of one module belonging to the object to allow the gripper to grasp the object. Let us call *corner module* the one in the middle, *side modules* the other two, and *bisector* the line starting from the outer corner of the corner module and dividing the object in two equal parts (Fig. 4.40d-(2)). Since the exact shape around the corner is not known, it is safer to grasp along one of the two side modules rather than on the corner module. If the *PCOM* is in one of the side modules or outside of the object, it is projected on the axis of the side module itself (Fig. 4.40d-(2)) or of the nearest one (evaluated with respect to the bisector) (Fig. 4.40d-(3)). If *PCOM* falls on the corner module, as in Fig. 4.40d-(4), the position of the *COG* is obtained by projecting the *PCOM* on the closest axis of the corner module and then shifting it towards the center of the nearest side module. A safety margin c_s is thus added either to the x (Fig. 4.40d-(4)) or to the y of the *PCOM*. This *safety shift* is important since our algorithm does not give any information on the shape of the corner of the object. In our experiments we used $c_s = 0.2$.

The direction of the grasp is the direction of the projection on the axis.

Similar reasoning applies for cases like those shown in Fig. 4.40d-(5)(6), where it is difficult to do assumptions on the object shape along the diagonal parts. In these cases, the bisector is considered vertical and the direction of the grasp can be either $\theta = 0$ or $\theta = \pm\frac{\pi}{4}$, depending on the direction of projection of the *PCOM*. When the projection of the *PCOM* falls on the axis of the corner module, as in Fig. 4.40d-(6), it is preferable to move the *COG* to the nearest corner of the side module.

• ***N* = 4.** A limit case is an object occupying a square of 2×2 modules. This case, similarly to the 1-module case, is treated choosing the direction of the grasp by default, while the *COG* is the center of the square. In all other cases, to simplify the algorithm and make it as scalable as possible, we do not consider one of the modules at the extremities and treat the object as it is 3-modules. The module which is not taken into account is the one whose center is the farthest from the *PCOM* (see Fig. 4.40e), *i.e.*, the one which affects less the *PCOM* position. In this way, central modules (2 and 5 in the Fig. 4.40a) are never removed and the original shape is changed only far from the *COG* so that a safe grasp is always achieved. Taking Fig. 4.40e-(1) as an example, after re-shaping the object as it is a 3-modules object it appears as a rectangle. If the gripper tried to grasp it from module 1, it would hit the portion of the object in module 4. However, since the removed module is always far from the *PCOM* and thus is the *COG*, this will never happen.

• ***N* = 5.** The grasping strategy depends on the position of the module that is not touched by the object. When modules are in a horseshoe, if the *PCOM* falls in the central modules 2 or 5 (as in Fig. 4.40f-(1)) the safest grasp is obtained projecting the *COG* to the axis of the central module covered by the object, because the weight of the object is well-balanced on the x-axis. If the *PCOM* falls anywhere else, for the sake of simplicity and scalability all the cases can be reduced to a 3-modules object case. If *PCOM* is on the left of the vertical bisector ($x_{PCOM} < 1.5$) modules 3 and 6 are removed (Fig. 4.40f-(2)), otherwise 1 and 4.

When modules occupy a 2×2 square plus a single module, if the *PCOM* falls in the square, the direction of the grasp is vertical ($\theta = \pi/2$), $x_{COG} = x_{PCOM}$, and $y_{COG} = 1$. Otherwise, the *COG* is obtained by the projection of the *PCOM* onto the axis of the single module (Fig. 4.40f-(3)).

• ***N* = 6.** The *COG* corresponds to the projection of the *PCOM* on the major axis of the SoftPad, and the direction of the grasp is vertical ($\theta = \pi/2$).

The complexity of the algorithm would increase with the number of modules. Thus, for $N > 6$, the idea is always to evaluate only the area around the *PCOM*, leading back the problem to simpler cases. Fig. 4.41 summarizes the main steps of the grasp planning strategy. Note that the *COG* computed as in this section is expressed in a reference frame where a unit corresponds to the side of a module (Fig. 4.40a). In this way, all computations can be generalized to SoftPads with modules of any size.

4.5.7 Grasp execution

After multiplying the components of the *COG* by the length and width of the SoftPad, the obtained *COG* and θ are sent to a robot arm equipped with a rigid gripper, that moves toward the desired grasping pose over the object. Once it reaches the computed grasping pose, the gripper starts moving down towards the SoftPad. The advantage of having a soft surface underneath the objects is that we do not need to precisely control the vertical motion of the manipulator, since the fingers can safely touch the SoftPad and slide over it, after caging the object. As soon as the pressure in the SoftPad due to the contact with the gripper overcomes a threshold t_g, the arm is stopped and the gripper is closed to grasp the object.

The actual amount of sliding motion performed by the gripper fingers depends on object size and gripper opening. If, for example, the object to be grasped has a larger height than fingers' length, the gripper will start closing as soon as its center touches the object, as also in this case a variation of pressure is sensed by the SoftPad. If the object, instead, is not as tall as the fingers and does not cover the whole area of the module in the direction of grasp, as in Fig. 4.37-(right), there is free space between the object and the jaws. The gripper will thus cage the object and start closing after touching the SoftPad, performing a *surface-constrained grasp* [188].

4.5.8 Experiments

The grasp planning strategy described in Section 4.5.5 was tested for 13 different objects, covering most of the cases that the algorithm can account for. To perform the planned grasps, we used a Sawyer collaborative robot arm equipped with a parallel jaw gripper with 9.5 cm long fingers. Depending on the object to be grasped, the gripper was mounted in three different ways, achieving a maximum width of $\{10, 6, 4\}$ cm respectively, and a corresponding minimum width of $\{4, 2, 0\}$ cm. During the experiments, the grasp execution was implemented as described in Section 4.5.7: the gripper was automatically positioned and oriented over the object according to the center and direction of grasp outputted by the grasp planner, and then closed on the object as soon as the pressure threshold t_g was overcome. The SoftPad inflation and reading,

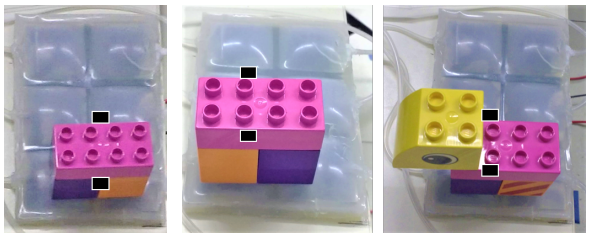

(a) (b)

Fig. 4.42 (a) Simple object (weight=38 g) laying on two modules: planned grasp ($COG = (0.5, 0.96)$, $\theta = 0$). (b) Two objects that have a similar plan: the one on the left because it is shifted towards module 1 ($COG = (0.5, 1.18, 0)$, $\theta = 0$), the one on the right (54 g) because it is heavier in correspondence to module 1 ($COG = (0.5, 1.21)$, $\theta = 0$).

the robot controller, and the information exchange between the SoftPad and the robot were implemented in ROS [208].

At the beginning of each experimental session, the SoftPad was inflated to achieve a pressure of 1.1 kPa in each module, corresponding to a height of 9 mm. We observed that the range of possible inflating pressures goes from 0.5 to 2.8 kPa. For lower values, the SoftPad is almost deflated and the evaluation of the variation of pressure in each module is not feasible. For higher values, modules become too stiff and their shape is such that the object cannot be stably placed over them. For the initial pressure, we chose an intermediate value in this range.

In the experiments, the threshold for the grasp planner was chosen so that it was possible to detect one Lego Duplo piece (12.6 g, $42 \times 31 \times 31$ mm): t_o =0.05 kPa. In general, this threshold should be selected based on the lightest item in the set of objects that need to be manipulated. The threshold for the initial phase of pressure adjustment was chosen as $t_{adj} =$ 0.03 kPa, whereas the threshold for the detection of the contact between the gripper and the SoftPad was $t_g = 0.09$ kPa. Note that t_g must be chosen to accurately avoid any false positive due to oscillations of measurements, which during the contact detection would lead to close in advance the gripper. The value of t_g can be greater than t_o, because the impact of a rigid gripper moving towards the SoftPad is easier to detect, as it produces larger pressure variations. Raw pressure measurements from the Pneumaticbox were filtered using a running average filter of 10 samples. Two experiments are presented, one shows the detailed functioning of the grasp planning strategy, the other illustrates that the devised algorithm works for a variety of objects.

Experiment 1: Working principles of the grasping strategy

The functioning of the grasp planning strategy based on SoftPad readings is shown considering an object composed of three Lego Duplo pieces. Fig. 4.42a illustrates the planned grasp, whereas Fig. 4.43 reports pressure values for each module during the grasp execution phases: the initial adjustment of the internal pressure of the modules, the detection of the object, and the detection of the contact with the robot.

As depicted in Fig. 4.40b, there are cases in which the planned grasp is similar for two different objects (cf. Section 4.5.5). Fig. 4.42b shows an example of this situation involving 2 adjacent modules. An object shifted towards module 1 and another object with the base

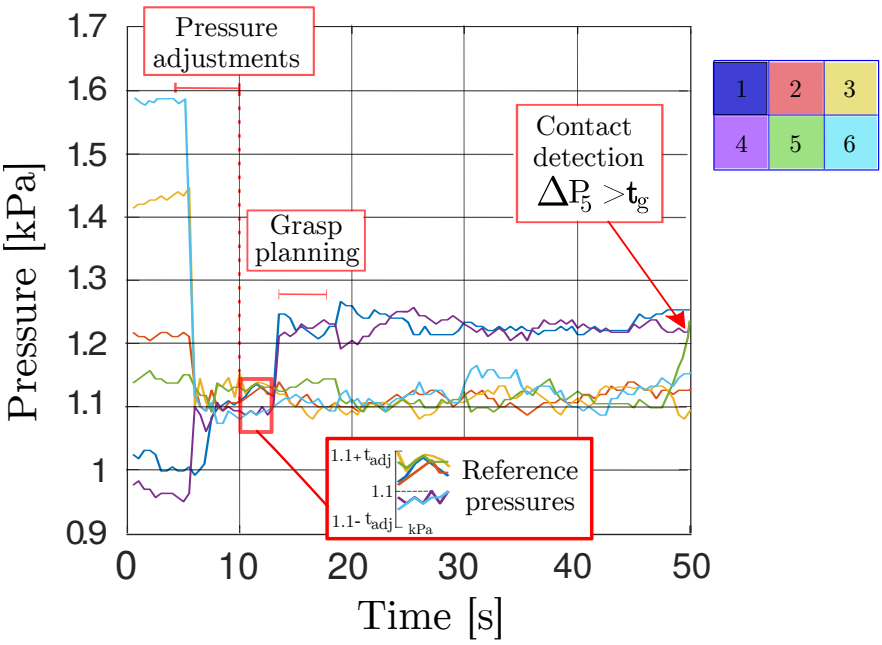

Fig. 4.43 Simple object laying on two modules: measured pressures during the grasping task. Having reliable data for the initial reference pressures and the pressures recorded after placing the object over the SoftPad is fundamental. Thus, after the pressure adjustments phase and at the beginning of the grasp planning phase, pressure values are read 10 times and the mean values are computed for each module.

centered between modules 1 and 2, but heavier in correspondence to module 1, are grasped similarly. The SoftPad not only detects objects' features but was primarily built for obtaining a safe gripper/environment interaction. Fig. 4.44 shows an experiment demonstrating that this aspect can also help to robustly grasp objects that cannot be picked up when laying on a rigid surface.

Experiment 2: SoftPad aided grasping of a variety of objects

We chose 11 different objects to show the potentialities of the grasp planning algorithm based on the SoftPad pressure readings. During the experimental trials, the robot approached the object with a velocity of 0.05 m/s, and each object was grasped and held for 15 s at a velocity of 0.05 m/s. For each object, we performed 5 trials. The planned center and direction of grasp obtained in one representative trial are depicted in Fig. 4.45 and reported in Table 4.10, where also objects' weights and success rate are listed.

Objects 1, 2, 3, and 6 are symmetric and with homogeneous weight, thus they were grasped from the middle. For objects 4 and 5, and for the charger, the center of the grasp is placed closer to the heaviest part of the object. The cylinder was filled with a heavy small part on one side, that is why the grasp center is not placed exactly in the middle of it. For the banana and the toy, the algorithm worked as in the case of 3-modules objects (Fig. 4.40d), while the limes were considered a 4-modules object (Fig. 4.40e).

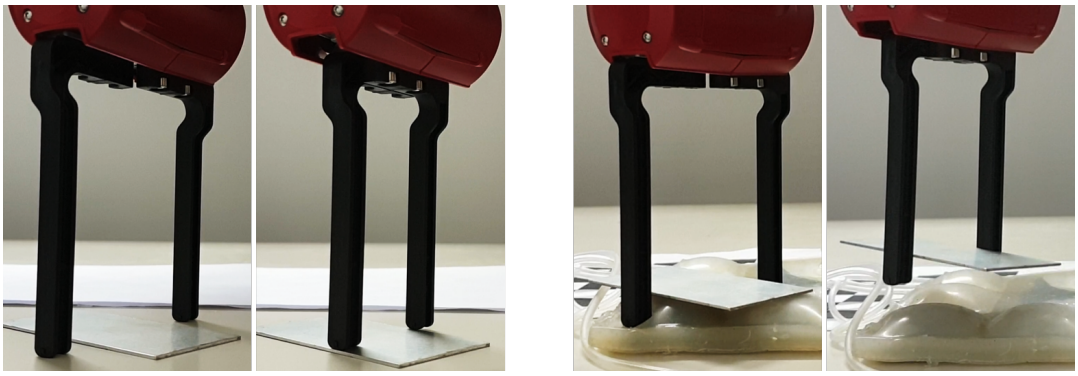

Fig. 4.44 A soft environment allows to safely and robustly grasp objects with a rigid gripper.

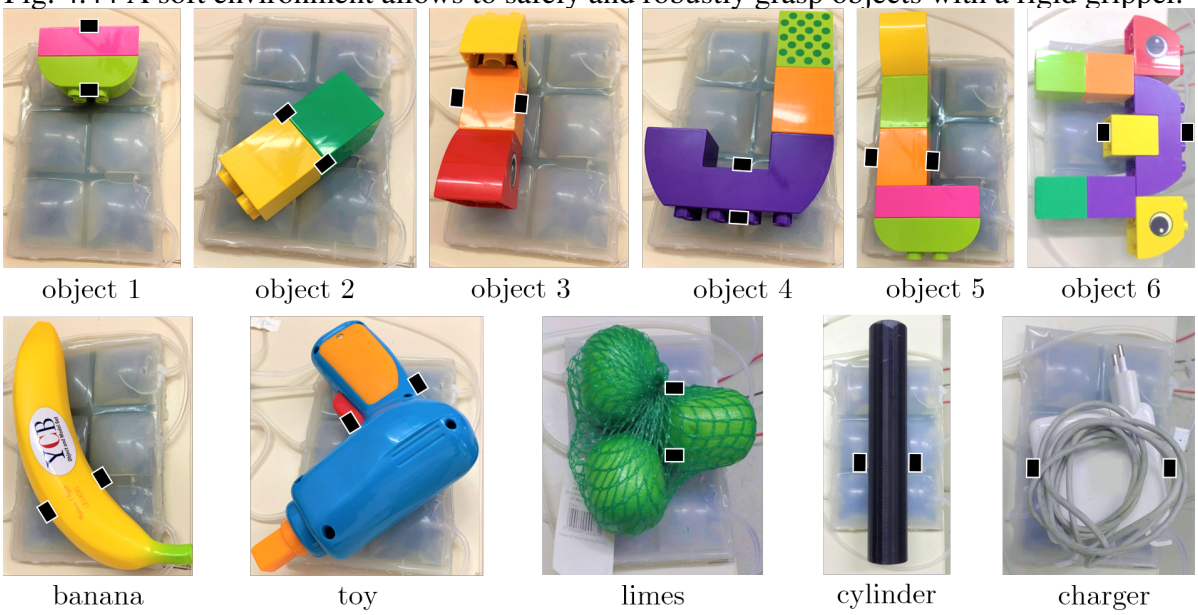

Fig. 4.45 Objects used in Experiment 2. The black rectangles indicate the planned position of the fingertips of the gripper.

Three failures were experienced. Two (object 5, charger) were due to a missing contact detection because the gripper touched the non-sensitive line between modules. The cylinder was not grasped in one case because the *COG* was not successfully detected, even if the angle of grasp was correct. These two issues could be easily overcome using a gripper with thicker tips and larger maximum width, respectively.

4.5.9 Conclusions

In this paper, we propose to exploit soft inclusions in the environment to perform robust grasps with rigid grippers. This is achieved through a grasping strategy that uses a sensorized soft layer, called SoftPad, to estimate object pose, shape, and center of mass. The great advantage of using the SoftPad with respect to having a vision system is the possibility to estimate the weight distribution. Besides, the same device can be employed to sense the contact between the gripper

Table 4.10 Weight, representative planned grasp, and success rate for the objects in Fig. 4.45. The banana and the Lego Duplo pieces are taken from the YCB Dataset [209].

Object	Weight (g)	Planned grasp $(x_{COG}, y_{COG}, \theta)$	Success rate
object 1	23.8	$(2.5, 1, 0)$	$5/5$
object 2	25.3	$(1.04, 0.96, \pi/4)$	$5/5$
object 3	44.4	$(1.5, 1.5, \pi/2)$	$5/5$
object 4	52	$(0.5, 1.2, 0)$	$5/5$
object 5	64.9	$(1.36, 1.5, \pi/2)$	$4/5$
object 6	122	$(1.55, 0.5, \pi/2)$	$5/5$
banana	59.8	$(1, 1, -\pi/4)$	$5/5$
toy	131.6	$(2, 1, -\pi/4)$	$5/5$
limes	187	$(1.5, 0.8, 0)$	$5/5$
cylinder	88.9	$(1.14, 1, \pi/2)$	$4/5$
charger	312.3	$(1.16, 1, \pi/2)$	$4/5$

and the SoftPad, thus performing the role that is usually left to force sensors placed on the hand fingertips or at the robot arm wrist. The grasp plan computation is based on assumptions that might not be valid for all objects, but, on the one hand, the possibility of sliding over the SoftPad solves possible uncertainties on the object pose, and, on the other hand, the SoftPad parameters (thresholds, inflating pressure) and physical characteristics (size, shape, material) can be changed depending on the application. The SoftPad concept is a first step towards the instrumentation of the environment with soft inclusions for exploiting extrinsic, adaptable compliance during grasping and manipulation tasks performed by rigid grippers. A similar device could be, for example, integrated inside a conveyor belt in a factory, or even placed over more complex surfaces thanks to its intrinsic compliance. In future work, we target to improve the grasping algorithm in terms of scalability and to investigate how to adapt the compliance of the SoftPad to ensure a safe and stable impact even in case of high robot velocities. We will also advance the simulation framework, to achieve a platform for the iterative design of the SoftPad.

Chapter 5

Conclusions

In the present era, we see a lot of conventional assistive application devices as well as devices for industrial application like manipulating objects, performing grasp operations, pick and place operations, etc. This thesis presents my contribution to the design and development of devices for rehabilitation and industrial applications. It is a collection of all of the work I carried out during my Ph.D. degree at the University of Siena. The main focus of this research was the development of devices that can be useful for rehabilitation purposes and the design of industrial grippers that can be used for grasping and manipulation operations. All devices have guiding principles that involve safety, ergonomics, and user comfort.

The thesis presented in Chapter 1 an introduction to the design of the device and developed. It depicted a literature review about rigid and soft devices being used. Explaining the structure of the thesis and different devices developed that are being used for research. The main challenge is the design of the robotics devices to fulfill the ergonomics in the case of mainly assistive devices and functional requirements for both assistive and industrial devices.

Chapter Chapter 2 has presented the modeling principles used for the design of these devices. It emphasizes the principle that we use to model the soft and rigid parts of the device for example in the case of Dual Sixth Finger, which is composed of soft and rigid links. Similarly, the modeling principle that we use for the model of Finray Sixth Finger. As Soft and Rigid parts are the most important parts since it forms a finger structure, modeling principle is very important to predict effectively the trajectory of the finger before realization using 3D Printer. In the case of soft rigid links, after devising the model, the model testing is also carried out on a physical prototype. Two fingers gripper is used to validate the model, different grasp operations are also performed with the gripper. Similarly, for the case of the Finray Mechanism model, model validation is carried out by comparison between the manufactured model of the finray finger and carrying out Finite Element Analysis. Later, a device is also developed to carry out different activities of daily livings.

Chapter 3 has presented the design and development of three assistive / rehabilitation devices. The first device introduced is a Multiple wearable robotic extra fingers device, that composed of two fingers, made up of soft and rigid links. The fingers can be rotated in different orientations thanks to the dovetail mechanism installed at the base of each finger. Each finger consists of seven soft and seven rigid links, where each soft and rigid link forms a module. A differential mechanism is also installed at the forehand part which allows a firm grasp of

the object we intend to pick and place. The device aims to facilitate the people with stroke, who have limited or no function of their hand. This device acts as an assistive device that helps the stroke patient to carry out different activities of daily life with ease and comfort, without being dependent on any other member of family or friends. Similarly, the second device introduced in this chapter is another assistive/rehabilitation device. It is another robotic finger device based on the effect of FinRay. The device is realized with ABS material with ribs made up of metallic pins. The device uses a linear actuator to provide flexion and extension of the finger. It is controlled by EMG based Interface that recognizes the signals by the up and down movement of frontalis muscles. It is very lightweight and provides enough force for firm grasping and manipulation of the objects. The third device introduced in this chapter is the Hand/Wrist Exoskeleton for Rehabilitation and Training. This is a device developed for patients/people who suffer from wrist and hand impairments. These people have limited movement of wrist and hands, and, need sessions from physiotherapists for rehabilitation. The device aims to make life easy for these people, by providing them with a solution that they can use at home to carry out rehabilitation/training exercises. The device consists of a mechanism to carry out different exercises for wrist movement and an exoskeleton for the hand to carry out individual finger exercises or complete hand exercises. Another valuable advantage of this device is the recording of the movement, it can record the rehabilitation/training exercises done by physiotherapists and later the patient can replay those exercises without the need of going to a physiotherapist again and again.

Chapter 4 describes different devices for Industrial applications. It describes five devices where four are related to industrial soft grippers and one is the soft environment that can be used with a rigid gripper. The first device introduced in this chapter is a Wireless Cooperative Gripper for safe Human Robot Interaction. This is an industrial gripper composed of four fingers each made up of soft rigid links. The device has been designed by following the guidelines of Intrinsic safety and adaptability, ease of reconfigurability, portability, and ease of interface. The developed device is easily reconfigurable since each finger contains a dovetail mechanism installed at the base, which allows the user to reorient all the fingers as per the desired grasp or the shape of the object. The gripper is fully portable and can be installed on a mobile robot platform or passive arm support. It is a stand-alone solution. A simple two-button interface is used to control the flexion and extension of the gripper's fingers. Another device introduced in this chapter is Bilateral Haptic Collaboration for Human Robot Cooperative Tasks, It is a wearable interface for bilateral haptic cooperation. It is a ring-shaped two-button interface. It provides the control for the Co-Gripper as well as vibrotactile feedback to the user. The user wears the device on the index finger. A study has been carried out to evaluate the effectiveness of feedback in carrying out grasping and re-grasping operations. Soft hands are simple, robust, and able of adapting to uncertain environments and operative conditions, however, their intrinsic compliance and underactuation reduce control capabilities and precision. To avoid this issue, a soft hand with an embedded environment in the form of a scoop has been added. Which simplifies object grasping. This allows grasping objects in narrow spaces as well. The device has been named The Soft Scoop Gripper. Clothes manipulation is always tricky and involves a lot of precision and accuracy. Often the robot or the end effectors don't succeed to grasp and manipulate the objects correctly. To cater for this problem a new device

Mag Gripper, which is a Soft Rigid Gripper Augmented with an Electromagnet to precisely handle clothes. It is embedded with an electromagnet and a two jaw gripper. The electromagnet attracts the metal piece embedded in the clothing and the two jaw gripper always provides a stable grasp. Thanks to this technique clothes are always grasped from the specified location and always with a stable grasp which is quite helpful for the robot. Although soft grippers are getting more and more popular still many industries are using rigid grippers for grasping and manipulation. Often the rigid gripper comes in contact with the environment where they have to pick the object which causes damage. Grasping with rigid grippers is also no easy because every time the user has to be precisely accurate.

References

[1] Bruno Siciliano and Oussama Khatib. *Robotics and the Handbook*, pages 1–6. Springer International Publishing, Cham, 2016.

[2] Bruno Siciliano. *Springer Handbook of Robotics*. Springer Handbook of Robotics, 2008.

[3] Ravi Balasubramanian and Veronica J Santos. *The human hand as an inspiration for robot hand development*, volume 95. Springer, 2014.

[4] Manuel G Catalano, Giorgio Grioli, Edoardo Farnioli, Alessandro Serio, Cristina Piazza, and Antonio Bicchi. Adaptive synergies for the design and control of the pisa/iit softhand. *The International Journal of Robotics Research*, 33(5):768–782, 2014.

[5] Raphael Deimel and Oliver Brock. A novel type of compliant and underactuated robotic hand for dexterous grasping. *The International Journal of Robotics Research*, 35(1-3):161–185, 2016.

[6] Kohei Nakajima, Helmut Hauser, Tao Li, and Rolf Pfeifer. Information processing via physical soft body. *Scientific reports*, 5(1):1–11, 2015.

[7] I. Hussain, F. Renda, Z. Iqbal, M. Malvezzi, G. Salvietti, L. Seneviratne, D. Gan, and D. Prattichizzo. Modeling and prototyping of an underactuated gripper exploiting joint compliance and modularity. *IEEE Robotics and Automation Letters*, 3(4):2854–2861, Oct 2018.

[8] F. Renda, F. Boyer, J. Dias, and L. Seneviratne. Discrete cosserat approach for multisection soft manipulator dynamics. *IEEE Transactions on Robotics*, 34(6):1518–1533, Dec 2018.

[9] Irfan Hussain, Gionata Salvietti, Monica Malvezzi, and Domenico Prattichizzo. On the role of stiffness design for fingertip trajectories of underactuated modular soft hands. In *Robotics and Automation (ICRA), 2017 IEEE International Conference on*, pages 3096–3101. IEEE, 2017.

[10] H. Poincaré. Sur une forme nouvelle des equations de la mecanique. *Compte Rendu de l'Academie des Sciences de Paris*, 132:369 – 371, 1901.

[11] F. Boyer and F. Renda. Poincare's equations for cosserat media: Application to shells. *Journal of Nonlinear Science*, 2016.

[12] F. Renda, M. Giorelli, M. Calisti, M. Cianchetti, and C. Laschi. Dynamic model of a multibending soft robot arm driven by cables. *Robotics, IEEE Transactions on*, 30(5):1109–1122, Oct 2014.

[13] F. Renda and L. Seneviratne. A geometric and unified approach for modeling soft-rigid multi-body systems with lumped and distributed degrees of freedom. In *2018 IEEE International Conference on Robotics and Automation (ICRA)*, pages 1567–1574, May 2018.

[14] Gionata Salvietti, Irfan Hussain, Monica Malvezzi, and Domenico Prattichizzo. Design of the passive joints of underactuated modular soft hands for fingertip trajectory tracking. *IEEE Robotics and Automation Letters*, 2(4):2008–2015, 2017.

[15] Stefano Baglioni, Filippo Cianetti, Claudio Braccesi, and Denis Mattia De Micheli. Multibody modelling of n dof robot arm assigned to milling manufacturing. dynamic analysis and position errors evaluation. *Journal of Mechanical Science and Technology*, 30(1):405–420, 2016.

[16] A Hovsovskỳ, J Pitel', K vZidek, M Tóthová, J Sárosi, and L Cveticanin. Dynamic characterization and simulation of two-link soft robot arm with pneumatic muscles. *Mechanism and Machine Theory*, 103:98–116, 2016.

[17] Benny Gamus, Lior Salem, Eran Ben-Haim, Amir D Gat, and Yizhar Or. Interaction between inertia, viscosity, and elasticity in soft robotic actuator with fluidic network. *IEEE Transactions on Robotics*, 34(1):81–90, 2017.

[18] Yuanqing Wu and Marco Carricato. Symmetric subspace motion generators. *IEEE Transactions on Robotics*, 34(3):716–735, 2018.

[19] D. Prattichizzo and J. Trinkle. Grasping. In B. Siciliano and O. Kathib, editors, *Handbook on Robotics*, pages 671–700. Springer, 2008.

[20] Júlia Borràs and Aaron M Dollar. Dimensional synthesis of three-fingered robot hands for maximal precision manipulation workspace. *The International Journal of Robotics Research*, 34(14):1731–1746, 2015.

[21] Matei Ciocarlie and Peter Allen. Data-driven optimization for underactuated robotic hands. In *2010 IEEE International Conference on Robotics and Automation*, pages 1292–1299. IEEE, 2010.

[22] Rahim Mutlu, Gursel Alici, Marc in het Panhuis, and Geoffrey M Spinks. 3d printed flexure hinges for soft monolithic prosthetic fingers. *Soft Robotics*, 3(3):120–133, 2016.

[23] E. Coevoet, T. Morales-Bieze, F. Largilliere, Z. Zhang, M. Thieffry, M. Sanz-Lopez, B. Carrez, D. Marchal, O. Goury, J. Dequidt, and C. Duriez. Software toolkit for modeling, simulation, and control of soft robots. *Advanced Robotics*, 2017.

[24] Olivier Goury and Christian Duriez. Fast, generic and reliable control and simulation of soft robots using model order reduction. *IEEE Transactions on Robotics*, 2018.

[25] Raphael Deimel and Oliver Brock. A compliant hand based on a novel pneumatic actuator. In *Robotics and Automation (ICRA), 2013 IEEE International Conference on*, pages 2047–2053. IEEE, 2013.

[26] Aaron M Dollar and Robert D Howe. The highly adaptive sdm hand: Design and performance evaluation. *The international journal of robotics research*, 29(5):585–597, 2010.

[27] Giorgio Grioli, Manuel Catalano, Emanuele Silvestro, Simone Tono, and Antonio Bicchi. Adaptive synergies: an approach to the design of under-actuated robotic hands. In *Intelligent Robots and Systems (IROS), 2012 IEEE/RSJ International Conference on*, pages 1251–1256. IEEE, 2012.

[28] Ondrej Pfaff, Simeon Simeonov, Ivan Cirovic, and Pavol Stano. Application of fin ray effect approach for production process automation. *Annals of DAAAM & Proceedings*, 22(1):1247–1249, 2011.

[29] Silas Alben, Peter G Madden, and George V Lauder. The mechanics of active fin-shape control in ray-finned fishes. *Journal of The Royal Society Interface*, 4(13):243–256, 2007.

[30] Christian Ivan Basson, Glen Bright, and Anthony John Walker. Testing flexible grippers for geometric and surface grasping conformity in reconfigurable assembly systems. *South African Journal of Industrial Engineering*, 29(1):128–142, 2018.

[31] ©FESTO. Multichoicegripper, 2014. 2014, [Online]. Available: https://www.festo.com/group/en/cms/10221.htm [Accessed: 15- Jan- 2018].

[32] C. E. Bryson and D. C. Rucker. Toward parallel continuum manipulators. In *2014 IEEE International Conference on Robotics and Automation*, pages 778–785, 2014.

[33] J. Till and D.C. Rucker. Elastic stability of cosserat rods and parallel continuum robots. *Robotics, IEEE Transactions on*, 33(3):718–733, 2017.

[34] C.B. Black, J. Till, and D.C. Rucker. Parallel continuum robots: Modeling, analysis, and actuation-based force sensing. *Robotics, IEEE Transactions on*, 34(1):29–47, 2018.

[35] Irfan Hussain, Giovanni Spagnoletti, Gionata Salvietti, and Domenico Prattichizzo. Toward wearable supernumerary robotic fingers to compensate missing grasping abilities in hemiparetic upper limb. *The International Journal of Robotics Research*, 36(13-14):1414–1436, 2017.

[36] Irfan Hussain, Muddasar Anwar, Zubair Iqbal, Rajkumar Muthusamy, Monica Malvezzi, Lakmal Seneviratne, Dongming Gan, Federico Renda, and Domenico Prattichizzo. Design and prototype of supernumerary robotic finger (srf) inspired by fin ray® effect for patients suffering from sensorimotor hand impairment. In *2019 2nd IEEE International Conference on Soft Robotics (RoboSoft)*, pages 398–403. IEEE, 2019.

[37] R. Featherstone. *Rigid Body Dynamics Algorithms*. Springer New York, 2008.

[38] F. Renda, V. Cacucciolo, J. Dias, and L. Seneviratne. Discrete cosserat approach for soft robot dynamics: A new piece-wise constant strain model with torsion and shears. In *2016 IEEE/RSJ International Conference on Intelligent Robots and Systems (IROS)*, pages 5495–5502, Oct 2016.

[39] J.M. Selig. *Geometric Fundamentals of Robotics*. Monographs in Computer Science. Springer New York, 2007.

[40] R. W. Brockett. Robotic manipulators and the product of exponentials formula. In *Mathematical Theory of Networks and Systems*, pages 120–129. Springer Berlin Heidelberg, 1984.

[41] R.M. Murray, Z. Li, and S.S. Sastry. *A Mathematical Introduction to Robotic Manipulation*. Taylor & Francis, Boca Raton, USA, 1994.

[42] Y. Wu, H. Lowe, M. Carricato, and Z. Li. Inversion symmetry of the euclidean group: Theory and application to robot kinematics. *IEEE Transactions on Robotics*, 32(2):312–326, April 2016.

[43] F. Renda, M. Cianchetti, H. Abidi, J. Dias, and L. Seneviratne. Screw-based modeling of soft manipulators with tendon and fluidic actuation. *Journal of Mechanism and Robotics*, 2017. doi:10.1115/1.4036579.

[44] Y. Wu and M. Carricato. Symmetric subspace motion generators. *IEEE Transactions on Robotics*, 34(3):716–735, June 2018.

[45] Gilbert Strang. The fundamental theorem of linear algebra. *The American Mathematical Monthly*, 100(9):848–855, 1993.

[46] K.M. Lynch and F.C. Park. *Modern Robotics: Mechanics, Planning, and Control*. Cambridge University Press, 2017.

[47] J. Baumgarte. Stabilization of constraints and integrals of motion in dynamical systems. *Computer Methods in Applied Mechanics and Engineering*, 1(1):1 – 16, 1972.

[48] Matthew T. Mason and J. Kenneth Salisbury. *Robot Hands and the Mechanics of Manipulation*. MIT Press, Cambridge, MA, May 1985.

[49] N. Fukaya, S. Toyama, T. Asfour, and R. Dillmann. Design of the tuat/karlsruhe humanoid hand. In *Proceedings. 2000 IEEE/RSJ International Conference on Intelligent Robots and Systems (IROS 2000) (Cat. No.00CH37113)*, volume 3, pages 1754–1759 vol.3, 2000.

[50] J. Butterfass, M. Grebenstein, H. Liu, and G. Hirzinger. DLR-hand II: next generation of a dextrous robot hand. In *Robotics and Automation, 2001. Proceedings 2001 ICRA. IEEE International Conference on*, volume 1, pages 109–114, 2001.

[51] Eric Martin, Alexis Lussier Desbiens, Thierry Laliberté, and Clément Gosselin. Sarah hand used for space operation on stvf robot.

[52] Vincenzo Niola, Cesare Rossi, Sergio Savino, and Francesco Timpone. Study of an underactuated mechanical finger driven by tendons. *International Journal of Automation Technology*, 11(3):344–354, 2017.

[53] Chiara Cosenza, Vincenzo Niola, and Sergio Savino. Analytical study for the capability implementation of an underactuated three-finger hand. In *New Trends in Medical and Service Robotics*, pages 161–168. Springer, 2019.

[54] Vincenzo Niola Francesco Penta Cesare Rossi and Sergio Savino. An underactuated mechanical hand: Theoretical studies and prototyping.

[55] Daniela Maffiodo and Terenziano Raparelli. Comparison among different modular sma actuated flexible fingers. In *The International Conference of IFToMM ITALY*, pages 324–331. Springer, 2018.

[56] Maria Cristina Valigi, Silvia Logozzo, and Gabriele Canella. A robotic 3d vision system for automatic cranial prostheses inspection. In *International Conference on Robotics in Alpe-Adria Danube Region*, pages 328–335. Springer, 2017.

[57] Faye Y Wu and Harry Asada. Bio-artificial synergies for grasp posture control of supernumerary robotic fingers. 2014.

[58] Fanny Ficuciello, Damiano Zaccara, and Bruno Siciliano. Synergy-based policy improvement with path integrals for anthropomorphic hands. In *2016 IEEE/RSJ International Conference on Intelligent Robots and Systems (IROS)*, pages 1940–1945, 2016.

[59] Fanny Ficuciello. Synergy-based control of underactuated anthropomorphic hands. *IEEE Transactions on Industrial Informatics*, 15(2):1144–1152, 2019.

[60] Marco Santello, Martha Flanders, and John F Soechting. Postural hand synergies for tool use. *Journal of neuroscience*, 18(23):10105–10115, 1998.

[61] Monica Malvezzi, Maria Cristina Valigi, Gionata Salvietti, Zubair Iqbal, Irfan Hussain, and Domenico Prattichizzo. Design criteria for wearable robotic extra–fingers with underactuated modular structure. In *The International Conference of IFToMM ITALY*, pages 509–517. Springer, 2018.

[62] Hiroaki Kobayashi, Kazuhito Hyodo, and Daisuke Ogane. On tendon-driven robotic mechanisms with redundant tendons. *The International Journal of Robotics Research*, 17(5):561–571, 1998.

[63] M. Malvezzi, G. Gioioso, G. Salvietti, and D. Prattichizzo. Syngrasp: A matlab toolbox for underactuated and compliant hands. *Robotics Automation Magazine, IEEE*, 22(4):52–68, December 2015.

[64] Matteo Bianchi and Minas V Liarokapis. Handcorpus, a new open-access repository for sharing experimental data and results on human and artificial hands. In *IEEE World Haptics Conference (WHC)*, 2013.

[65] Yuhan Hu, Sang-won Leigh, and Pattie Maes. Hand development kit: Soft robotic fingers as prosthetic augmentation of the hand. In *Adjunct Publication of the 30th Annual ACM Symposium on User Interface Software and Technology*, pages 27–29, 2017.

[66] Fuda Ning, Weilong Cong, Jingjing Qiu, Junhua Wei, and Shiren Wang. Additive manufacturing of carbon fiber reinforced thermoplastic composites using fused deposition modeling. *Composites Part B: Engineering*, 80:369–378, 2015.

[67] Lionel Birglen and Clement M Gosselin. Force analysis of connected differential mechanisms: Application to grasping. *The International Journal of Robotics Research*, 25(10):1033–1046, 2006.

[68] Mahbub Ahmed, Md Islam, Justin Vanhoose, and Mosfequr Rahman. Comparisons of elasticity moduli of different specimens made through three dimensional printing. *3D Printing and additive manufacturing*, 4(2):105–109, 2017.

[69] Federico Parietti and Harry Asada. Supernumerary robotic limbs for human body support. *IEEE Transactions on Robotics*, 32(2):301–311, 2016.

[70] Faye Y Wu and H Harry Asada. "hold-and-manipulate" with a single hand being assisted by wearable extra fingers. In *2015 IEEE International Conference on Robotics and Automation (ICRA)*, pages 6205–6212. IEEE, 2015.

[71] Dariush Mozaffarian, Emelia J Benjamin, Alan S Go, Donna K Arnett, Michael J Blaha, Mary Cushman, Sandeep R Das, Sarah De Ferranti, Jean-Pierre Després, Heather J Fullerton, et al. Heart disease and stroke statistics—2016 update: a report from the american heart association. *circulation*, 133(4):e38–e360, 2016.

[72] Irfan Hussain, Gionata Salvietti, and Domenico Prattichizzo. On control interfaces for the robotic sixth finger. In *Proceedings of the 7th Augmented Human International Conference 2016*, pages 1–2, 2016.

[73] G. Salvietti, I. Hussain, D. Cioncoloni, S. Taddei, S. Rossi, and D. Prattichizzo. Compensating hand function in chronic stroke patients through the robotic sixth finger. *Transaction on Neural System and Rehabilitation Engineering*, 2016.

[74] I. Hussain, G. Salvietti, G. Spagnoletti, and D. Prattichizzo. The soft-sixthfinger: a wearable emg controlled robotic extra-finger for grasp compensation in chronic stroke patients. *IEEE Robotics and Automation Letters*, 1(2):1000 –1006, July 2016.

[75] D. Prattichizzo, M. Malvezzi, I. Hussain, and G. Salvietti. The sixth-finger: a modular extra-finger to enhance human hand capabilities. In *Proc. IEEE Int. Symp. in Robot and Human Interactive Communication*, Edinburgh, United Kingdom, 2014.

[76] F. Y. Wu and H. H. Asada. Implicit and intuitive grasp posture control for wearable robotic fingers: A data-driven method using partial least squares. *IEEE Transactions on Robotics*, 32(1):176–186, Feb 2016.

[77] Irfan Hussain, Giovanni Spagnoletti, Gionata Salvietti, and Domenico Prattichizzo. an emg interface for the control of motion and compliance of a supernumerary robotic finger. *Frontiers in neurorobotics*, 10:18, 2016.

[78] Joseph R Davidson and Changki Mo. Mechanical design and initial performance testing of an apple-picking end-effector. In *ASME International Mechanical Engineering Congress and Exposition (IMECE)*, pages 13–19, 2015.

[79] Roberto Merletti, Alberto Botter, Amedeo Troiano, Enrico Merlo, and Marco Alessandro Minetto. Technology and instrumentation for detection and conditioning of the surface electromyographic signal: state of the art. *Clinical Biomechanics*, 24(2):122–134, 2009.

[80] Andrea Merlo and Isabella Campanini. Technical aspects of surface electromyography for clinicians. *The Open Rehabilitation Journal*, 3(1), 2010.

[81] Dario Farina and Roberto Merletti. Comparison of algorithms for estimation of emg variables during voluntary isometric contractions. *Journal of Electromyography and Kinesiology*, 10(5):337–349, 2000.

[82] Joe Falco, Karl Van Wyk, Shuo Liu, and Stefano Carpin. Grasping the performance: Facilitating replicable performance measures via benchmarking and standardized methodologies. *Robotics & Automation Magazine, IEEE*, 22(4):125–136, 2015.

[83] Berk cCalli, Aaron Walsman, Arjun Singh, Siddhartha Srinivasa, Pieter Abbeel, and Aaron M. Dollar. Benchmarking in manipulation research: The YCB object and model set and benchmarking protocols. *CoRR*, abs/1502.03143, 2015.

[84] World Health Organization. *World health statistics 2016: monitoring health for the SDGs sustainable development goals*. World Health Organization, 2016.

[85] Emily M Agree. The potential for technology to enhance independence for those aging with a disability. *Disability and health journal*, 7(1):S33–S39, 2014.

[86] Michael Anthonius Lim and Raymond Pranata. Letter to the editor regarding 'the challenging battle of mankind against covid-19 outbreak: Is this global international biological catastrophe the beginning of a new era?'–is telehealth the future of orthopaedic and rehabilitation in post-covid-19 era?, 2020.

[87] Peter S Lum, Sasha B Godfrey, Elizabeth B Brokaw, Rahsaan J Holley, and Diane Nichols. Robotic approaches for rehabilitation of hand function after stroke. *American journal of physical medicine & rehabilitation*, 91(11):S242–S254, 2012.

[88] Cathrin Bütefisch, Horst Hummelsheim, Petra Denzler, and Karl-Heinz Mauritz. Repetitive training of isolated movements improves the outcome of motor rehabilitation of the centrally paretic hand. *Journal of the neurological sciences*, 130(1):59–68, 1995.

[89] HI Krebs, N Hogan, BT Volpe, ML Aisen, L Edelstein, and C Diels. Overview of clinical trials with mit-manus: a robot-aided neuro-rehabilitation facility. *Technology and Health Care*, 7(6):419–423, 1999.

[90] Massimo Bergamasco, Benedetto Allotta, L Bosio, Luca Ferretti, G Parrini, GM Prisco, Fabio Salsedo, and G Sartini. An arm exoskeleton system for teleoperation and virtual environments applications. In *Proceedings of the 1994 IEEE International Conference on Robotics and Automation*, pages 1449–1454. IEEE, 1994.

[91] Ludovic Dovat, Olivier Lambercy, Roger Gassert, Thomas Maeder, Ted Milner, Teo Chee Leong, and Etienne Burdet. Handcare: a cable-actuated rehabilitation system to train hand function after stroke. *IEEE Transactions on Neural Systems and Rehabilitation Engineering*, 16(6):582–591, 2008.

[92] Mourad Bouzit, Grigore Burdea, George Popescu, and Rares Boian. The rutgers master ii-new design force-feedback glove. *IEEE/ASME Transactions on mechatronics*, 7(2):256–263, 2002.

[93] Olivier Lambercy, Ludovic Dovat, Roger Gassert, Etienne Burdet, Chee Leong Teo, and Theodore Milner. A haptic knob for rehabilitation of hand function. *IEEE Transactions on Neural Systems and Rehabilitation Engineering*, 15(3):356–366, 2007.

[94] Lorenzo Masia, Hermano Igo Krebs, Paolo Cappa, and Neville Hogan. Design and characterization of hand module for whole-arm rehabilitation following stroke. *IEEE/ASME Transactions on Mechatronics*, 12(4):399–407, 2007.

[95] Fuhai Zhang, Lei Hua, Yili Fu, Hongwei Chen, and Shuguo Wang. Design and development of a hand exoskeleton for rehabilitation of hand injuries. *Mechanism and Machine Theory*, 73:103–116, 2014.

[96] Christopher J Nycz, Tobias Bützer, Olivier Lambercy, Jumpei Arata, Gregory S Fischer, and Roger Gassert. Design and characterization of a lightweight and fully portable remote actuation system for use with a hand exoskeleton. *IEEE Robotics and Automation Letters*, 1(2):976–983, 2016.

[97] Heidi C Fischer, Kathy Stubblefield, Tiffany Kline, Xun Luo, Robert V Kenyon, and Derek G Kamper. Hand rehabilitation following stroke: a pilot study of assisted finger extension training in a virtual environment. *Topics in stroke rehabilitation*, 14(1):1–12, 2007.

[98] RARC Gopura, DSV Bandara, Kazuo Kiguchi, and George KI Mann. Developments in hardware systems of active upper-limb exoskeleton robots: A review. *Robotics and Autonomous Systems*, 75:203–220, 2016.

[99] Stefan Hesse, Henning Schmidt, Cordula Werner, and Anita Bardeleben. Upper and lower extremity robotic devices for rehabilitation and for studying motor control. *Current opinion in neurology*, 16(6):705–710, 2003.

[100] Benedetto Allotta, Roberto Conti, Lapo Governi, Enrico Meli, Alessandro Ridolfi, and Yary Volpe. Development and experimental testing of a portable hand exoskeleton. In *2015 IEEE/RSJ International Conference on Intelligent Robots and Systems (IROS)*, pages 5339–5344, 2015.

[101] Hermano Igo Krebs, Bruce T Volpe, Dustin Williams, James Celestino, Steven K Charles, Daniel Lynch, and Neville Hogan. Robot-aided neurorehabilitation: a robot for wrist rehabilitation. *IEEE transactions on neural systems and rehabilitation engineering*, 15(3):327–335, 2007.

[102] Abhishek Gupta, Marcia K O'Malley, Volkan Patoglu, and Charles Burgar. Design, control and performance of ricewrist: a force feedback wrist exoskeleton for rehabilitation and training. *The International Journal of Robotics Research*, 27(2):233–251, 2008.

[103] Nicholas W Bartlett, Valentina Lyau, William A Raiford, Dónal Holland, Joshua B Gafford, Theresa D Ellis, and Conor J Walsh. A soft robotic orthosis for wrist rehabilitation. *Journal of Medical Devices*, 9(3), 2015.

[104] Craig D Takahashi, Lucy Der-Yeghiaian, VH Le, and Steven C Cramer. A robotic device for hand motor therapy after stroke. In *9th International Conference on Rehabilitation Robotics, 2005. ICORR 2005.*, pages 17–20. IEEE, 2005.

[105] EJ Koeneman, RS Schultz, SL Wolf, DE Herring, and JB Koeneman. A pneumatic muscle hand therapy device. In *The 26th Annual International Conference of the IEEE Engineering in Medicine and Biology Society*, volume 1, pages 2711–2713. IEEE, 2004.

[106] Ismail Ben Abdallah, Yassine Bouteraa, and Chokri Rekik. Design and development of 3d printed myoelectric robotic exoskeleton for hand rehabilitation. *International Journal on Smart Sensing & Intelligent Systems*, 10(2), 2017.

[107] Pilwon Heo, Gwang Min Gu, Soo-jin Lee, Kyehan Rhee, and Jung Kim. Current hand exoskeleton technologies for rehabilitation and assistive engineering. *International Journal of Precision Engineering and Manufacturing*, 13(5):807–824, 2012.

[108] Giuseppe Turchetti, Nicola Vitiello, Stefano Romiti, Elie Geisler, and Silvestro Micera. Why effectiveness of robot-mediated neurorehabilitation does not necessarily influence its adoption. *IEEE Reviews in Biomedical Engineering*, 7:143–153, 2014.

[109] Annette De Vito Dabbs, Brad A Myers, Kenneth R Mc Curry, Jacqueline Dunbar-Jacob, Robert P Hawkins, Alex Begey, and Mary Amanda Dew. User-centered design and interactive health technologies for patients. *Computers, informatics, nursing: CIN*, 27(3):175, 2009.

[110] Mihai Dragusanu, Tommaso Lisini Baldi, Zubair Iqbal, Domenico Prattichizzo, and Monica Malvezzi. Design, development, and control of a tendon-actuated exoskeleton for wrist rehabilitation and training. In *2020 IEEE International Conference on Robotics and Automation (ICRA)*, pages 1749–1754. IEEE, 2020.

[111] M. Malvezzi, T. Lisini Baldi, A. Villani, F. Ciccarese, and D. Prattichizzo. Design, development, and preliminary evaluation of a highly wearable exoskeleton. In *Proc. IEEE Int. Symp. in Robot and Human Interactive Communication*, Napoli, IT, September 2020.

[112] M. Dragusanu, T. Lisini Baldi, Z. Iqbal, D. Prattichizzo, and M. Malvezzi. Design, development and control of a tendon-actuated exoskeleton for wrist rehabilitation and training. In *Proc. IEEE Int. Conf. on Robotics and Automation*, Paris, FR, June 2020.

[113] Francisco J Valero-Cuevas, M Elise Johanson, and Joseph D Towles. Towards a realistic biomechanical model of the thumb: the choice of kinematic description may be more critical than the solution method or the variability/uncertainty of musculoskeletal parameters. *Journal of biomechanics*, 36(7):1019–1030, 2003.

[114] T. L. Baldi, F. Farina, A. Garulli, A. Giannitrapani, and D. Prattichizzo. Upper body pose estimation using wearable inertial sensors and multiplicative kalman filter. *IEEE Sensors Journal*, pages 1–1, 2019.

[115] Thomas R Kratochwill, John Hitchcock, RH Horner, J Rl Levin, SL Odom, DM Rindskopf, and WR Shadish. Single-case designs technical documentation. *What works clearinghouse*, 2010.

[116] Di Ao, Rong Song, and Jinwu Gao. Movement performance of human–robot cooperation control based on emg-driven hill-type and proportional models for an ankle power-assist exoskeleton robot. *IEEE Transactions on Neural Systems and Rehabilitation Engineering*, 25(8):1125–1134, 2016.

[117] László Monostori. Cyber-physical production systems: roots, expectations and r&d challenges. *Procedia Cirp*, 17:9–13, 2014.

[118] Mario Hermann, Tobias Pentek, and Boris Otto. Design principles for industrie 4.0 scenarios. In *System Sciences (HICSS), 2016 49th Hawaii International Conference on*, pages 3928–3937. IEEE, 2016.

[119] Raphael Deimel, Clemens Eppner, José Alvarez-Ruiz, Marianne Maertens, and Oliver Brock. Exploitation of environmental constraints in human and robotic grasping. In *International Symposium on Robotic Research*, 2013.

[120] Raymond R Ma, Lael U Odhner, and Aaron M Dollar. A modular, open-source 3d printed underactuated hand. In *Robotics and Automation (ICRA), 2013 IEEE International Conference on*, pages 2737–2743. IEEE, 2013.

[121] Robotq. 3-finger adaptive robot gripper @ONLINE, February 2018. https://robotiq.com/products/3-finger-adaptive-robot-gripper.

[122] John R Amend, Eric Brown, Nicholas Rodenberg, Heinrich M Jaeger, and Hod Lipson. A positive pressure universal gripper based on the jamming of granular material. *IEEE Transactions on Robotics*, 28(2):341–350, 2012.

[123] L. Birglen, T Lalibertè, and C. Gosselin. *Underactuated Robotic Hands*, volume 40 of *Springer Tracts in Advanced Robotics*. Springer, 2008.

[124] Schunk. Co–act gripper @ONLINE, February 2018. https://schunk.com/de_en/co-act/.

[125] On Robot. Rg6 collaborative gripper @ONLINE, February 2018. https://onrobot.com/products/.

[126] G. Salvietti, I. Hussain, M. Malvezzi, and D. Prattichizzo. Design of the passive joints of underactuated modular soft hands for fingertip trajectory tracking. *IEEE Robotics and Automation Letters*, 2(4):2008–2015, 2017.

[127] Robots and robotic devices – Collaborative robots. Standard, International Organization for Standardization, 2016.

[128] Robots and robotic devices – Safety requirements for industrial robots – Part 1: Robots . Standard, International Organization for Standardization, 2011.

[129] Robots and robotic devices – Safety requirements for industrial robots – Part 1: Robot systems and integration . Standard, International Organization for Standardization, 2011.

[130] Masashiro Morioka and Shinsuke Sakakibara. A new cell production assembly system with human–robot cooperation. *CIRP annals*, 59(1):9–12, 2010.

[131] Jörg Krüger, Terje K Lien, and Alexander Verl. Cooperation of human and machines in assembly lines. *CIRP Annals-Manufacturing Technology*, 58(2):628–646, 2009.

[132] Shigeo Hirose and Yoji Umetani. The development of soft gripper for the versatile robot hand. *Mechanism and machine theory*, 13(3):351–359, 1978.

[133] Andrea Krasa Sethi and Suresh Pal Sethi. Flexibility in manufacturing: a survey. *International journal of flexible manufacturing systems*, 2(4):289–328, 1990.

[134] Hoda A ElMaraghy. Flexible and reconfigurable manufacturing systems paradigms. *International journal of flexible manufacturing systems*, 17(4):261–276, 2005.

[135] Ramesh Kolluru, Kimon P Valavanis, SS Smith, and Nikos Tsourveloudis. Design fundamentals of a reconfigurable robotic gripper system. *IEEE Transactions on Systems, Man, and Cybernetics-Part A: Systems and Humans*, 30(2):181–187, 2000.

[136] F. Sanfilippo, G. Salvietti, H. Zhang, H. P. Hildre, and D. Prattichizzo. Efficient modular grasping: an iterative approach. In *Proc. IEEE Int. Conf. on Biomedical Robotics and Biomechatronics*, pages 1281–1286, Rome, Italy, 2012.

[137] Rethik robotics. Sawyer collaborative robot, February 2018. http://www.rethinkrobotics.com/sawyer/.

[138] Claudio Pacchierotti, Gionata Salvietti, Irfan Hussain, Leonardo Meli, and Domenico Prattichizzo. The hring: A wearable haptic device to avoid occlusions in hand tracking. In *Haptics Symposium (HAPTICS), 2016 IEEE*, pages 134–139. IEEE, 2016.

[139] R. R. Ma, L. U. Odhner, and A. M. Dollar. A modular, open-source 3d printed underactuated hand. In *2013 IEEE International Conference on Robotics and Automation*, pages 2737–2743, May 2013.

[140] John Brooke et al. Sus-a quick and dirty usability scale. *Usability evaluation in industry*, 189(194):4–7, 1996.

[141] Arash Ajoudani, Andrea Maria Zanchettin, Serena Ivaldi, Alin Albu-Schäffer, Kazuhiro Kosuge, and Oussama Khatib. Progress and prospects of the human–robot collaboration. *Autonomous Robots*, pages 1–19, 2018.

[142] Andrea Cherubini, Robin Passama, André Crosnier, Antoine Lasnier, and Philippe Fraisse. Collaborative manufacturing with physical human–robot interaction. *Robotics and Computer-Integrated Manufacturing*, 40:1–13, 2016.

[143] G Salvietti, Z Iqbal, I Hussain, D Prattichizzo, and M Malvezzi. The Co-Gripper: A Wireless Cooperative Gripper for Safe Human Robot Interaction. In *2018 IEEE/RSJ International Conference on Intelligent Robots and Systems (IROS)*, pages 4576–4581. IEEE, 2018.

[144] Kyle B Reed and Michael A Peshkin. Physical collaboration of human-human and human-robot teams. *IEEE Transactions on Haptics*, 1(2):108–120, 2008.

[145] C. Pacchierotti, S. Sinclair, M. Solazzi, A. Frisoli, V. Hayward, and D. Prattichizzo. Wearable haptic systems for the fingertip and the hand: taxonomy, review, and perspectives. *IEEE Transactions on Haptics*, 10(4):580–600, 2017.

[146] Andrea Casalino, Costanza Messeri, Maria Pozzi, Andrea Maria Zanchettin, Paolo Rocco, and Domenico Prattichizzo. Operator awareness in human–robot collaboration through wearable vibrotactile feedback. *IEEE Robotics and Automation Letters*, 3(4):4289–4296, 2018.

[147] W. Kim, M. Lorenzini, K. Kapicioglu, and A. Ajoudani. Ergotac: A tactile feedback interface for improving human ergonomics in workplaces. *IEEE Robotics and Automation Letters*, 3(4):4179–4186, Oct 2018.

[148] Irfan Hussain, Leonardo Meli, Claudio Pacchierotti, Gionata Salvietti, and Domenico Prattichizzo. Vibrotactile haptic feedback for intuitive control of robotic extra fingers. In *World Haptics*, pages 394–399, 2015.

[149] HCCH Levitt. Transformed up-down methods in psychoacoustics. *The Journal of the Acoustical society of America*, 49(2B):467–477, 1971.

[150] Joost CF De Winter. Using the student's t-test with extremely small sample sizes. *Practical Assessment, Research & Evaluation*, 18(10), 2013.

[151] Jill L Drury, Jean Scholtz, and Holly A Yanco. Awareness in human-robot interactions. In *SMC'03 Conference Proceedings. 2003 IEEE International Conference on Systems, Man and Cybernetics. Conference Theme-System Security and Assurance (Cat. No. 03CH37483)*, volume 1, pages 912–918. IEEE, 2003.

[152] Sotiris Makris, Panagiotis Karagiannis, Spyridon Koukas, and Aleksandros-Stereos Matthaiakis. Augmented reality system for operator support in human–robot collaborative assembly. *CIRP Annals*, 65(1):61–64, 2016.

[153] Valeria Villani, Fabio Pini, Francesco Leali, and Cristian Secchi. Survey on human–robot collaboration in industrial settings: Safety, intuitive interfaces and applications. *Mechatronics*, 55:248–266, 2018.

[154] Clemens Eppner and Oliver Brock. Visual detection of opportunities to exploit contact in grasping using contextual multi-armed bandits. In *Intelligent Robots and Systems (IROS), 2017 IEEE/RSJ International Conference on*, pages 273–278. IEEE, 2017.

[155] Clemens Eppner, Raphael Deimel, Jos Alvarez-Ruiz, Marianne Maertens, and Oliver Brock. Exploitation of environmental constraints in human and robotic grasping. *The International Journal of Robotics Research*, 34(7):1021–1038, 2015.

[156] Lael U Odhner and Aaron M Dollar. Dexterous manipulation with underactuated elastic hands. In *Robotics and Automation (ICRA), 2011 IEEE International Conference on*, pages 5254–5260. IEEE, 2011.

[157] M. Pozzi, G. Salvietti, J. Bimbo, M. Malvezzi, and D. Prattichizzo. The closure signature: A functional approach to model underactuated compliant robotic hands. *IEEE Robotics and Automation Letters*, 3(3):2206–2213, July 2018.

[158] G. Salvietti, Z. Iqbal, I Hussain, and M. Prattichizzo, D. Malvezzi. The co-gripper: a wireless cooperative gripper for safe human robot interaction. In *Proc. IEEE/RSJ Int. Conf. Intelligent Robots and Systems*, Madrid, Spain, 2018.

[159] A. Bicchi. On the closure properties of robotic grasping. *The Int. J. of Robotics Research*, 14(4):319–334, 1995.

[160] I. Hussain, F. Renda, M. I. Zubair, M. Malvezzi, G. Salvietti, L. Seneviratne, D. Gan, and D. Prattichizzo. Modeling and prototyping of an underactuated gripper exploiting joint compliance and modularity. *IEEE Robotics and Automation Letters*, 2018.

[161] Jineesh Ayippadath Gopi and Golok Bihari Nando. Modeling of young's modulus of thermoplastic polyurethane and polydimethylsiloxane rubber blends based on phase morphology. *Advances in Polymer Science and Technology: An International Journal*, pages 43–51, 2014.

[162] Andrew T Miller, Steffen Knoop, Henrik I Christensen, and Peter K Allen. Automatic grasp planning using shape primitives. In *2003 IEEE International Conference on Robotics and Automation (Cat. No. 03CH37422)*, volume 2, pages 1824–1829. IEEE, 2003.

[163] Life hacks - how to fold a t-shirt in just 2 seconds. https://optse.ztat.net/projects/lifehack/UK/13_UK_LifeHack_05_FoldTShirt.mp4. Accessed: 2020-07-04.

[164] Dimitra Triantafyllou, Ioannis Mariolis, Andreas Kargakos, Sotiris Malassiotis, and Nikos Aspragathos. A geometric approach to robotic unfolding of garments. *Robot. Auton. Syst.*, 75(PB):233–243, January 2016.

[165] M. Cusumano-Towner, A. Singh, S. Miller, J. F. O'Brien, and P. Abbeel. Bringing clothing into desired configurations with limited perception. In *2011 IEEE International Conference on Robotics and Automation*, pages 3893–3900, 2011.

[166] C. Bersch, B. Pitzer, and S. Kammel. Bimanual robotic cloth manipulation for laundry folding. In *2011 IEEE/RSJ International Conference on Intelligent Robots and Systems*, pages 1413–1419, Sep. 2011.

[167] A. Doumanoglou, A. Kargakos, T. Kim, and S. Malassiotis. Autonomous active recognition and unfolding of clothes using random decision forests and probabilistic planning. In *2014 IEEE International Conference on Robotics and Automation (ICRA)*, pages 987–993, May 2014.

[168] Y. Li, Danfei Xu, Yonghao Yue, Y. Wang, S. Chang, E. Grinspun, and P. K. Allen. Regrasping and unfolding of garments using predictive thin shell modeling. In *2015 IEEE International Conference on Robotics and Automation (ICRA)*, pages 1382–1388, May 2015.

[169] Enric Corona, Guillem Alenyà, Antonio Gabas, and Carme Torras. Active garment recognition and target grasping point detection using deep learning. *Pattern Recognition*, 74:629–641, 2018.

[170] Matthew Bell and Devin Balkcom. Grasping non-stretchable cloth polygons. *The International Journal of Robotics Research*, 29(6):775–784, 2010.

[171] Stephen Miller, Jur van den Berg, Mario Fritz, Trevor Darrell, Ken Goldberg, and Pieter Abbeel. A geometric approach to robotic laundry folding. *The International Journal of Robotics Research*, 31(2):249–267, 2012.

[172] J. Stria, D. Prusa, V. Hlavac, L. Wagner, V. Petrik, P. Krsek, and V. Smutny. Garment perception and its folding using a dual-arm robot. In *2014 IEEE/RSJ International Conference on Intelligent Robots and Systems*, pages 61–67, Sep. 2014.

[173] Vladimír Petrík, Vladimír Smutný, Pavel Krsek, and Václav Hlavác. Robotic garment folding: Precision improvement and workspace enlargement. In *TAROS*, 2015.

[174] A. Doumanoglou, J. Stria, G. Peleka, I. Mariolis, V. Petrík, A. Kargakos, L. Wagner, V. Hlavác, T. Kim, and S. Malassiotis. Folding clothes autonomously: A complete pipeline. *IEEE Transactions on Robotics*, 32(6):1461–1478, Dec 2016.

[175] P. Yang, K. Sasaki, K. Suzuki, K. Kase, S. Sugano, and T. Ogata. Repeatable folding task by humanoid robot worker using deep learning. *IEEE Robotics and Automation Letters*, 2(2):397–403, April 2017.

[176] Yoshihisa Tsurumine, Yunduan Cui, Eiji Uchibe, and Takamitsu Matsubara. Deep reinforcement learning with smooth policy update: Application to robotic cloth manipulation. *Robotics and Autonomous Systems*, 112:72 – 83, 2019.

[177] Adrià Colomé and Carme Torras. Dimensionality reduction for dynamic movement primitives and application to bimanual manipulation of clothes. *IEEE Transactions on Robotics*, 34:602–615, 2018.

[178] J. Borràs, G. Alenyà, and C. Torras. A grasping-centered analysis for cloth manipulation. *IEEE Transactions on Robotics*, 36(3):924–936, 2020.

[179] A. Ramisa, G. Alenyà, F. Moreno-Noguer, and C. Torras. Using depth and appearance features for informed robot grasping of highly wrinkled clothes. In *2012 IEEE International Conference on Robotics and Automation*, pages 1703–1708, May 2012.

[180] L. Twardon and H. Ritter. Interaction skills for a coat-check robot: Identifying and handling the boundary components of clothes. In *2015 IEEE International Conference on Robotics and Automation (ICRA)*, pages 3682–3688, 2015.

[181] Thuy-Hong-Loan Le, Michal Jilich, Alberto Landini, Matteo Zoppi, Dimiter Zlatanov, and Rezia Molfino. On the development of a specialized flexible gripper for garment handling. 2013.

[182] P. N. Koustoumpardis, K. X. Nastos, and N. A. Aspragathos. Underactuated 3-finger robotic gripper for grasping fabrics. In *2014 23rd International Conference on Robotics in Alpe-Adria-Danube Region (RAAD)*, pages 1–8, Sep. 2014.

[183] Clemens Eppner, Raphael Deimel, Jos; Álvarez Ruiz, Marianne Maertens, and Oliver Brock. Exploitation of environmental constraints in human and robotic grasping. *Int. J. Rob. Res.*, 34(7):1021–1038, June 2015.

[184] Debanik Roy. Development of novel magnetic grippers for use in unstructured robotic workspace. *Robotics and Computer-Integrated Manufacturing*, 35:16 – 41, 2015.

[185] B. Calli, A. Walsman, A. Singh, S. Srinivasa, P. Abbeel, and A. M. Dollar. Benchmarking in manipulation research: Using the yale-cmu-berkeley object and model set. *IEEE Robotics Automation Magazine*, 22(3):36–52, 2015.

[186] Carme Torras. Assistive robotics: research challenges and ethics education initiatives. *Dilemata*, 30:63–77, 2019.

[187] Josie Hughes, Utku Culha, Fabio Giardina, Fabian Guenther, Andre Rosendo, and Fumiya Iida. Soft manipulators and grippers: A review. *Frontiers in Robotics and AI*, 3:69, 2016.

[188] Raphael Deimel, Clemens Eppner, José Álvarez-Ruiz, Marianne Maertens, and Oliver Brock. Exploitation of environmental constraints in human and robotic grasping. In *Robotics Research*, pages 393–409. Springer, 2016.

[189] M. Pozzi, G. Salvietti, J. Bimbo, M. Malvezzi, and D. Prattichizzo. The closure signature: A functional approach to model underactuated compliant robotic hands. *IEEE Robotics and Automation Letters*, 3(3):2206–2213, July 2018.

[190] Joao Bimbo, Enrico Turco, Mahdi Ghazaei Ardakani, Maria Pozzi, Gionata Salvietti, Valerio Bo, Monica Malvezzi, and Domenico Prattichizzo. Exploiting robot hand compliance and environmental constraints for edge grasps. *Frontiers in Robotics and AI*, 6:135, 2019.

[191] F. Vigni, E. Knoop, D. Prattichizzo, and M. Malvezzi. The role of closed-loop hand control in handshaking interactions. *IEEE Robotics and Automation Letters*, 4(2):878–885, 2019.

[192] Weiwei Wan, Kensuke Harada, and Fumio Kanehiro. Planning grasps for assembly tasks. *arXiv preprint arXiv:1903.01631*, 2019.

[193] Pedro J Sanz, Antonio Requena, Jose M Inesta, and Angel P Del Pobil. Grasping the not-so-obvious: vision-based object handling for industrial applications. *IEEE Robotics & Automation Magazine*, 12(3):44–52, 2005.

[194] Cosimo Della Santina, Visar Arapi, Giuseppe Averta, Francesca Damiani, Gaia Fiore, Alessandro Settimi, Manuel G Catalano, Davide Bacciu, Antonio Bicchi, and Matteo Bianchi. Learning from humans how to grasp: a data-driven architecture for autonomous grasping with anthropomorphic soft hands. *IEEE Robotics and Automation Letters*, 4(2):1533–1540, 2019.

[195] Hao Dang, Jonathan Weisz, and Peter K Allen. Blind grasping: Stable robotic grasping using tactile feedback and hand kinematics. In *ICRA*, pages 5917–5922, 2011.

[196] Raphael Deimel and Oliver Brock. A novel type of compliant and underactuated robotic hand for dexterous grasping. *The International Journal of Robotics Research*, 35(1-3):161–185, 2016.

[197] Chung-Hsien Kuo, Hung-Chyun Chou, and Sheng-Yu Tasi. Pneumatic sensor: A complete coverage improvement approach for robotic cleaners. *IEEE Transactions on Instrumentation and Measurement*, 60(4):1237–1256, 2011.

[198] H. Nozawa, S. Lee, J. Kim, and K. Inoue. Human-robot cooperation for heavy object manipulation based on sensing pneumatic pressure in air cushions. In *2012 IEEE/ASME International Conference on Advanced Intelligent Mechatronics (AIM)*, pages 391–396, July 2012.

[199] Yuki Akamatsu, Taro Nakamura, and Yuta Kusaka. Development of a soft manipulator with flexible joints using smart fluid and pneumatics cushion for collision with human. In *IEEE/ASME international conference on advanced intelligent mechatronics*, pages 1–6. IEEE, 2007.

[200] Daoxiong Gong, Rui He, Jianjun Yu, and Guoyu Zuo. A pneumatic tactile sensor for co-operative robots. *Sensors*, 17(11):2592, 2017.

[201] C. Gaudeni and D. Prattichizzo. A mathematical model of the pneumatic force sensor for robot-assisted surgery. In *IEEE World Haptics Conference 2019*, pages 598–603, Tokyo, Japan, July 2019.

[202] Taeyeong Kim, Dong-min Kim, Bong Jae Lee, and Jungchul Lee. Soft and deformable sensors based on liquid metals. *Sensors*, 19(19):4250, 2019.

[203] SS Suprapto, AW Setiawan, H Zakaria, W Adiprawita, and B Supartono. Low-cost pressure sensor matrix using velostat. In *2017 5th International Conference on Instrumentation, Communications, Information Technology, and Biomedical Engineering (ICICI-BME)*, pages 137–140. IEEE, 2017.

[204] Liangliang Wang and Zheng Wang. Mechanoreception for soft robots via intuitive body cues. *Soft robotics*, 2019.

[205] Akitsugu Misaki, Kyoko Imanishi, Shinichiro Takasugi, Mika Wada, Shuji Fukagawa, and Masutaka Furue. Body pressure sensing mattress for bedsore prevention. *SEI technical review*, 78:95–99, 2014.

[206] Soft Robotics Toolkit. Soft gripper fabrication guide, 2016.

[207] DC Pamplona and DEJS Mota. Numerical and experimental analysis of inflating a circular hyperelastic membrane over a rigid and elastic foundation. *International Journal of Mechanical Sciences*, 65(1):18–23, 2012.

[208] Morgan Quigley, Ken Conley, Brian P. Gerkey, Josh Faust, Tully Foote, Jeremy Leibs, Rob Wheeler, and Andrew Y. Ng. Ros: an open-source robot operating system. In *ICRA Workshop on Open Source Software*, 2009.

[209] B. Calli, A. Walsman, A. Singh, S. Srinivasa, P. Abbeel, and A. M. Dollar. Benchmarking in manipulation research: Using the yale-cmu-berkeley object and model set. *IEEE Robotics Automation Magazine*, 22(3):36–52, Sept 2015.

[210] F. Bullo and R. M. Murray. Proportional derivative (pd) control on the euclidean group. In *European Control Conference*, pages 1091–1097, 1995.

List of figures

List of tables

Muhammad
Zubair Iqbal
30.08.2021
23:25:19
GMT+01:00

Appendix A

Appendix

A.1 Nomenclature

In the following, the expressions for the adjoint representation ($\in \mathbb{R}^{6\times6}$) of the Lie group $SE(3)$ are given.

$$\mathrm{Ad}_{\boldsymbol{g}}(X) = \begin{pmatrix} \boldsymbol{R} & \mathbf{0}_{3\times3} \\ \widetilde{\mathsf{u}}\boldsymbol{R} & \boldsymbol{R} \end{pmatrix}, \mathrm{Ad}^*_{\boldsymbol{g}}(X) = \begin{pmatrix} \boldsymbol{R} & \widetilde{\mathsf{u}}\boldsymbol{R} \\ \mathbf{0}_{3\times3} & \boldsymbol{R} \end{pmatrix},$$

$$\mathrm{ad}_{\boldsymbol{\xi},\boldsymbol{\eta}}(X) = \begin{pmatrix} \widetilde{\mathsf{k}},\widetilde{\mathsf{w}} & \mathbf{0}_{3\times3} \\ \widetilde{\mathsf{q}},\widetilde{\mathsf{v}} & \widetilde{\mathsf{k}},\widetilde{\mathsf{w}} \end{pmatrix}, \mathrm{ad}^*_{\boldsymbol{\xi},\boldsymbol{\eta}}(X) = \begin{pmatrix} \widetilde{\mathsf{k}},\widetilde{\mathsf{w}} & \widetilde{\mathsf{q}},\widetilde{\mathsf{v}} \\ \mathbf{0}_{3\times3} & \widetilde{\mathsf{k}},\widetilde{\mathsf{w}} \end{pmatrix}$$

A.2 Kinematics

We firstly introduce the kinematics of a clutched soft body and then we include a rigid body clamped and analyse how it alters the formulation.

Soft Body A single soft body element, indicated with i index of a multi-body soft-rigid structure is modelled as a Cosserat beam undergoing constant deformation [43]. According to the Cosserat beam theory, the configuration of a deformable body with respect to the spatial frame at a certain time is defined as a curve

$$\boldsymbol{g}_i(\cdot) : X \mapsto \boldsymbol{g}_i(X) = \begin{pmatrix} \mathbf{R}_i & \mathbf{u}_i \\ \mathbf{0}^T & 1 \end{pmatrix} \in SE(3),$$

where $X \in [0, L]$ is the material abscissa parameter (with L the length of the soft articulation), $\mathbf{R}_i \in SO(3)$ is the orientation matrix and $\mathbf{u}_i \in \mathbb{R}^3$ is the position vector.

The strain state of the soft arm $\boldsymbol{\xi}_i(\cdot) : X \mapsto \boldsymbol{\xi}_i(X)$ is defined as the infinitesimal displacement between two consecutive points in the configuration space. The components of this field are specified as

$$\widehat{\boldsymbol{\xi}}_i = \begin{pmatrix} \tilde{\mathsf{k}}_i & \mathsf{p}_i \\ \mathbf{0}^T & 0 \end{pmatrix} \in 3), \boldsymbol{\xi}_i = \left(\mathsf{k}_i^T, \mathsf{p}_i^T\right)^T \in \mathbb{R}^6,$$

where $\mathsf{p}_i(X) \in \mathbb{R}^3$ represents the linear strains of the soft body and $\mathsf{k}_i(X) \in \mathbb{R}^3$ the angular strains, while the hat $\widehat{\ }$ and the tilde $\widetilde{\ }$ represent the isomorphisms between twist vector representation and matrix representation of the Lie algebras $\mathfrak{se}(3)$ and $\mathfrak{so}(3)$ respectively.

Under the constant strain assumption, we can express the configuration as a function of strain, using the matrix exponential method, which gives:

$$\boldsymbol{g}_i(X) = e^{X\widehat{\boldsymbol{\xi}}_i}\,, \tag{A.1}$$

where we have considered $\boldsymbol{g}_i(0) = \boldsymbol{I}_4$, *i.e.*, we let the spatial frame to be coincident with the frame at the base of the soft body. The exponential law can be analitically calculated as in [39]:

$$\begin{aligned} e^{X\widehat{\boldsymbol{\xi}}_i} = \boldsymbol{I}_4 + X\widehat{\boldsymbol{\xi}}_i + \frac{1}{\theta_i^2}\left(1-\cos\left(X\theta_i\right)\right)\widehat{\boldsymbol{\xi}}_i^2 \\ + \frac{1}{\theta_i^3}\left(X\theta_i - \sin\left(X\theta_i\right)\right)\widehat{\boldsymbol{\xi}}_i^3, \end{aligned} \tag{A.2}$$

where $\theta_i^2 = \mathsf{k}_i^T\mathsf{k}_i$.

In the classical Cosserat beam theory the strain twist $\boldsymbol{\xi}_i$ could take any value in the six dimensional Lie algebra $\mathfrak{se}(3)$ (as long as physical constrains as material non-penetrability are met). However, it is useful to consider constrained strain state ($\boldsymbol{\xi}_i \in \mathfrak{m}_i \subset \mathfrak{se}(3)$), which can be the result of mechanical properties (directional stiffness of materials) or modeling assumptions (constant curvature models). Thus, we define

$$\boldsymbol{\xi}_i = \boldsymbol{B}_i\boldsymbol{q}_i + \bar{\boldsymbol{\xi}}_i\,, \tag{A.3}$$

where $\bar{\boldsymbol{\xi}}_i$ is a given twist which allows to model for fixed yet non zero strains, *e.g.* inextensibility, and the columns of $\boldsymbol{B}_i \in \mathbb{R}^{6\times n_i}$ form a basis for the screw system $\mathfrak{m}_i$. The screw system of motion is given by $\mathfrak{m}_i \equiv \text{span}\{\boldsymbol{B}_i, \bar{\boldsymbol{\xi}}_j\}$, while the number of DoF n_i is determined by the dimension of the equivalent joint vector $\boldsymbol{q}_i \in \boldsymbol{R}^{n_i}$. For example if we restrict the soft articulation to inextensible bending and torsional motions for all the modules of the finger, $n_i = n = 2$ and we have

$$\boldsymbol{B}_i = \boldsymbol{B} = \begin{pmatrix} 1 & 0 & 0 & 0 & 0 & 0 \\ 0 & 0 & 1 & 0 & 0 & 0 \end{pmatrix}^{\mathrm{T}} \tag{A.4}$$

$$\bar{\boldsymbol{\xi}}_i = \bar{\boldsymbol{\xi}} = \begin{pmatrix} 0 & 0 & 0 & 1 & 0 & 0 \end{pmatrix}^{\mathrm{T}}, \tag{A.5}$$

where the body frames considered to define the configuration are defined as shown in Fig. 2.1.

Soft-Rigid finger The configuration of a body in a soft-rigid structure is given by the concatenation of the rigid motion between the adjacent frames in the chain that connects the base frame to the body frame. Considering a modular structure, let us define $\boldsymbol{g}_{ib}$ and $\boldsymbol{g}_{bj}$ the fixed rigid transformations between the tip frame of the soft body i, the phalanx's body frame and base frame of the soft body j respectively. Then, the configuration $\boldsymbol{g}_{sj_b}$ of the phalanx of the j^{th} module with respect to the spatial frame, is given by $\boldsymbol{g}_{sj_b} = \boldsymbol{g}_1(L)\boldsymbol{g}_{1b}\boldsymbol{g}_{b2}\cdots\boldsymbol{g}_j(L)\boldsymbol{g}_{jb}$ which,

introducing eq. (A.1), becomes

$$\boldsymbol{g}_{sj_b} = e^{L\widehat{\boldsymbol{\xi}}_1}\boldsymbol{g}_{1b}\boldsymbol{g}_{b2}\cdots e^{L\widehat{\boldsymbol{\xi}}_j}\boldsymbol{g}_{jb}\,. \tag{A.6}$$

The configuration of a generic cross section of the soft joint of the j^{th} module identified by X, is given by

$$\boldsymbol{g}_{sj}(X) = e^{L\widehat{\boldsymbol{\xi}}_1}\boldsymbol{g}_{1b}\boldsymbol{g}_{b2}\cdots\boldsymbol{g}_{bj}e^{X\widehat{\boldsymbol{\xi}}_j}\,. \tag{A.7}$$

It is worth to observe that, eq. (A.6), and (A.7) represent the PoE formula [40] for a soft-rigid structure and allow to obtain the configuration of any body and cross section of the system from the knowledge of the joint variables $\boldsymbol{q}$ only.

A.3 Differential Kinematics

The velocity twist $\boldsymbol{\eta}_j$ of a body j in a multi-body system is given by the time evolution of the configuration $\boldsymbol{g}_{sj}$. Without loss of generality, let us consider a soft body j in this section. With respect to the body frame, the velocity twist is obtained by

$$\widehat{\boldsymbol{\eta}}_j(X) = \boldsymbol{g}_{sj}^{-1}\partial\boldsymbol{g}_{sj}/\partial t = \boldsymbol{g}_{sj}^{-1}\dot{\boldsymbol{g}}_{sj}\,. \tag{A.8}$$

The component of this field are specified as $\boldsymbol{\eta}_j = \left(\mathsf{w}_j^T, \mathsf{v}_j^T\right)^T \in \mathbb{R}^6$, where $\mathsf{v}_j(X) \in \mathbb{R}^3$ and $\mathsf{w}_j(X) \in \mathbb{R}^3$ are respectively the linear and angular velocity of the cross section X at a given instant of time.

The time derivative of a single transformation $e^{X\widehat{\boldsymbol{\xi}}}$ can be evaluated by Hausdorff formula for the derivatives in Lie groups [210], which states

$$\frac{\partial}{\partial t}e^{X\widehat{\boldsymbol{\xi}}} = \left(\int_0^X e^{s\widehat{\boldsymbol{\xi}}}\dot{\widehat{\boldsymbol{\xi}}}e^{-s\widehat{\boldsymbol{\xi}}}ds\right)e^{X\widehat{\boldsymbol{\xi}}}\,. \tag{A.9}$$

Now, introducing (A.7) in (A.8), writing the result in the adjoint representation and using (A.3), we obtain

$$\boldsymbol{\eta}_j(X) = \sum_{i=1}^{j}\mathrm{Ad}^{-1}_{\boldsymbol{g}_i\cdots\boldsymbol{g}_j(X)}\mathrm{T}_{\boldsymbol{g}_i}\boldsymbol{B}\dot{\boldsymbol{q}}_i = \sum_{i=1}^{j}{}^j\boldsymbol{S}_i\dot{\boldsymbol{q}}_i\,, \tag{A.10}$$

where $\mathrm{T}_{\boldsymbol{g}_i}(X) = \int_0^X e^{s\mathrm{ad}_{\boldsymbol{\xi}_i}}ds$ represents the tangent operator of the exponential map [39]. The index i of (A.10) run over all the bodies in the chain and the quantities related to i in the series is evaluated at L for $i \neq j$ and X when $i = j$. Finally, making use of the joint vector $\boldsymbol{q} = \left[\boldsymbol{q}_1^T\cdots\boldsymbol{q}_N^T\right]^T \in \mathbb{R}^{2N}$ (where, N is the total number of modules.) we obtain the differential kinematics equation of the system in the form

$$\boldsymbol{\eta}_j(X) = \boldsymbol{J}_j\dot{\boldsymbol{q}}\,, \tag{A.11}$$

which defines the geometric Jacobian of body j, $\boldsymbol{J}_j(X) = [{}^j\boldsymbol{S}_1 \cdots {}^j\boldsymbol{S}_j\, \boldsymbol{0}_{6\times 6} \cdots] \in \mathbb{R}^{6\times 2N}$ whose components ${}^j\boldsymbol{S}_i(X) \in \mathbb{R}^{6\times 2}$ are as for equation (A.10). Considering the consecutive rigid phalanges of the same j^{th} module, equation (A.10) becomes

$$\boldsymbol{\eta}_{jb} = \sum_{i=1}^{j} {}^{jb}\boldsymbol{S}_i \dot{\boldsymbol{q}}_i = \boldsymbol{J}_{jb}\dot{\boldsymbol{q}}\,, \tag{A.12}$$

where the only difference with $\boldsymbol{\eta}_j(L)$ is represented by the fixed rigid transformation $\boldsymbol{g}_{jb}$, *i.e.*, $\boldsymbol{J}_{j_b} = \mathrm{Ad}^{-1}_{\boldsymbol{g}_{jb}}\boldsymbol{J}_j(L)$. In particular, for the tip phalanx $j \leftarrow N$.

Appendix B

Publications

B.1 List of Publications

International Journal Articles

1. Z. Iqbal, M. Pozzi, D. Prattichizzo, G. Salvietti, Detachable Robotic Grippers for Human-Robot Collaboration, Frontiers in Robotics and AI, section Soft Robotics, 2021.

2. C. Armanini, I. Hussain, Z. Iqbal, D. Gan, D. Prattichizzo, F. Renda. Discrete Cosserat Approach for Closed-Chain Soft Robots: Application to the Fin-Ray Finger. IEEE Transactions on Robotics, doi: 10.1109/TRO.2021.3075643

3. I. Hussain, M. Malvezzi, D. Gan, Z. Iqbal, L. Seneviratne, D. Prattichizzo, F. Renda. Compliant gripper design, prototyping, and modeling using screw theory formulation. International Journal of Robotics Research, (0):1-1, 2020.

4. S. Marullo, S. Bartoccini, G. Salvietti, M. Z. Iqbal, D. Prattichizzo. The Mag-Gripper: A Soft-Rigid Gripper Augmented With an Electromagnet to Precisely Handle Clothes. IEEE Robotics and Automation Letters, 5(4):6591-6598, 2020.

5. C. Gaudeni, M. Pozzi, Z. Iqbal, M. Malvezzi, D. Prattichizzo. Grasping with the SoftPad, a soft sensorized surface for exploiting environmental constraints with rigid grippers. IEEE Robotics and Automation Letters, 5(3):3884-3891, 2020.

6. G. Salvietti, Z. Iqbal, D. Prattichizzo. Bilateral Haptic Collaboration for Human-Robot Cooperative Tasks. IEEE Robotics and Automation Letters, 5(2):3517-3524, 2020.

7. M. Malvezzi, Z. Iqbal, M. C. Valigi, M. Pozzi, D.Prattichizzo, G. Salvietti. Design of Multiple Wearable Robotic Extra Fingers for Human Hand Augmentation . Robotics, 8(102):1-21, 2019.

8. I. Hussain, F. Renda, Z. Iqbal, M. Malvezzi, G. Salvietti, L. Seneviratne, D. Gan, D. Prattichizzo, Modeling and prototyping of an underactuated gripper exploiting joint compliance and modularity. IEEE Robotics and automation letters, 3(4):2854-2861, 2018

International Conferences

1. M. Pozzi, C. Gaudeni, Z. Iqbal, D. Prattichizzo, M. Malvezzi. Modeling a sensorized soft layer for adding compliance to the environment in robotic manipulation. In Advances in Italian Mechanism Science, Pages 370-377, Cham, 2021.

2. M. Pozzi, C. Gaudeni, Z. Iqbal, D. Prattichizzo, M. Malvezzi, Modeling a Sensorized Soft Layer for Adding Compliance to the Environment in Robotic Manipulation, The International Conference of IFToMM ITALY, Pages 370-377, 2020.

3. M. Dragusanu, T. Lisini Baldi, Z. Iqbal, D. Prattichizzo, M. Malvezzi. Design, Development and Control of a Tendon-actuated Exoskeleton for Wrist Rehabilitation and Training. In Proc. IEEE Int. Conf. on Robotics and Automation, Paris, FR, June 2020.

4. G. Salvietti, Z. Iqbal, M. Malvezzi, T. Eslami, D. Prattichizzo. Soft Hands with Embodied Constraints: The Soft ScoopGripper. In Proc. IEEE Int. Conf. on Robotics and Automation, Pages 2758-2764, Montreal, Canada, May 2019.

5. I. Hussain, M. Anwar, Z. Iqbal, R. Muthusamy, M. Malvezzi, L. Seneviratne, D. Gan, F. Renda, D. Prattichizzo, Design and prototype of supernumerary robotic finger (SRF) inspired by fin ray® effect for patients suffering from sensorimotor hand impairment, IEEE International Conference on Soft Robotics (RoboSoft), Pages 398-403, 2019.

6. G. Salvietti, Z. Iqbal, I Hussain, D. Prattichizzo, M. Malvezzi. The Co-Gripper: a Wireless Cooperative Gripper for Safe Human Robot Interaction. In Proc. IEEE/RSJ Int. Conf. Intelligent Robots and Systems, Pages 4576-4581, Madrid, Spain, 2018.

7. I. Hussain, Z. Iqbal, M. Malvezzi, L. Seneviratne, D. Gan, D. Prattichizzo. Modeling and Prototyping of a Soft Prosthetic Hand Exploiting Joint Compliance and Modularity. In 2018 IEEE International Conference on Robotics and Biomimetics (ROBIO), Pages 65-70, Kuala Lumpur, Malaysia, December 2018.

Book Chapters

1. I. Hussain, Z. Iqbal, M. Malvezzi, D. Prattichizzo, G. Salvietti. How to 3D-Print Compliant Joints with a Selected Stiffness for Cooperative Underactuated Soft Grippers. In Human-Friendly Robotics 2019. HFR 2019, F. Ferraguti, V. Villani, L. Sabattini, M. Bonfé (eds.), Vol. 12, pp. 139-153, Springer, Cham, 2020.

2. M. Malvezzi, M. C. Valigi, G. Salvietti, Z. Iqbal, I. Hussain, D. Prattichizzo, Design criteria for wearable robotic extra–fingers with underactuated modular structure, The International Conference of IFToMM ITALY, pages 509-517, 2018.

Muhammad Zubair Iqbal
30.08.2021
23:25:19
GMT+01:00